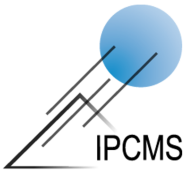

Université de Strasbourg

IPCMS: CNRS - UMR 7504

Thèse de Doctorat

FIRST-PRINCIPLES SIMULATIONS OF THE INTERACTION OF METAL-ORGANIC MOLECULES WITH A SURFACE AND AS BUILDING BLOCKS FOR NANODEVICES

par

Burak Özdamar

présentée en vue d'obtenir le grade de

Docteur de l'Université de Strasbourg

Spécialité: Physique de la matière condensée et des matériaux

Soutenue publiquement le 28/10/2016 à l'IPCMS devant le jury composé de:

Prof. Dr. Roberto Marquardt	UdS-LCQ	Président
Prof. Dr. Jürg Hutter	UZH-CMSZH	Rapporteur
Prof. Dr. Andres Saul	AMU-CINaM	Rapporteur
Prof. Dr. Fabrizio Cleri	UL1-IEMN	Rapporteur
Dr. Sébastien Le Roux	UdS-IPCMS	Examinateur
Prof. Dr. Mauro Boero	UdS-IPCMS	Directeur de thèse

Tired of lying in the sunshine staying home to watch the rain
You are young and life is long and there is time to kill today
And then one day you find ten years have got behind you
No one told you when to run, you missed the starting gun.

Roger Waters

Abstract

UNIVERSITÉ DE STRASBOURG

Institut de Physique et Chimie des Matériaux de Strasbourg

Doctor of Philosophy

FIRST-PRINCIPLES SIMULATIONS OF THE INTERACTION OF METAL-ORGANIC MOLECULES WITH A SURFACE AND AS BUILDING BLOCKS FOR NANODEVICES

by Burak Özdamar

The purpose of this study is to investigate the interaction of organometallic complexes with transition metals. This topic in question has a broad array of applications in a number of domain; realization of nanojunctions for molecular nanoelectronics, biological imaging and nanocatalysis. Within this general framework, this PhD project aims to model the fundamental interactions of molecular building blocks at the atomic level in order to understand their role in the assembly and functionalization of nanostructures. The principal tool used in this study is first-principles simulation methods such as the Born-Oppenheimer and Car-Parrinello molecular dynamics. The first chapter presents an emphasis of the current developments in the related field alongside of a retrospective on the historical developments that leads today's knowledge. The second chapter presents the basic elements of the theory behind the methods that were used in the thesis, whose development has also been contributed during this research project. Lastly, the third chapter which is organized in three sub-chapters enumerates and describes the results of the various systems studied:

i) Interaction of single Fe and Co atoms with ferrocene molecule which is also deposited on a Cu(111) slab in the perspective of possible molecular junctions.

ii) Effects of water molecule traces on the ligand desorption process of precursor molecules, Fe and Co stearate, for functionalized Fe and Co oxide nanoparticle synthesis.

iii) Investigation of the interaction of transition metals, Pt and Pd, with buckminsterfullerene (C_{60}) molecule in the purpose of hydrogen storage and nanocatalysis applications.

Majority of the work presented in this thesis has already been accepted in various journals for publication.

- B. Özdamar, C. Massobrio, M. Boero. Stability and Destabilization Processes in the Formation of Ferrocene-Based Metal–Organic Molecule–Metal Nano-Junctions. *J. Phys. Chem. C*, 120:1382, 2016.
- B. Özdamar, M. Boero, C. Massobrio, D. Felder-Flesch, S. Le Roux. Exohedral M-C_{60} and M_2-C_{60} (M = Pt, Pd) systems as tunable-gap building blocks for nanoarchitecture and nanocatalysis. *J. Chem. Phys.*, 143:114308, 2015.
- M. Boero, A. Bouzid, S. Le Roux, B. Özdamar, and C. Massobrio. First-Principles Molecular Dynamics Methods: An Overview in Molecular Dynamics Simulations of Disordered Materials: From Network Glasses to Phase-Change Memory Alloys. C. Massobrio, J. Du, M. Bernasconi, and S. P. Salmon (Eds.), (pp. 33-55). Springer International Publishing, 2015. ISBN: 978-3-319-15674-3.

Acknowledgements

First and foremost, I would like to express my deepest gratitude to my supervisor Mauro Boero for conveying his vast knowledge in all aspects of computational physics and chemistry. This thesis would never have been complete, thorough and yet possible without his continuous and sincere assistance. For over three years of my PhD study, I have learned a lot from him, not only limited to science but also about social skills, if need be. I could never have thought a supervisor more intellectual, devoted, charitable and friendlier than him.

I would like to thank Carlo Massobrio for his insightful contributions to my PhD study and his tips and tricks about acquiring the harmony in everyday life.

I would also like to thank Jürg Hutter, Roberto Marquardt, Fabrizio Cleri, Andres Saul and Sébastien Le Roux for accepting to attend as jury members and for their efficient and helpful corrections and suggestions.

I am grateful to Assil Bouzid first for his friendship to help me adjust to Strasbourg in my early days and also for sparing his time to familiarize me with the functioning of CPMD. I would like to acknowledge Assil for his contributions to the calculations of stearate compounds.

I am also thankful to Ziyad Chaker for his excellent friendship and for involving me with his fruitful (and generally challenging) scientific and philosophical discussions.

I would like to thank Guido Ori and Emilie Delahaye with whom I share an office at different periods of my stay in IPCMS.

I cannot pass without mentioning and thanking Hashim Jabbar, Jérôme Hurst, Adam Brandstetter-Kunc, Michal Studniarek, Ousmane Ly, Beata Taudul, Kevin Makles, Stanislav Makarchuk, Moussa Gueye and many others for their friendship.

I would like to extend my deepest feelings to Burcu Onurlu for her emotional support and self-devotion when I was on the verge of losing my motivation.

Last but not least, I am thankful to my parents for their endless support and encouragements.

Contents

List of Figures

List of Tables

Résumé

UNIVERSITÉ DE STRASBOURG

Institut de Physique et Chimie des Matériaux de Strasbourg

Philosophiæ doctor

ÉTUDE PAR SIMULATIONS À L'ÉCHELLE ATOMIQUE DE L'INTERACTION DE MOLÉCULES ORGANOMÉTALLIQUES AVEC UNE SURFACE ET BRIQUES ÉLÉMENTAIRES POUR LA RÉALISATION DE NANO-DISPOSITIFS

par Burak Özdamar

Ce travail de thèse est focalisé sur l'interaction de molécules organométalliques avec des métaux de transition. Cette thématique a un large éventail d'applications dans plusieurs domaines tels que la réalisation de nanojonctions pour la nano-électronique, la bioimagerie et le stockage d'énergie magnétique, la nano-catalyse et les applications biomédicales. Dans ce cadre général, ce projet de thèse vise la modélisation à l'échelle atomique des interactions fondamentales entre les briques moléculaires afin de comprendre leur rôle dans l'assemblage et la fonctionnalisation des nanostructures. L'outil principal utilisé est la dynamique moléculaire à partir des premiers principes selon les approches Born-Oppenheimer et Car-Parrinello. La première partie de cette thèse présente une rétrospective du domaine afin de donner une vision d'ensemble des méthodes utilisées et de l'état de l'art dans ce domaine. Le deuxième chapitre donne les éléments de base de la théorie et les méthodes qui ont été utilisées dans la thèse, au développement desquels on a aussi contribué pendant ce projet de recherche. Les résultats obtenus et leur discussion

critique constituent le corps principal de cette ouvrage de thèse. Ceci est organisé dans un chapitre unique (troisième chapitre), divisé en trois sous-chapitre pour des raisons de clarté.

L'électronique moléculaire est un domaine de recherche de pointe et innovant en nanotechnologie qui a pour but d'étudier l'exploitation de molécules individuelles censées fonctionner comme des dispositifs électroniques indépendants capables d'imiter le comportement de composants conventionnels comme des commutateurs, des transistors ou encore des diodes dans un circuit microélectronique. Composés organométalliques organisés en couches portant des métaux de transition au cœur du complexe (notamment ferrocènes et cobaltocènes) ont été et sont toujours les cibles privilégiées de cette ligne de recherche en raison de leur structure tridimensionnelle, par rapport aux complexes bidimensionnelles de phthalocyanine. Dans ce scenario, nous nous sommes focalisés sur le ferrocène, composé organométallique découvert il y a plus d'un demi-siècle, mais dont les applications pratiques sont encore au stade pionnier au niveau mondial et, en particulier, au sein de l'IPCMS qui participe activement à ces études. Comprendre et maîtriser le comportement des états d'interface est donc l'enjeu cruciale pour la réalisation des analogues moléculaires de dispositifs semi-conducteurs utilisés couramment. Pour cette raison, dans une première étape de ce travail, la déposition d'atomes métalliques de transition, tels que Fe et Co, sur du ferrocène déposé sur un substrat de cuivre Cu(111) a été la cible de nos calculs de dynamique moléculaire par premiers principes.

Déposition d'un atome de métal de transition au-dessus d'une molecule de ferrocène

Les tubes à vide, inventé en 1904 par John Ambrose Fleming, ont été un composant de premier plan qui amplifie le signal dans les circuits électriques jusqu'à l'invention du transistor. Le premier exemple d'un transistor bipolaire était de type point-contact et il est présenté au marché en 1947. Le domaine des semi-conducteurs s'est accéléré après l'invention du transistor et a montré une forte tendance à la miniaturisation. Après l'introduction de circuits intégrés, les puces électronique

ont trouvé leur chemin dans pratiquement chaque dispositif électronique depuis plus d'un demi-siècle.

Gordon Moore a présenté la *loi de Moore* en 1965 qui prédit que le nombre de transistors dans les microprocesseurs double en deux ans. Des développements rapides dans le domaine de l'électronique ont été effectués par de nombreux groupes tant dans l'académie que l'industrie dans des champs divers de la miniaturisation de composants électroniques à la découverte de méthodes de synthèse différentes. Cependant, des effets quantiques commencent à s'immiscer et certains problèmes apparaissent comme les tailles des composants devenant plus petits. Le courant de fuite est encore une autre problème qui contribue aux inconvénients existants; la couche d'isolation est exigée pour être progressivement meilleure et plus délicate pour empêcher les court-circuits.

"L'électronique moléculaire" ou "l'électronique à l'échelle moléculaire" est un domaine émergent qui a pour but d'étudier des molécules individuelles qui fonctionnent comme des dispositifs électroniques indépendants capables d'imiter le comportement de composants conventionnels comme des commutateurs, des transistors et des diodes dans un circuit microélectronique.

Bien qu'il y ait plusieurs études sur la nanoélectronique à base de molécules [1], le point de départ "officiel" de l'électronique moléculaire est souvent attribué au travail théorique pionnier d'Aviram et Ratner en 1974 [2].

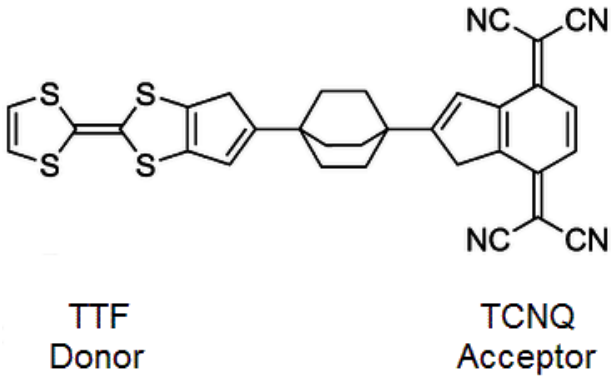

FIGURE 1: Redresseur moléculaire proposé par Aviram et Ratner en 1974. TTF en tant que groupe de donateurs, TCNQ comme un groupe accepteur relié par un pont σ.

Ceci a été basé sur la possibilité qu'une molécule biologique(organique) pourrait être utilisée comme une diode de jonction p-n quand un donneur (D) et un groupe (A) accepteur sont séparés par un groupe d'entretoise (σ); c'est-à-dire "accepteur-isolant-donneur" (D-σ-A) diode moléculaire comme esquissé dans la Figure 1.

Les composés organométalliques en couches portant des métaux de transition ont attiré une grande attention en raison de leur structure tridimensionnelle par opposition aux phthalocyanines en deux dimensions [4]. Un des composés organométalliques le plus important qui a été découvert il y a plus d'un demi-siècle est le fer bis-cyclopentadiényle [5], dit ferrocène (voir Figure 2).

Il a posé un jalon dans le domaine de la chimie organométallique avec ses propriétés uniques et intrigantes, et par conséquent a ouvert la voie à la découverte de blocs similaires de construction moléculaire en 3D. Dans un travail expérimental effectué par Engtrakul et Sita [6], une molécule ferrocène est destinée à être utilisée comme une diode en reliant les deux unités pridyl qui vont acquérir des potentiels d'oxydo-réduction différents en appliquant une tension de polarisation.

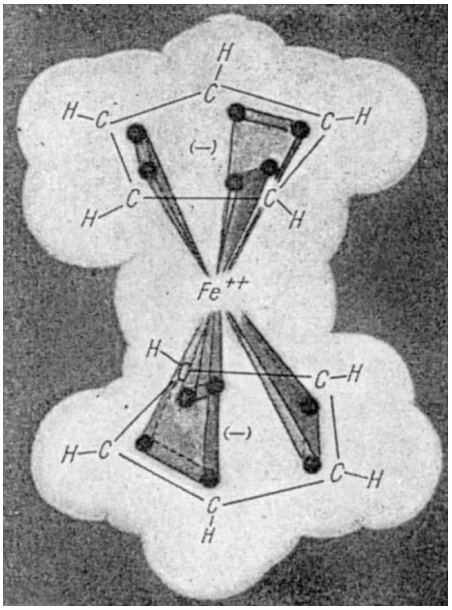

FIGURE 2: Un dessin de la molécule du fer bis-cyclopentadiényle, autrement dit, ferrocène [3].

Par ailleurs, ferrocène a été déposé à l'IPCMS avec succès au dessus de Cu(111) expérimentalement, formant une monocouche sans donner lieu à une décomposition [7]. La déposition d'un seul atome de cuivre sur la monocouche de ferrocène a été réalisé aussi utilisant des simulations théoriques par premiers principes, dynamique moléculaire de Born-Oppenheimer en particulier [8]. Comprendre et par conséquent affiner le comportement des états d'interface est la partie la plus cruciale dans la réalisation des analogues moléculaires de dispositifs semi-conducteurs. Pour cette raison, dans ce travail, la déposition d'atomes de

métaux de transition tels que Fe et Co au dessus du ferrocène en utilisant des simulations théorique a été ciblé.

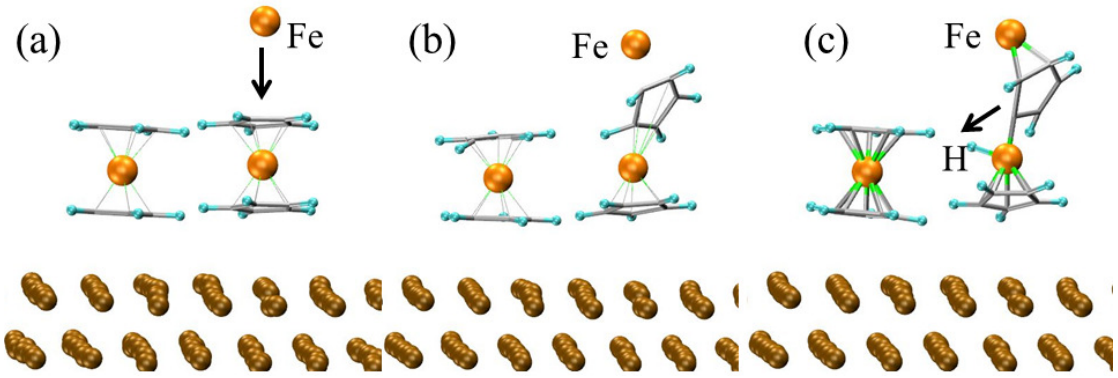

FIGURE 3: Procédure de déposition d'un atome de fer sur l'une des deux molécules de ferrocène physisorbée sur la surface de Cu(111). (A) approche de l'atome Fe. (B) Déstabilisation de l'anneau supérieure Cp par l'atome Fe qui approche. (C) Départ de l'anneau supérieure Cp / complexe Fe accompagné par transfert de H. Le code de couleur est cyan pour H, gris pour C, orange pour Fe et brun pour Cu.

Ces simulations ont montré que l'approche du fer, d'abord placé à une distance d'environ 3.5 Å au-dessus de l'anneau supérieure C_5H_5, se déroule d'une manière sans barrières. L'atome Fe se rapproche progressivement de l'anneau d'hydrocarbure et finalement il atteint une distance d'équilibre de 2,0 Å au-dessus de l'anneau. Cependant, contrairement au cas de déposition de Cu [8], une déstabilisation de la molécule de ferrocène se produit. L'anneau supérieure C_5H_5 se coordonne assez fortement avec l'atome Fe déposé et forme un complexe stable. Cet anneau supérieur quitte alors le ferrocène auquel il appartenait au début de la simulation, et le complexe nouvellement formé Fe–C_5H_5 devient un groupement indépendant qui part du substrat, laissant exposé le Fe appartenant au ferrocène à l'origine physisorbée. Ce processus est esquissé dans les panneaux (a) et (b) de la Figure 3. La déstabilisation qui se produit après la déposition de fer, bien qu'ayant une conséquence négative évidente pour la réalisation pratique d'une nanojunction à première vue, ne doit pas être considéré comme un échec pur. En fait, les complexes de fer–cyclopentadiényle représentent des précurseurs utiles pour les complexes de carbène de fer et une partie catalytique importante [9, 10].

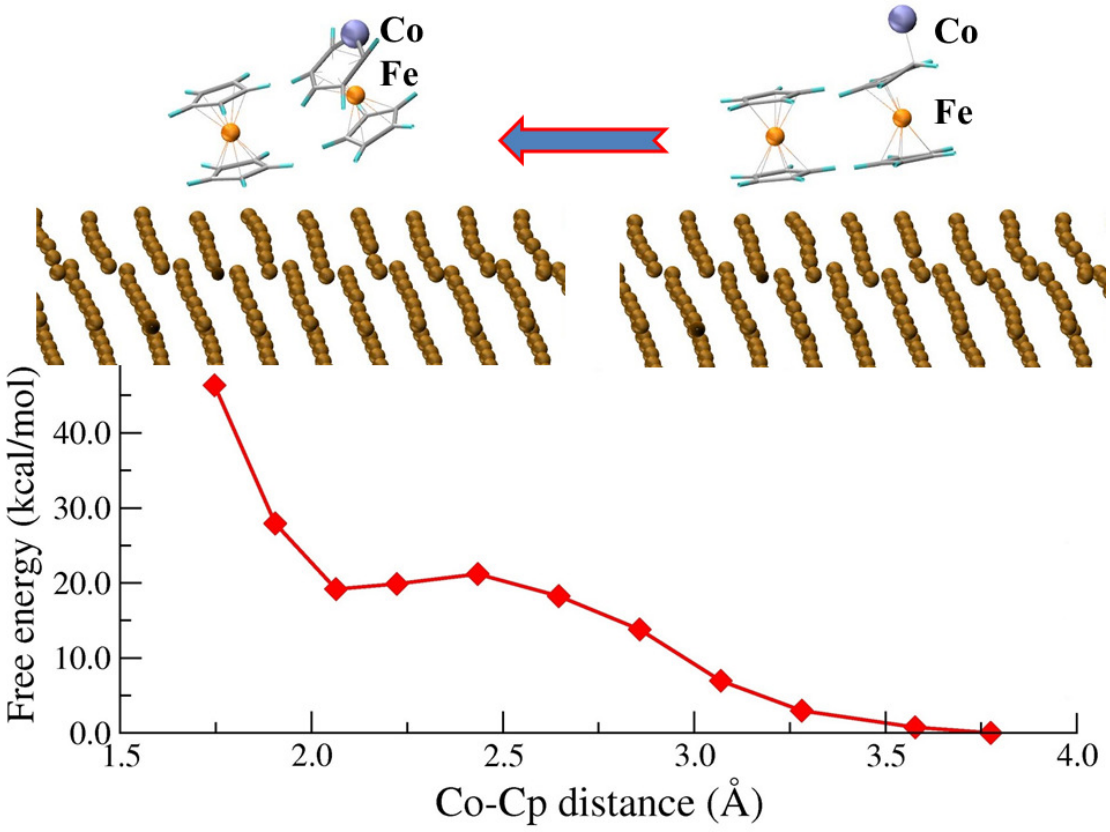

FIGURE 4: La déposition d'un atome de cobalt sur une des deux molécules de ferrocene physisorbé sur un substrate de Cu(111). Une barrière d'énergie libre d'environ 21.17 kcal/mol doit être surmontée. Les panneaux supérieurs montrent l'approche de Co et l'insertion de cet atome dans l'anneau supérieure Cp. Ce nouveau composé métastable est finalement désorbé à partir du substrat. Le code de couleur est identique à celle de Figure 3 avec l'atome de Co en bleu.

Une deuxième série de simulations a été réalisée mettant l'accent sur la déposition de Co sur le ferrocène physisorbée. En contradiction avec Fe ([Ar] $3d^6 4s^2$), la structure électronique de Co ([Ar] $3d^7 4s^2$) constitue une seule orbitale d supplémentaire. Toute tentative de déposition d'un atome de Co sur le ferrocène au sein du protocole adopté pour la simulation de l'atome Fe n'a pas donné lieu à la formation d'un complexe Co-ferrocène, ni de processus de déstabilisation. En fait, l'atome de Co initialement placé à une distance d'environ 3.5 Å de l'anneau supérieure Cp ne pouvait pas approcher plus proche à moins de 3.0-2.8 Å. Contrairement a la déposition de fer, il existe une barrière qui empêche l'atome Co d'approcher vers l'anneau Cp. Pour estimer cette barrière et analyser une voie possible de coordonner Co sur le ferrocène déposé, la technique d'échantillonnage de l'énergie

libre connu sous le nom de “Blue Moon ensemble” ont été utilisée [11]. Le panneau supérieure de la Figure 4 montre l'évolution de l'atome Co. La courbe rouge de la Figure 4 signifie l'énergie libre en fonction de la distance de Co-Cp. En contraignant l'approche de l'atome de Co, le système doit surmonter une barrière de 21.17 kcal/mol (0.92 eV) pour arriver à nouveau minimum. Ce minimum ne correspond pas à une coordination simple de Co avec l'anneau Cp, mais à une insertion complète de l'atome de Co dans le cycle hydrocarboné. Cette nouvelle structure est en effet stable, bien que ne résultant pas d'une formation de nanojunction, l'approche de Co peut être un moyen viable pour extraire des unités de ferrocène sélectivement à partir d'une monocouche déposée pour créer des motifs moléculaires ou des propriétés catalytiques pour la polymérisation des alcynes [12].

Précurseur pour la synthèse de nanoparticule d'oxydes de Fe et Co: Stéarate de Fe et le stéarate de Co

Les nanoparticules (NP) fonctionnalisés d'oxyde de métal ont été étudiées largement dans la littérature pour leur large champ d'applications allant des dispositifs magnétiques et électroniques à des applications biomédicales; agents de stockage de données et de fluides magnétiques pour le système micro / nanoélectromécanique (MEMS / NEMS) ainsi que des agents pour l'imagerie par résonance magnétique et des modules de distribution de médicaments contrastant l'image peuvent être donnés comme exemples [13]. Les propriétés physiques et chimiques des NPs dépendent fortement non seulement de leur composition, mais aussi de leur taille et de la morphologie [14].

Le groupe expérimentale à l'IPCMS ont mis au point un protocole de synthèse d'oxyde de fer par décomposition thermique de stéarate de fer en présence d'acide oléique -utilisé comme un ligand stabilisant- dans un solvant à haut point d'ébullition. En contrôlant la quantité d'acide oléique, la température de réaction, le taux de chauffage et de la nature des solvants, des NP d'oxyde de fer enrobées d'acide oléique ont été synthétisés avec une taille moyenne dans la plage de 4 à 28 nm [15]. Comme les efforts expérimentaux révèlent, bien que le fer et le cobalt stéarate aient des configurations identiques, les processus de désorption de ces deux espèces ont des modes bien distincts. La synthèse de nanoparticules d'oxyde de cobalt par

décomposition thermique de stéarate Co a été montrée plus difficile par rapport à celle de Fe_3O_4, dans des conditions expérimentales identiques.

Il existe plusieurs méthodes pour la synthèse de nanoparticules d'oxyde métallique. Parmi ces techniques, la décomposition thermique spontanée représente l'une des approches les plus efficaces pour affiner la distribution de la taille et la morphologie des NPs d'oxyde métallique presque monodisperses avec un rendement considérablement élevé. Cette technique contient la décomposition du précurseur métallique à haute température dans un solvant non aqueux en présence du ligand correspondant. Divers complexes métalliques portant les sels d'acides gras tels que l'acétate, oléate et stéarate ont été utilisés comme précurseurs pour la synthèse [16]. Même si les stéarates sont généralement insolubles dans l'eau en raison des longues chaînes hydrocarbonées hydrophobes, des molécules d'eau, de même que l'humidité atmosphérique, peut approcher le cation métallique afin de former une couche d'hydratation [17]. En conséquence, le but principal de ce travail est d'étudier les effets induits par la présence de molécules d'eau sur la structure et la stabilité des composés de stéarate. Bien que cette méthode soit assez simple et économique, les interactions des impuretés organiques pourraient conduire à des problèmes potentiels. En outre, la présence des molécules d'eau à travers le cation métallique provoque le ligand précurseur à former des liaisons hydrogène. En conséquence, la barrière d'activation élevée cause le processus de désorption se produisant d'une manière non favorable. Figure 5 montre les configurations initiales des composés M-stéarate.

Le "Blue Moon ensemble" [11] a été utilisée de nouveau pour estimer le barrière d'énergie libre du processus de désorption. La coordonnée de réaction choisie est la distance entre l'atome de métal central et le ligand, comme indiqué dans le Figure 5a. Des simulations Car-Parrinello de dynamique moléculaire (CPMD) ont été réalisées dans le schéma de DFT en utilisant le code CPMD [18]. La fonctionnelle d'échange-corrélation BLYP a été utilisée pour décrire les contributions d'échanges et de corrélations [19]. Les interactions de cœur-valence de Fe et Co ont été décrites par la pseudopotentiel conservant la norme de Troullier-Martins [20]. Les états 2s et 2p pour C et 1s pour H ont été explicitement traités comme des électrons de valence dans l'approche pseudopotentiel. Les orbitales des électrons de valence ont été représentées en termes d'ondes planes avec un "cut-off" d'énergie de 80

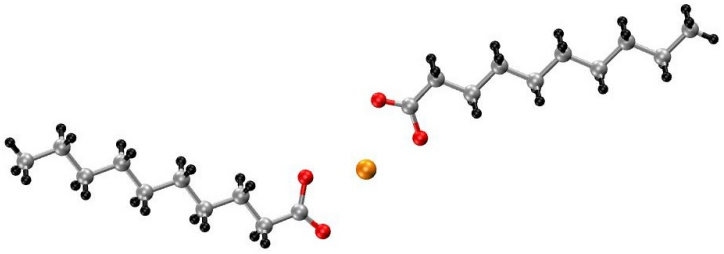

(A) M-stearate en condition sèche.

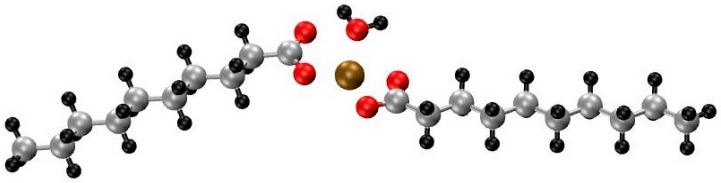

(B) M-stearate avec une molécule d'eau autour de centre métallique.

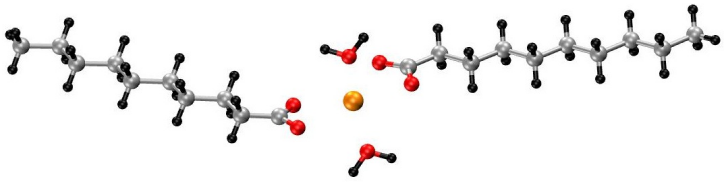

(C) M-stearate avec deux molécule d'eau: Coordination octaédrique de M-O.

FIGURE 5: Configurations initiales des composés M-stéarate, M=Fe, Co.

Ry. Les interactions van der Waals ont également été inclus selon la formulation D2 de Grimme [21].

La simulation du système à base de fer dans des conditions sèches a été réalisée avec la géométrie équilibrée donnée dans la Figure 5a. La coordonnée de réaction est déterminée comme la distance entre Fe-COO et la distance d'équilibre est d_{Fe-COO} = 2.31 Å. L'application de la dynamique contrainte proposée par l'approche Blue Moon a été réalisée à partir de la distance d'équilibre avec des incréments environ 0.1 Å. L'évolution structurelle finale du système a base de fer a été donnée dans la Figure 6.

Le profil de l'énergie libre résultant du processus de désorption est donné dans la Figure 7. Après avoir surmonté l'état de transition où la barrière d'énergie libre est ΔF = 15.02 kcal/mol (0.65 eV), le partage d'oxygène continue jusqu'au distance de Fe-C atteint d_{Fe-COO} = 3.52 Å. Comme l'application de contrainte procède,

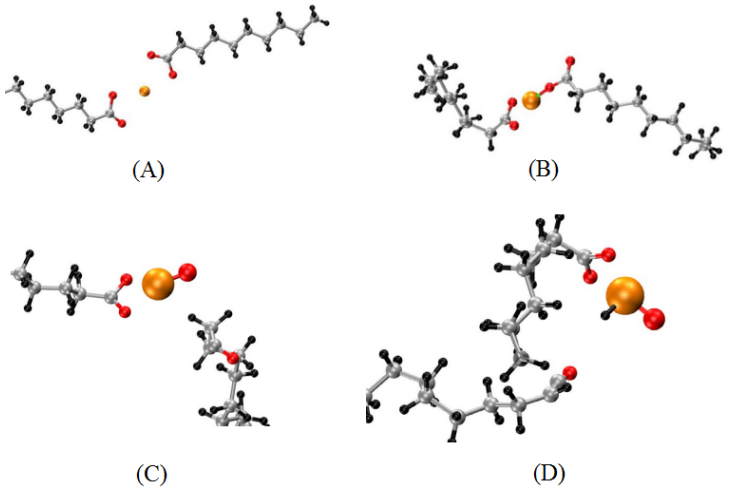

FIGURE 6: Évolution structurelle du stéarate de fer dans des conditions sèches. Le fer est oxydé après avoir surmonté le barrière de transition et de germe de FeO est formé. Les distances de Fe-COO sont 2,31, 3,07, 3,52, 4,52 Å.

l'atome de carbone est poussé plus loin du fer, accompagné d'un transfert de β-hydrogène comme on peut le voir dans la Figure 6(D). Le plateau dans la force de contrainte moyenne et l'énergie libre à partir de $d_{Fe-COO} \sim 4.00$ Å indique que l'interaction du fer avec la chaîne de carbone est terminée.

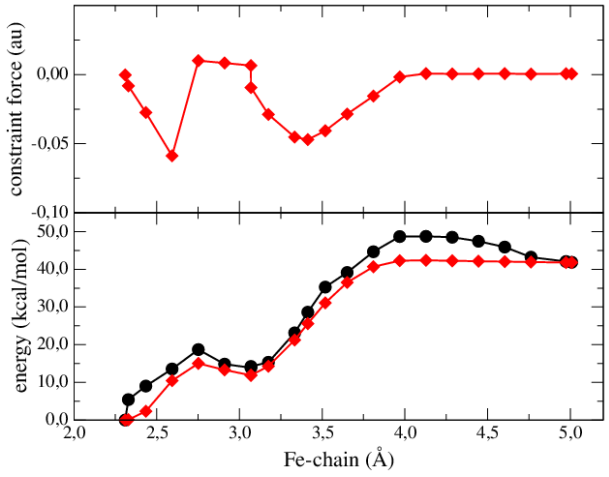

FIGURE 7: La force de contrainte (la panneau supérieur) et l'énergie libre et total (la panneau inférieur) pour le désorption de la chaîne pour la système a base de fer a la température 300 K dans la condition sèche. La courbe rouge et noir montrent le profil d'énergie libre et l'énergie total.

A la lumière de ces informations préliminaires, le système à base de cobalt a été étudié dans des conditions identiques. Le profil d'énergie libre de ce système a été

donné dans la Figure 8. Selon le profil, la barrière d'énergie pour dépasser l'état de transition est $\Delta F = 20.85$ kcal/mol (0.90 eV) lorsque la distance Co-COO indique $d_{Co-COO} = 2.75$ Å, au même point où le système à base de fer possède une barrière d'énergie libre de 15.02 kcal/mol (0.65 eV). Ce résultat fondamental peut être une des raisons principales qui provoque la différence dans la formation de nanoparticules de fer et de cobalt lors de la réaction de décomposition thermique rapportés par l'équipe expérimentale à l'IPCMS.

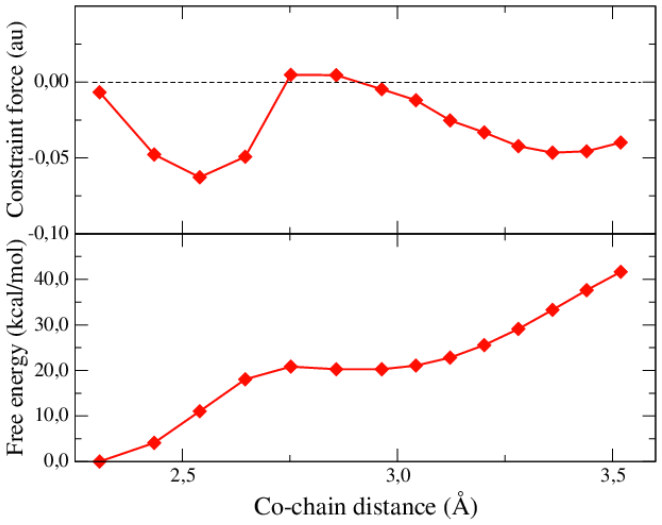

FIGURE 8: La force de contrainte (la panneau supérieur) et l'énergie libre (la panneau inférieur) pour le désorption de la chaîne pour la système à base de cobalt à la température 300 K dans la condition sèche.

La simulation du système à base de fer avec une molécule d'eau a été réalisée avec les mêmes paramètres. Cependant, l'échappement de la molécule d'eau de la couche d'hydratation de l'atome de fer transforme la configuration à celle des conditions sèches. Figure 9 et Figure 10 montrent le profil d'énergie libre et l'évolution structurelle du système concerné, respectivement. La molécule d'eau s'est éloignée dans une courte durée. Comme prévu à partir des résultats de son analogue dans des conditions sèches, le germe de FeO peut se former.

Un calcul identique donne des résultats similaires pour le cas de cobalt. Cependant, la simulation de la même configuration a été répétée à partir des conditions initiales avec une seconde contrainte sur la distance eau–cobalt pendant l'équilibration afin de stabiliser la molécule d'eau. Toutefois, un comportement similaire a été observé avec cette tentative aussi, la molécule d'eau s'est retirée du voisinage

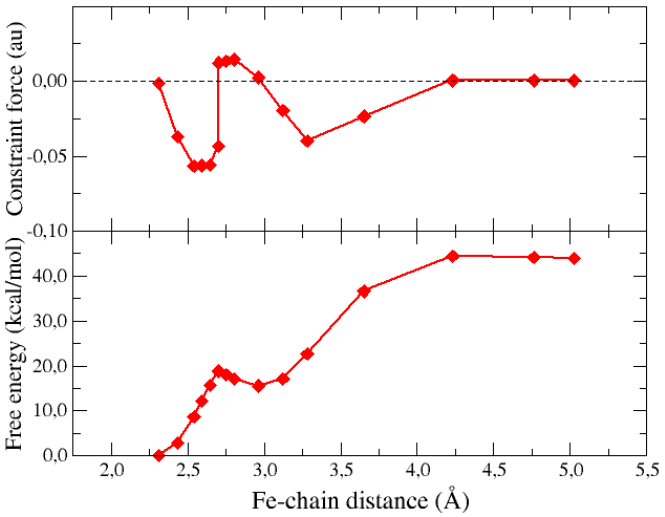

FIGURE 9: La force de contrainte (la panneau supérieur) et l'énergie libre (la panneau inférieur) pour le désorption de la chaîne pour la système à base de fer à la température 300 K en présence d'une molécule d'eau. La barrière d'énergie pour dépasser l'état de transition est 18.86 kcal/mol (0.82 eV) lorsque la distance Fe-COO = 2.70 Å.

du métal dès que la contrainte sur la molécule d'eau est éliminée. On peut donc conclure que la coordination du métal de transition ne peut pas accommoder même une seule molécule d'eau lorsque la couche d'hydratation n'est pas complet. La comparaison des profils d'énergie libre des deux systèmes (Figure 7 et Figure 9) soutient également cette idée.

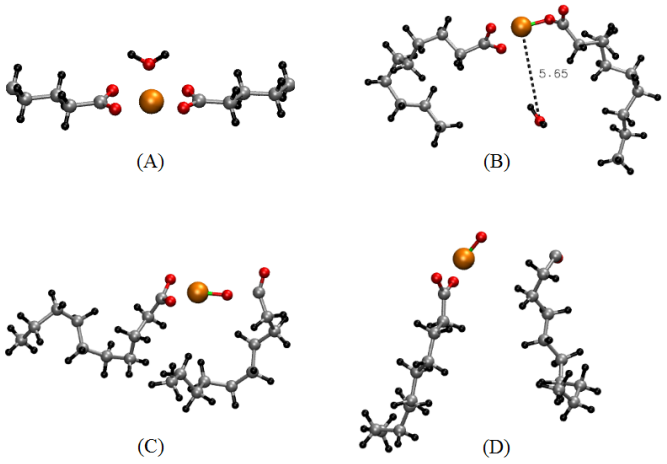

FIGURE 10: L'évolution structurelle de la stéarate de fer en présence d'une molécule d'eau à 300 K. Le système devient comme la condition sèche puisque le molécule d'eau s'échappe de la couche de hydratation du métal.

Des études informatiques ont été exécutées pour évaluer l'effet de traces d'eau sur ces scénarios. Les stéarates de Fe et Co ont montré que la formation de précurseurs d'oxyde de fer pour synthétiser des NPs continue avec une barrière d'activation significativement inférieure que le processus analogue pour Co en absence de traces d'eau, c'est-à-dire, environ 15 kcal/mol pour la stéarate de Fe contre presque 21 kcal/mol pour la stéarate de Co. Puisque la géométrie de coordination de Fe et Co est tétraédrique ou octaédrique, il a été trouvé qu'un seule molécule d'eau ne peut pas être retenu autour de la couche de hydratation du métal, donc les systèmes de 1-H_2O transforment aux conditions sèches. La tentative de se rétracter de la chaîne d'hydrocarbure du centre de Fe provoque le mécanisme d'échange dissociatif en présence des deux molécule d'eau. La fragmentation des chaînes hydrocarbure peut mener à la formation de Co-OH ou même des précurseurs d'hydroxyde de cobalt.

Les systèmes exohedral de fullerène M–C_{60} et M_2–C_{60} (M = Pt, Pd)

La conception de sources d'énergie novatrices, vertes, renouvelables et durables est devenue une priorité dans le monde entier dans la recherche fondamentale et appliquée. Dans ce scénario mondial, le stockage et la livraison d'hydrogène jouent un rôle de premier plan en raison de deux problèmes majeurs: (i) sa production semble être un processus propre promu par un nombre relativement simple électrocatalyse, et (ii) son application dans les piles à combustible entraîne la production d'eau respectueuse de l'environnement, ainsi que de la chaleur et de l'électricité.

Des candidats prometteurs pour le stockage d'hydrogène et sa production sont les "Pile à combustible à membrane d'échange de protons" (Proton exchange membrane fuel cell (PEMFC)), en raison de leur capacité élevée et une large gamme d'applications. En contradiction avec les batteries traditionnelles, le PEMFC est un système ouvert, donc propulseur et comburant doivent être alimentés en continu. Dans un tel scénario, la conception du support catalytique semble être une question clé dans le développement de PEMFC. L'utilisation de nanoparticules déposées sur des agrégats de noir de carbone est un moyen efficace pour réaliser des nanostructures avec un rapport optimal surface/volume. Nous avons récemment

mis l'accent sur l'amélioration de la stabilité du support catalytique en PEMFC en explorant la possibilité d'utiliser la molécule buckminsterfullerène (C_{60}) comme support pour le catalyseur métallique. Le but est d'utiliser des cages de fullerène comme un moyen de transporter et de livrer des dopants en raison de leur haute résistance aux attaques chimiques externes et de leur stabilité thermodynamique. Les structures de carbone comme les nano-cages et les nanotubes étant moins sensible à la corrosion que le noir de carbone, on peut en déduire que C_{60} pourrait être un bon candidat pour le remplacer ainsi. Par ailleurs, on peut lier des métaux de transition tels que le platine et le palladium, à C_{60} en utilisant des liaisons de coordination pour créer métallo-fullerènes [22].

Compte tenu de l'insuffisance des champs de force classiques pour décrire les systèmes composés de C_{60} en interaction avec des atomes métalliques, nous nous appuyons sur les simulations des premiers principes dans le cadre théorie fonctionnelle de la densité (DFT) [23]. Cela permet de rendre compte des deux propriétés structurales et électroniques, ce dernier étant le problème majeur dans les PEMFC. Plus précisément, nous présentons une étude systématique des fullerènes en interaction avec des atomes Pt et Pd visant à identifier les structures stables, résultant d'emplacements spécifiques des atomes métalliques et leur nombre (un ou deux) sur la surface externe de la C_{60}. L'information géométrique est étayée par une analyse approfondie de la liaison et de la structure électronique des modifications locales en termes de fonctions et de centres de Wannier maximale localisées.

Une première série de simulations a été réalisée sur des systèmes contenant N=61 atomes: 60 C et 1 atome de métal, soit Pt ou Pd. Après avoir trouvé la conformation la plus stable M-C_{60}, un second ensemble de simulations a été effectué sur des systèmes de N=62 atomes: 60 C et 2 atomes métalliques, soit deux Pt, deux Pd, ou une paire de Pd-Pt. Cinq configurations initiales différentes ont été préparées, différant par la position de l'atome de métal sur la surface du C_{60} comme résumées dans la Figure 11. La stabilité des différentes configurations sont résumées dans le Table 1 en termes d'énergies totales relatives. Dans ce tableau, les effets de la dynamique moléculaire amortie deviennent évidents en comparant les première et seconde colonnes, en se référant à la configuration initiale et finale, respectivement. Dans certains cas, l'atome de métal se dresse au sommet d'une liaison C-C entre soit deux hexagones (π-66) ou un hexagone et un pentagone (σ-65). Ces

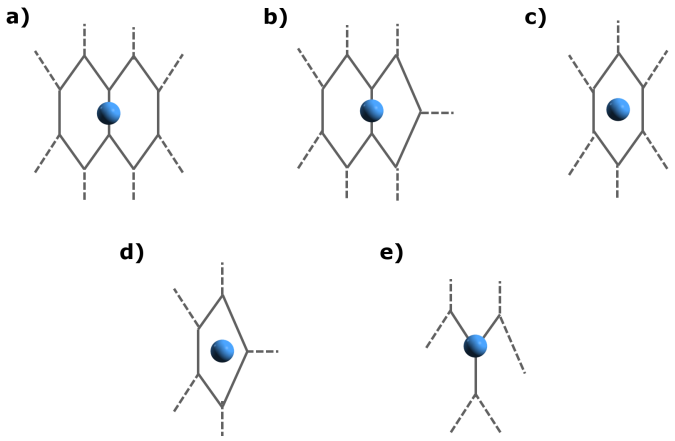

FIGURE 11: Représentation schématique des configurations initiales utilisées dans nos simulations. Les étiquettes de (a) à (e) se réfèrent à la position de l'atome de métal (Pt ou Pd, sphères bleues) sur le fullerène.

configurations restent stables même après des simulations CPMD pendant 1,5-2.0 ps. Plus précisément, le (a) π-66 complexe est le plus stable pour les deux cas, alors que le (b) σ-65 complexe est situé au-dessus de ce minimum à 0.47 eV (Pt) et 0.21 eV (Pd). Le fait que la configuration σ-65 est moins stable que le π-66 est confirmée par une simule dynamique courte d'environ 1,5 à 2,0 ps.

TABLE 1: Configurations initiales et finales de systèmes M–C_{60} (M=Pt, Pd) et les différences d'énergie relatifs entre les structures stables finales pour chaque système. ΔE est en eV.

	Pt		Pd	
Initial	Final	ΔE (eV)	Final	ΔE (eV)
a	a	0.0	a	0.0
b	b	0.47	b	0.21
c	a	0.0	a	0.0
d	b	0.47	b	0.21
e	a	0.0	a	0.0

Cependant, le complexe (σ-65) doit être conservé comme un site possible d'équilibre alternatif pour le complexe métal-fullerène. Nos calculs indiquent que la présence d'un atome de métal sur un site π-66 est responsable d'une diminution du gap

d'énergie du système; 1,24 eV pour Pt et 1,12 eV pour Pd par rapport à 1,66 eV pour le fullerène isolé (voir Figure 12).

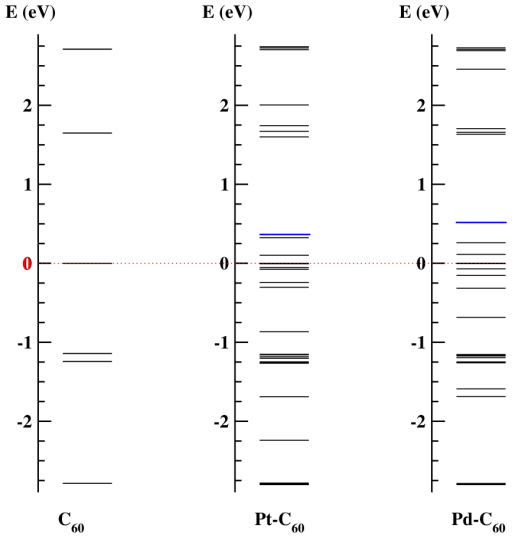

FIGURE 12: Les niveaux d'énergie Kohn-Sham pour les systèmes M-C_{60} (M= Pt, Pd) par rapport au fullerène isolé. Le panneau de gauche se réfère à la molécule de C_{60} à l'état pur, tandis que les panneaux centraux et de droite se rapportent aux systèmes Pd–C_{60} et Pt–C_{60}, respectivement.

Les WFCs (fonctions de Wannier) maximum localisées fournissent un complément d'information utiles sur la nature des liaisons chimiques. Leurs élargissement associés permettent d'identifier le nombre d'états électroniques - et dans quelle mesure - ils contribuent à la liaison métal-fullerène. Dans le panneau gauche de la Figure 13, tous les WFCs sont présentés comme des sphères rouges.

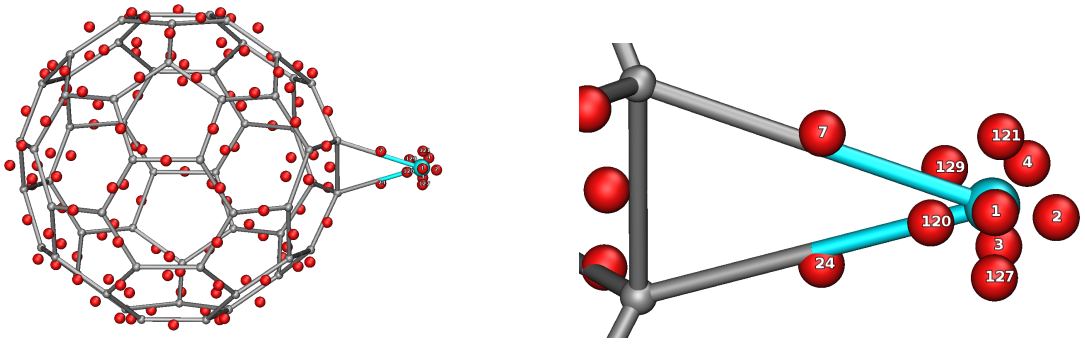

(A) (B)

FIGURE 13: Les WFC pour le complexe fullerène-Pt (panneau gauche) et des détails autour de l'interface Pt-C_{60} (panneau droite) où deux centres spécifiques, marqués 7 et 24, participent aux liaisons métal-C_{60}.

Plus intéressant pour nos besoins est la distribution de ces centres dans la région entre l'atome métallique Pt et la liaison π-66, montré dans le panneau de droite de la même figure. Une première caractéristique est la distribution isotrope de huit WFCs autour du site Pt, tous provenant principalement d'une combinaison des états 5d de Pt.

En cas de présence de deux atomes métalliques dans le système, plusieurs possibilités s'ouvrent pour l'emplacement de l'atome de métal supplémentaire sur la base de la symétrie du système. Plus précisément, huit configurations différentes sont 'a priori' possibles. Ceux-ci sont marqués de (a) à (h) et résumées dans la Figure 14. En outre, une configuration supplémentaire, identifiée par l'étiquette (i), peut être inclus en tenant compte de la structure (h) après l'inversion de la position des deux atomes métalliques, Pt et Pd.

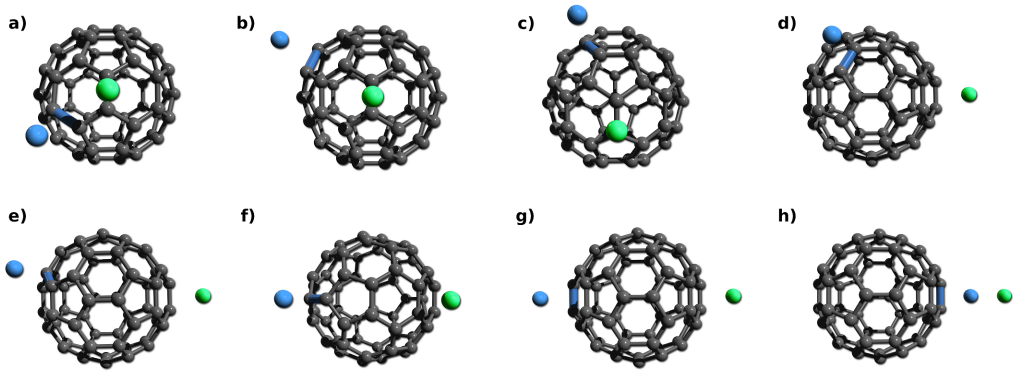

FIGURE 14: Représentation schématique des configurations initiales pour les systèmes M_2–C_{60}. Le premier atome métallique (en vert) se trouve sur la position d'équilibre (au-dessus d'une liaison π-66) déterminée dans l'étude de M–C_{60}. Puis un second atome métallique (en bleu) est ajouté au-dessus d'un autre liaison π-66 (entre deux anneaux C_6). Sur la base de la symétrie du C_{60} huit configurations initiales différentes sont possibles. A partir de (a) à (g), la distance entre les deux atomes M s'augmente. Pour $M_1 \neq M_2$, il est possible de définir une configuration supplémentaire (i) si l'ordre des positions est inversée.

Lorsque les deux atomes de métal sont du Pt, toutes les configurations de (b) à (h) sont moins stables que la configuration (a) de ~ 0.2 eV. De façon analogue, si les deux atomes de métal sont du Pd, les configurations marqués de (b) à (g) sont plus énergétique que la structure (a) de ~ 0.2 eV. Une différence notable se pose lorsque les deux atomes métalliques sont adjacents comme dans la configuration (h). En effet, en raison des distances différentes par rapport nature et l'équilibre de

Pt par rapport à Pd [24], l'alignement des deux atomes de Pd sur le même côté du fullerène est énergétiquement plus coûteux par rapport à un système métastable (la configuration (a)) de 0.81 eV.

L'ajout d'un deuxième atome de métal résulte en une nouvelle diminution du gap énergétique en ce qui concerne à la fois le fullerène isolé et le complexe de métal-C_{60}. La raison est l'apparition des états métalliques $5d^9 6s^1$ (Pt) et $4d^{10}$ (Pd) dans le gap d'énergie du C_{60}, qui deviennent des orbitales d_{z^2} et $d_{x^2-y^2}$ localisées entre les centres métalliques et le fullerène.

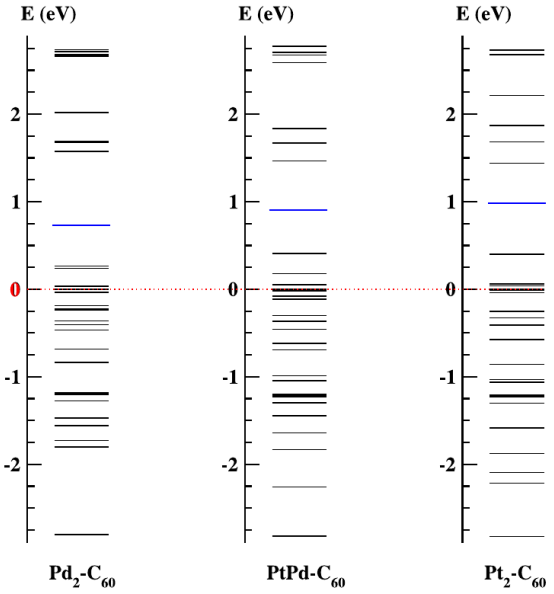

FIGURE 15: La structure de bandes pour les systèmes M_2–C_{60} (M= Pt, Pd). De gauche à droite respectivement pour: Pd_2–C_{60}, PtPd–C_{60} et Pt_2–C_{60}.

En se concentrant sur l'utilisation de complexes métallo-fullerène comme blocs de construction pour les nanostructures enclins à avoir des applications dans les piles à combustible, la catalyse et la nanoélectronique, nous avons étudié comment Pt et Pd peuvent être logés de façon stable sur la surface externe de fullerènes. Les détails à l'échelle atomique de l'interaction entre un C_{60} avec un ou deux atomes métalliques ont montré que la grande symétrie du fullerène et la structure fondamental électronique favorise la formation de sites d'adsorption Pt et Pd sur des liaisons π-66. L'interaction additionnelle entre deux atomes métalliques présents simultanément sur le fullerène est la force motrice qui établit une distinction entre les configurations stables et instables.

La majorité des travaux présentés dans cette thèse a déjà été accepté dans divers revues pour publication.

- B. Özdamar, C. Massobrio, M. Boero. Stability and Destabilization Processes in the Formation of Ferrocene-Based Metal- Organic Molecule-Metal Nano-Junctions. *J. Phys. Chem. C*, 120:1382, 2016.

- B. Özdamar, M. Boero, C. Massobrio, D. Felder-Flesch, S. Le Roux. Exohedral M-C_{60} and M_2-C_{60} (M = Pt, Pd) systems as tunable-gap building blocks for nanoarchitecture and nanocatalysis. *J. Chem. Phys.*, 143:114308, 2015.

- M. Boero, A. Bouzid, S. Le Roux, B. Özdamar, and C. Massobrio. First-Principles Molecular Dynamics Methods: An Overview in Molecular Dynamics Simulations of Disordered Materials: From Network Glasses to Phase-Change Memory Alloys. C. Massobrio, J. Du, M. Bernasconi, and S. P. Salmon (Eds.), (pp. 33-55). Springer International Publishing, 2015. ISBN: 978-3-319-15674-3.

Bibliography

[1] H. Kuhn. On possible ways of assembling simple organized systems of molecules. In A. Rich, N. Davidson, and L. Pauling, editors, Structural Chemistry and Molecular Biology, pages 566–571. Freeman, San Francisco, 1968.

[2] A. Aviram and M. A. Ratner. Molecular rectifiers. Chemical Physics Letters, 29:277, 1974.

[3] E. O. Fischer and R. Jira. How metallocene chemistry and research began in Munich. J. Org. Chem., 637:7, 2001.

[4] T. Zhang, L. Zhu, Z. Tian, and J. Wang. Structural, Electronic, and Magnetic Properties of Neutral and Charged Transition Metal-Bis(dicarbollide) Sandwich Clusters. J. Phys. Chem. C, 115:14542, 2011.

[5] G. Wilkinson, M. Rosenblum, M. C. Whiting, and R. B. Woodward. The Structure of Iron Bis-Cyclopentadienyl. J. Am. Chem. Soc., 74:2125, 1952.

[6] C. Engtrakul and L. R. Sita. Ferrocene-Based Nanoelectronics: 2,5-Diethynylpyridine as a Reversible Switching Element. Nano Lett., 1:541, 2001.

[7] B. W. Heinrich, L. Limot, M. V. Rastei, C. Iacovita, J. P. Bucher, D. Mbongo Djimbi, C. Massobrio, and M. Boero. Dispersion and localization of electronic states at a ferrocene/Cu(111) interface. Phys. Rev. Lett., 107:216801, 2011.

[8] D. Mbongo Djimbi, S. Le Roux, C. Massobrio, and M. Boero. Metal-organic molecule-metal nano-junctions: a close contact between first-principles simulations and experiments. J. Phys.: Condens. Matter, 26:104206, 2014.

[9] M. Brookhart and W. B. Studabaker. Cyclopropanes from reactions of transition metal carbene complexes with olefins. Chem. Rev., 87:411, 1987.

[10] A. Archambeau, F. Miege, C. Meyer, and J. Cossy. Intramolecular cyclopropanation and C-H insertion reactions with metal carbenoids generated from cyclopropenes. Acc. Chem. Res., 48:1021, 2015.

[11] M. Sprik and G. Ciccotti. Free energy from constrained molecular dynamics. J. Chem. Phys, 109:7737, 1998.

[12] N. Agenet, V. Gandon, K. P. C. Vollhardt, M. Malacria, and C. Aubert. Cobalt-catalyzed cyclotrimerization of alkynes: The answer to the puzzle of parallel reaction pathways. J. Am. Chem. Soc., 129:8860, 2007.

[13] S. Kinge, M. Crego-Calama, and D. N. Reinhoudt. Self-Assembling Nanoparticles at Surfaces and Interfaces. ChemPhysChem, 9:20, 2008.

[14] C. T. Dinh, T. D. Nguyen, F. Kleitz, and T. O. Do. Shape-Controlled Synthesis of Metal Oxide Nanocrystals. In R.-S. Lui, editor, Controlled Nanofabrication: Advances and Applications, volume 3, chapter 10, page 327. CRC Press, 2012.

[15] W. Baaziz, B. P. Pichon, C. Lefevre, C. Ulhaq-Bouillet, and J.-M. Greneche et al. High Exchange Bias in Fe(3-delta)O4@CoO Core Shell Nanoparticles Synthesized by a One-Pot Seed-Mediated Growth Method. J. Phys. Chem. C, 117:11436, 2013.

[16] N. R. Jana, Y. Chen, and X. Peng. Size-and shape-controlled magnetic (Cr, Mn, Fe, Co, Ni) oxide nanocrystals via a simple and general approach. Chem. Mater., 16:3931, 2004.

[17] J. E. Macdonald, C. J. Brooks, and J. G. C. Veinot. The influence of trace water concentration on iron oxide nanoparticle size. Chem. Commun., page 3777, 2008.

[18] CPMD; Copyright IBM Corp. 1990-2016, Copyright MPI für Festkörperforschung Stuttgart 1997-2001, http://www.cpmd.org/.

[19] A. D. Becke. Density-functional exchange-energy approximation with correct asymptotic behavior. Phys. Rev. A, 38:3098, 1988; C. Lee, W. Yang, and R. G. Parr. Development of the Colle-Salvetti correlation-energy formula into a functional of the electron density. Phys. Rev. B, 37:785, 1988.

[20] N. Troullier and J. L. Martins. Efficient Pseudopotentials for Plane-Wave Calculations. 43:1993, 1991.

[21] S. Grimme. Semiempirical GGA-type density functional constructed with a long-range dispersion correction. J. Comput. Chem, 27:1787, 2006.

[22] B. Y. Sun, Y. Sato, K. Suenaga, T. Okazaki, and N. Kishi et al. Entrapping of exohedral metallofullerenes in carbon nanotubes: (CsC60)n@SWNT nano-peapods. J. Am. Chem. Soc., 127:17972, 2005.

[23] W. Kohn and L. J. Sham. Self-consistent equations including exchange and correlation effects. Phys. Rev, 140:A1133, 1965.

[24] G. W. Graham, P. J. Schmitz, and P. A. Thiel. Growth of Rh, Pd, and Pt films on Cu(100). Phys. Rev. B, 41:3353, 1990.

Chapter 1

Introduction

Contents

Having an atomic level knowledge of structural and dynamical features of organized and assembled systems is particularly important to better understand the functions and properties of many-body complex nano structures. However, obtaining the information about the details of the atomic structure of materials by conventional experimental methods is not possible to several extents. Starting from the late 1940s, the appearance of computers allowed mankind to inspect these complex problems by resorting to so-called "computer experiments". In addition to the vast developments in theoretical and experimental methods, also the evolution of computational resources paved the way for the realization of more and more sophisticated computer experiments in numerous research fields such as materials science and engineering, astrophysics, economics, particle physics and even sociology. Making use of computational capabilities also provides countless benefits where the "traditional" experiments are impractical due to requirement of extreme conditions such as very low or high temperatures and pressures or even the non-existence in nature of systems designed "ad hoc". Another interesting aspect disclosed by computer modelling is the possibility to replicate an existing system to better control its features in different environments which would be a tedious task in real life.

1.1 State of the art

The field of semiconductor electronics has nowadays a long history. Vacuum tubes, invented in 1904 by John Ambrose Fleming, were the first examples of electronic devices working as a basic valve with the purpose of controlling the current. They enabled the diffusion of radio, television, telephone and even digital computers. John Bardeen and Walter Brattain of Bell Labs were the first to devise a point-contact transistor in 1947. This archetype of transistor consisted of 3 gold wire contacts connected to a germanium slab. Analog electronics picked up pace after the invention of the bipolar junction transistor by William Shockley the following year, and finally the era of silicon electronics began with the introduction of the first commercially available silicon transistor manufactured at Texas Instruments in 1954. Figure 1.1 shows the evolution of amplification devices from vacuum tubes to integrated circuits.

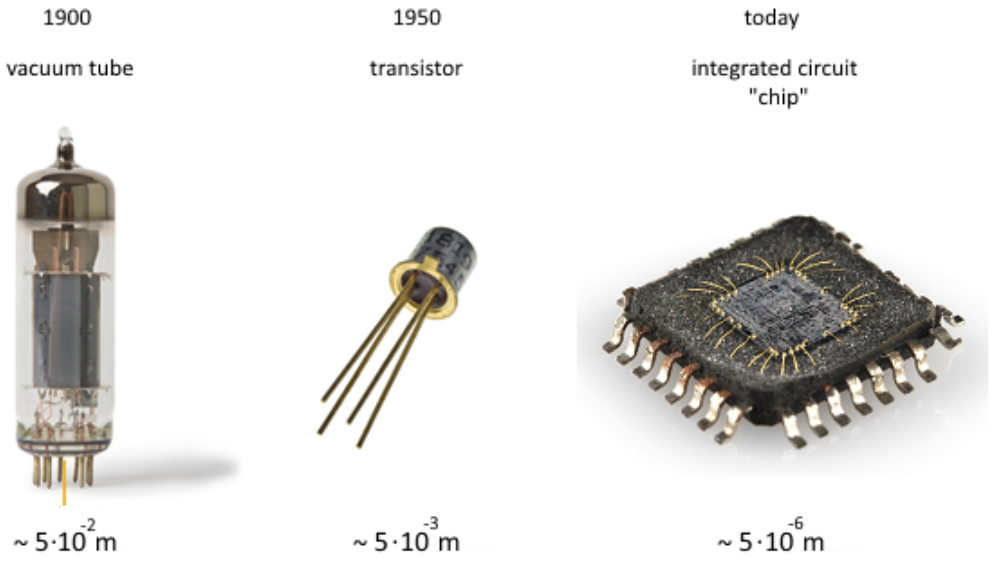

FIGURE 1.1: Miniaturization of amplification devices starting from vacuum tubes to integrated circuits.

Moore's Law, coined in 1965 by the co-founder of Intel Corporation Gordon Moore, stated in its early years that the number of transistors on a cm^2 of a microprocessor die doubles every year. Moore's original statement referred to the transistor density also indicates the corresponding cost, size and speeds of the components.

The prediction of Moore held out for one decade, however this empirical observation was corrected in the course of time after implementations to the contemporary developments in the field to doubling every two years in 1975 [1]. The corrected prediction is reflecting the current advancements in the field of electronics, nonetheless serious complications exist. The year 2020 seems to be the foreseen limit for Moore's Law [2]. Figure 1.2 demonstrates the increase in the number of transistors on a microprocessor die over a time range of 40 years starting from early 1970s until 2010.

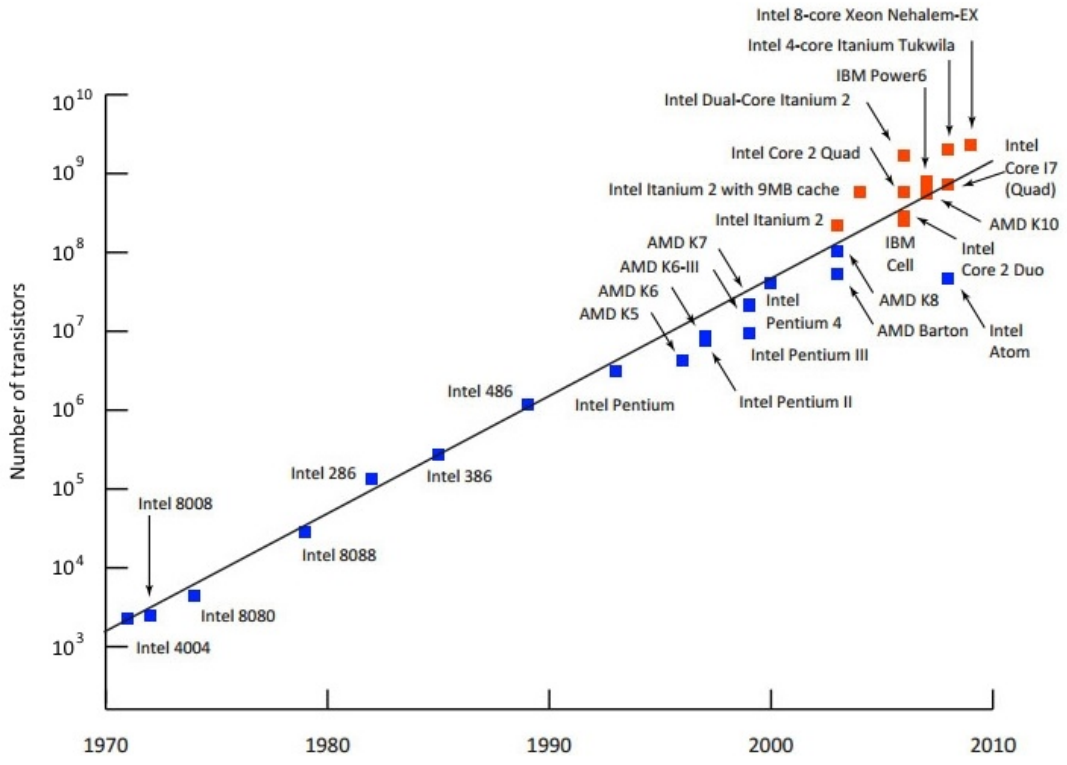

FIGURE 1.2: Evolution of the number of transistors on a single microprocessor die.

Rapid developments in the field of electronics have been carried out by numerous groups both in academy and industry in various fields from miniaturization of electronic components to discovery of different synthesis methods [3]. It is now possible to manufacture devices with sizes smaller than 20 nm in semiconductor technology [4]. While miniaturization allows the manufacturer to etch more than 10^9 transistors on an area in the order of cm^2 of a modern microprocessor, quantum effects begin to interfere and certain problems emerge as the components get

smaller [5]. Financial bottlenecks can also be given as an example along with physical and technical limitations, since costs of manufacturing processes demand more and more increased funding with the reduction in size [6, 7]. Current leakage is yet another issue which contributes to the existing drawbacks; the insulating layer is required to be progressively finer and more delicate in order to prevent shorts [8]. Thermal dissipation of the device set in to be problematic since overheating results in serious instabilities of the device. All these limitations in the silicon electronics call for more compact materials. This, in turn, implies development of new materials and realization of molecular junctions.

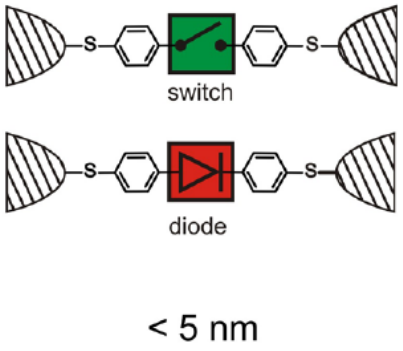

FIGURE 1.3: Schematic representation of a hypothetical molecular junction.

"Molecular electronics" or "molecular-scale electronics" is a newly-emerging field which aims to study individual molecules that function as self-contained electronic devices able to mimic the behaviour of conventional components such as switches, transistors and diodes in a microelectronic circuit. The ambitious and intuitive notion of combining molecular structures with electronics was brought forward by H. Kuhn in 1968 giving rise to the field of molecular engineering [9]. Soon after, the first study in which molecules were used as building blocks of electronic components was published in 1971 by Mann and Kuhn [10]. The idea was to position fatty acid salts of cadmium between metal electrodes in order to investigate the theoretically proposed exponential dependence of tunnelling conductance with respect to the thickness of the layer.

Although Mann and coworkers provided us with the early steps of molecule-based nanoelectronics, the "official" starting point of molecular electronics is often attributed to the pioneering theoretical work of Aviram and Ratner in 1974 [11].

This was based on the possibility that an organic molecule could be used as a p-n junction diode when a donor(D) and an acceptor(A) group are separated by a (σ) spacer group; namely a donor-insulator-acceptor (D-σ-A) molecular diode as sketched in Figure 1.4. The basic idea was to realize molecular components that are analogous to their silicon counterparts bearing the same functionality, but with an evident smaller size.

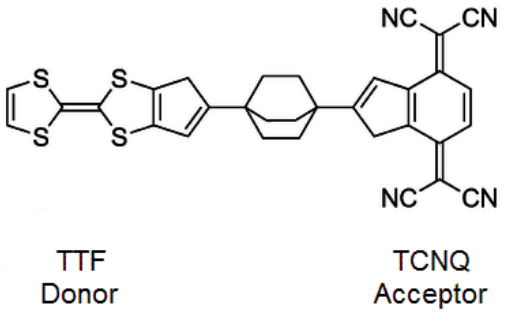

FIGURE 1.4: Molecular rectifier proposed by Aviram and Ratner in 1974. TTF as a donor group, TCNQ as an acceptor group connected by a σ bridge.

It is becoming feasible to tune the π-electron density in order to realize electron-poor (p-type) and electron-rich (n-type) sites by substituting functional groups to organic molecules [12]. Specifically in Ref.[11], D was designed to be a one-electron donor with low ionization potential, while A was a one-electron acceptor with high electron affinity. Aviram and Ratner proposed tetrathiafulvalene (TTF) and 7,7,8,8-tetracyano-*p*-quinodimethane (TCNQ) for the donor and acceptor moieties, respectively since the energy barrier of TTF^{+}-σ-$TCNQ^{-}$ is lower than that of TTF^{-}-σ-$TCNQ^{+}$ [13]. The spacer group was a covalent σ bridge (bicyclo[2.2.2]octane) acting as an effective barrier for charge transport between the two π-conjugated A-D segments which are directly connected to the metallic anode and cathode electrodes. As a consequence of the wise selection of the A and D molecular subunits, in forward bias, the Fermi level of the metallic electrode of the acceptor side is aligned with the lowest unoccupied molecular orbital (LUMO) of the acceptor, as well as the highest occupied molecular orbital (HOMO) of the donor subunit is aligned with the metallic electrode of the donor side.

Charge transfer occurs from the metallic electrode of A towards the metallic electrode of D due to the asymmetry of the overall configuration in a three step process: I) from the cathode to the LUMO of the acceptor, II) from the LUMO

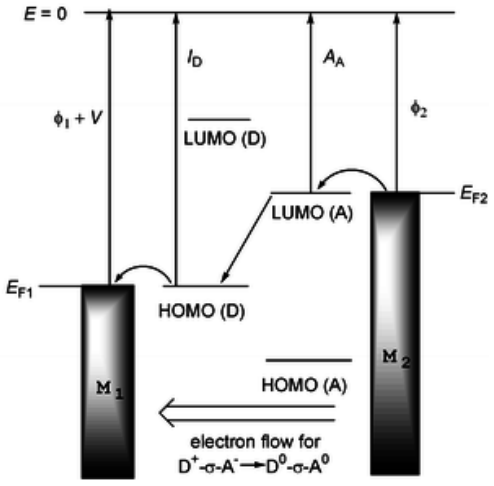

FIGURE 1.5: The mechanism proposed by Aviram and Ratner, showing the electron flow from the excited zwitterion state TTF^+-σ-$TCNQ^-$ to the ground state TTF-σ-TCNQ. Adapted from [14].

of the acceptor to the HOMO of the donor, and lastly III) from the HOMO of the donor to the anode. For the reverse bias, the tunneling via the bridge molecule is not possible as the required voltage is considerably higher than it is for the forward bias [15, 16]. The difference of the ionisation potential of the donor and the electron affinity of the acceptor subunits is 4 eV [13, 17]. Even though the mentioned molecules were asserted only theoretically, their similar counterparts, e.g. TTF, pyrene, N,N-dialkylaniline for donor and 5-bromo-2-(2-hydroxyethoxy)-TCNQ for acceptor, have been reported by Metzger and coworkers [18, 19].

Early attempts to achieve a rectification behavior were conducted experimentally using hemiquinone molecules attached to Au/Ag surfaces by Aviram et al. [20]. Although the results of this study seemed to be satisfactory and successful, further investigations revealed that the results were not favourable since an identical rectifying behaviour was observed in molecules that lacks acceptor and donor subunits. The authors concluded that the contact of the scanning tunneling microscopy (STM) tip and the sample was responsible for this particular behaviour. The aforecited publication was, therefore, retracted [21].

Similar studies aimed at realizing organic field effect transistors (OFETs) with single planar molecules started with unsubstituted bis(phthalocyaninato) molecules in the early 1990s. These molecules were selected because of their high thermal

stabilities and promising electronic, optical and chemical properties to form semiconductors [22]. Thin film field-effect transistors based on rare earth complexes of thulium and lutetium bisphthalocyanines (Pc_2Lu and Pc_2Tm) have been synthesized and characterized by Guillaud and coworkers in 1990 [23]. One of the early studies to demonstrate a rectification behavior in which base-substituted copper-phthalocyanine was bound to highly-oriented pyrolytic graphite (HOPG) by wet chemistry was reported by Pomerantz et al. in 1992 [24]. Rectification was successfully achieved thanks to the presence of a Cu 4,4′,4″,4‴-tetraaza-29H,31H-phthalocyanine (CuTAP) molecule, since pristine HOPG and its only acidified (but not treated with CuTAP) counterpart displayed the same current-voltage (I/V) characteristics. However, it has been reported in this study that by eliminating the dissimilarity in the workfunctions of the STM tip and the sample, it is possible to acquire more accurate I/V characteristics.

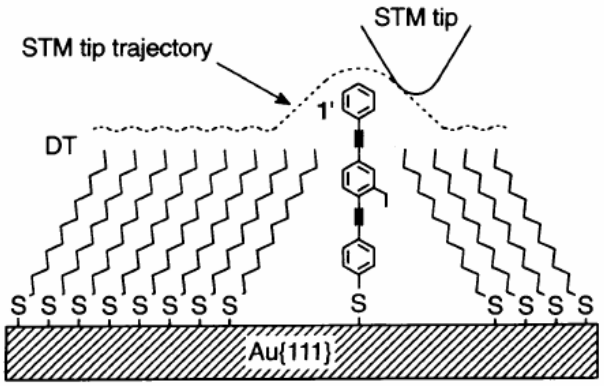

FIGURE 1.6: A schematic representation of n-dode-canethiol (DT) and 4,4'-di(phenylene-ethynylene)-benzothioacetate (DPEBT) SAM on Au{111}. From [25]. Reprinted with permission from AAAS.

It required nearly two decades of technological advancement following the theoretical work of Aviram and Ratner to realize an effective charge transfer in molecular wires experimentally. This was accomplished by anchoring 4,4'-di(phenylene-ethynylene)-benzenethiolate derivatives onto an Au (111) surface and examining the electronic properties of the resulting assembled systems by STM [25]. Figure 1.6 shows the schematic representation of the experimental setup. It is noteworthy to mention that although the term "wire" could suggest the image of thin metallic contacts which represent ohmic behaviour, molecular wires diverge from

this fact and rather show nonlinear characteristics when they are assembled in order to serve as basic circuit elements like switches and transistors [26, 27].

Fundamental improvements in the architecture of molecule-based nanoscale devices still represent a tough challenge since increased functionality would depend on the complexity of the prospective structures. For this reason, besides planar functional groups which are attached to organic molecules, organic layers containing sandwiched molecules have attracted great attention and therefore established new configurations, double decker metal–molecule–metal hybrid structures for instance [28, 29]. Once again, phthalocyanine molecule is widely used in its double-decker form [30, 31] and also has been subject to theoretical studies for applications in single molecular magnets (SMM) [32].

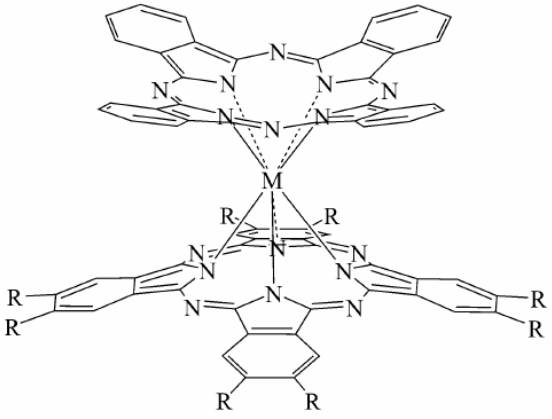

FIGURE 1.7: Molecular structures of sandwich bis(phthalocyaninato) rare earth double-decker complexes used as semiconductors of p-type OFET. From [31]. Reprinted with permission from Springer.

Figure 1.7 shows the molecular structure of a double-decker rare-earth bis(phthalocyaninato) sandwich molecule which can be used as an p-type OFET. Molecular structure of double-decker lanthanide complex phthalocyaninato-terbium(III) anion ($TbPc_2^-$) has been investigated using density functional theory (DFT) and with its dispersion included counterpart DFT-D. Monolayer of perylene-3,4,9,10-tetracarboxylicacid-dianhydride, namely PTCDA, is deposited on Ag(111) surface aiming to serve as an organic semiconductor whose structure and scanning tunnelling spectroscopy (STS) spectra was given in Figure 1.8. Structural and

electronic properties have been investigated by STS and formation of 2D-like delocalized interfacial states of the heterojunction between the organic molecule and the metal surface has been reported [33].

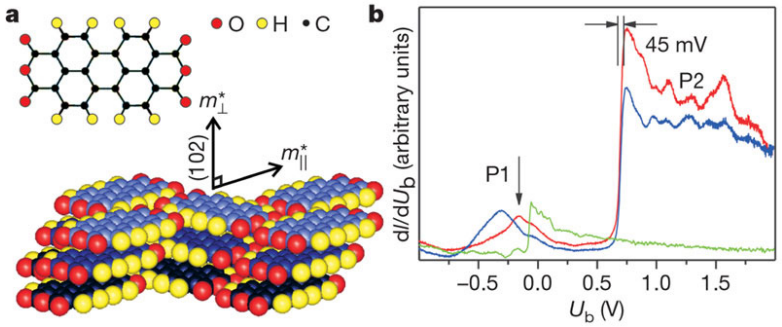

FIGURE 1.8: Structure and electronic properties of PTCDA/Ag(111). (a) Bulk crystal structure (α-phase). (b) STS spectra of a PTCDA/Ag(111) monolayer. From [33]. Reprinted with permission from Nature Publishing Group.

Along with planar molecules, the interaction of stacked monolayers of metal-phthalocyanines (MePc, Me=Sn or Cu) with heterostructures comprised of both PTCDA and Ag(111) substrate has drawn the attention of experiments [34]. It has been found that the interaction between PTCDA and Ag(111) increases although the CuPc molecule is only weakly physisorbed onto this bilayer [35, 36]. The interface states of phthalocyanine/Ag(111) [37] and PTCDA/Ag(111) [38] have been observed by time- and angle-resolved two-photon photoemission. Both studies indicate that the organic molecules are able to hybridize with the Ag(111) substrate. Copper phthalocyanine (CuPc)/PTCDA double-layer structures were also studied experimentally in order to explore possible donor/acceptor heterojunction capabilities [39].

Organometallic layered compounds carrying transition metals have attracted great attention because of their three-dimensional structure as opposed to the more common two-dimensional phthalocyanines [40]. One of the most important organometallic compound which has been discovered over half a century ago is iron bis-cyclopentadienyl, termed ferrocene [41]. Chapter 3.1.1 has been devoted to detail the properties of ferrocene. It has set a milestone in the field of organometallic chemistry with its unique and intriguing properties, and consequently led the

way to the discovery of similar 3D molecular building blocks. An early illustration of ferrocene is given in Figure 1.9. Promising ferrocene analogues, (M)-bis(dicarbollide) (M= Sc, Ti, V, Cr, Mn) sandwich clusters have been investigated for their electronic and magnetic properties, since they could potentially be used in spintronics applications [40]. So far, the majority of the studies were theoretical investigations using density functional theory approach.

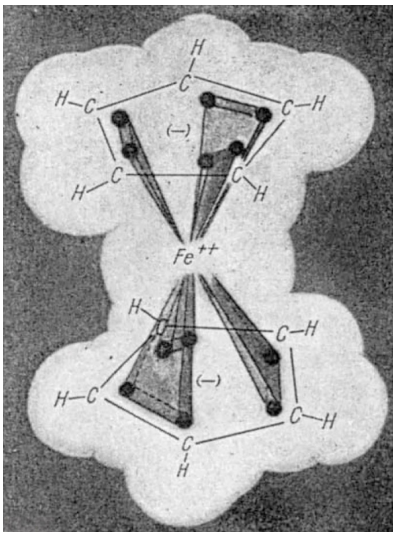

FIGURE 1.9: An early drawing of the iron bis-cyclopentadienyl, namely ferrocene. This promising double-decker molecule aroused great interest in many research fields, especially in the domain of organometallics following its first synthesize in 1951 by Peter L. Pauson and his coworker Thomas J. Kealy. Taken from [42].

In an experimental work conducted by Engtrakul and Sita, ferrocene was intended to be used as a diode by linking two of them with 2,5-diethynylpyridyl units [43]. The role of the pyridyl molecule is to ensure that the ferrocene moieties are not in direct contact with each other. The reason is sketched in Figure 1.10. In state 1, when the spacer pyridyl is neutral, charge transfer can occur between the metal terminals regardless of the applied bias potential. However, oxidation of the nitrogen of the pyridyl moiety forces the two ferrocene to acquire different redox potentials by causing the electrons to delocalize which, in turn, hinders the electron-hopping conduction in the forward bias while the system is in state 2. On the other hand, current rectification and switching can be realized in the reverse bias in which the barrier does not exist.

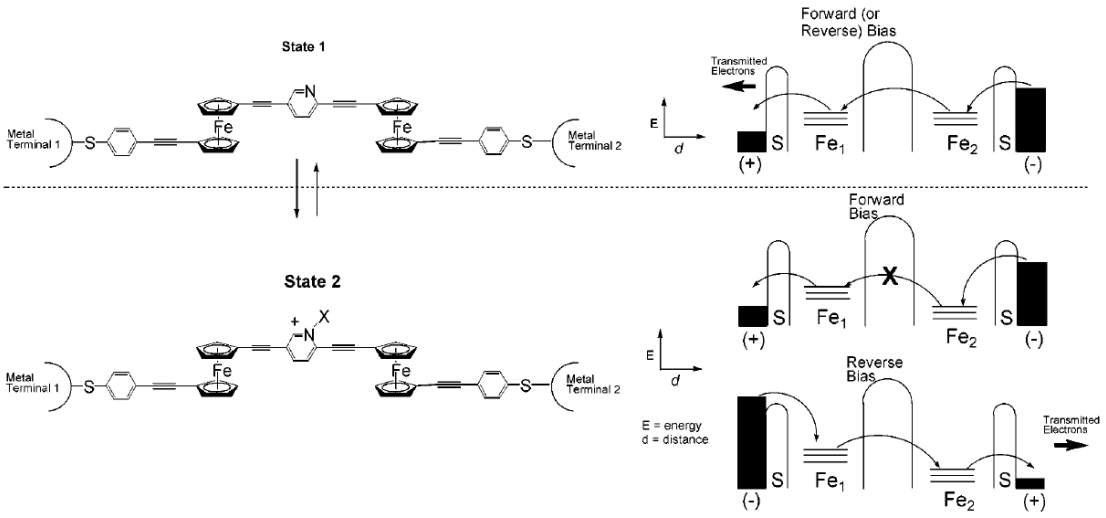

FIGURE 1.10: Electron-hopping mechanism in the ferrocene-based diode. From [43]. Reprinted with permission from American Chemical Society.

Redox- and nonredox-active pairs of ferrocene containing molecules, along with other multi-decker sandwich complexes, attached to a silicon surface were investigated to be used as molecular capacitors [44, 45]. In this study, ferrocene containing molecules are linked to the silicon substrate through linker molecules which act as a tunneling barrier between the two moieties which are connected to the electrodes. By applying a voltage, redox-active molecules can be charged, and these voltages are typically low, namely in the order of 500-600 mV. Charge retention time is directly associated with the tunneling probability and can be fine-tuned by manipulating the length of the linking subunits [44]. Figure 1.11 shows the schematic capacitor circuit and the ferrocene containing molecule with its nonredox-active analog.

Studies combining phthalocyanine and ferrocene have also been reported [46]. It has been shown that two ferrocene centers can be linked to either side of a double-decker rare earth sandwich (phthalocyaninao)-(porphyrinato) complex resulting in a strong electronic interaction. Additionally, ferrocene is also combined with already existing promising nanoparticles such as buckminsterfullerenes to form double-decker buckyferrocenes [47]. Ferrocene, with its electron donor capabilities, is an excellent candidate to be integrated with fullerenes. When combined with electron acceptor fullerene, the resulting conjugation can be used to fine-tune the electronic coupling of the two interfaces [48]. Schematic configurations

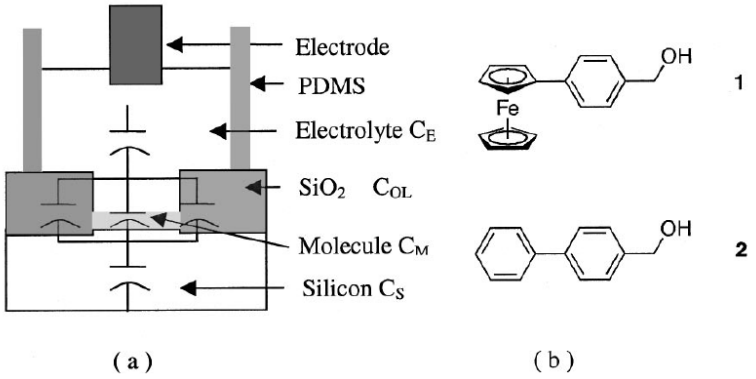

FIGURE 1.11: (a) Schematic of the electrolyte-molecule-silicon capacitor with a simplified equivalent circuit. (b) The structure of the ferrocene derivative (1) and the nonredox-active analog (2). From [44]. Reprinted with permission from AIP Publishing LLC.

of example molecules are given in Figure 1.12. Furthermore, the interaction of fullerenes with transition metals as potential gap-tunable building blocks will also be a complementary study presented in this thesis.

To complement experiments, first-principle atomistic simulations of ferrocene grafted onto semiconductor Si(100) surface was carried out to investigate its electrochemical behavior [49, 50]. Ferrocene is also investigated theoretically for its transport properties to be exploited in terahertz applications. One cyclopentadienyl (Cp) ring of a ferrocene molecule is attached to gold electrodes via sulfur atoms, while the other ring is left free to rotate. In this setup, ferrocene can be tuned to have two regimes; oscillating or spinning by varying the distance between the contacts and the transmission function [51]. Rotation of ferrocene can also be established by connecting π-dimerizable fragments to the Cp rings. Electrochemical control of the rings' rotational motion is possible by changing the charge state of the linking molecules. The resulting ferrocene-based carousel offers interesting applications as a molecular switch [52]. Sato and co-workers prepared a molecular wire from methoxy-terthiophene and hexyl-sexithiophene derivatives 5,5″-diferrocenyl-3,3″-dimethoxy-2,2′:5′,2″-terthiophene (FMTT) and 5,5⁗-diferrocenyl-3″,4‴,3⁗-tetrahexyl-2,2′:5′,2″:5″,2‴:5‴,2⁗:5⁗,2⁗⁗-sexithiophene (FHST) by connecting two terminal ferrocenes in order to shed light on the oxidation process. Electrochemical measurements indicated that charge transfer can occur through the wire for both

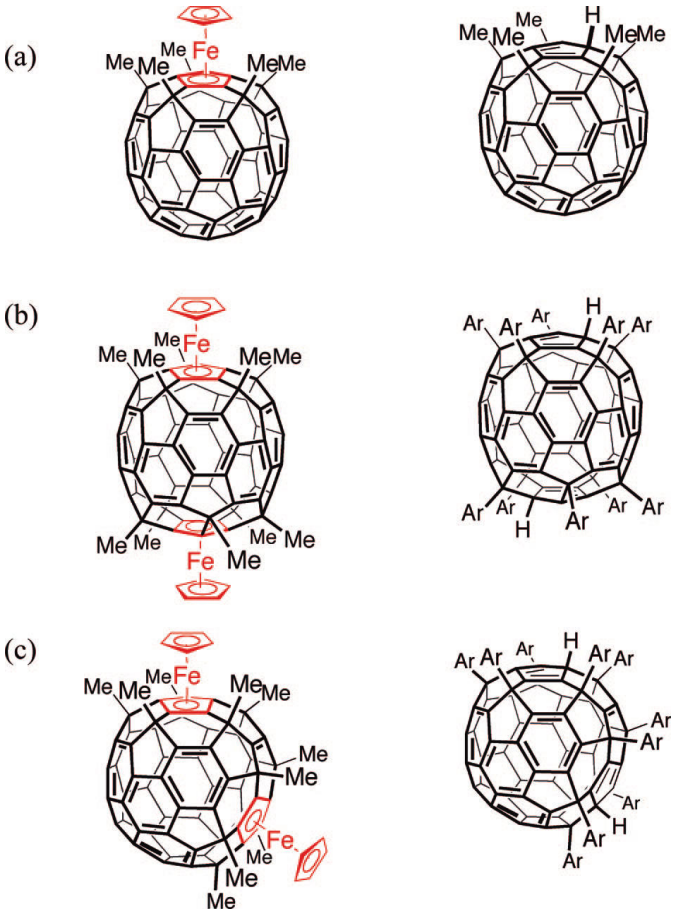

FIGURE 1.12: Structural formulas of (a) single-decker buckyferrocene, $Fe(C_{60}Me_5)Cp$, and the respective reference compound, $C_{60}Me_5H$, and (b) highly symmetric D_{5d} and (c) lower symmetric C_{2v} double-decker buckyferrocenes, $Fe_2(C_{60}Me_{10})Cp_2$, and their respective reference compounds, $C_{60}Ar_{10}H_2$ (Ar = C_6H_4-nBu). From [48]. Reprinted with permission from American Chemical Society.

configurations [53]. Very recently, electrochemical and spectroscopic characterizations of graphene oxide (GO) nanosheets functionalized with ferrocenyl groups have been reported by Lu and co-workers [54]. Strong coupling of ferrocene complexes across GO nanosheets has shown that intervalence charge transfer between ferrocene centers is very strong and effective, therefore the resultant complex provides a convincing support to the feasibility of molecular electronic device based on graphene.

The studies of metallocene adsorption date back not longer than three decades. Adsorption of ferrocene molecule on different surfaces such as Cu(100) [55], Ag(100)

[55–58], Si(111)-2×1 [50], Si(111)-7×7 including B-Si(111) with various boron concentrations [59], Mo(112) [60], graphite [61, 62] and silica[63] has appeared in the literature rather recently. The slow progress is mainly due to the easy dissociation of ferrocene upon deposition if not properly handled and if the deposition temperature is too high. Indeed, low temperatures are required [64, 65] to efficiently deposit ferrocene onto a Cu(111) surface. The metallic substrate on which the ferrocene to be deposited has a strong influence on the orientation of the molecule [56, 58, 61] and thus on the functionality of the assembled nanostructure. Various spectroscopic methods such as high resolution electron energy loss (HREEL), angle resolved thermal desorption spectroscopy (ARTDS), and STM have been employed in order to gain insight into the adsorption nature, surface chemistry and potential uses of ferrocene [60, 61]. Preferential orientations of ferrocene have been reported, showing that its molecular axis is generally perpendicular to the surface of a Ag(100), Mo(112), Cu(111) substrate and parallel to the surface on Cu(100) [58]. It has also been reported that ferrocene is adsorbed on Au(111) [66] and Pt(111) [67] in a dissociative manner. Rivera et al. [68], on the other hand, demonstrated experimentally that ferrocene in acetonitrile solution can be deposited associatively onto gold thin films.

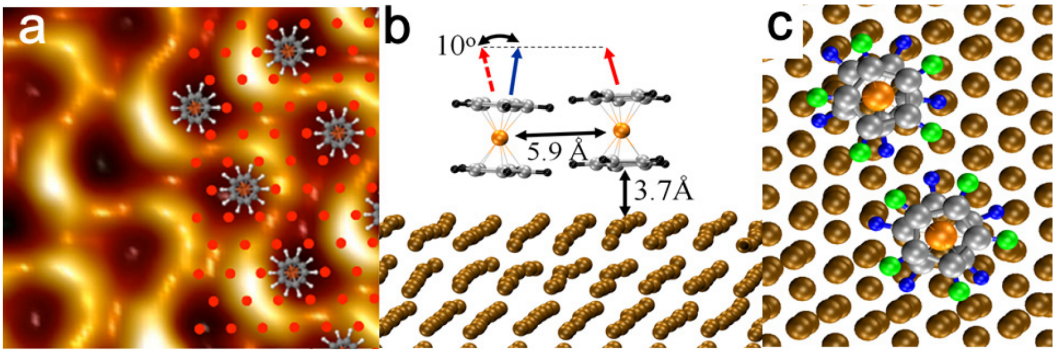

FIGURE 1.13: (a) STM image of a Cu(111) surface onto which a ferrocene monolayer has been deposited. Side view (b) and top view (c) of the stable configuration of two ferrocene molecules on the Cu(111) surface as provided by our simulations. In panel (c) H atoms belonging to the top Cp rings are shown as green spheres, while the bottom ones are shown as blue spheres. From [69].

In 2011, ferrocene was physisorbed onto the Cu(111) surface experimentally, forming a monolayer without giving rise to decomposition at 150 K [70]. Besides the successful experimental approach, first-principles simulation methods have been resorted to realize the subsequent Cu atom deposition on top of the deposited

ferrocene in order to inspect the susceptibility of interface states to the local modifications. STM image of the physisorbed ferrocene monolayer and schematic representations of the resulting configuration have been given in Figure 1.13. It has been reported that ferrocene physisorption is mediated by 2D-like interface states resembling Shockley states and that upon single Cu atom deposition, 0.3 e charge has been transferred to the Cu (111) slab from the deposited Cu [69].

As it was given non-exhaustively in this chapter, there has been a vast number of studies in order to investigate physical, electronic and chemical properties of ferrocene and its conceivable applications following its synthesis. Inspired from the mentioned Cu deposition study; deposition of single transition metal atoms such as Fe and Co on top of organometallic molecule ferrocene deposited onto Cu(111) substrate is intended to be investigated by means of computational efforts in the present work. Next chapter is dedicated to summarize the basic theory and specific details of the simulation techniques utilized in this thesis. The third and last chapter, which is divided into three subchapters, constitutes the main body of the present work where the obtained results are presented.

Chapter 2

Theoretical Background

Contents

2.1 Classical Molecular Dynamics

Atomistic simulations whose purpose is to understand, model and analyse the behaviour of individual atoms constituting a complex system, can be roughly divided into two main families: Monte Carlo (MC) and molecular dynamics (MD); MC methods are stochastic sampling of the phase space describing the target system. MD, instead, is a deterministic technique to explore this same phase space via equations of motion. The main framework of MC simulations is to visit all the possible configurations of the system with the intention of finding the conformation or set of conformations which has the lowest total energy. Due to the scope of this thesis, the discussion is limited to molecular dynamics. Interested readers are referred to available reviews [71, 72].

Molecular dynamics is a computer simulation method which aims at determining the trajectories of molecules in the course of time by solving Newton's equations of motion. This technique was first introduced and benchmarked in 1957 by Alder and Wainwright to study the collisions of hard spheres [73]. Rahman, on the other hand, contributed to the method by simulating an 864-atom liquid argon system using a realistic potential energy function (PEF), more precisely a truncated Lennard-Jones PEF, in 1964 [74]. This study was considered to be a significant breakthrough in the field as it was historically the first calculation of dynamical properties such as the diffusion coefficients for a realistic system. Nowadays, MD is being used extensively to study a wealth of systems ranging from solid state physics, to solution chemistry and molecular biochemistry with appreciable accuracy [75]. A subsequent milestone was introduced in 1985 by Roberto Car and Michele Parrinello [76], where the forces acting on the atoms were computed from the density functional theory (DFT), realizing the first unification of the two worlds, MD and DFT. Classical molecular dynamics (CMD), it can be summarized as a deterministic technique governed by the laws of classical mechanics; Newton's 2^{nd} law of motion, to be more precise.

Consider a system consisting of N interacting particles with masses m_i. The forces F_i on individual particles i are computed through the negative gradient of an analytical potential energy function $V(\mathbf{r}_1,\ldots,\mathbf{r}_N)$. This function bears the information for the interaction of the particles.

$$\mathbf{F}_i = -\nabla V(\mathbf{r}_1, \ldots, \mathbf{r}_N) = m_i \frac{d^2\mathbf{r}_i}{dt^2} \tag{2.1}$$

Apart from the interaction model; CMD, like every particle simulation method, requires certain steps in order to proceed. Second requirement is an integrator which is utilised to numerically solve the equations of motion and propagate the positions and the velocities of the particles in time. Position Verlet algorithm, velocity Verlet algorithm and leap-frog method can be given as examples to Verlet type algorithms [77, 78]. Another class of integrators encompasses predictor-corrector schemes such as Nordsieck-Gear Algorithm [79, 80]. Verlet algorithm is used in this thesis for its time-reversibility, and stability characteristics.

Many analytical methods for solving Newton's equations of motion assume that the positions of the atoms and the dynamic properties of the system, such as the velocities and the accelerations, can be developed by using the Taylor expansion. Following this fact, the position of the particles $\mathbf{r}$(t) is expanded in two forms; forwards and backwards in time.

$$\mathbf{r}(t + \Delta t) = \mathbf{r}(t) + \Delta t \frac{\partial \mathbf{r}(t)}{\partial t} + \frac{1}{2!}\Delta t^2 \frac{\partial^2 \mathbf{r}(t)}{\partial t^2} + \frac{1}{3!}\Delta t^3 \frac{\partial^3 \mathbf{r}(t)}{\partial t^3} + \mathcal{O}(\Delta t^4) \tag{2.2}$$

$$\mathbf{r}(t - \Delta t) = \mathbf{r}(t) - \Delta t \frac{\partial \mathbf{r}(t)}{\partial t} + \frac{1}{2!}\Delta t^2 \frac{\partial^2 \mathbf{r}(t)}{\partial t^2} - \frac{1}{3!}\Delta t^3 \frac{\partial^3 \mathbf{r}(t)}{\partial t^3} + \mathcal{O}(\Delta t^4) \tag{2.3}$$

Adding the above equations yield the basic Verlet algorithm which is utilized to advance the positions of the particles without the necessity of calculating the velocities.

$$\mathbf{r}(t + \Delta t) = 2\mathbf{r}(t) - \mathbf{r}(t - \Delta t) + \Delta t^2 \frac{\partial^2 \mathbf{r}(t)}{\partial t^2} + \mathcal{O}(\Delta t^4) \tag{2.4}$$

Having said that, the velocity information is necessary for calculating the kinetic energy. Subtracting Equation 2.3 from Equation 2.2 and arranging the terms yields the following equation that is used to calculate the velocities of the particles at time t;

$$\mathbf{v}(t) = \frac{\mathbf{r}(t+\Delta t) - \mathbf{r}(t-\Delta t)}{2\Delta t} + \mathcal{O}(\Delta t^2) \tag{2.5}$$

However, the main drawback with the basic Verlet algorithm is the need of future and past position information in order to calculate the current velocity of the atoms. For this reason, one needs an algorithm which calculates the velocity information based on the current position. Therefore, velocity Verlet algorithm was developed to serve this purpose.

Taylor expansion of the velocity up to the 3^{rd} order yields,

$$\begin{aligned} \mathbf{v}(t+\Delta t) &= \mathbf{v}(t) + \Delta t \frac{\partial \mathbf{v}(t)}{\partial t} + \frac{1}{2!}\Delta t^2 \frac{\partial^2 \mathbf{v}(t)}{\partial t^2} + \mathcal{O}(\Delta t^3) \\ &= \mathbf{v}(t) + \Delta t\ \dot{\mathbf{v}}(t) + \frac{1}{2!}\Delta t^2 \ddot{\mathbf{v}}(t) + \mathcal{O}(\Delta t^3) \end{aligned} \tag{2.6}$$

Similarly, expand the acceleration up to the 2^{nd} order,

$$\dot{\mathbf{v}}(t+\Delta t) = \dot{\mathbf{v}}(t) + \Delta t\ \ddot{\mathbf{v}}(t) + \mathcal{O}(\Delta t^2) \tag{2.7}$$

Substituting the 2^{nd} order derivative of the velocity term of the Equation 2.7 in Equation 2.6 and arranging the terms using $\dot{v}(t) = F(x)/m$ yield,

$$\mathbf{v}(t+\Delta t) = \mathbf{v}(t) + \frac{\Delta t}{2m}\left[F(x(t)) + F(x(t+\Delta t))\right] \tag{2.8}$$

Now the positions and the velocities of the particles can be updated according to the current force, then the new forces can be computed using the new positions without needing to occupy two sets of position information in the memory.

The third and the last requirement to govern a molecular simulation is the thermodynamic ensemble. Statistical mechanics is an excellent tool to study the properties of individual atoms and molecules which constitutes the system in order to gather information about the macroscopic phenomena. There are four principal ensembles to describe a physical system.

- Microcanonical ensemble (NVE): fixed number of atoms, N, fixed volume, V, and fixed energy, E.
- Canonical ensemble (NVT): fixed number of atoms, N, fixed volume, V, and fixed temperature, T.
- Grand canonical ensemble (μVT): fixed chemical potential, μ, fixed volume, V, and fixed temperature, T.
- Isobaric-Isothermal ensemble (NPT): fixed number of atoms, N, fixed pressure, P, and fixed temperature, T.

Despite the versatile nature of CMD, there exists some limitations to this method.

Force field dependence: The physical modelling of the system is characterized by the interatomic potential. Therefore, the obtained properties of the simulated system depends on the reliability of the interaction potential. Transferability is yet another aspect to take into consideration so that the interaction potential could be compatible for a wide variety of systems. Computational efforts have been devoted to address this issue [81].

Omitting the electrons: In CMD, the atoms are treated as point particles interacting according to a force field, thus the presence of electrons are neglected. Since bond formation/breaking is the basic characteristic of chemical reactions, this omission renders MD an inadequate method to study the changes in chemical nature [82].

2.2 Temperature Control

The kinetic temperature of the system is equal to its average kinetic energy $\langle E_k \rangle$ by means of the velocity (or momenta) of the particles. According to the equipartition theorem, each degree of freedom contributes to the kinetic energy of the system as much as $\frac{1}{2}k_BT$, where k_B is the Boltzmann constant. Therefore, for a system of N particles having masses m_i with velocities v_i, the relation between the kinetic energy and the temperature can be written as follows,

$$\frac{1}{2}\sum_i m_i\langle v_i^2\rangle = (3N - N_c)\frac{k_B T}{2} \tag{2.9}$$

where N_c is the total number of constrains. Standard molecular dynamics simulations are carried out naturally in microcanonical ensemble (NVE). However in real life, in order to better reflect the natural behavior of the experiments and better capture the thermal fluctuations, one must use a thermostat in order to control the temperature. This is possible by employing canonical ensemble (NVT).

2.2.1 Velocity scaling

The most straightforward way to control the temperature of a system is to manipulate the velocities of the particles accordingly. This is achieved by multiplying the velocities by a factor λ. So the velocities which give the desired temperature is written as $v_0 = \lambda v_i$. When substituted in the energy equation, the factor λ is found as follows.

$$\begin{aligned}
\Delta T &= T_0 - T \\
&= \frac{1}{3n_{DoF}k_B}\left[\frac{1}{2}\sum_i m_i\lambda^2 v_i^2 - \frac{1}{2}\sum_i m_i v_i^2\right] \\
&= (\lambda^2 - 1)T \\
\lambda &= \sqrt{\frac{T_0}{T}}
\end{aligned} \tag{2.10}$$

However, as it was expressed before, velocity scaling does not reproduce the correct thermodynamical properties of the system and does not correspond with the real dynamics of the experiments as this method fails to generate the natural energy fluctuations in the system. It is unphysical to scale the velocities at every step to adjust the temperature since kinetic and potential energies are constantly involved in an exchange with each other.

2.2.2 Nosé-Hoover Thermostat

A better way to control the temperature is to couple the system with a heat reservoir, i.e. thermostat. The purpose of the thermostat, on the other hand, is not to fix the temperature constant as this procedure would also imply keeping the kinetic energy constant. This would conflict with the purpose of realizing simulations in canonical (NVT) ensemble. Preserving the fluctuations in the temperature around a target value and keeping the average temperature constant is rather the true aim of a thermostat.

Nosé-Hoover algorithm (or sometimes called as *extended system method*) employs the method of modified Hamiltonian (or Lagrangian) by introducing additional degrees of freedom which control the parameters of the thermostat. Although this method was first introduced by Andersen to control the pressure of the system, the original idea for constant-temperature calculations was conceived by Shuichi Nosé [83, 84] in 1984 and developed further by William G. Hoover the following year [85].

Consider a system with N particles having masses m, potential energy U, and momenta p. The Lagrangian of the extended system with an additional degree of freedom s which functions as an external system is given as,

$$\mathcal{L} = \sum_i \frac{\mathbf{p}_i^2}{2ms^2} - U\left(\mathbf{r_i} - \mathbf{r_j}\right) + \frac{p_s^2}{2Q} - gk_BT \ln s \tag{2.11}$$

where g is the number of degrees of freedom; $3N + 1$, including the new variable s. p_s is the conjugate momenta to s and equal to $p_s = Q\dot{s}$. Temperature control realized by a thermostat is essentially kinetic energy transfer between the system and the heat reservoir. The coupling between these two entities are controlled by Q, the virtual "heat bath mass". The two sets of real and virtual variables are related through the following transformation [86].

$$t' = \int_0^t \frac{\mathrm{d}t}{s} \text{ and } r_i' = r_i,\ p_i' = \frac{p_i}{s} \tag{2.12}$$

Soon, Hoover proposed that the variable s was redundant and must be eliminated from the resulting equations of motion. Instead, he reformulated the Nosé's contribution by adding a thermodynamic friction coefficient $\zeta = p_s/Q$. The following equations are called Nosé-Hoover equations of motion [87].

$$\begin{aligned} \frac{\mathrm{d}\mathbf{q}_i}{\mathrm{d}t'} &= \mathbf{p}'_i/m \\ \frac{\mathrm{d}\mathbf{p}_i}{\mathrm{d}t'} &= \mathbf{F}_i - \zeta\mathbf{p}'_i \\ \frac{\mathrm{d}\zeta}{\mathrm{d}t'} &= \frac{1}{Q}\left[\sum_i^N \mathbf{p}_i'^2/m - gk_BT\right] \end{aligned} \tag{2.13}$$

The friction parameter ζ adjusts the acceleration of the particles throughout the simulation, so that the kinetic energy of the system fluctuates between two boundaries.

2.3 Tackling the Schrödinger Equation

The sole purpose of electronic structure calculations is to gain insight about the properties of a system. These calculations are called first-principles methods or "ab-initio" methods if they are performed by only using the information gathered from the atoms which constitutes the system without referring to any kind of empirical data[1]. Since it completely relies on the physical principles, mostly quantum mechanics, and also being independent of a specific system of species, ab-inito methods can be adapted to any kind of system conveniently. The fundamental requirement to perform an electronic structure calculation is to solve the stationary, non-relativistic, many-body Schrödinger equation (Eq. 2.14) and determine the eigenfunctions of the many-body Hamiltonian which contains all the information about the observables of the system.

[1] Apart from the approximations introduced in the exchange-correlation functionals which will be discussed in Chapter 2.4.4.

$$\hat{\mathcal{H}}\Psi(\mathbf{r}_1, \mathbf{r}_2, ..., \mathbf{r}_N, \mathbf{R}_1, \mathbf{R}_2, ..., \mathbf{R}_M) = E\Psi(\mathbf{r}_1, \mathbf{r}_2, ..., \mathbf{r}_N, \mathbf{R}_1, \mathbf{R}_2, ..., \mathbf{R}_M) \tag{2.14}$$

The Hamiltonian $\hat{\mathcal{H}}$ for a system of N electrons with masses m_e interacting with M nuclei with masses M_α and charges $Z_\alpha e$ through Coulomb interaction written in SI units is given by

$$\begin{aligned}\hat{\mathcal{H}} = &-\sum_{i=1}^{N}\frac{\hbar^2}{2m_e}\nabla_i^2 - \sum_{\alpha=1}^{M}\frac{\hbar^2}{2M_\alpha}\nabla_\alpha^2 + \sum_{i<j=1}^{N}\frac{1}{4\pi\varepsilon_0}\frac{e^2}{|\mathbf{r}_i - \mathbf{r}_j|} \\ &- \sum_{i=1}^{N}\sum_{\alpha=1}^{M}\frac{1}{4\pi\varepsilon_0}\frac{Z_\alpha e^2}{|\mathbf{r}_i - \mathbf{R}_\alpha|} + \sum_{\alpha<\beta=1}^{M}\frac{1}{4\pi\varepsilon_0}\frac{Z_\alpha Z_\beta e^2}{|\mathbf{R}_\alpha - \mathbf{R}_\beta|}\end{aligned} \tag{2.15}$$

where the terms represent the kinetic energy of the electrons ($\hat{T}_e$) and of the nuclei ($\hat{T}_N$), potential energy due to repulsion between electrons ($\hat{V}_{ee}$), potential energy due to attraction between electrons and nuclei ($\hat{V}_{eN}$) and the potential energy due to repulsion between nuclei ($\hat{V}_{NN}$), respectively. By setting the reduced Planck constant $\hbar$, mass of an electron m_e, modulus of its charge $|e|$, and the permittivity of free space $4\pi\varepsilon_0$ equal to unity converts the complicated looking Hamiltonian into somewhat user-friendly counterpart in atomic units.

$$\begin{aligned}\hat{\mathcal{H}} = &\sum_{i=1}^{N} -\frac{1}{2}\nabla_i^2 + \sum_{\alpha=1}^{M} -\frac{1}{2M_\alpha}\nabla_\alpha^2 + \sum_{i<j=1}^{N}\frac{1}{|\mathbf{r}_i - \mathbf{r}_j|} \\ &- \sum_{i=1}^{N}\sum_{\alpha=1}^{M}\frac{Z_\alpha}{|\mathbf{r}_i - \mathbf{R}_\alpha|} + \sum_{\alpha<\beta=1}^{M}\frac{Z_\alpha Z_\beta}{|\mathbf{R}_\alpha - \mathbf{R}_\beta|}\end{aligned} \tag{2.16}$$

The above equation is also known as the exact, non-relativistic, molecular Hamiltonian and Eq. 2.14 can as a result be written in short as follows in the absence of any additional external field:

$$[\hat{T}_e + \hat{T}_N + \hat{V}_{ee} + \hat{V}_{eN} + \hat{V}_{NN}]\Psi(\mathbf{r}, \mathbf{R}) = E\Psi(\mathbf{r}, \mathbf{R}) \tag{2.17}$$

Although the Schrödinger equation seems nothing but like an innocent eigenvalue problem, obtaining its exact analytical solution is impossible for systems having more than one electron due to the nature of the Hamiltonian, that is, the existence of two-body interactions. In fact, this analytical solution is only limited for just a handful of truly simple systems such as particle in a box, quantum harmonic oscillator or hydrogen molecular ion (HMI, $H_2{}^+$) at most. For this reason, one must make use of clever approximations and the first step would be separating the motions of electrons and nuclei by taking advantage of the significant mass difference between them.

Nuclei and electrons have similar magnitudes of charge, therefore the forces exerted mutually by these particles are also in the similar order of magnitude, and hence the resulting momenta. However, even in the simplest system, say in an hydrogen atom, the mass of the nucleus is approximately 1800 times larger than that of an electron. This mass ratio can easily climb up to 10^5 for Fe atom. Consequently, electrons with much lighter masses must have much higher velocities compared to massive nuclei; and therefore can follow the alterations in the nuclei configuration by rapidly relaxing to their instantaneous ground-state. This is called the *clamped nuclei approximation*, and as a consequence one can consider the nuclei stationary, and therefore the kinetic energy of the nuclei can be taken zero. In addition, the Coulomb interaction between the nuclei is nothing but a constant which contributes to the eigenvalues only by a constant. The remaining part of the Hamiltonian can be written as follows:

$$\hat{\mathcal{H}}_e = \sum_{i=1}^{N} -\frac{1}{2}\nabla_i^2 + \sum_{i<j=1}^{N} \frac{1}{|\mathbf{r}_i - \mathbf{r}_j|} - \sum_{i=1}^{N}\sum_{\alpha=1}^{M} \frac{Z_\alpha}{|\mathbf{r}_i - \mathbf{R}_\alpha|} \tag{2.18}$$

If the Hamiltonian can be written as a sum of two or more terms which explicitly depend on variables that are independent of each other, the total solution to the Schrödinger equation, the total eigenfunction, is the product of the eigenfunctions of corresponding separated Hamiltonians, likewise the eigenvalues are the sum of the separated Hamiltonians. A quick glance over the Hamiltonian (Eq. 2.16) reveals that V_{eN}, the Coulomb interaction term between the electrons and the nuclei clearly hinders us to perform this helpful separation. We will now assume that

the total wavefunction can be written as a product of the electronic and nuclear parts owing to the clamped nuclei approach. The nuclear wavefunction depends only on the atomic coordinates whereas the electronic wavefunction explicitly depends on the electronic coordinates and also parametrically depends on the atomic coordinates.

$$\Psi(\mathbf{r},\mathbf{R}) = \psi_e(\mathbf{r};\mathbf{R})\chi_n(\mathbf{R}) \tag{2.19}$$

Plug the total Hamiltonian into the Schrödinger equation making the necessary separation;

$$(\hat{T}_e + \hat{V}_{ee} + \hat{V}_{eN})\psi_e(\mathbf{r};\mathbf{R})\chi_n(\mathbf{R}) + (\hat{T}_N + \hat{V}_{NN})\psi_e(\mathbf{r};\mathbf{R})\chi_n(\mathbf{R}) = E\psi_e(\mathbf{r};\mathbf{R})\chi_n(\mathbf{R}) \tag{2.20}$$

Keeping in mind that the electronic Schrödinger equation is given as,

$$\begin{aligned} \hat{\mathcal{H}}_e\psi_e(\mathbf{r};\mathbf{R}) &= E_e\psi_e(\mathbf{r};\mathbf{R}) \\ \{\hat{T}_e + \hat{V}_{ee} + \hat{V}_{eN}\}\psi_e(\mathbf{r};\mathbf{R}) &= E_e\psi_e(\mathbf{r};\mathbf{R}) \end{aligned} \tag{2.21}$$

Since $\chi_N(\mathbf{R})$ does not depend explicitly on electronic coordinates;

$$\hat{T}_e(\psi_e(\mathbf{r};\mathbf{R})\chi_N(\mathbf{R})) = (\hat{T}_e\psi_e(\mathbf{r};\mathbf{R}))\chi_N(\mathbf{R}) \tag{2.22}$$

Let's treat the kinetic energy operator of the nuclei by applying the chain rule;

$$\begin{aligned} \hat{T}_N\psi_e(\mathbf{r};\mathbf{R})\chi_N(\mathbf{R}) &= -\sum_\alpha \frac{1}{2M_\alpha}\nabla_\alpha^2[\psi_e(\mathbf{r};\mathbf{R})\chi_N(\mathbf{R})] \\ &= -\sum_\alpha \frac{1}{2M_\alpha}\Big[\nabla_\alpha^2\psi_e(\mathbf{r};\mathbf{R})\chi_N(\mathbf{R}) + \psi_e(\mathbf{r};\mathbf{R})\nabla_\alpha^2\chi_N(\mathbf{R}) \\ &\quad +2(\nabla_\alpha\psi_e(\mathbf{r};\mathbf{R}))(\nabla_\alpha\chi_N(\mathbf{R}))\Big] \\ &\approx \psi_e(\mathbf{r};\mathbf{R})\hat{T}_N\chi_N(\mathbf{R}) \end{aligned} \tag{2.23}$$

We can neglect the first and the third term of the resulting equation since the contribution coming from the first and second derivative of electronic wavefunction with respect to nuclear coordinates is in the order of $m/M_\alpha \approx 0$ as mentioned before. As a consequence Eq. 2.20 can be rewritten as follows after plugging the terms in the curly brackets of the Eq. 2.21:

$$\left\{\hat{T}_N + E_e + \hat{V}_{NN}\right\}\chi_n(\mathbf{R}) = E\chi_n(\mathbf{R}) \tag{2.24}$$

To wrap up the current discussion; the resulting equation signifies that to obtain the total energy of the system, one first solves the Schrödinger equation using the electronic Hamiltonian to acquire the total electronic energy in the presence of static nuclei. This energy is treated as a potential energy which the nuclei experiences. In other words, the nuclei moves on a Potential Energy Surface (PES) created by the electrons. Although nuclei and electrons can be treated at different time scales, one still has to struggle with the solution of the daunting many-body Schrödinger equation by using the electronic Hamiltonian which will yield the electronic wavefunction Ψ_e and corresponding electronic energies E_e.

There exists two broad classes of techniques to solve the Schrödinger equation analytically: variational method and perturbation theory. The former can be applied to both wavefunction-based and density-based techniques. Hartree-Fock method or configuration interaction (CI) can be an example to a wavefunction-based technique in the variational method scheme; while Møller-Plesset perturbation theory [88] to the latter of the two.

In 1928, Douglas Hartree suggested the idea of approximating the electronic wavefunction ψ_e as a direct product of single particle wavefunctions [89].

$$\psi_e(\mathbf{x}_1, \mathbf{x}_2, ..., \mathbf{x}_N) = \phi_1(\mathbf{x}_1)\phi_2(\mathbf{x}_2)...\phi_N(\mathbf{x}_N) \tag{2.25}$$

This approach, however, has a notable drawback: it is unable to satisfy the antisymmetric principle which states that the wavefunction of a multi-fermionic system must be antisymmetric, so it must change sign under odd permutations of any set

of electronic spatial coordinates in addition to $\mathbf{s}$, the spin degree of freedom.[2] Electrons are spin-$1/2$ particles, therefore requisite of an antisymmetric wavefunction is an inevitable consequence of Pauli exclusion principle; two like-spin electrons can not occupy the same quantum state simultaneously.

$$\Psi(\mathbf{x}_1, \ldots, \mathbf{x}_i, \ldots, \mathbf{x}_j, \ldots, \mathbf{x}_N) = -\Psi(\mathbf{x}_1, \ldots, \mathbf{x}_j, \ldots, \mathbf{x}_i, \ldots, \mathbf{x}_N) \tag{2.26}$$

It was later understood that Hartree method was giving poor agreement with the experimental data. This problem was corrected by expanding the current approach to form the Hartree-Fock theory [90]. Fock suggested to write the total wavefunction as a fully antisymmetrized product of spin orbitals which spans all the permutations of the electronic coordinates in order to take the electron exchange interactions into account.

$$\Psi_{HF} = \frac{1}{\sqrt{N!}}\Big[\phi_1(\mathbf{x}_1)\phi_2(\mathbf{x}_2)\ldots\phi_N(\mathbf{x}_N) - \phi_1(\mathbf{x}_2)\phi_2(\mathbf{x}_1)\ldots\phi_N(\mathbf{x}_N) + \ldots\Big] \tag{2.27}$$

Soon afterwards Slater showed that the resulting electronic wavefunction can simply be written as a single $N \times N$ determinant of spin orbitals [91] where $1/\sqrt{N!}$ is the normalization coefficient.

$$\Psi_{HF}(\mathbf{x}_1, \ldots, \mathbf{x}_N) = \frac{1}{\sqrt{N!}} \begin{vmatrix} \phi_1(\mathbf{x}_1) & \phi_1(\mathbf{x}_2) & \ldots & \phi_1(\mathbf{x}_N) \\ \phi_2(\mathbf{x}_1) & \phi_2(\mathbf{x}_2) & \ldots & \phi_2(\mathbf{x}_N) \\ \vdots & \vdots & \ddots & \vdots \\ \phi_N(\mathbf{x}_1) & \phi_N(\mathbf{x}_2) & \ldots & \phi_N(\mathbf{x}_N) \end{vmatrix} \tag{2.28}$$

The expectation value of the Hamiltonian using the above single Slater determinant electronic wavefunction yields the HF energy;

$$E_{HF} = \langle \Psi_{HF} | \hat{\mathcal{H}}_e | \Psi_{HF} \rangle \tag{2.29}$$

[2] Spin labels were omitted up to now; $\mathbf{x}_i = \{\mathbf{r}_i, s_i\}$ is called the spin orbital.

The purpose is to find the best wavefunction which minimizes the expectation value of $\hat{\mathcal{H}}_e$ keeping in mind the restriction on the orthonormality of one-particle states $\phi_1 \dots \phi_N$. Variational principle states that the true ground state energy is always lower than that of the outcome of the expectation value of the Hamiltonian. Variational theorem seeks the wavefunction which gives the lowest electronic energy possible by tweaking its parameters.

Making the assumption that the electronic wavefunction can approximately be written as a single Slater determinant renders HF theory to lack the correlation between the electrons. This approximation is identical to consider the electrons as occupying single orbitals which in turn causes Hartree-Fock theory to fail to describe the electronic structure within desired accuracy. Each electron feels the presence of the other electrons, as a result all the electrons move in an average field created by the other electrons. Hartree-Fock method is also called "mean field theory".

Hartree-Fock theory employs the most fundamental quantum mechanical approach to lead one to the solution of the Schrödinger equation. For many-body electronic systems which are expressed by the Hamiltonian, external potential term V_{ext} completely establishes the Hamiltonian and determines all the ground state properties of the system together with the total number of particles. Then the eigenfunctions of the Hamiltonian are acquired by variationally minimizing the energy functional $E[\Psi]$. However, considering the number of particles in a typical system, one has to deal with hundreds or thousands of non-linear differential equations. Therefore, it is much more convenient to solve the electronic structure problem by using the density which depends on only 3 variables instead of the many-electron wavefunction, which gives an approach independent of the system size.

2.4 Density Functional Theory

The idea of expressing electronic energy in terms of the electron density was first envisaged by Thomas and Fermi in 1920s [92] [93]. The proposition was to describe the electrons as uniform clouds of negative charge wandering around the nucleus. The electron-electron interaction was treated classically along with the electron-nucleus. In contrast to the current many-body problem, TF model was an extremely simplified version.

As a result, the most important drawback of TF model is the negligence of the many-body correlation effects which were added by Dirac afterwards. However, what really renders TF model historically important is its demonstration of the possibility of obtaining the electronic energy only from the electron density.

Kinetic energy of the electrons is expressed as follows in TF model.

$$T_{TF}[\rho(\mathbf{r})] = C_F \int [\rho(\mathbf{r})]^{5/3} \, \mathrm{d}^3\mathbf{r} \tag{2.30}$$

where C_F is

$$C_F = \frac{3}{10} \left(3\pi^2\right)^{2/3} \tag{2.31}$$

2.4.1 Definition of the Density

Instead of solving the Schrödinger equation directly using the wavefunction treatment, one must switch from the wavefunction to the electron density, the principle observable of this approach. Given that the fact that it is impossible to locate the exact position of an electron like a classical particle according to the uncertainty principle, electron density gives the probability of finding the electron in a given volume.

The expectation value of the single-particle probability density operator for the many-body wavefunction gives the electron density of the system.

$$\hat{\rho}(\mathbf{r}) = \sum_{i=1,N} \delta(\mathbf{r} - \mathbf{r}_i) \tag{2.32}$$

$$\begin{aligned}\rho(\mathbf{r}) =& \langle\Psi|\hat{\rho}(\mathbf{r})|\Psi\rangle = \sum_{i=1,N} \int \Psi^*(\mathbf{r}_1, \ldots, \mathbf{r}_N)\delta(\mathbf{r} - \mathbf{r}_i)\Psi(\mathbf{r}_1, \ldots, \mathbf{r}_N)\mathrm{d}s_1\mathrm{d}\mathbf{x}_2 \ldots \mathrm{d}\mathbf{x}_N \\ =& \int \Big[|\Psi(\mathbf{r}, \mathbf{r}_2, \ldots, \mathbf{r}_N)|^2 \mathrm{d}\mathbf{r}_2\mathrm{d}\mathbf{r}_3 \ldots \mathrm{d}\mathbf{r}_N + |\Psi(\mathbf{r}_1, \mathbf{r}, \ldots, \mathbf{r}_N)|^2 \mathrm{d}\mathbf{r}_1\mathrm{d}\mathbf{r}_3 \ldots \mathrm{d}\mathbf{r}_N + \ldots\Big] \\ =& N \int |\Psi(\mathbf{r}, \ldots, \mathbf{r}_N)|^2 \mathrm{d}\mathbf{r}_2 \ldots \mathrm{d}\mathbf{r}_N\end{aligned} \tag{2.33}$$

Assuming that the wavefunction is normalized, upon integration over all space the density gives the total number of electrons.

$$\int \rho(\mathbf{r})\mathrm{d}\mathbf{r} = N \tag{2.34}$$

2.4.2 Hohenberg-Kohn Theorems

Despite its importance, Hohenberg-Kohn theorems do not manifest the direct approach to apply the Density Functional Theory but define the significance of the density observable. In 1964, Hohenberg and Kohn proved that electronic Hamiltonian can entirely be written as a functional of the electron density and therefore the ground state (GS) properties of a system is defined by the density itself in an exact manner.

In order to complete the migration from wavefunction to the density approach, one must define all the terms in the Hamiltonian in terms of the density. Let's recall the resulting clamped-nuclei Hamiltonian as a consequence of the Born-Oppenheimer approximation (Eq. 2.18).

$$\begin{aligned}\hat{\mathcal{H}} =& \sum_{i=1}^{N} -\frac{1}{2}\nabla_i^2 + \sum_{i<j=1}^{N} \frac{1}{|\mathbf{r}_i - \mathbf{r}_j|} - \sum_{i=1}^{N}\sum_{\alpha=1}^{M} \frac{Z_\alpha}{|\mathbf{r}_i - \mathbf{R}_\alpha|} \\ =& \hat{T} + \hat{V}_{ee} + \hat{V}_{en}\end{aligned}$$

The Coulomb interaction between the static nuclei and the electrons can be written as an external potential $\hat{V}_{ext}$.

$$\hat{V}_{en} = \hat{V}_{ext} = -\sum_{i=1}^{N}\sum_{\alpha=1}^{M}\frac{Z_\alpha}{|\mathbf{r}_i - \mathbf{R}_\alpha|} \tag{2.35}$$

Then the remaining part of the Hamiltonian is defined as the Hohenberg-Kohn functional $\hat{F}_{HK}$,

$$\begin{aligned}\hat{F}_{HK} =& -\frac{1}{2}\sum_i \nabla_i^2 + \sum_{i<j=1}^{N}\frac{1}{|\mathbf{r}_i - \mathbf{r}_j|} \\ =& \hat{T} + V_{ee}\end{aligned} \tag{2.36}$$

$\hat{F}_{HK}$ is independent of any external field, so it is identical for any arbitrary system consisting of N electrons. It is, therefore, said to be a universal function.

The expectation value of the Hamiltonian gives the total energy.

$$E = \langle\Psi|\hat{F}_{HK} + \hat{V}_{ext}|\Psi\rangle = \langle\Psi|\hat{F}_{HK}|\Psi\rangle + \langle\Psi|\hat{V}_{ext}|\Psi\rangle \tag{2.37}$$

Let's first calculate the expectation value of the nuclei-electron interaction potential,

$$\begin{aligned}&\langle\Psi(\mathbf{r}_1,\ldots,\mathbf{r}_N)|\hat{V}_{ext}|\Psi(\mathbf{r}_1,\ldots,\mathbf{r}_N)\rangle = \\ &\qquad = -\sum_{i=1}^{N}\sum_{\alpha=1}^{M}\int \Psi^*(\mathbf{r}_1,\ldots,\mathbf{r}_N)\frac{Z_\alpha}{|\mathbf{r}_i - \mathbf{R}_\alpha|}\Psi(\mathbf{r}_1,\ldots,\mathbf{r}_N)\mathrm{d}\mathbf{r}_1\ldots\mathrm{d}\mathbf{r}_N \\ &\qquad = -\sum_{i=1}^{N}\sum_{\alpha=1}^{M}\int |\Psi(\mathbf{r}_1,\ldots,\mathbf{r}_N)|^2\frac{Z_\alpha}{|\mathbf{r}_i - \mathbf{R}_\alpha|}\mathrm{d}\mathbf{r}_1\ldots\mathrm{d}\mathbf{r}_N\end{aligned} \tag{2.38}$$

Expanding the summation over the electronic index i gives a similar calculation to that of the density. As a result, the nuclear-electron interaction energy $E_{ext}[\rho(\mathbf{r})]$ can be written as a functional of the density as follows,

$$E_{ext}[\rho(\mathbf{r})] = \int \rho(\mathbf{r}) V_{ext}(\mathbf{r})\ \mathrm{d}\mathbf{r} \tag{2.39}$$

Eq. 2.37 becomes as follows for any arbitrary external field $v(\mathbf{r})$ which is not only limited to Coulomb interaction,

$$E\left[\rho(\mathbf{r})\right] = F_{HK}\left[\rho(\mathbf{r})\right] + \int \rho(\mathbf{r}) v(\mathbf{r})\ \mathrm{d}\mathbf{r} \tag{2.40}$$

The first HK theorem expresses that for a system of interacting particles, the external potential V_{ext} is uniquely determined, to within a constant, by the ground state electron density $\rho(\mathbf{r})$ [94]. This, in turn, establishes the Hamiltonian operator $\hat{\mathcal{H}}$, therefore the full many-body ground state wavefunction is also a functional of the ground state electron density. The proof can be shown by using *reductio ad absurdum* as was originally given by Hohenberg and Kohn. It is important to state that the Hamiltonian will be considered to produce non-degenerate states. However, it is also noteworthy that Levy [95, 96] and Lieb [97, 98] independently introduced the constraint search formalism to generalize the discussion for degenerate GS's.

Assume that there exists two different Hamiltonians, $\hat{\mathcal{H}}_1$ and $\hat{\mathcal{H}}_2$ which have different ground state energies E_1 and E_2 with different normalized ground state wavefunctions Ψ_1 and Ψ_2, respectively. These Hamiltonians differ only in their potential energy terms which are arising from the same ground state density such that;

$$\hat{\mathcal{H}}_1 = \hat{F} + \hat{V}^1_{ext} \quad , \quad \hat{\mathcal{H}}_2 = \hat{F} + \hat{V}^2_{ext} \tag{2.41}$$

The ground state energies are found as such,

$$E_1[\rho(\mathbf{r})] = \langle \Psi_1 | \hat{\mathcal{H}}_1 | \Psi_1 \rangle \quad , \quad E_2[\rho(\mathbf{r})] = \langle \Psi_2 | \hat{\mathcal{H}}_2 | \Psi_2 \rangle \tag{2.42}$$

Let's rewrite the above expectation value equations as follows and add them side by side;

$$\begin{aligned} E_1 <& \langle \Psi_2 | \hat{\mathcal{H}}_1 | \Psi_2 \rangle \\ =& \langle \Psi_2 | \hat{\mathcal{H}}_2 | \Psi_2 \rangle + \langle \Psi_2 | (\hat{\mathcal{H}}_1 - \hat{\mathcal{H}}_2) | \Psi_2 \rangle \\ =& E_2 + \int \rho(\mathbf{r}) [V_{ext}^1(\mathbf{r}) - V_{ext}^2(\mathbf{r})] \, \mathrm{d}\mathbf{r} \end{aligned} \tag{2.43}$$

and similarly Ψ_1 is not the ground state of $\hat{\mathcal{H}}_2$,

$$\begin{aligned} E_2 <& \langle \Psi_1 | \hat{\mathcal{H}}_2 | \Psi_1 \rangle \\ =& \langle \Psi_1 | \hat{\mathcal{H}}_1 | \Psi_1 \rangle + \langle \Psi_1 | (\hat{\mathcal{H}}_2 - \hat{\mathcal{H}}_1) | \Psi_1 \rangle \\ =& E_1 + \int \rho(\mathbf{r}) [V_{ext}^2(\mathbf{r}) - V_{ext}^1(\mathbf{r})] \, \mathrm{d}\mathbf{r} \end{aligned} \tag{2.44}$$

Since Ψ_2 is not the ground state wavefunction of $\hat{\mathcal{H}}_1$, the outcome of the expectation value will always be greater than the true ground state energy E_1. The same thought process also applies for the second equation.

Consequently, adding the resulting equations of Eq. 2.43 and 2.44 ends up with an obvious contradiction which deducts that two different external potential cannot give rise to same density for the ground state.

$$E_1 + E_2 < E_1 + E_2 \tag{2.45}$$

The second Hohenberg-Kohn theorem states that there exists a universal functional E[ρ] which is determined in terms of the density. The minimum can be found by invoking the variational principle as it was introduced in the HF approach, however this time it applies to the electron density.

As given in Equation 2.40 the energy is a functional of the density for a given potential $v(\mathbf{r})$,

$$E\left[\rho(\mathbf{r})\right] = F_{HK}\left[\rho(\mathbf{r})\right] + \int \rho(\mathbf{r}) v(\mathbf{r}) \, \mathrm{d}\mathbf{r}$$

We know that the true GS density uniquely determines the GS energy,

$$\begin{aligned} E_1 = E_1[\rho_{GS}] =& \langle \Psi_1 | \hat{\mathcal{H}}_1 | \Psi_1 \rangle \\ =& \langle \Psi_1 | \hat{F} | \Psi_1 \rangle + \langle \Psi_1 | \hat{V}^1_{ext} | \Psi_1 \rangle \end{aligned} \tag{2.46}$$

However, an arbitrary density, ρ', different than GS density will produce a higher energy according to the variational principle.

$$\begin{aligned} \int \rho'(\mathbf{r})\ v_{ext}(\mathbf{r}) \mathrm{d}\mathbf{r} + F[\rho'(\mathbf{r})] &> \int \rho_{GS}(\mathbf{r})\ v_{ext}(\mathbf{r}) \mathrm{d}\mathbf{r} + F[\rho_{GS}(\mathbf{r})] \\ E_v[\rho'(\mathbf{r})] &> E_v[\rho_{GS}(\mathbf{r})] \end{aligned} \tag{2.47}$$

The minimization of the energy functional gives the exact ground state density; i.e. density that minimizes the energy functional is the true ground state electron density. The minimization of the energy functional with the constraint on the electron density that its integration will yield the total number of electrons, $\int \rho(\mathbf{r}) \mathrm{d}\mathbf{r} = N$, be positive, $\rho(\mathbf{r}) > 0$, and be continuous.

$$\delta \Big[F[\rho(\mathbf{r})] + \int \rho(\mathbf{r}) v_{ext}(\mathbf{r})\ \mathrm{d}\mathbf{r} - \mu \Big(\int \rho(\mathbf{r}) \mathrm{d}\mathbf{r} - N \Big) \Big] = 0 \tag{2.48}$$

with Lagrange multiplier that yields the chemical potential, μ,

$$\frac{\delta E[\rho]}{\delta \rho(\mathbf{r})} = \mu = V_{ext}(\mathbf{r}) + \frac{\delta F_{HK}[\rho(\mathbf{r})]}{\delta \rho(\mathbf{r})} \tag{2.49}$$

2.4.3 Kohn-Sham Equations

As mentioned before, although Hohenberg-Kohn theorems constitute a concrete basis for DFT by demonstrating that it is possible to migrate from wavefunction concept to density approach in order to calculate the properties of the system, do not exactly show how to obtain the ground state density. Kohn and Sham (KS) [99] provided the equations which establishes the way of finding the ground state electron density with KS equations since directly minimizing the energy functional is not the most efficacious way.

Kohn and Sham brought the non-interacting single-particle orbital concept back into play which is similar to that of the Hartree-Fock approximation. KS put forward a fictitious non-interacting system that produces the same density to that of its interacting counterpart. One can separate the energy functional as follows,

$$E\left[\rho(\mathbf{r})\right] = T_s[\rho(\mathbf{r})] + V_H[\rho(\mathbf{r})] + E_{\mathrm{xc}}[\rho(\mathbf{r})] + \int \rho(\mathbf{r}) v(\mathbf{r})\, \mathrm{d}\mathbf{r} \tag{2.50}$$

where $T_s[\rho(\mathbf{r})]$ is the kinetic energy functional of the non-interacting electrons simply given as the sum of the kinetic energies of each particle,

$$T_s[\rho(\mathbf{r})] = -\frac{1}{2}\sum_{i}^{N} \int \phi_i^*(\mathbf{r}) \nabla^2 \phi_i(\mathbf{r}) \mathrm{d}\mathbf{r} \tag{2.51}$$

with density $\rho(\mathbf{r})$ which is expressed as the sum of one-electron Kohn-Sham orbitals $\{\phi_i\}$ where f_i is the occupation number of the i^{th} orbital.

$$\rho(\mathbf{r}) = \sum_{i}^{N} f_i |\phi_i(\mathbf{r})|^2 \tag{2.52}$$

$V_H[\rho(\mathbf{r})]$ is the Hartree potential which the Coulomb interaction between the electron clouds is approximately equal,

$$V_{ee}[\rho(\mathbf{r})] \approx V_H[\rho(\mathbf{r})] = \int \frac{\rho(\mathbf{r}')}{|\mathbf{r} - \mathbf{r}'|} \mathrm{d}\mathbf{r}' \tag{2.53}$$

Since $T_s[\rho(\mathbf{r})]$ can only be written as a functional of the KS orbitals, Equation 2.49 takes the form,

$$\mu = \frac{\delta T_s[\rho(\mathbf{r})]}{\delta \rho(\mathbf{r})} + V_{eff}(\mathbf{r}) \tag{2.54}$$

where $V_{eff}(\mathbf{r})$ is the effective potential in which the fictitious system evolve,

$$\begin{aligned} V_{eff}(\mathbf{r}) =& V_{ext}(\mathbf{r}) + V_H(\mathbf{r}) + V_{xc}(\mathbf{r}) \\ =& V_{ext}(\mathbf{r}) + \int \frac{\rho(\mathbf{r}')}{|\mathbf{r} - \mathbf{r}'|} \mathrm{d}\mathbf{r}' + \frac{\delta E_{xc}[\rho(\mathbf{r})]}{\delta \rho(\mathbf{r})} \end{aligned} \tag{2.55}$$

The solution for a system in the potential V_{eff} is given by a single-particle Schrödinger-like equation.

$$\left[\frac{1}{2}\nabla^2 + V_{eff}(\mathbf{r})\right] \phi_i(\mathbf{r}) = \varepsilon_i \phi_i(\mathbf{r}) \tag{2.56}$$

Equations 2.52, 2.55, and 2.56 constitutes the Kohn-Sham equations. These equations substitute the notion of the energy functional minimization which replaced the problematic treatment of computationally expensive many-body Schrödinger equation of an interacting system. In KS scheme, single-particle wavefunctions are being revisited in the framework of a non-interacting system. The effective potential is a functional of the density, therefore it depends indirectly on the KS orbitals. On the other hand, the changes in the external potential affect the orbitals in turn. For this reason, KS equations must be solved self-consistently. Starting with an initial guess for the density, the solution of the Schrödinger-like equation for the orbitals is used to construct the new density. This reciprocation continues until the calculation reaches to a predetermined convergence value.

Lastly, $E_{xc}[\rho(\mathbf{r})]$, exchange-correlation energy is simply the difference between the kinetic and potential energies of the interacting and non-interacting system.

$$E_{\mathrm{xc}}[\rho(\mathbf{r})] = (T[\rho(\mathbf{r})] - T_s[\rho(\mathbf{r})]) + (V_{ee}[\rho(\mathbf{r})] - V_H[\rho(\mathbf{r})]) \tag{2.57}$$

This contribution corresponds to a small fraction of the total energy and can be approximated surprisingly well by using fairly simple methods which will be discussed in the following section.

Putting all the terms together, the total energy can finally be written as follows,

$$E_{KS}[\rho(\mathbf{r})] = -\frac{1}{2}\sum_{i}^{N}\int \phi_i^*(\mathbf{r})\nabla^2\phi_i(\mathbf{r})\mathrm{d}\mathbf{r} + \int \rho(\mathbf{r})V_{ext}(\mathbf{r})\ \mathrm{d}\mathbf{r} + \frac{1}{2}\int\int \frac{\rho(\mathbf{r})\rho(\mathbf{r}')}{|\mathbf{r}-\mathbf{r}'|}\mathrm{d}\mathbf{r}\mathrm{d}\mathbf{r}' + E_{\mathrm{xc}}[\rho(\mathbf{r})] \quad (2.58)$$

2.4.4 Exchange and Correlation Functionals

The Kohn-Sham theory is said to be *exact* as far as the functional approach is concerned. However, exact functional form of the exchange-correlation energy $E_{xc}[\rho(\mathbf{r})]$ is not known for an arbitrary inhomogeneous electron gas, for this reason approximations must be introduced.

According to the intricacy and accuracy of the methods, John Perdew [100] visualized the path from the Hartree world towards the *heaven of chemical accuracy* as depicted in Table 2.1.

TABLE 2.1: Chemical accuracy diagram "Jacob's ladder" depicted by J.Perdew for different classes of exchange-correlation functionals.

Heaven of chemical accuracy

Semi-Empirical		*Non-Empirical*
	Exact Functional	
M06	Hybrid Meta-GGA	
B3LYP, B1B95	Hybrid GGA	PBE0
mPWB95	Meta-GGA	TPSS
BP86, BLYP	GGA	PBE, PW91
	LDA	

Hartree World

The methods can be divided into five different groups; however for the sake of conciseness, only Local Density Approximation (LDA) and Generalized Gradient Approximation (GGA) will be mentioned in this section.

2.4.4.1 Local Density Approximation (LDA)

Introduced by Hohenberg and Kohn in their well-known publication [94], *Local Density Approximation* is the simplest and the most popular approach where the exchange-correlation energy per each infinitesimal volume of electron density of the real inhomogeneous system is taken to be as that of a uniform (homogeneous) electron gas (UEG, HEG or also known as Jellium). In other words, LDA method aims to approximate the exchange-correlation energy of the real system locally by assuming it as the energy density of an HEG. The energy functional $E_{xc}[\rho(\mathbf{r})]$ is simply given by,

$$E_{xc}^{\mathrm{LDA}}[\rho(\mathbf{r})] = \int \rho(\mathbf{r})\varepsilon_{xc}(\rho(\mathbf{r}))\mathrm{d}\mathbf{r} \ , \tag{2.59}$$

Exchange-correlation energy per particle of a homogeneous electron gas of density ρ is represented by $\varepsilon_{xc}[\rho(\mathbf{r})]$ and it can be separated into two parts: exchange (ε_x) and correlation (ε_c).

$$\varepsilon_{xc}(\rho(\mathbf{r})) = \varepsilon_x(\rho(\mathbf{r})) + \varepsilon_c(\rho(\mathbf{r})) \tag{2.60}$$

Exchange-correlation potential V_{xc} which will later be inserted into Equation 2.55 becomes,

$$V_{xc}(\mathbf{r}) = \frac{\delta E_{xc}^{\mathrm{LDA}}[\rho(\mathbf{r})]}{\delta\rho(\mathbf{r})} = \varepsilon_{xc}(\rho(\mathbf{r})) + \rho(\mathbf{r})\frac{\mathrm{d}\varepsilon_{xc}(\rho(\mathbf{r}))}{\mathrm{d}\rho(\mathbf{r})} \tag{2.61}$$

Exchange energy $E_x^{LDA}[\rho(\mathbf{r})]$ for an HEG of volume V is known analytically and given as it was introduced by Bloch [101] and Dirac [102] in 1930;

$$E_x^{LDA}[\rho(\mathbf{r})] = -\frac{3}{4}\left(\frac{3}{\pi}\right)^{1/3}\int \rho^{4/3}(\mathbf{r})\ \mathrm{d}\mathbf{r} \tag{2.62}$$

The contribution from the correlation part is not known explicitly but the ground state energy of the uniform electron gas was calculated by Ceperley and Alder using quantum Monte Carlo calculations [103, 104] and parametrized by Perdew and Zunger [105].

Due to its point of origin, LDA is intuitively thought to be valid only for the systems that are having slowly varying densities such as intrinsic semiconductors. That being sad, it gives surprisingly accurate results even for strongly inhomogeneous systems despite its simplicity. Its success originates from the fact that LDA overestimates exchange while it underestimates correlation which in turn ends up compensating each other and as a result, gives satisfactory results for atomic, molecular and solid state systems, including metals [106].

2.4.4.2 Generalized Gradient Approximation (GGA)

Even though LDA is the simplest method, it gives insufficient results for the systems with rapidly varying densities, such as for molecules. To remedy this flaw, gradient expansion approximation (GEA) [94] is introduced by Hohenberg and Kohn where the higher order gradients of the electron density is also taken into account as well as the gradient itself in order to factor in the inhomogeneity of the electron density. This can be considered as a correction to the LDA calculation without bringing a significant additional computational load. Although GEA had serious shortcomings in its early years, later formed a basis for generalized gradient approximation which is the most commonly used method of exchange-correlation functional. GGA functionals are sometimes called semilocal and gives better results for the systems with inhomogeneous densities. The accuracy of energy barriers, molecular geometries, atomization energies and total energies are increased with the use of GGAs [107]. Exchange-correlation energy can be written as follows,

$$E_{xc}^{GGA}[\rho_\uparrow, \rho_\downarrow, \nabla\rho_\uparrow, \nabla\rho_\downarrow] = \int f^{GGA}(\rho_\uparrow, \rho_\downarrow, \nabla\rho_\uparrow, \nabla\rho_\downarrow)\mathrm{d}\mathbf{r} \tag{2.63}$$

where f^{GGA} is a function of the electron density and its gradient. The exchange and correlation parts are usually calculated separately.

$$E_{xc}^{GGA} = E_x^{GGA} + E_c^{GGA} \tag{2.64}$$

and the exchange energy E_x^{GGA} reads,

$$E_x^{GGA}[\rho(\mathbf{r})] = \int \rho(\mathbf{r})\varepsilon_x[\rho(\mathbf{r})]F_x^{GGA}(s)\mathrm{d}\mathbf{r} \tag{2.65}$$

where s is the dimensionless reduced density gradient,

$$s(\mathbf{r}) = \frac{|\nabla\rho(\mathbf{r})|}{2k_F(\mathbf{r})\rho(\mathbf{r})} \tag{2.66}$$

with the local Fermi wavevector $k_F(\mathbf{r}) = (3\pi^2\rho(\mathbf{r}))^{1/3}$.

The characteristic of different functionals stems from the choice of enhancement factor F_x^{GGA} which expresses how the LDA energy is enhanced. There exist a wide range of functionals in the GGA family such as Perdew-Wang (PW91), Perdew-Burke-Ernzerhof (PBE) and Becke-Lee-Yang-Parr (BLYP). BLYP functional was used in this thesis, whose the exchange part was developed by Becke [108] and the correlation part by Lee-Yang-Parr [109].

$$F_x^{B88}(s) = 1 + \frac{\beta x^2(s)}{c[1 + \beta x(s) sinh^{-1}x(s)]} \tag{2.67}$$

where $x(s)$ is given by

$$x(s) = 2(3\pi^2)^{1/3}s \tag{2.68}$$

The only empirical parameter present in this functional is β and it is calculated by fitting the energies of first 6 noble gases, namely He through Rn. The exchange energy then becomes,

$$E_x^{B88} = E_x^{LDA} - \beta \sum_\sigma \int \rho_\sigma^{4/3} \frac{x_\sigma^2}{(1 + 6\beta x(s) sinh^{-1} x(s))} \mathrm{d}\mathbf{r} \tag{2.69}$$

2.5 Solving the Kohn-Sham equations

Now that the effective potential is determined, the KS equations are derived and ready to be solved self-consistently; one needs to make an initial guess for the density, hence needs a recipe to represent the unknown electron wavefunctions in terms of the linear superposition of known wave equations. Theoretically, any kind of function is suitable to be used as a basis. That being said, the behavior of the basis function should reflect that of the real wavefunction. For the sake of conciseness, only the plane wave (PW) basis set will be represented in this chapter. Other than PW basis set, the options are plentiful. Potential independent localized basis sets or atomic sphere methods can also be given as examples.

2.5.1 Plane wave basis set

According to the Bloch's theorem [110]; $\psi_i(\mathbf{r})$, the solution of the single-particle Schrödinger equation (Equation 2.56) within a periodic potential can be expanded in terms of the product of cell periodicity and a wave-like part,

$$\psi_{i,k}(\mathbf{r}) = f_i(\mathbf{r}) e^{i\mathbf{k}\cdot\mathbf{r}} \tag{2.70}$$

where $f_i(\mathbf{r})$ is an arbitrary function having the same periodicity with the lattice, therefore it can also be expanded in terms of plane waves,

$$f_i(\mathbf{r}) = \sum_{\mathbf{G}} c_{i,\mathbf{G}} e^{i\mathbf{G}\cdot\mathbf{r}} \tag{2.71}$$

Substituting Equation 2.71 back into Equation 2.70 yields that electron wavefunction can be expanded in terms of plane waves,

$$\psi_{i,\mathbf{k}}(\mathbf{r}) = \sum_{G} C_{i,\mathbf{k}+\mathbf{G}} e^{i(\mathbf{k}+\mathbf{G})\cdot\mathbf{r}} \tag{2.72}$$

where $C_{i,\mathbf{k}}$ are the Fourier (variational) coefficients and the $\mathbf{G}$ are reciprocal space lattice vector.

It may seem practical to have an infinite number of plane waves to acquire an exact solution, however having a finite memory and calculation time pretty much hampers this notion. It requires a vast number of plane waves to describe the electrons due to their high kinetic energy and rapid oscillations. Defining a kinetic energy cut-off, E_{cut}, serves to truncate the set of plane waves by including only the wavevectors that satisfies the following relation.

$$\frac{1}{2}|\mathbf{k}+\mathbf{G}|^2 \leq E_{cut} \tag{2.73}$$

Using plane waves (PW) brings a number of perks which Gaussian or Slater functions lack. PWs are independent of the atomic species of the system; this property not only allows one to implement the same basis set system-wide which induces quite a flexibility, but also prevents the formation of Pulay forces that arises if the basis set is incomplete [111]. Unlike localized basis sets, it is possible to increase the accuracy in the plane-wave approach by increasing the cut-off energy which accounts for expanding the basis set. On the other hand, augmenting the cut-off energy introduces a computational bottleneck which is aimed to be reduced by implementing the pseudopotential approach in order to achieve the desired efficiency in DFT calculations.

2.5.2 Pseudopotentials

Numeric calculations become proportionally more and more costly in terms of computational demand with the vast number of electrons. The core electrons are tightly bound at the region close to the core; thus as a requirement of the

Pauli exclusion principle, valence electrons must rapidly oscillate in the vicinity of the nucleus in order to assure their orthogonality with core electrons which, in turn, ends up with the demand of a large number of plane waves to be described accurately. Core electrons are chemically inert; they remain unaffected by the chemical environment, while the physical and chemical properties of the matter are described almost only by overlapping of the valence electrons; especially in semiconductors and metals. Therefore, it is redundant to devote the valuable computational resources to describe the core electrons. This problem can be tackled by the use of pseudopotential (PP) approximation [112]. Fermi was the first to introduce the idea of PP as early as 1927 [93, 113], however it was after the work of Philips and Kleinman [114] that this approach attracted a great amount of attention to be improved further.

In short, the notion of pseudopotential approach is to replace the strong core-valence electron interaction with a weaker but an effective pseudopotential. As a matter of fact, the error introduced by performing this replacement is actually lower than implementing LDA approximation for the exchange-correlation functional [115]. Early examples of PPs were generated by fitting empirical data such as band structure, however, modern DFT calculations are inclined to utilise parameter-free ionic pseudopotentials for transferability reasons. In 1979, Hamann and coworkers [116] introduced norm-conserving pseudopotentials which was later to be improved by Bachelet and coworkers [117].

The all-electron orbitals and their pseudo counterparts must behave very close to each other, if not identical, beyond the core radius r_c so that the charge densities match through the integral given in Equation 2.74. Besides, the logarithmic derivatives of the real and pseudo wavefunction and their first energy derivatives must agree beyond the core radius r_c. These two requirements are crucial for the norm conservation property and the intended behaviour of a pseudopotential is illustrated in Figure 2.1.

$$\int_0^{r'} r^2 |\phi_{nl}^{ps}(r)|^2 dr = \int_0^{r'} r^2 |\phi_{nl}^{ae}(r)|^2 dr \quad , \quad for\ r' \geq r_c \tag{2.74}$$

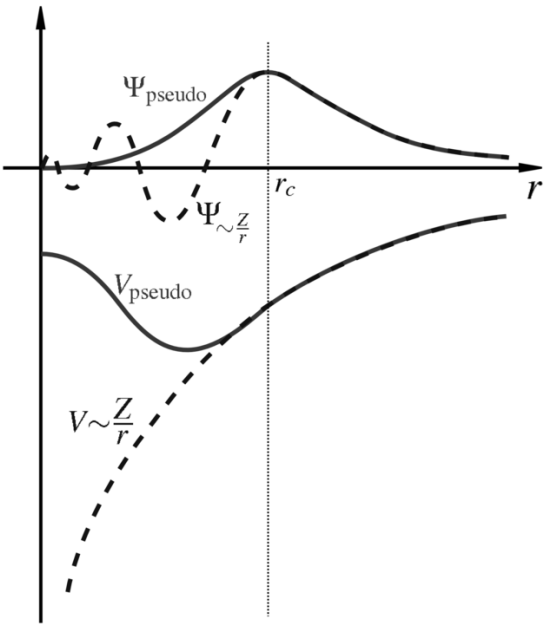

FIGURE 2.1: The schematic representation of true all-electron potential with its wavefunction (dashed lines) and pseudopotential with its pseudo wavefunction (solid line). Both pairs agree beyond the core radius r_c.

Wavefunctions of all-electron system and pseudopotential approach must also agree beyond a core radius r_c.

$$\phi_{nl}^{ps}(r) = \phi_{nl}^{ae}(r) \tag{2.75}$$

As the choice of the core radius affects the number of plane waves, softer PPs have been developed to reduce this large basis of plane waves with by requiring a low cut-off energy. One of the most common examples of soft and ultra-soft PPs have been developed by Troullier and Martins [118] and Vanderbilt [119].

Generating pseudopotentials is not a straightforward procedure, therefore a vast number of studies [120–122] has been devoted on this approximation following the criteria brought forward by Hamann et al. [116]. PPs are generated for a given "prototype" of atomic configuration. That being sad, the most general form of a pseudopotential is given as,

$$V_{pp} = \sum_{lm} |Y_{lm}\rangle \delta V_l(r) \langle Y_{lm}| \tag{2.76}$$

where Y_{lm} are the spherical harmonics and $V_l(r)$ is the pseudopotential for the angular momentum l. This representation is called "semi-local form" of a non-local PP as the radial part is local while the angular part is non-local, i.e. l-dependent.

In 1982, a unique scheme which composes the angular momentum differently than the other methods was proposed by Kleinman and Bylander (KB) [123] with the purpose of reducing the integrals to be calculated. This approach was also called fully non-local form or the Kleinman-Bylander transformation and aims to reduce the number integrals from being proportional to the square of the number of plane waves to a linear relation. The fully non-local KB form is given as,

$$V_{KB} = V_{loc} + \sum_{lm} \frac{|\delta V_l(r)\phi_{lm}\rangle\langle\phi_{lm}\delta V_l(r)\rangle}{\langle\phi_{lm}|\delta V_l(r)|\phi_{lm}\rangle} \tag{2.77}$$

with eigenvalues ϕ_{lm} of the pseudo Hamiltonian.

2.5.2.1 Non-linear core correction

The so-called valence and core regions can be clearly separated by a cut-off radius, however same procedure is not always valid for the core and valence electron densities. If the overlap of the two densities is neglected, especially in the case of heavy elements, it causes significant errors in both energy, band gap [124] and dielectric constant [125]; thus the overall electronic structure. To remedy this, two methods can be used: I) semi-core states [115]: the overlapping core electrons can be considered as a part of valence electrons or II) non-linear core corrections [126]: the effects originating from the core electrons can be factored into the valence part perturbatively. Including NLCC is essential for metallic spin-polarized systems that have shallow semicore states.

If one assumes the linearity of the core and valence charge densities ρ_c and ρ_v, the following relation is only satisfied in the absence of an overlap, while this is rarely true in reality.

$$V_{xc}[\rho_c + \rho_v] = V_{xc}[\rho_c] + V_{xc}[\rho_v] \tag{2.78}$$

The ionic PP can be extracted by the following procedure [127],

$$V_l^{ion}(\mathbf{r}) = V_l^{atomic}(\mathbf{r}) - V_H[\rho_v] - V_{xc}[\rho_c + \rho_v] \tag{2.79}$$

where V_l^{atomic} is the l-dependent screened atomic PP which will be modified accordingly in the energy functional Equation 2.50.

2.6 Born-Oppenheimer Molecular Dynamics

As it was mentioned in Section 2.1, the main drawback of the classical molecular dynamics method is obtaining the molecular interactions by only relying on the potential energy functions or classical (semi-empirical) force fields which essentially fails to describe bond making and bond breaking processes. It was mentioned also in Section 2.3 that the ab-initio methods proceed with the basic laws of quantum mechanics and don't solely depend on experimental predictions; this is where ab-initio methods acquire its predictive power and broad applicability.

As explained in Section 2.3, Born-Oppenheimer Molecular Dynamics (BOMD) is a method taking advantage of the Born-Oppenheimer approximation which exploits the huge difference between the masses of ions and electrons. Heavy and thus slow ions are considered to be stationary and are followed by the electrons adiabatically. Total electronic energy is calculated for a given nuclear configuration at an instant t. Subsequent to acquiring the energy, the ions are then moved according to the laws of classical dynamics.

Many molecular properties of systems, such as vibrational frequencies, physical structures, ionization energies, including electric and magnetic properties and many more, can be calculated by using Kohn-Sham orbitals which gives the ground state density and the forces on the atoms is also one of these properties. The total derivative of the total energy with respect to nuclear coordinates will give the forces on the atoms.

$$\mathbf{F} = -\frac{\partial E}{\partial \mathbf{R}_I} \tag{2.80}$$

The relationship between the derivative of the total energy with respect to a parameter, nuclear coordinates in the present case, and the expectation value of the derivative of the Hamiltonian operator with respect to the same parameter was put forward by the the **Hellman-Feynman theorem** which was proved independently to be correct by numerous scientists including Pauli and Güttinger [128–131] within the course of time.

Ground state energy, E(λ) is given by the expectation value of the Hamiltonian;

$$E(\lambda) = \langle\psi(\lambda)|H(\lambda)|\psi(\lambda)\rangle \tag{2.81}$$

Differentiating both sides yields,

$$\frac{dE}{d\lambda} = \langle\frac{d\psi}{d\lambda}|H|\psi\rangle + \langle\psi|H|\frac{d\psi}{d(\lambda)}\rangle + \langle\psi(\lambda)|\frac{dH}{d(\lambda)}|\psi(\lambda)\rangle \tag{2.82}$$

Since $\psi(\lambda)$ is the eigenvector of H(λ) with the eigenvalue E(λ), one can write,

$$\frac{dE}{d\lambda} = E\left[\langle\frac{d\psi}{d\lambda}|\psi\rangle + \langle\psi|\frac{d\psi}{d\lambda}\rangle\right] + \langle\psi|\frac{dH}{d\lambda}|\psi\rangle \tag{2.83}$$

The terms in the square brackets is the derivative of the inner product of orbitals; since it is a constant, its derivative vanishes;

$$\langle\frac{d\psi}{d\lambda}|\psi\rangle + \langle\psi|\frac{d\psi}{d\lambda}\rangle = \frac{d}{d\lambda}\left[\langle\psi|\psi\rangle\right] = 0 \tag{2.84}$$

What is left from Equation 2.82 is the Hellman-Feynman theorem which signifies that in order to obtain the forces, it is sufficient to calculate the derivative of the Hamilton operator instead of tackling the change in the wavefunctions.

$$\frac{dE}{d\lambda} = \langle\psi(\lambda)|\frac{dH}{d\lambda}|\psi(\lambda)\rangle \tag{2.85}$$

Rewriting the derivative of the energy term as in Equation 2.80 into Equation 2.85 with ionic positions **R** yields,

$$\mathbf{F} = -\langle\psi|\frac{dH}{dR_I}|\psi\rangle \tag{2.86}$$

After calculating the forces on the atoms using Hellman-Feynman theorem, the nuclei are propagated in time as much as the timestep Δt. The Newton's equations of motion are solved using various algorithms; Verlet algorithm and predictor-corrector approach can given as examples. Since only the nuclei are dynamically treated in this method, integration timestep can be chosen relatively larger.

The equations which are needed to be solved iteratively are as follows;

$$M_I\ddot{\mathbf{R}}_I = -\nabla_{R_I} \min_{\{\psi_i\}} E^{tot}[\{\psi_i\},\{\mathbf{R}_I\}] \tag{2.87}$$

$$\hat{\mathcal{H}}_e\psi_0(\mathbf{r};\mathbf{R}) = E_e\psi_0(\mathbf{r};\mathbf{R}) \tag{2.88}$$

Electronic structure is calculated each time the ions displace to their updated positions at a later time $t + \Delta t$. The trajectory followed by the ions is given in Figure 2.2. This procedure requires the electrons to be in their ground state, thus the diagonalization of the Hamiltonian at each time step, which in turn lengthens the required computational time, restricting the time scale of the simulation. Additionally, insufficient optimization of the wavefunctions causes the Pulay forces to arise [111] when the wavefunctions are represented within the plane wave basis set approach.

2.7 Car-Parrinello Molecular Dynamics

Matrix diagonalization methods are computationally expensive, which in turn leads to restriction on the simulation time scale. In 1985, Roberto Car and Michele Parrinello [76] introduced a new method to treat the electronic degrees of freedom as classical variables in order to reduce the computational demand needed for the diagonalization in Equation 2.87.

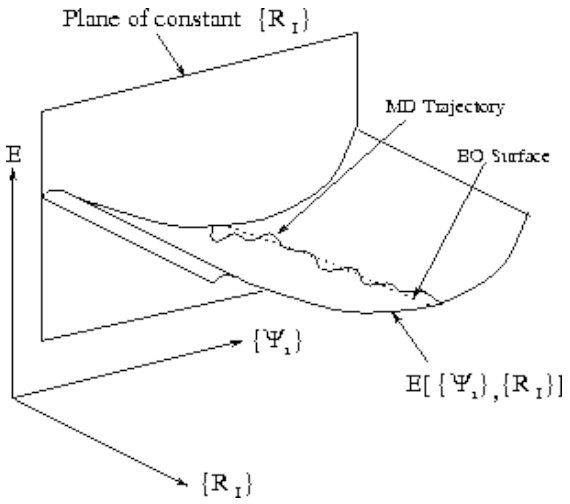

FIGURE 2.2: Schematic representation of potential energy surface. Taken from [132].

CP method uses a modified classical Lagrangian in order to combine the fictitious dynamics of the electronic degrees of freedom with classical molecular dynamics evolution of the atomic nuclei. The Car-Parrinello Lagrangian is given as follows.

$$\mathcal{L}_{CP} = \mu \sum_i \int |\dot{\psi}_i(\mathbf{r})|^2 \mathrm{d}\mathbf{r} + \frac{1}{2} \sum_{I=1}^{N} M_I \dot{\mathbf{R}}_I^2 - E_{tot}[\{\psi_i\}; \{\mathbf{R}\}] - \sum_{ij} \lambda_{ij} \left(\int \mu \psi_i^*(\mathbf{r}) \psi_j(\mathbf{r}) \mathrm{d}\mathbf{r} - \delta_{ij} \right) + \frac{1}{2} \sum \mu_q \dot{\alpha}_q^2 \quad (2.89)$$

The first term is the kinetic energy of the electrons. μ is the fictitious mass parameter associated with the electronic degrees of freedom. The second term is the kinetic energy of the ions with masses M_I. The third term is the total DFT energy. λ_{ij} in the fourth term are Lagrange multipliers which ensure the orthonormality of the Kohn-Sham orbitals. From the classical molecular dynamics point of view, the orthonormality constraint can be considered as an additional force imposed on the wavefunctions. However this does not cause a drift in the energy since the constraint is holonomic. Finally, additional degrees of freedom (α_q) can be added into the CP Lagrangian in order to control various quantities such as temperature and pressure.

$$\frac{d}{dt}\frac{\partial \mathcal{L}}{\partial \dot{q}} - \frac{\partial \mathcal{L}}{\partial q} = 0 \tag{2.90}$$

Simply, application of the Euler-Lagrange equation (Equation 2.90) for both parameters $q = R$ and $q = \psi_i$ yields the corresponding Car-Parrinello equations.

$$M_I \ddot{\mathbf{R}}_I = -\frac{\partial E_{tot}\left[\{\psi_i\}, \{\mathbf{R}_I\}\right]}{\partial \mathbf{R}_I} + \sum_{ij} \lambda_{ij}\psi_j(\mathbf{r}, t) \tag{2.91}$$

$$\mu \ddot{\psi}_i(\mathbf{r}, t) = -\frac{\delta E_{tot}\left[\{\psi_i\}, \{\mathbf{R}_I\}\right]}{\delta \dot{\psi_i}^*(\mathbf{r}, t)} + \sum_{j} \lambda_{ij}\psi_j(\mathbf{r}, t) \tag{2.92}$$

In order for the electronic and nuclear motion to be separate adiabatically, the fictitious mass has to be chosen carefully. There must not be an overlap between the frequency spectra of the electronic and ionic degrees of freedom. The lowest frequency of the electronic subsystem is given by,

$$\omega_{min} = \sqrt{\left(\frac{2(E_{gap})}{\mu}\right)} = \sqrt{\left(\frac{2(\epsilon_{LUMO} - \epsilon_{HOMO})}{\mu}\right)} \tag{2.93}$$

Similarly, the highest frequency of the electronic subsystem is determined by E_{cut}, the plane wave cut-off energy as follows,

$$\omega_{max} \approx \sqrt{\left(\frac{2(E_{cut})}{\mu}\right)} \tag{2.94}$$

The largest timestep allowed is inversely proportional to the highest frequency ω_{max},

$$\Delta t \propto \left(\frac{\mu}{E_{cut}}\right)^{1/2} \tag{2.95}$$

For systems that have narrow or zero band gap such as metals, it is problematic to govern CP method as the ω_{min} in Equation 2.93 will approach to zero; however

it is possible to address this issue by separating the thermostat frequencies of the two subsystems; ionic and electronic degrees of freedom [133].

2.8 van der Waals interactions

van der Waals (vdW) dispersion forces appear due to the interactions of dipoles and play an essential role in determining the properties and stability of molecular and even non-polar monoatomic systems. Although the correct ground state energies of many-body systems can be obtained by density functional theory approach successfully, this promising method lacks the ability to describe the interactions between rapidly fluctuating charge distributions; interacting dipoles eventually [134]. Whether used with local or semi-local exchange-correlation functionals (LDA and GGA, respectively), DFT fails to account for the weak long-range intermolecular interactions between atoms or molecules [135]. For the last two decades, vdW correction to DFT grew into one of the most prized subjects [136]. It is also essential for the adsorption process on metallic substrates by accounting for the metal-screening effects [137]. On the other, it has been found that unless the dispersion coefficient C_6 is adjusted according to ab-initio data, the adsorption energy is overestimated [138]. A number of methods has been developed to include weak interactions over the course of time [139, 140]. DFT-D2 method which was put forward by Grimme was used in the present study due to its convenience to calculate the properties of weakly bounded systems [141].

Grimme proposed including a semi-empirical dispersion correction to the DFT total energy in order to include the van der Waals interactions [142].

$$E_{\mathrm{DFT-D2}} = E_{\mathrm{KS-DFT}} + E_{\mathrm{disp}} \tag{2.96}$$

where the dispersion energy E_{disp} is given by an attractive semi-empirical pairwise potential,

$$E_{disp} = -S_6 \sum_{i=1}^{N-1} \sum_{j=i+1}^{N} \frac{C_6^{ij}}{R_{ij}^6} f_{dmp}(R_{ij}) \tag{2.97}$$

S_6 is the global scaling factor and C_6^{ij} represents the dispersion coefficients for an atomic pair ij. $f_{dmp}(R_{ij})$ is the damping function defined by the following equation with R_{ij} being the interatomic distances for the pair ij.

$$f_{dmp}(R_{ij}) = \frac{1}{1 + e^{-d(R_{ij}/R_r - 1)}} \tag{2.98}$$

The value of the parameter S_6 must be chosen specifically for the system being studied and also the density functional being used. S_6 values for most popular GGA functionals are given in the Table 2.2.

TABLE 2.2: S_6 values for various GGA functionals. [142]

Functional	S_6
BLYP	1.20
BP86	1.05
B3LYP	1.05
PBE	0.75
PW91	0.70

2.9 Constrained Dynamics - Free energy calculation

In statistical mechanics, the reversible work which drives the system from one state to another, termed free energy, is a fundamental piece of information.[3] Although molecular dynamics simulations are versatile ways to sample local minima and to provide access on the statistical information of a system, within the ergodic principle, some thermodynamic quantities are not explicit functions of phase space coordinates. Moreover, statistical fluctuations occurring during molecular dynamics are insufficient to overcome activation barriers significantly higher than a few k_BT, where k_B is the Boltzmann constant and T is the absolute temperature of

[3]Its importance is stated as "The free energy of a reaction is its single most important thermodynamic property." by P.W. Atkins in his milestone book "The Second Law". [143]

the system. Free energy, entropy and related thermodynamical quantities are generally not explicit functions of the coordinates of the system, but depend on the total volume of the accessible phase space of the system connected through the canonical partition function Z. Hence, it is not possible to measure the aforementioned quantities of the system by direct use of the outcome of the dynamical simulations. The free energy of a system is defined by the following equation

$$F = -k_B T \ln Z(N, V, T) \tag{2.99}$$

Yet, the knowledge of the absolute free energy of a system is neither particularly interesting nor helpful unless one is dealing with phase transitions [144]; it is rather the free energy difference between different states of the system which gives crucial insights about, for instance, stability of products with respect to some initial reactants along a given reactive pathway. Figure 2.3 shows a typical free energy diagram of a reaction described by a properly selected reaction coordinate, generally depending on a reduced subset of the dynamically evolving variables (coordinates, velocities, etc.).

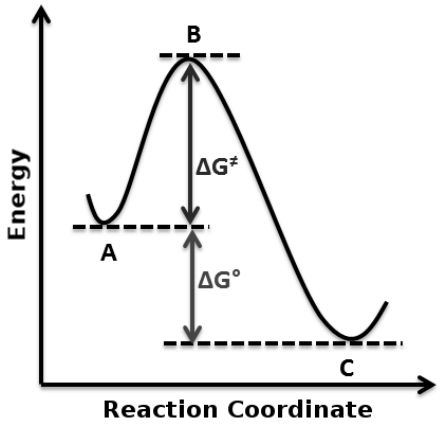

FIGURE 2.3: Free energy profile contains information about the favorability of a reaction.

$\Delta G^{\neq}$ indicates the activation barrier while ΔG° reflects the free energy difference between the reactants and the products. The latter is the useful piece of information to discover the favorability of a particular reaction.

According to Equation 2.99, the probability of visiting the states which are higher in energy by a few k_BT is noticeably reduced. Therefore, the probability of finding the system in one of these conformations with relatively higher free energy, especially in proximity of the transition state, is so low that a standard molecular dynamics would never be able to sample this portion of the phase space within an affordable simulation time. Furthermore, statistical errors pile up due to inadequate sampling in this region. One way of reducing the errors is to extend the simulation time scale. With the latest advancements in modern computational techniques, it is now possible to realize classical molecular dynamics simulations in the order of microseconds even with tens of thousands of atoms [145]. Even so, the timescale of chemical or biological reactions can reach up to milliseconds, seconds or even hours; folding of complex proteins is one of the many examples that could be cited. Therefore, increasing the simulation time in order to sample the whole phase space is somewhat impractical. One has to resort to specialized techniques to approach these quantities.

Among the available techniques nowadays routinely used, thermodynamic integration (TI) is one of the most straightforward methods to calculate the free energy difference of two different states using MC or MD simulations. For a reaction coordinate which can be approximated by a parameter ξ, the free energy difference along a reaction path can be computed as,

$$F(\xi_2) - F(\xi_1) = \int_{\xi_1}^{\xi_2} \frac{\mathrm{d}F(\xi)}{\mathrm{d}\xi} \mathrm{d}\xi \tag{2.100}$$

It is essential to vary the parameters of increments sufficiently small to ensure the reversibility of the sampled path and to keep the the system at the equilibrium in the course of the simulation; only if these conditions are satisfied it is possible to achieve a uniform sampling within each interval, since the work done along the constrained (reaction) coordinate contains the information about the free energy difference if the path followed stays reversible [144].

Auxiliary coordinates, generally expressed as an analytic function of a subset of cartesian coordinates of the system, such as, for instance, the distance between two atoms or from a surface, can be used to drive (or bias) the dynamics of the

simulation in a controlled manner. Apart from the distance parameters, specifying coordination numbers, radius of gyration, angles between two or more bonds are just a few examples of the possible constraints that can be imposed to a given system. These parameters are also referred to as reaction coordinates, collective variables or order parameters, and are used to describe the transformations of a system evolving dynamically from an initial reference state to a final desired state. These two initial and final values of the reaction coordinates are indicated as ξ_1 and ξ_2, respectively, here and in the following chapters.

The free energy of a system constrained by a parameter ξ is defined as following,

$$F(\xi) = -k_B T \ln Z(\xi) \tag{2.101}$$

where the partition function Z is given by

$$Z = \int \delta[\xi(q) - \xi] \exp(-\beta H(q,p))\ d^3q\ d^3p \tag{2.102}$$

Since our scope is to calculate the free energy difference along a reaction coordinate ξ, the canonical partition function is modified to include the parameter (constraint) defining our reaction coordinate, therefore the free energy F(ξ) is expressed as follows;

$$F(\xi) = -k_B T \ln \int \exp(-\beta H(q,p))\ \delta[\xi - \xi(q)]\ d^3q\ d^3p \tag{2.103}$$

The delta function ensures that the integration is executed for the coordinates q equal to the sampled value of ξ, such that $\xi(q) = \xi$. Differentiating the Equation 2.103 with respect to the reaction coordinate gives;

$$\frac{dF}{d\xi} = \frac{\int \frac{\partial H}{\partial \xi} \exp(-\beta H)}{\int \exp(-\beta H)} = \left\langle \frac{\partial H}{\partial \xi} \right\rangle_{\xi} \tag{2.104}$$

which gives the following relation upon integration when substituted into the Equation 2.100,

$$F(\xi_2) - F(\xi_1) = \int_{\xi_1}^{\xi_2} \mathrm{d}\xi \left\langle \frac{\partial H}{\partial \xi} \right\rangle_{\xi}^{cond.} \tag{2.105}$$

According to the Equation 2.104, the free energy $F(\xi)$ can be considered as the potential of mean force and also, at variance with the absolute free energy, the free energy gradient $\partial F/\partial \xi$ and thus the free energy difference between two states can be calculated from the statistical average of the generalized force $f_\xi = -\partial H/\partial \xi$ which is subject to a condition evaluated at $\xi(q) = \xi$. The subscript $\langle \ldots \rangle_{\xi}^{cond.}$ represents the ensemble average constrained by the value of ξ. The average of such an observable is given by the following relation.

$$\langle \mathcal{O} \rangle_{\xi} = \frac{\langle \mathcal{O}\ \delta[\xi - \xi(q)] \rangle}{\langle \delta[\xi - \xi(q)] \rangle} \tag{2.106}$$

Now, although the problem is reduced to approach the free energy directly from its derivative, another setback is the necessity to estimate this average correctly. The "Blue Moon" ensemble method allows one to estimate the conditional ensemble average of observables via the time average over a trajectory fixed at a predetermined value of the reaction coordinate $\xi(q) = \xi'$ and $\dot{\xi}(q, \dot{q}) = 0$.

2.9.1 Blue Moon sampling

The Blue Moon ensemble is a technique which was first developed by Carter and Ciccotti in 1989, then refined and improved by Ciccotti and Sprik in 1998 in order to compute the free energy difference (or potential of mean force) along a reaction coordinate in molecular dynamics approaches to inspect rare events and activated processes which occur "once in a blue moon". Being these processes characterized by a very low probability, they are clearly rare events located at with high energy barriers and difficult to visit via regular molecular dynamics, even temperature enhanced ones. This is particularly true in first principles dynamical simulations, since atoms are bound together by quantum mechanical forces, not by analytic functions (e.g harmonic potentials for bond stretching), and excessively high temperatures can result in a disruption of the whole system. A versatile

solution is then represented by the Blue Moon ensemble approach, allowing to compute not only static properties such as the free energy of a specific state but also rare events such as conformational rearrangements, chemical reactions, nucleation, diffusion, growth, transition events.

The Blue Moon ensemble method aims at bridging the deterministic approach of molecular dynamics and the statistical mechanics by allowing to compute as time average the statistical average of an observable which is restricted to vary within a given set of values of the parameter $\xi(q) = \xi^{'}$, namely through the time average of constrained trajectories. Constraining a parameter to a specific value implies that its time derivative is zero. This is the principal reason why conditional averages do not correspond to their time averages. It was first demonstrated by Carter and Ciccotti [146] that the conditional and constrained averages of velocity independent observables are related by

$$\langle \mathcal{O}(\mathbf{r}) \rangle_{\xi}^{cond.} = \frac{\left\langle Z^{-1/2} \mathcal{O}(\mathbf{r}) \right\rangle_{\xi}}{\left\langle Z^{-1/2} \right\rangle_{\xi}} \tag{2.107}$$

where Z is the weighting factor to compensate for the configurational bias introduced by the mechanical constraint and it is given by

$$Z = \sum_{i} \frac{1}{m_i} \left(\frac{\partial \xi}{\partial \mathbf{r}_i} \right)^2 \tag{2.108}$$

Exploiting the Equation 2.107 to calculate the effective mean force from the Equation 2.105 gives the following relation [147],

$$\frac{dF}{d\xi} = \frac{\left\langle Z^{-1/2} \left[\partial V / \partial \xi - k_B T / 2 \partial \ln |\mathbf{M}| / \partial \xi \right] \right\rangle_{\xi}}{\left\langle Z^{-1/2} \right\rangle_{\xi}} \tag{2.109}$$

where V is the potential energy function. M is the metric matrix which includes kinetic contribution as a form of its logarithmic derivative and it is given by,

$$\mathbf{M}_{\alpha\beta} = \sum m_i \frac{\partial \mathbf{r}_i}{\partial u_\alpha} \frac{\partial \mathbf{r}_i}{\partial u_\beta} = (\mathbf{J}^T \mu \mathbf{J})_{\alpha\beta} \tag{2.110}$$

In order to derive Blue Moon relations, one needs to make a change of variables from Cartesian coordinates to a new set of generalized coordinates in order to perform a partial derivative with respect to the reaction coordinate ξ. This operation will introduce the Jacobian determinant for this coordinate transformation which would bring an extra burden to the calculation, as it can be seen from the Equation 2.109. To overcome this additional difficulty, instead of this approach, it has been demonstrated by Mulders et al. [148] that using the constraint force to reach the free energy difference is a neater way to avoid coordinate transformations.

$$\dot{\mathbf{u}} = \frac{\partial H}{\partial \mathbf{p}^u} \tag{2.111}$$

$$\dot{\mathbf{p}}^u = -\frac{\partial H}{\partial \mathbf{u}} - \lambda \delta_{\xi \mathbf{u}} \tag{2.112}$$

where $\mathbf{u}$ is the collective representation of the generalized coordinates $\mathbf{q}$ and the constraint $\sigma(\mathbf{r}) = \xi(\mathbf{r}) - \xi' = 0$.

Disfavored configurations in the phase space can be visited by constraining the system by applying holonomic constraints to the Hamiltonian. Thus, activation barriers and rate constant of a chemical reaction can be estimated by generating an ensemble of configurations subject to these constraints.

$$\frac{\mathrm{d}F}{\mathrm{d}\xi} = \frac{\langle (\partial H/\partial \xi)\ \delta(\xi - \xi') \rangle}{\langle \delta(\xi - \xi') \rangle} = \frac{\left\langle Z^{-1/2}[-\lambda + k_B T G] \right\rangle_\xi}{\left\langle Z^{-1/2} \right\rangle_\xi} \tag{2.113}$$

where λ_ξ is the Lagrange multiplier of the constraint and G is the geometric correction factor.

$$G = \frac{1}{Z^2} \sum_{i,j}^{N} \frac{1}{m_i m_j} \frac{\partial \xi}{\partial r_i} \cdot \frac{\partial^2 \xi}{\partial r_i \partial r_j} \cdot \frac{\partial \xi}{\partial r_j} \tag{2.114}$$

For simple distance constraints in the form of $\xi(\mathbf{r}^N) = |\mathbf{r}_i - \mathbf{r}_j|$, Z turns out to be a constant, and hence G vanishes. The free energy gradient becomes the average of the constraint force λ which means that the derivative of the free energy along a reaction coordinate is directly associated with the constraint force.

$$\frac{\partial F}{\partial \xi} = -\langle \lambda \rangle_{\xi} \tag{2.115}$$

The free energy difference for simple distance constraints can then be obtained by direct integration of the average of the Lagrange multiplier associated with the constraint on the reaction coordinate; [4]

$$F(\xi_2) - F(\xi_1) = \int_{\xi_1}^{\xi_2} \langle \lambda \rangle_{\xi} \, \mathrm{d}\xi \tag{2.116}$$

A sample application used in the present work is given in Appendix A.1.

[4]The current section is assembled from numerous reviews and articles, the interested reader is referred to Refs.[147–174] for a more comprehensive treatment.

Chapter 3

Results and Discussion

Contents

In this chapter, the results of the studied systems will be presented with their corresponding motivations and computational details.

3.1 Single transition metal atom deposition on ferrocene molecule deposited on Cu(111) substrate

Post–scaling electronics is a current challenge pushing the fabrication of devices down to molecular and atomic sizes. Traditional processes for integrating simple elements such as junctions, diodes and transistors on a chip have already shown all their limitations by stimulating the upsurge of more efficient devices issued from the innovative impulse of nanoscience and nanotechnology [175]. In this general scenario, the bottom-up approaches proposed over the years for the realization of nano-junctions has received a new boost when researchers started using three-dimensional double-decker organometallic compounds as building blocks [64, 65, 67, 176]. Ferrocene, $Fe(C_5H_5)_2$, is one of the most intriguing and versatile organometallic sandwich compounds, being in the spotlight of research since the 70s. At variance with planar molecules, namely phthalocyanine, which are another major target in metal–metalorganic molecules interfaces [33, 38, 177], ferrocene is easily available as three-dimensional metal-organic molecule with a zero-spin ground state. Such molecule is well suited as a building block for applications oriented to spintronics and hetero nano-junctions [178, 179].

Joined experimental and computational efforts in IPCMS have already shown how to realize efficiently non-dissociative ferrocene deposition onto a metallic Cu(111) substrate [69, 70]. In those pioneering works, a) the interaction between ferrocene molecules and the substrate and b) the interaction between adjacent ferrocene molecules have been focused. These results have shown that the physisorption of $Fe(C_5H_5)_2$ is mediated by the presence of interface states between the Cu(111) metal surface and the organometallic molecule. Compact layers of ferrocene are seen to contribute to a 2D-like interface state that closely resembles a Shockley state [180, 181]. The structural stability of the resulting nano-junction at finite temperature have been assessed by depositing further Cu metal atoms on the adsorbed ferrocene.

Although this promising molecular building block is rather robust and it does not feature a high degree of complexity; from an experimental point of view, it is

very difficult to manipulate and dissociation can easily occur during deposition as reported by Paul and coworkers [67], depending on the experimental set-up and thermodynamical conditions. In the present work, this problem has been addressed by focusing on the effects of the deposition of different types of metal atoms on the physisorbed ferrocene. In synergy with undergoing experiments [176, 182], the main target of the present work is the deposition of Fe and Co atoms on the ferrocene molecules physisorbed on a Cu(111) substrate and how the different chemical nature of the atoms is responsible for different phenomena that can lead to the dissociation of the $Fe(C_5H_5)_2$ compound or to the formation of new organometallic species. This makes ferrocene a template or precursor for the in-situ generation of new chemical architectures, as pioneered in recent experiments [67]. In this perspective, the results presented here are prone to disclose new perspectives in the design and realization of molecular devices for next generation nanoelectronics and site-controlled nano-catalysts.

3.1.1 Ferrocene

Ferrocene, $Fe(C_5H_5)_2$, is an organometallic sandwich compound with two cyclopentadienyl rings (C_5H_5)(Cp) situated equidistantly at opposite sides of a single iron atom. The rings are situated 3.32 Å apart while the Fe-C and C-C (within the same Cp ring) bond lengths read 2.06 Å and 1.40 Å, respectively [183, 184]. Oxidation state of iron is +2 in this molecule and the two Cp rings contribute six electrons each and the iron atom acquires the electron configuration of Kr with its six d-electrons. See Figure 3.1 for a 3D representation.

Ferrocene, which is also called dicyclopentadienyl iron, was first synthesized unintentionally in the year 1951 by Peter L. Pauson and his colleague Thomas J. Kealy in an attempt to synthesize fulvalene, a molecule with aromatic properties and with a chemical formula of $C_{10}H_8$ [185]. This unexpected resulting product was an orange-colored "extraordinarily stable" compound since it was soluble in concentrated sulfuric acid without leading to decomposition and it was also stable in bases and insoluble in water. Nitric acid, on the other hand, oxidizes ferrocene

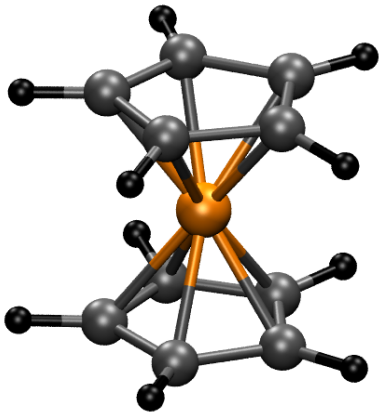

FIGURE 3.1: 3D representation of the ferrocene molecule. The color code is black for H, gray for C and orange for Fe.

to form ferricinium ion [186]. Ferrocene was the first example of a stable compound which was composed of only a hydrocarbon and a transition metal back then.

Only after two months following the work of P. L. Pauson, Samual A. Miller and his co-workers John A. Tebboth and John F. Tremaine also reported the unintentional synthesis of ferrocene although the study was completed in 1949 [187, 188]. Even though both groups achieved to synthesize ferrocene successfully, the structures they proposed were incorrect (see Figure 3.2). Ernst Otto Fischer [189] and Geoffrey Wilkinson [41] conducted studies on the electronic structure of ferrocene and shared the Nobel Prize for Chemistry in 1973 for their contribution to organometallic chemistry [190].

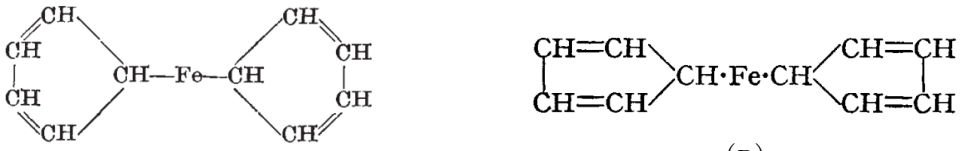

(A) (B)

FIGURE 3.2: Ferrocene configurations proposed by (A) P. L. Pauson et al. and (B) S. A. Miller et al. Both proposals were incorrect and corrected by G. Wilkinson et al.

It is considered to be an important molecule as its discovery evoked great interest in the field of organometallic chemistry by also leading the way to discoveries of its Co, Ni, Cr, Pb, Ru, and Os analogues [191–193], and hence ferrocene became

a milestone in the history of organometallic chemistry. Even though molecules with their carbons bonded directly with transition metals (Ti, Fe, Co, Ni etc.) were thought to be unstable, discovery of ferrocene provoked great interest by proving the otherwise with its high thermal stability [194]. Some of the sandwich compounds coordinated with cyclopentadienyl rings with their colors in solid state have been tabulated in Table 3.1.

TABLE 3.1: Typical sandwich compounds and their colors in solid state. (Cp = η^5-C_5H_5). Adapted from [194].

	4	5	6	7	8	9	10
4	Cp_2TiCl_2	Cp_2V	Cp_2Cr	Cp_2Mn	Cp_2Fe	Cp_2Co	Cp_2Ni
	Red	Black	Scarlet	Brown	Orange	Black	Green
5	Cp_2ZrCl_2	Cp_2NbCl_2	Cp_2MoCl_2	Cp_2TcH	Cp_2Ru		
	White	Brown	Green	Yellow	Yellow		
6	Cp_2HfCl_2	Cp_2TaCl_2	Cp_2WCl_2	Cp_2ReH	Cp_2Os		
	White	Brown	Green	Yellow	White		

Structural stability and electronic properties of manganese complexes (C_mH_m)-Mn-(C_nH_n) for m,n = 5,6 has been reported in the literature [195]. It has been found that $(C_5H_5)Mn(C_6H_6)$ obeys the 18-electron rule as ferrocene $Fe(C_5H_5)_2$ and dibenzenechromium $Cr(C_6H_6)_2$ do and therefore is a stable compound. Additionally, the anionic cluster $[Mn(C_5H_5)_2]^-$ is more stable than its neutral counterpart which possesses 17 valence electron.

Similar to many other metallocenes, ferrocene displays fluxional behaviour i.e. stereochemical non-rigidity, which originates from the low interconversion barrier between its different conformations [196]. XRD studies show that ferrocene has two configurations; staggered and eclipsed. The point group symmetry of the staggered conformation is D_{5d} while it is D_{5h} for its eclipsed counterpart. Corresponding conformers are given in Figure 3.3. Additionally, electron diffraction studies have shown that the eclipsed conformation of ferrocene is more stable in gas phase and the internal rotational energy barrier of Cp ligands to transform from eclipsed to staggered conformation has been found to be around 0.9 $\pm$ 0.3 kcal mol^{-1}

[197, 198] which is quite low as the energy barrier range of 5-20 kcal mol^{-1} is considered typical for such conversions [199].

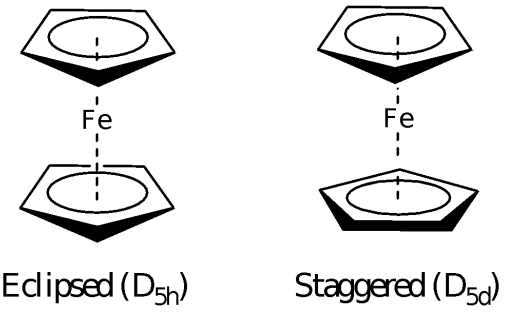

FIGURE 3.3: Eclipsed and staggered conformations of ferrocene molecule. Rotational energy barrier of 0.9 ± 0.3 kcal mol^{-1} needs to be overcome in order to transform from eclipsed to staggered conformer.

Although cyclopentadiene, C_5H_5, is unstable even in room temperature and can only exist until undergoing dimerization by Diels-Alder reaction to form dicyclopentadiene, the stability of dicyclopentadienyl iron originates from the interaction of its π-orbitals and the d-orbitals of the iron, hence rendering this molecule very stable even at high temperatures, up to 500 °C [200]. Electron density distribution of the isolated ferrocene molecule can be seen in Figure 3.4.

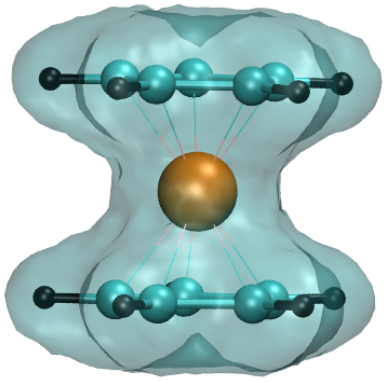

FIGURE 3.4: Electron density distribution of the isolated ferrocene molecule. The isosurface value is 0.12 $e/Å^3$. The color code is orange for Fe, cyan for C and black for H.

3.1.2 Computational Details

As explained in Chapter 1, understanding and consequently fine-tuning the behavior of interface states is the most crucial part in the realization of molecular analogs of semiconductor devices. For this reason, in the present work, deposition of single transition metal atoms such as Fe and Co on top of the ferrocene molecule on Cu(111) substrate has been targeted. The investigation tool will be first-principles molecular dynamics (FPMD) simulations within density functional theory (DFT) approach [94, 99]. The interaction between valence and core electrons was treated with norm-conserving Troullier-Martins pseudopotentials [118] with semicore states for Cu and Fe since these transition metals are prone to undergo ionization, core polarization and changes of oxidation state during the deposition process [201]. Non-linear core corrections were added for Co since the electronic structure of metallic systems with non-polarized spin is shown to yield more accurate results with NLCC [202]. 2s and 2p states for C and 1s for H were explicitly treated as valence electrons in the pseudopotential scheme. Exchange and correlation contributions are treated with the generalized gradient approximation according to the Becke exchange functional and Lee–Yang–Parr correlation functional [108, 109]. Valence electron orbitals have been represented in terms of plane waves with a cut-off energy of 90 Ry. van der Waals interactions were also included according to Grimme's D2 formulation [142] since it has been demonstrated recently for adsorption of benzene (C_6H_6) on Cu(111), Ag(111), and Au(111) substrates that vdW correction to DFT energy yields considerably better fitting adsorption energies to experimental data [203]. Nosé-Hoover thermostat is implemented for controlling the ionic temperature [83–85]. Simulation temperature is chosen to be 150 K for reasons of consistency with the corresponding experimental deposition study [70].

The simulated systems consist of a Cu(111) substrate of 420 Cu atoms composing a slab of five layers whose surface corresponds to an area of 17.894 $\times$ 26.565 Å, with two bottom layers kept fix to the bulk crystallographic positions. An empty space of 15 Å is included above the uppermost layer, thereby simulating a surface system. The overall slab thickness is necessary to properly keep into account the relaxation of the inner layers and their response to the deposition of molecules. All simulations have been performed with the CPMD code [204].

Two distinct deposition processes are investigated in this study, differing by the chemical nature of the deposited atom. Accordingly, on top of one of these $Fe(C_5H_5)_2$ molecules, one single Fe atom or Co atom is deposited following the simulation protocol reported before [69, 70]. Whenever standard first-principle dynamical simulations cannot follow the atom deposition processes within an affordable time scale due to relatively high free-energy barriers, Blue Moon ensemble (BME) constrained dynamics technique has been applied [147, 172].

3.1.3 Iron deposition

Focusing on these issues and following the indications from experimentalists, a first set of simulations targeted the approach of a single Fe atom to the upper Cp–ring of one of the two ferrocene molecules adsorbed on the Cu(111) surface. These simulations have shown that the approach of iron, initially placed at a distance of about 3.5 Å above the upper C_5H_5 ring, proceeds in a barrierless way. The Fe atom gradually approaches the hydrocarbon ring and eventually it reaches an equilibrium distance of 2.0 Å from the Cp–ring. However, contrary to the case of Cu deposition, a destabilization of the ferrocene molecule occurs. The upper C_5H_5 ring coordinates with the deposited Fe atom rather strongly and forms a stable complex. This upper Cp–ring then leaves the ferrocene to which it belongs at the beginning of the simulation and this newly formed Fe–C_5H_5 system becomes an independent moiety that departs from the substrate, leaving exposed the Fe atom belonging to the originally physisorbed ferrocene. This process is sketched in panels (a) and (b) of Figure 3.5. In these conditions, a physisorbed Fe–C_5H_5 complex remains on the Cu(111) surface as a new and different building block for which the ferrocene molecule represents just a precursor, in line with the suggestions for transformation and reassembling of deposited ferrocene reported by Paul and coworkers [67].

The destabilization process can also involve a hydrogen transfer from the departing Cp–ring to the exposed Fe atom, as shown in panel (c) of Figure 3.5. Agostic interaction is a term coined by Malcolm Green in the year 1983 which specifically defines "the situations in which a hydrogen atom is covalently bonded simultaneously to both a carbon atom and to a transition metal atom" [205]. The bond

length of metal to hydrogen is typically in the range of 1.8-2.3 Å with metal-hydrogen-carbon bond angles of 90-140 degrees [206].

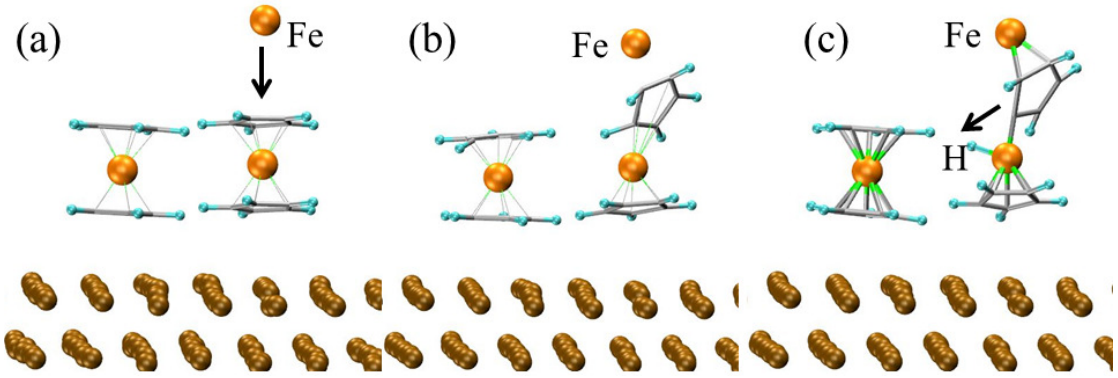

FIGURE 3.5: Main snapshots of the deposition process of an atom of iron on one of the two ferrocene molecules physisorbed on a Cu(111) substrate. (a) Approach of the Fe atom. (b) Destabilization of the upper Cp ring by the approaching Fe atom. (c) Departure of the upper Cp–ring / Fe complex accompanied by H transfer. The color code is cyan for H, gray for C, orange for Fe and brown for Cu.

This results after a strong agostic interaction taking place between the Fe metal center and the distorted Cp ring. Such an interaction is rather common in metal-hydrocarbon systems and often represents the trigger for catalytic reactions promoted by transition metals [206, 207]. Indeed, despite the fact that for Fe deposition the realization of a junction is jeopardized, the unshielded Fe atom can become an active catalytic site well suited to bind subsequent deposited molecules. This destabilization process is due to the chemical nature of the atom used for the deposition with respect to the metal already present in the selected double–decker molecule. In fact, in this case, the same atom, namely Fe, is present in the ferrocene complex. Thus, a second Fe atom that is not sandwiched between the two Cp–rings is therefore prone to bind to another available moiety and starts competing with the Fe of the $Fe(C_5H_5)_2$ present on the Cu(111) surface. As a "fair" result of this competition, the bottom Cp–ring, interacting with the 2D electronic state at the metal surface, remains in its place carrying the coordinated Fe. At the same time, the upper Cp–ring forms an analogous complex with the incoming Fe atom and two Fe–C_5H_5 are formed. The upper one being not physisorbed, leaves the vicinity to search for a suitable location on Cu(111) where no adsorbents and no steric repulsions would hinder its own adsorption.

As mentioned, this destabilization, although having an evident negative consequence for the practical realization of a nanojunction at first glance, should not be regarded as a pure failure. In fact, cyclopentadienyl–iron complexes represent useful precursors for iron carbene complexes and an important catalytic moiety [208, 209]. Hence, the deposition of Fe, in contrast with Cu, represents a viable way not to form nanojunctions, but a route to realize nanocatalysts where the control of the active, or to be activated, sites is granted by the ordered array of pristine ferrocene molecules physisorbed onto a Cu(111) substrate. By a proper selection of deposited atoms, such as Fe in this case, the metal atom sandwiched between two cyclic hydrocarbon molecules can be exposed, thus becoming an active catalytic center.

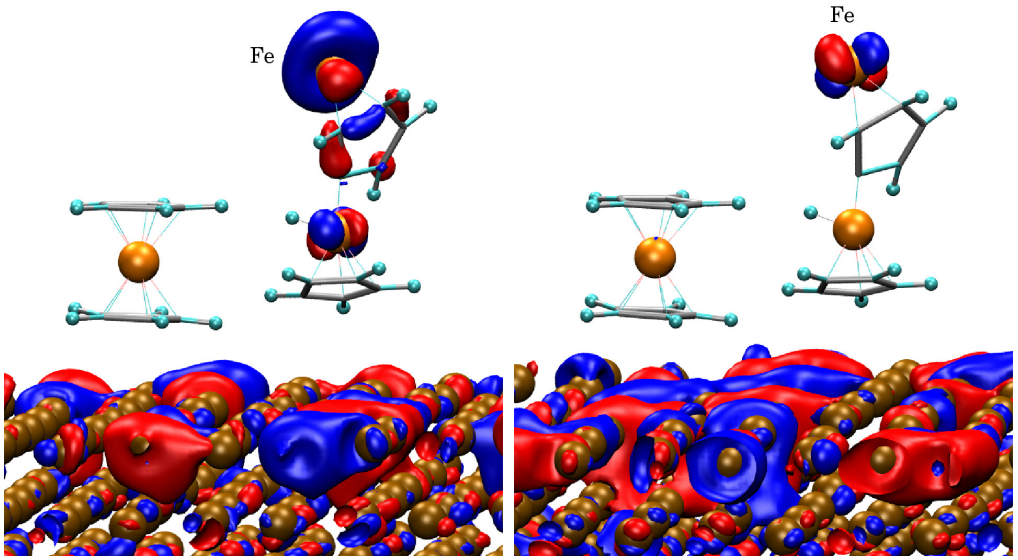

FIGURE 3.6: Highest occupied (left panel) and lowest unoccupied (right panel) Kohn-Sham states for the final configuration of the system after the deposition of iron. Positive and negative amplitudes are represented in red and blue, respectively, at isosurfaces values of $\pm$ $9{\times}10^{-3}$ $(\mathrm{e/\AA^3})^{1/2}$. The color code is identical to that of Figure 3.5.

The analysis of the highest occupied Kohn-Sham (HOKS) orbital and the lowest unoccupied one (LUKS) is summarized in Figure 3.6 for the resulting destabilized structure. Namely, the HOKS orbital is a mixture of the surface state, the $d_{x^2-y^2}$ state of the (now) unshielded Fe of the destabilized ferrocene, plus a d_{z^2} contribution from the deposited Fe. Minor contributions from the removed Cp ring are also

visible. The corresponding eigenvalues for these two states are (HOKS -4.178 and LUKS -4.177 eV) characterized by a tiny energetic separation of about 0.001 eV, reminding clearly that the system has a strong metallic character, as expected also on the basis of the former works [69]. Yet, this makes the unoccupied states easily accessible by electron donors, thus making the system a potentially highly reactive nanocatalyst. The fact that surface states mix with the ferrocene (dissociated or not) molecular orbitals is not a surprise, since this feature was already observed and assessed also experimentally [70]. Instead, contrary to the case of pure ferrocene [69, 70], the LUKS of this destabilized system, does no longer resembles a purely ferrocene molecular orbital, but again a mixing of the Cu(111) surface state and a $d_{x^2-y^2}$ orbital belonging to the deposited Fe atom. Being this Fe, in the present configuration, the most unshielded (by Cp rings) one, this indicates that this Fe site is able to accept electrons and, as such, can become and active catalytic center. It can be inferred that an identical fate will be true for the Fe atom of the ferrocene which has lost its upper Cp ring.

3.1.4 Cobalt deposition

A second series of simulations was conducted focusing on the deposition of Co on the physisorbed ferrocene. At variance with Fe ([Ar] $3d^6 4s^2$), the electronic structure of Co ([Ar] $3d^7 4s^2$) includes only one additional diffuse $d-$orbital. This is, however, not without consequences and causing the cobalt deposition to proceed differently compared to the iron case. Indeed, any attempt at depositing a Co atom on the ferrocene within the simulation protocol adopted for the Fe atom did not result in the formation of any Co–ferrocene complex, neither destabilization processes could be observed. As a matter of fact, the Co atom initially placed at a distance of about 3.5 Å from the upper Cp–ring could not approach closer than about 3.0–2.8 Å. This behavior was observed for any initial velocity attributed to the Co atom compatible with the range of temperature between 0 and 200 K. Apparently, the different electronic structures of the two transition metals, iron belonging to the metalorganic molecule and the approaching cobalt, do not allow for a barrierless approach of Co to the Cp–ring contrary to the former case. Although a better analysis of the electronic structure will be given in the ongoing

discussion, it seems that the presence of an additional d valence electron causes an electrostatic repulsion with the electron–rich C_5H_5 ring.

To estimate this barrier and to analyze a possible pathway to coordinate Co to the deposited ferrocene, free energy sampling technique known as Blue Moon ensemble has been utilized [147]. Technical breakdown of this approach is given and detailed in Chapter 2.9. In these simulations, the reaction coordinate was selected to be the distance between the Co atom and the center of the upper Cp–ring on which the metal atom is expected to be adsorbed. Left panel of the Figure 3.7 demonstrates the corresponding reaction coordinate d and the initial configuration of cobalt deposition system starting from 3.5 Å of Co-Cp ring distance. To calculate the free energy barrier, Co atom is constrained to approach towards the Cp ring with $\sim$ 0.1 Å of decrements for a number of subsequent simulation runs.

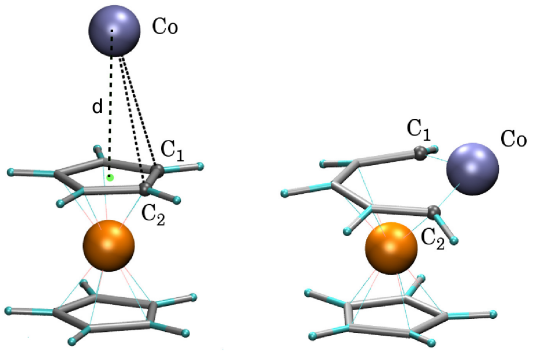

FIGURE 3.7: Close-up view of initial and final configuration of Co deposition process resulting in its insertion in the Cp ring. The distance d marks the reaction coordinate for the Blue Moon approach. See Table 3.2 for details.

By constraining the approach of the Co atom, it has been discovered that the system has to overcome a barrier of 21.17 kcal/mol (0.92 eV). The result is summarized in Figure 3.8. More precisely, not a significant modification occurs up to a Co–Cp distance of about 2.40 Å and the free energy increases monotonically indicating that no stable coordination of the Co is possible. Beyond this distance, the Co atom starts to interact with the Cp ring as shown in the upper left panel of Figure 3.8. At variance with the former case, in which the Fe atom remains just coordinated to the hydrocarbon ring, here the interaction after the overcoming of

the barrier is rather strong and the system finds a new stable minimum at about 2.06 Å.

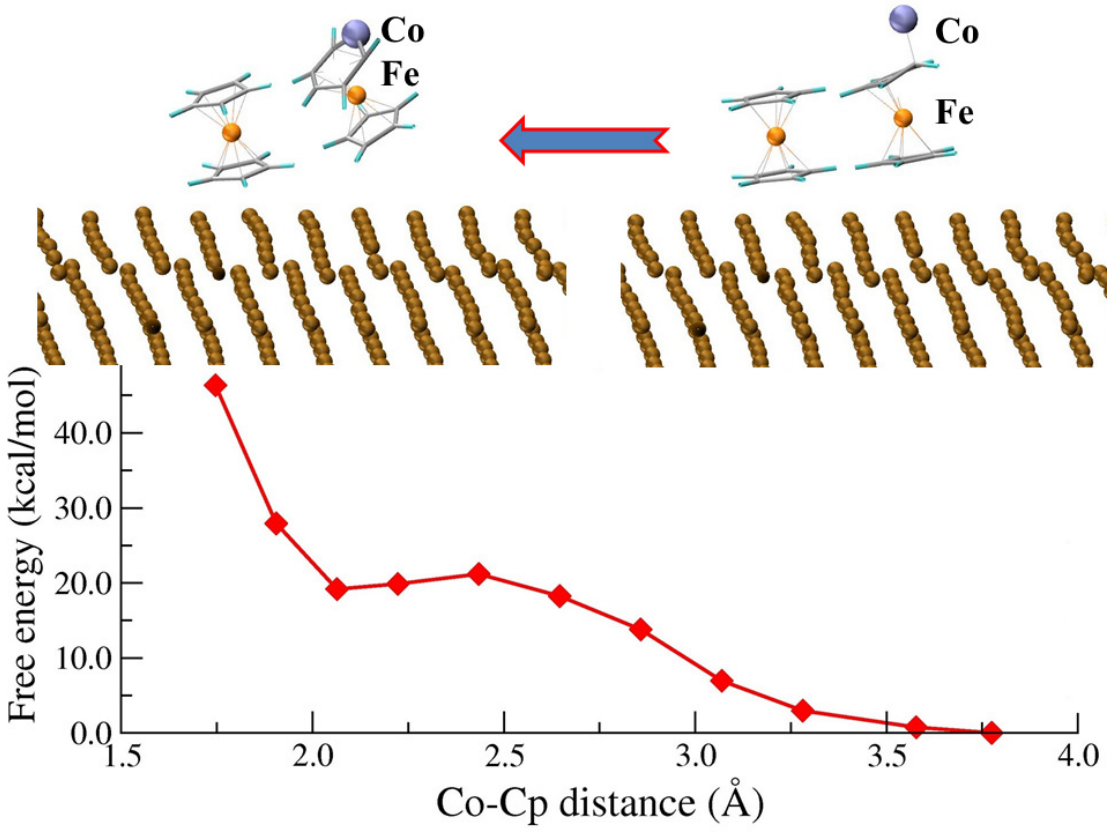

FIGURE 3.8: Deposition of an atom of cobalt on one of the two ferrocene molecules physisorbed on a Cu(111) substrate. A free energy barrier of about 21.17 kcal/mol has to be overcome. The upper panels show the approach of Co and the insertion of this atom in the upper Cp–ring. This metastable new compound is eventually desorbed from the substrate. The red curve shows the free energy profile as a function of the approaching distance. The color code is identical to that of Figure 3.5 with the Co atom in blue.

This new minimum does not correspond to a simple Co–Cp coordination but to a complete insertion of the Co atom in the hydrocarbon ring (see the upper left panel of Figure 3.8) which becomes a six–member ring in which one vertex of the resulting hexagon is occupied by the Co atom. The distances between certain carbon atoms of the Cp ring and the cobalt were given in Table 3.2 for both initial and final configurations of the system along with those of an isolated pristine ferrocene. It is important to note that physisorption of ferrocene on Cu(111) substrate has apparently shortened the upper half of molecule by 0.013 Å; yet the

insertion of the cobalt causes the Fe - Cp_{upper} distance to shrink by 0.037 Å while it has a very minor impact on the Fe - Cp_{lower} distance.

TABLE 3.2: Evolution of the main Co–C distances for the insertion of the Co atom into the Cp ring. Pristine signifies the ferrocene in gas phase. Distances are in Å.

	Pristine	Initial	Final
C_1 - C_2	1.413	1.431	2.793
Co - C_1	–	3.387	1.754
Co - C_2	–	3.370	1.791
Fe - Cp_{upper}	1.661	1.648	1.611
Fe - Cp_{lower}	1.658	1.656	1.651

The resultant structure is not entirely unknown. Indeed, a similar structure, termed cobaltacyclopentadiene, in which the Co is inserted as a member of a Cp ring is realized upon oxidative coupling of the precursor CpCo(bisalkyne) complex [210, 211]. This new structure is indeed stable, as subsequent unconstrained dynamical simulations have shown. Either in an NVT ensemble with the target temperature fixed to 150 K or in an NVE ensemble with all temperature controls removed, the newly formed hexagonal structure does not dissociate, neither does this modified ferrocene-like double–decker structure. On the contrary, this block, on longer simulation times of the order of a few tens of ps, desorbs from the Cu(111) substrate as a whole and eventually leaves the surface. In this respect, the use of Co, although not resulting in a nanojunction formation, can be a viable way to extract ferrocene units selectively from a deposited monolayer to create motifs and patterns. Moreover, the Co–containing six–member ring structure is prone to have catalytic properties for the polymerization of alkynes [210].

Figure 3.9 shows the electron density distribution of the cobalt deposition system in its initial and final states. The fact that not just a simple Co–Cp coordination is realized, but an actual new chemical compound, is confirmed by the inspection of the electronic structure of the final system with respect to the initial one. In fact, as shown in the right panel of Figure 3.9 the presence of a non–zero electronic density between the Co site and the two adjacent carbon atoms C_1 and C_2, clearly indicates the formation of new Co–C chemical bonds. It is noteworthy that this system, at variance with the Fe deposition one, carries an odd number of electrons,

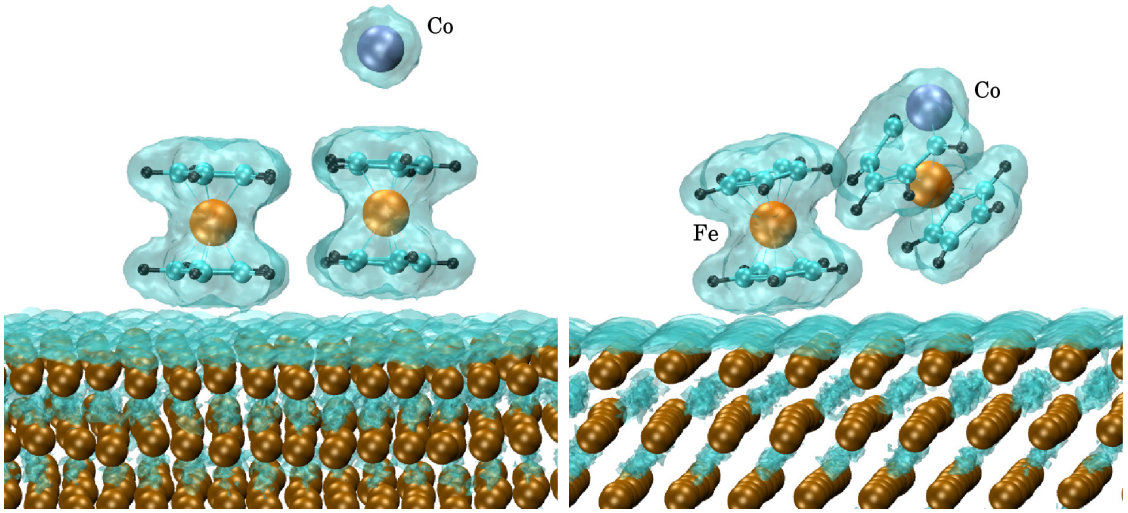

FIGURE 3.9: Electron density distribution at the beginning stage of Co deposition (a) and at the end of the process leading to the insertion of the Co atom inside the Cp ring (b). The non–zero electron density joining the Co atom to its neighbor C_1 and C_2 atoms in panel (b) account for the formation of chemical bonds. The electron density is shown at an isosurface value of $\pm$ $2{\times}10^{-2}$ $(e/Å^3)^{1/2}$.

hence the singly occupied HOKS reflects the distribution of the spin density. This is shown in Figure 3.10 for the initial and final configurations of the system.

Namely, the electronic distribution of the spin resulting from the unpaired electron is composed of a mixture of delocalized electronic states of the substrate and $d-$orbitals (d_{z^2} and $d_{x^2-y^2}$) of all the transition metals (Fe and Co) present in the system. This is true at any moment of the Co insertion process, from the very beginning to the complete insertion of the cobalt inside the Cp ring. Again, for an occupied electronic state this is not unexpected on the basis of both experiments and calculations [70].

The mixed character of the orbitals, including both contributions from the Cu(111) support and molecular orbitals of the physisorbed ferrocene molecules, is also evident in all the doubly occupied orbitals located at energies lower than the singly occupied HOKS. An example is reported in the left panel of Figure 3.11. Consistently with the fact that the deeper the energy eigenvalue, the smaller the

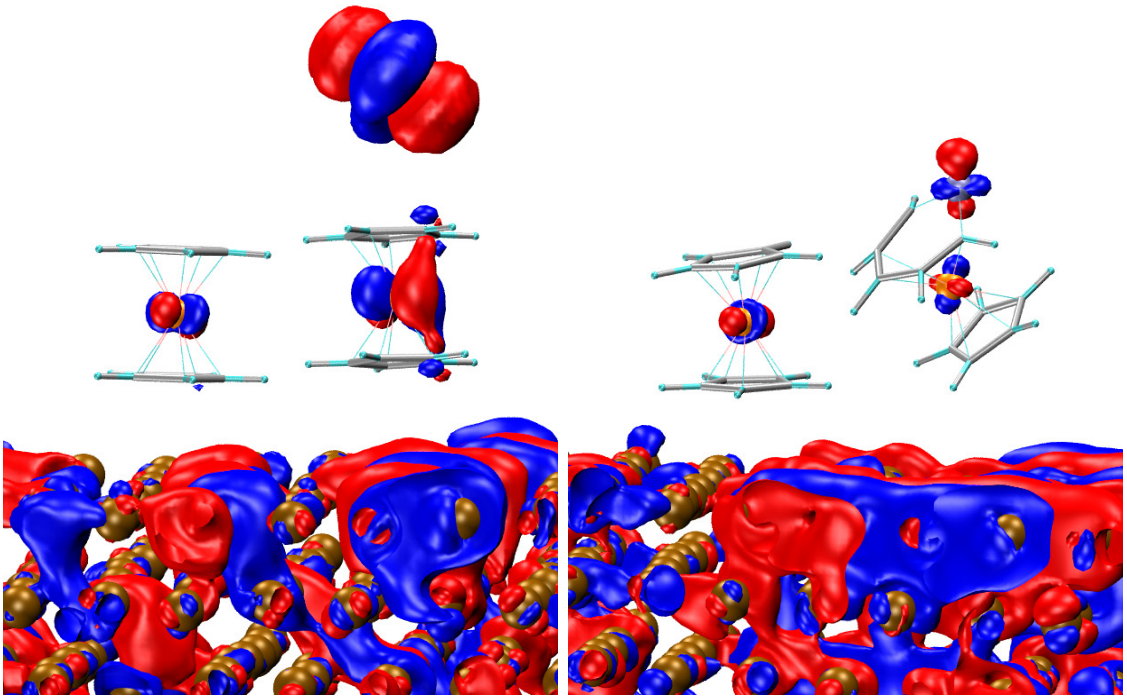

FIGURE 3.10: HOKS states of the cobalt system for the initial (left panel) and final (right panel) configurations. Isosurfaces are shown at values of $\pm$ 6×10^{-3} (e/Å^3)$^{1/2}$ in red (positive values) and blue (negative values).

contribution to the surface Shockley state [69, 70, 180], this HOKS-1 state shows a lower contribution to the Shockley state with respect to the HOKS case.

Consistently with the experimental evidence [70], when unoccupied states are considered (right panel of Figure 3.11), these turn out to be constituted exclusively by molecular orbitals with total absence of contribution from the substrate. The major lobes are located on the structure containing the Co inserted in the Cp ring, with a large amplitude on the Co site. Additionally, the small gap between corresponding states (singly occupied HOKS: -4.157 eV and LUKS: -4.150 eV) of the resulting complex indicates its metallic behaviour and electron acceptor character. This corroborates the idea of a potential catalytic activity of this six–membered hydrocarbon/cobalt ring [210].

Hence, a stable junction cannot be formed for the case of cobalt deposition too. Yet, these results offer an interesting way for patterning a ferrocene monolayer

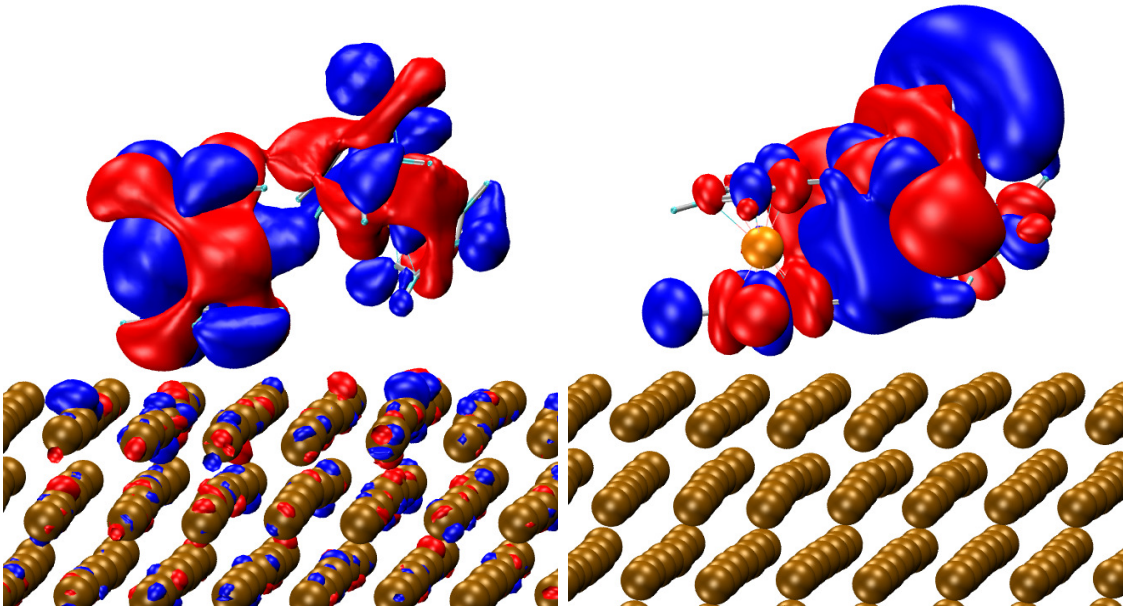

FIGURE 3.11: HOKS-1 and LUKS states of the cobalt system for the final configuration. These two states correspond to the last doubly–occupied and the first unoccupied states. Isosurfaces are shown at values of $\pm\ 6{\times}10^{-3}$ $(\mathrm{e}/\mathrm{\AA}^3)^{1/2}$ in red (positive values) and blue (negative values).

adsorbed on the metallic substrate. By depositing Co atoms at appropriate temperature, i.e. initial kinetic energy suitable to overcome the free energy barrier, it seem possible to selectively remove ferrocene monomers in the zone subject to Co attack provided that the adsorbed system behaves stable when subject to this range of temperature. This is clearly a possibility to create arrays or specific patterns at the nanometer scale, as required by next–generation molecular electronics and engineering.

In addition to the current discussion, inspired from the final position of the inserted Co atom where it lodges itself into the pentagon of carbons, four auxiliary systems comprised of Fe and Co have been prepared in order to study and compare the stabilities and properties of Co-C and Fe-C bonds. The stable configurations of these systems are presented in Figure 3.12. The optimized configurations are achieved after a cycle of geometry optimization with a total convergence criteria of 10^{-6} Hartree following a damped molecular dynamics run [212] for 6 ps, in order to make sure that the systems are not stuck into a false local minimum.

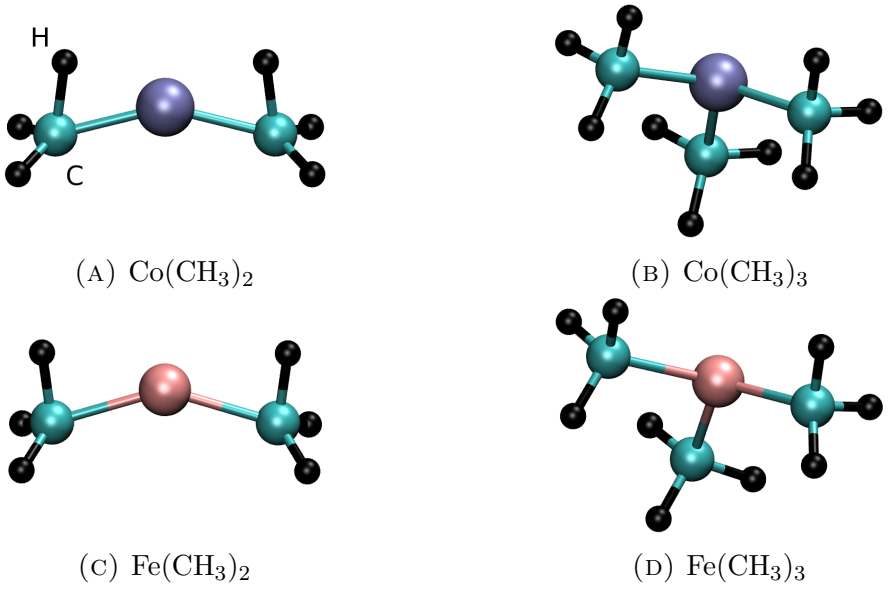

(A) $Co(CH_3)_2$ (B) $Co(CH_3)_3$

(C) $Fe(CH_3)_2$ (D) $Fe(CH_3)_3$

FIGURE 3.12: Equilibriated configurations of Co and Fe auxiliary systems following the geometry optimization. The color code is pink for Fe, purple for Co, cyan for C and black for H.

Metal-carbon bond lengths read 1.81 ± 0.01 Å (Fe) and 1.75 ± 0.01 Å (Co) for $M(CH_3)_2$ species. Referring to Table 3.2, final Co-C distances of the Co deposition study is consistent within 2% with the corresponding auxiliary system. On the other hand, C-M-C bond angles do not represent similar accordance for two configurations; which is 145 (Fe) and 150 (Co) degrees for auxiliary $M(CH_3)_2$ systems, while it reads 104 degrees for the Co deposition case. This contrast is, however, expected, given the cyclic structure of the cobaltacyclopentadiene ring. M-C-H bond angles, on the other hand, read 80 (Fe) and 71 (Co) degrees with the H atom that is marked in Figure 3.12 (A). The stabilities of double and triple metal-carbon bonds are compared and it was found that H has a tendency to approach to the metal in the $Co(CH_3)_2$ case.

3.2 Precursor molecules for the synthesis of Fe and Co oxide nanoparticles and related dissociation processes

Functionalized metal and metal oxide nanoparticles (NP) have received special attention and represent a forefront research worldwide because of their broad range of applications from magnetic and electronic devices to biomedical applications. Just to mention a few, data storage units and magnetic fluids for micro/nano-electromechanical system(MEMS/NEMS) devices, along with image contrasting agents for magnetic resonance imaging and drug delivery modules, represent a continuously growing and non-exhaustive examples of application of these NPs [213–219]. Yet, physical and chemical properties of NPs, as well as the possibility of tuning their size and morphology, strongly depend on the nature and intimate chemistry of the precursor molecules used as elementary building blocks for the synthesis [220–222].

Depending on the target, the magnetic properties of NPs must be properly tuned and their sizes, composition and shape have to be designed according to the application to which they are intended. This is the case for biomedical applications (magnetic resonance imaging (MRI), cell sorting, hyperthermia, drug deliver, etc.), where, beside the basic request of non–toxicity, in a magnetic particle-based bioseparation process, a magnetically activated separation of biological moieties must be ensured. This has then to be benchmarked on conventional routinely used methods to provide a direct comparison. However, to this aim, NPs must possess a high magnetic moment to enable efficient separation. Another promising biomedical application of magnetic NPs is the treatment of cancer by magnetic hyperthermia. The amount of heat generated by a magnetic NP strongly depends on the NP magnetic properties which must display high saturation magnetization, accompanied by a high anisotropy energy. These properties depends crucially on the NP size, composition and shape [223–225] and, in turn, these depend on the precursors used to synthesize the NP, on their stereochemistry and on their interaction with the environment before and after the synthesis process.

These precursors, which are mainly stearates, consists generally of a metallic center surrounded by organic ligands. Hence, contaminations and interactions of the ligands play also a non–negligible role which affects the size distribution and morphology of NPs [226]. NPs with sizes below 20 nm are prone to have a wealth of applications in all the fields briefly mentioned above [227]. For these reasons, it is essential to synthesize NPs under finely controlled conditions in order to tune the desired sizes and shapes [228]. As a complementary information, we recall that embedding nanoparticles into higher dimensional nanostructures such as, for instance, nanocages or nanotubes, expands the possibilities of their potential applications towards hybrid functionalized materials for next–generation electronic devices, nanocatalysts and theranostics. For all these reasons, special attention is given to the role of the ligand–NPs interactions starting from the NPs nucleation-to-growth process to the post-functionalization stages, being all these subsequent steps responsible for the final magnetic and electronic properties of the nano-object. In the case of metal oxide–based NPs, the control of their initial precursors, their relevant interactions and functionalizing ligands allows to rationalize, at least up to a certain extent, the relations between NPs size, morphology, surface stability, reactivity and, ultimately, their resulting magnetic properties. This is a basic prerequisite for any application whether biomedical or in the field of data storage and, as such, it deserves careful consideration. In fact, according to the nature of the transition metal and the chemistry of the functionalizing ligands, different NPs possessing different magnetic properties (and morphology) can be realized. Yet, the fine tuning of the magnetic response of the resulting NPs are still at a pioneering stage but represent one of the major issues being essential requisites particularly for biomedical applications such as diagnostics in MRI applications and therapeutics for specific forms of metastasis [229–231].

Current synthetic methods used to produce NPs represent to date a viable way to get nanoparticles with narrow size distributions, tunable sizes and, to a certain extent, specific magnetic and electronic properties. Yet, there is still room for improvements. Various synthesis methods have been proposed over the years for the preparation of metal oxide magnetic NPs with a range of nanograin sizes, such as solid-, solution- and vapour-phase [232, 233] methods. Sol-gel [234], hydrothermal method [235] and thermal decomposition [236–239] are typical examples of

solution-phase approaches. Among these techniques, spontaneous thermal decomposition represents one of the most effective approaches to fine control the size distribution and morphology of nearly monodisperse metal oxide NPs with significantly high yield. Such a versatile aspect is the result of the fast reaction [240–242] that thermal decomposition triggers. The key issue is the release of the precursor ligands under the action of a sufficiently high temperature that gives rise to the decomposition of the metal–organic precursor in non-aqueous solvent. Furthermore, it allows to control the size and morphology of the resulting NPs and their in situ functionalization, thereby limiting their aggregation in suspension.

Various metallic complexes carrying as ligands fatty acid salts such as acetates, oleates and stearates have been used as efficient precursors for the NPs synthesis [243]. The complexes used can vary from one synthetic method to another, but all share a common characteristic coordination of two or more organic bidentate ligands to a transition metal. NPs are formed through the thermal decomposition of these complexes, consisting in the release of the organic ligands, and subsequent aggregation of the unscreened metal atoms. Oleic acid, oleylamine is a typical prototype ligand, whereas octyl ether and octadecene are the typical solvents. Different ratios of solvent mixture are also used in order to achieve specific stoichiometry distributions of the NPs [244]. Nonetheless, despite the relatively simple synthesis protocol and a rather comprehensive documented literature devoted to this method, the influence of the synthesis parameters on the control of the NP morphology is still far from being clarified. The complex interplay among the nature of the metal complex, the nature of the ligands (carboxylic acid or amine ligands) and impurities (e.g. presence of water as residual humidity in the experimental apparatus) are still a matter of debate and escape fine control. Such a synthesis method is the one exploited at IPCMS and for which our close contact with experimentalists of our institute provide a solid background to benchmark simulations. For these reasons, this section of the present thesis will focus on this class of stearates and their decomposition processes. In this context, the interactions of impurities with these precursors are a major source of problems in terms of nature and stability of the produced NPs and, consequently, on all applications targeting (e.g. gas sensing), since the stability of the device must be ensured in the long run [245]. Moreover, traces of water or the presence of hydrochloric acid

(HCl) can also affect shape, size and morphology of NPs as shown in Figure 3.13. Specifically, the size of the NPs tend to diminish if water molecules are present during the synthesis reaction [246].

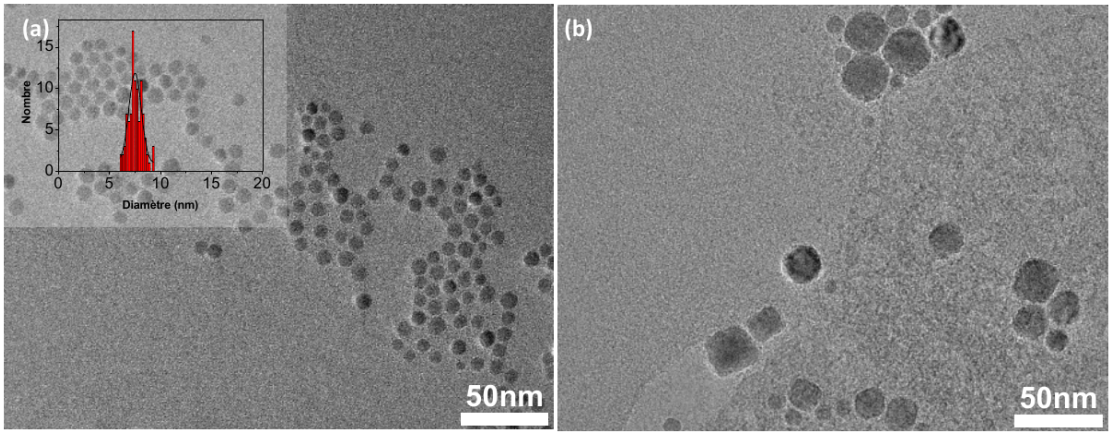

FIGURE 3.13: The effect of the presence of a) water molecules and b) HCl on the size distribution of NPs. Taken from [246].

Clearly, the choice of the precursor has a great influence on the properties of the resulting NPs [247] and the temperature at which the thermal dissociation occurs, in turn, depends on the metal–organic precursors [248]. The stearates on which we focus are basically salts and esters of stearic acid. A schematic representation of these organometallic complexes, namely iron and cobalt stearates, is given in Figure 3.14 where the +2 is the general oxidation state of the metal cation coordinated to a CH_3-$(CH_2)_{16}$-COO^- organic ligand.

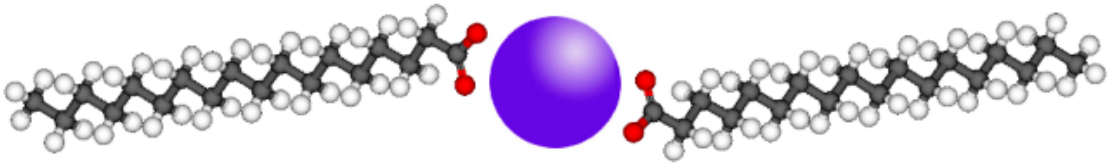

FIGURE 3.14: Schematic representation of the M-stearate used in our atomic–scale simulations and in experiments.

Stearates are known to be generally insoluble in water due to the long hydrophobic organic chains. Yet, water molecules, which are rather ubiquitous and present even in ordinary atmospheric moisture, can approach the metal cation along the directions roughly orthogonal to the plane in which the stearate is shown in Figure 3.14 to form what would correspond to a hydration shell of these metal cations

in solution [249]. In the following sections, therefore, this thesis will present the results of our investigation on the effects of the presence or absence of water in the thermal decomposition processes of these stearates.

Our experimental partners at IPCMS have developed a synthesis protocol for iron and cobalt oxide NPs starting by thermal decomposition their corresponding stearates, especially in the presence of oleic acid, used as stabilizing ligand, in high–temperature boiling solvent. By controlling the amount of oleic acid, the reaction temperature, the heating rate and the nature of the solvents, NPs, specifically iron oxide ones, coated with oleic acid have been synthesized. Their size distribution span a range of 4-28 nm [250]. Nonetheless, the case of Co–based NPs has been shown to be more problematic than the Fe–based ones. Indeed, experiments reveal that, although iron and cobalt stearates have identical configurations, desorption processes for these two complexes proceed with quite distinct features. In identical experimental conditions, the synthesis of cobalt oxide NPs via thermal decomposition of Co stearates is more difficult than the synthesis of Fe_3O_4 NPs.

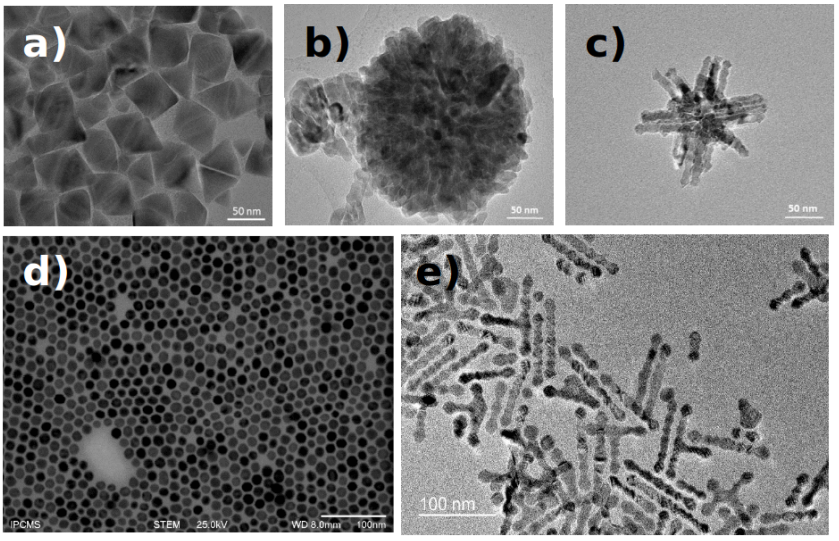

FIGURE 3.15: HRTEM images of CoO nanoparticles by using a) oleic acid, b) hexadecylamine and c) a mixture of oleic acid and hexadecylamine (mass ratio of 1:1). d) and e) two types of MnO NPs synthesized by thermal decomposition of a manganese stearate synthesized normally in the same conditions.

The main reason is the fact that a Co stearate decomposes at higher temperatures than its iron counterpart to grow cobalt oxide nanoparticles [251, 252]. In an

attempt at improving the yield of cobalt oxide NPs, the synthesis of CoO NPs has been performed by using amine ligands. These ligands are known to destabilize the iron stearate precursor via the acid–base reaction occurring between amine ligands and carboxylate ligands of the iron complex, leading to its decomposition at low temperature. The use of the iron stearate complex has evidenced the formation of smaller NPs with amine ligands, as opposed to what has been observed for carboxylate ligands.

Hence, the synthesis of CoO NPs has been tested with oleylamine as a replacement of the oleic acid. Yet, experimentalists observed that even if the CoO NPs yield increases, the morphology and size of CoO NPs were completely different from what expected (and seen in the case of Fe–based stearates), as seen in Figure 3.15. This observation allows one to infer that the effect of ligands on the morphology of CoO NPs is not trivial and depends strongly on the experimental conditions. To complete the picture, we can add that also MnO NPs have been synthesized via thermal decomposition of a manganese stearate, following the same protocol and synthetic procedure summarized above (see Figure 3.15).

To promote the nucleation of metal oxide nanoparticles, the central metal atom must detach from the precursor complex upon the thermal decomposition process. However, since both Fe and Co are in a four–fold and planar coordination in the pristine stearate [253, 254], with the oxygens of the carboxylate moiety ($RCOO^-$) forming a plane, the insertion of the water molecules around the metal cation can proceed along the directions roughly orthogonal to the plane defined by these four oxygen atoms. This can produce either a five- (approach of one water molecule) or six–fold coordination (approach of two H_2O molecules from the two opposite sides). As a result, a carboxylate group of the precursor can form hydrogen bonds with these approaching water molecules, with the possibility of promoting even a (temporary) proton transfer between the O atoms of the ligand and the H_2O molecule in the vicinity, resulting in a Zundel-like complex [255]. This, in turn, can result in a higher activation barrier for the metal–ligand desorption, thus jeopardizing the thermal decomposition. As a result, nucleation and growth may become slow, if not completely hindered. Since high energy barriers hamper a statistically sufficient sampling of the conformational space in a molecular dynamics simulation, the free energy sampling approach known as "Blue Moon ensemble"

[147] analogous to what has been used in the former section of this thesis was used (see also Chapter 2.9) to map the free energy profile and follow the reaction pathway of the desorption processes. Figure 3.16 shows the initial configurations of the studied M-stearate systems. Additional computational details relevant to this section of our dissertation are given in the next paragraph.

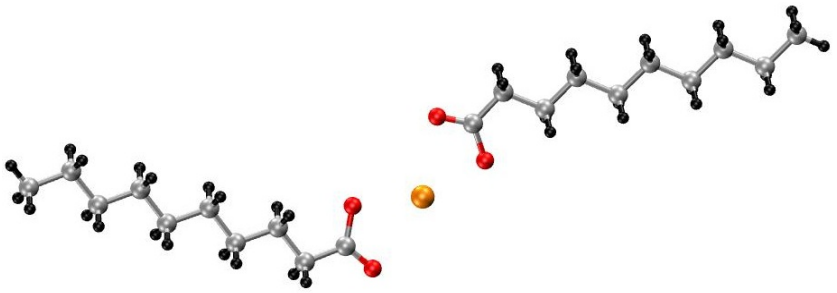

(A) M-stearate in dry conditions.

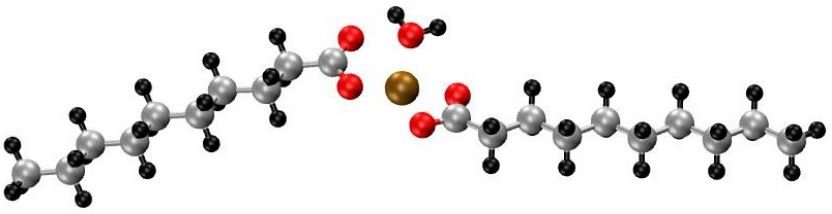

(B) M-stearate with one H_2O molecule: Octahedral M-O coordination with one vacant site.

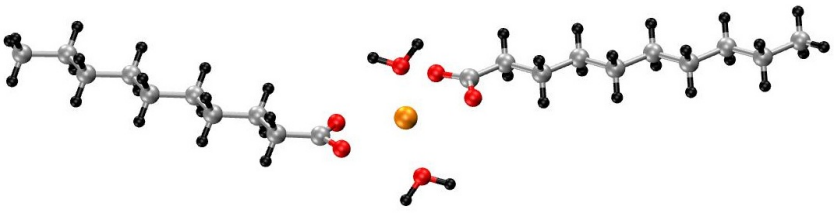

(C) M-stearate with two H_2O molecules: Octahedral M-O coordination.

FIGURE 3.16: Initial configurations of the quenched M-stearate compounds, M=Fe, Co. The color code is black for H, gray for C, red for O and orange for M.

3.2.1 Computational Details

In order to study the effects of water molecule traces on the desorption process of precursor molecules iron stearate and cobalt stearate, both systems have been prepared in three different conditions: (i) in dry conditions, (ii) in the presence of a single water molecule around the metal center and (iii) with two water molecules coordinated to the metal atom. This study is also expected to shed light on the different nature of iron and cobalt NPs despite their identical configurations as far as the desorption processes is concerned. First principles molecular dynamics simulations have been performed within the DFT framework [76] using the CPMD [204] code.

Becke exchange functional and Lee–Yang–Parr correlation functional (BLYP) has been used to describe the exchange and correlation contributions [108, 109]. Core-valence interactions of Fe and Co have been described by norm-conserving Troullier-Martins pseudopotentials [118]. 2s and 2p states for C and 1s for H were explicitly treated as valence electrons in the pseudopotential approach. Valence electron orbitals have been represented in terms of plane waves with a cut-off energy of 80 Ry. van der Waals interactions were also included according to Grimme's D2 formulation [142]. Free energy profile of the desorption process has been acquired as a function of metal-COO distance which has been increased gradually -not more than 0.10 Å- starting from the corresponding equilibrium distances. Each consecutive step of configuration with new metal-COO distance has been dynamically evolved long enough (∼3 ps) to ensure that both the average force on the constraint and the total energy of the system converges to an ergodic limit as the system evolves over time.

3.2.2 M-stearates in dry conditions (M=Fe, Co)

The simulation of iron-based system in dry conditions started from the corresponding equilibrated geometry given in Figure 3.16a. The system have been quenched and stabilized first by performing a damped molecular dynamics run [212]. Fe-O coordination distance of 2.00 Å acquired after this step is also another indication of sufficient minimization [256]. On the other hand, configurations may suffer

from minute structural fluctuations and non-planar ligand coordinations in ambient temperature. The reaction coordinate is chosen to be the distance between Fe-COO chain (measured as the Fe-C distance) and this equilibrium distance is d_{Fe-COO} = 2.31 Å. The constrained dynamics application suggested by the Blue Moon approach has been performed starting from the equilibrium distance with approximately 0.1 Å increments to detach the coordinated ligand from the metal center. The overall time-scale of this particular simulation is 102 ps. Structural evolution of the system is summarized in Figure 3.17 where the corresponding Fe-COO distances are 2.31, 3.07, 3.52, 4.52 Å.

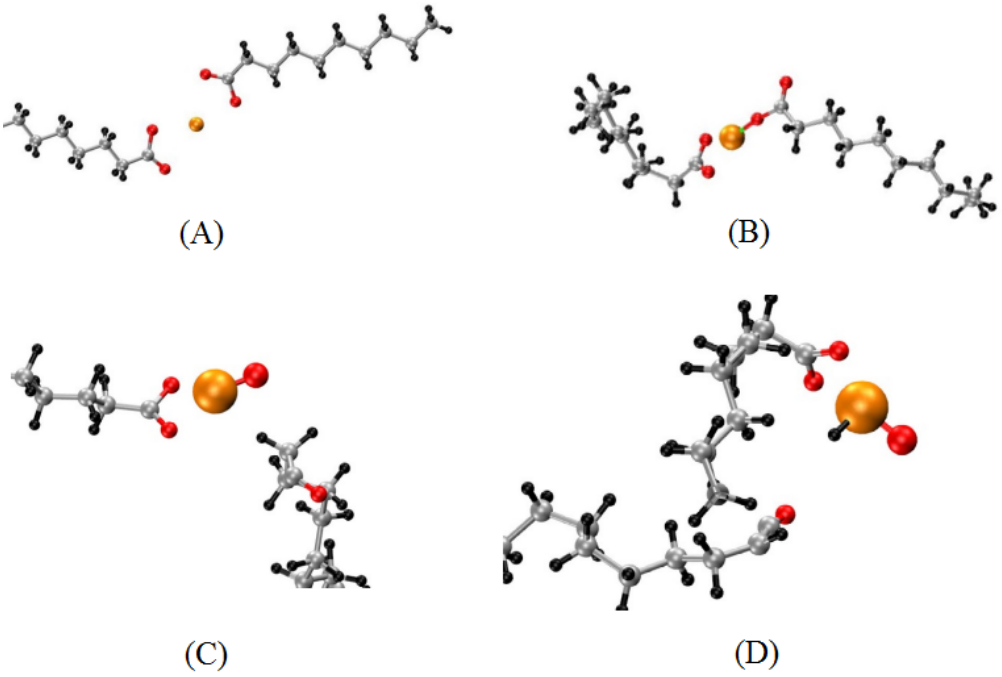

FIGURE 3.17: Structural evolution of the iron stearate in dry conditions. Iron is oxidized after overcoming the transition barrier and FeO seed is formed as a result. Corresponding Fe-COO distances are 2.31, 3.07, 3.52, 4.52 Å in their respective order.

The resulting free energy profile of the desorption process is given in Figure 3.18. The monotonic increase in both the total (black curve) and free energy (red curve) shown in the lower panel of the energy profile continues until d_{Fe-COO} reaches 2.75 Å where the square planar coordination of the iron and oxygens begins to compromise (see the panel (B) of Figure 3.17). Since the reaction coordinate is determined to be the Fe-C distance, the iron captures an oxygen from the carboxylate group

as a result of their non-planar coordination at finite temperatures, mostly originating from the entropic contribution from the hydrocarbon chain. Total energy, as indicated by the black curve, corresponds to the sum of this entropic contribution and the free energy difference. After overcoming this transition state where the free energy barrier is $\Delta F = 15.02$ kcal/mol (0.65 eV), oxygen share continues until the Fe-COO distance reads $d_{Fe-COO} = 3.52$ Å as shown in the panel (C) of the Figure 3.17. As the constraint application proceeds, the carbon of the hydrocarbon chain is pushed further away from the iron, accompanied by a β-hydrogen transfer as can be seen from the panel (D) of the same figure. The plateau in both the average constraint force and the free energy (Figure 3.18) starting with $d_{Fe-COO} \sim 4.00$ Å indicates that the interaction of the iron with the carbon chain is terminated. The resulting FeO seed can aggregate to form target nanoparticles in the presence of other homogeneous seeds. The bonded hydrogen does not impair the formation of the FeO nanoparticles since it can be back-transfered to the COO moiety.

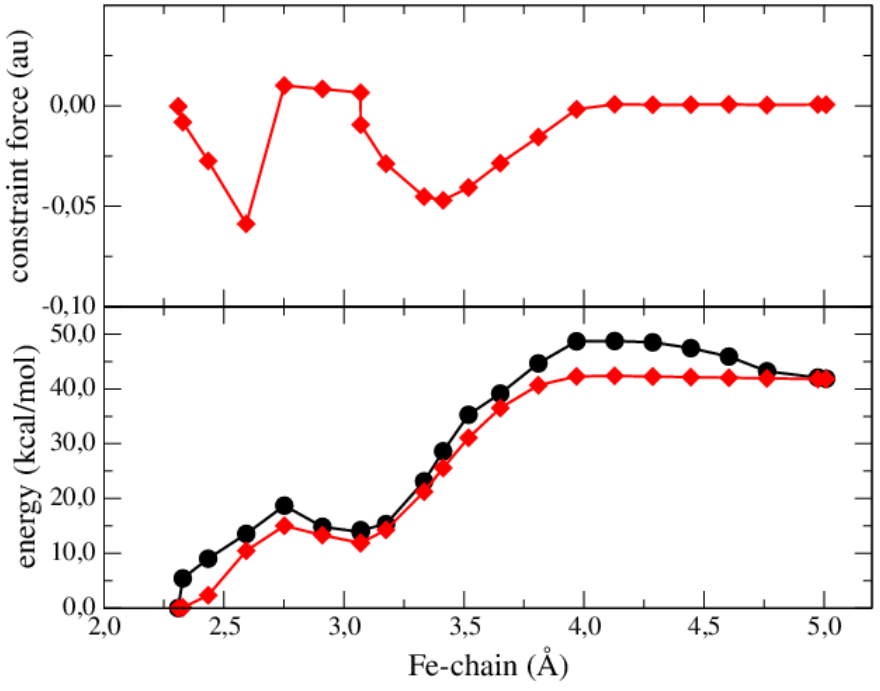

FIGURE 3.18: Constraint force (upper panel) and free and total energies (lower panel) for the desorption of the chain in Fe-based stearates at 300 K in dry conditions. The red curve describes the free energy profile while the total energy is shown by the black curve.

In the light of these preliminary information, cobalt-based system has been studied within identical conditions. However, there is one point worthy of notice. In order to examine whether the choice of the reaction coordinate has an influence on the reaction pathway followed by the systems and the resulting free energy profile, two studies have been performed with different reaction coordinates for the cobalt-based system in dry conditions. Two variations are shown in Figure 3.19.

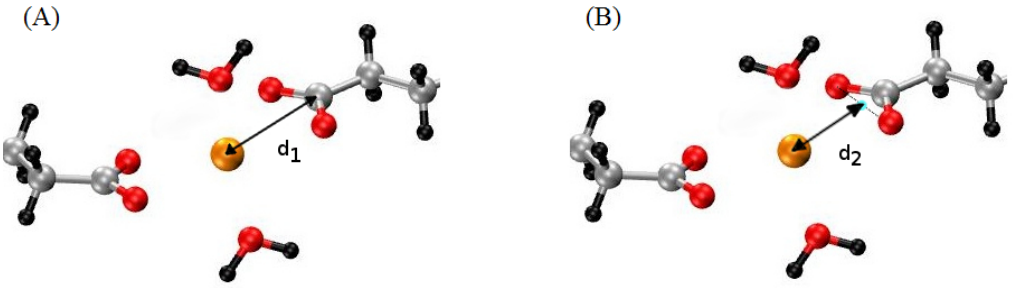

FIGURE 3.19: Choices of two different reaction coordinates. The distance between the central metal atom to A) the carbon atom of the carboxylate group (d_1 = 2.31 Å), B) the center of mass of the oxygen atoms of the carboxylate group (d_2 = 1.82 Å).

In the first case, the reaction coordinate is chosen to be the distance from the metal center to the carbon of the precursor ligand, identical to what has been performed for the iron-based system in dry conditions. In the other case, a massless dummy atom is placed at the center of mass of the oxygens of the carboxylate group. The purpose of such a modification is to investigate whether the desorption process advances in a neater fashion for the case where the two oxygens of the chain are pushed simultaneously. This dummy atom is introduced only in the aim of applying the corresponding constraint with one reaction coordinate instead of two in order to cut down the computational cost; its existence does not contribute to the dynamical calculations. The equilibrium distances of these variations, d_1 and d_2, are 2.31 and 1.82 Å, respectively. Free energy profiles of the systems simulated with these choices have been given in Figures 3.20 and 3.21.

According to the profile (Figure 3.20), the energy barrier to surpass the transition state is ΔF = 20.85 kcal/mol (0.90 eV) when the Co-COO distance reads d_{Co-COO} = 2.75 Å, the identical point where the iron-based system possesses a free energy barrier of 15.02 kcal/mol (0.65 eV). This fundamental finding may be one of the main reasons which causes the discrepancy in the formation of iron and cobalt

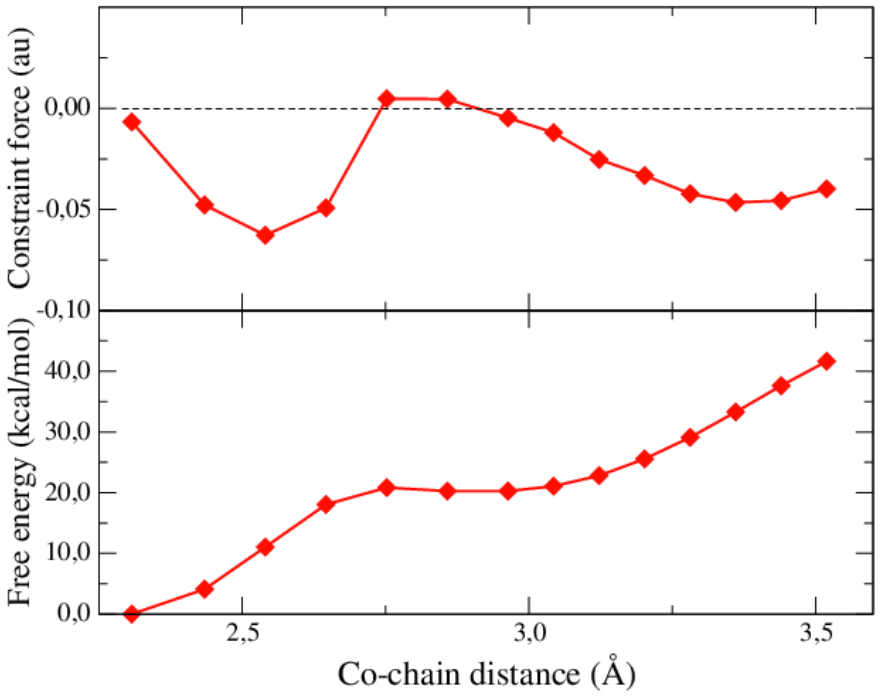

FIGURE 3.20: Constraint force (upper panel) and free energy (lower panel) for the desorption of the chain for Co-stearate at 300 K in dry conditions. The energy barrier to surpass the transition state is 20.85 kcal/mol when d_{Co-COO} = 2.75 Å.

nanoparticles upon thermal decomposition reaction reported by the experimental team of IPCMS as mentioned in the introduction of the current chapter. Despite the identical experimental conditions, formation of cobalt oxide nanoparticles advances with difficulty; that is, the spherical morphology of resulting CoO NPs slightly differs when compared to that of Fe_3O_4 NPs [246].

The free energy profile of the cobalt-based system in dry conditions with the alternative reaction coordinate depicted in Figure 3.19 (B) along with the average constraint force has been presented in Figure 3.21. Critical distances, where the sign changes of the free energy curve might indicate possible conformational changes were marked. These particular points correspond to Co-COO distances of 1.82, 2.25, 2.73 and 3.36 Å where the first and the last belonging to the initial and the final configurations, respectively. The configurations of the systems for specified Co-COO distances along with their HOMO states have been summarized in Figure 3.22.

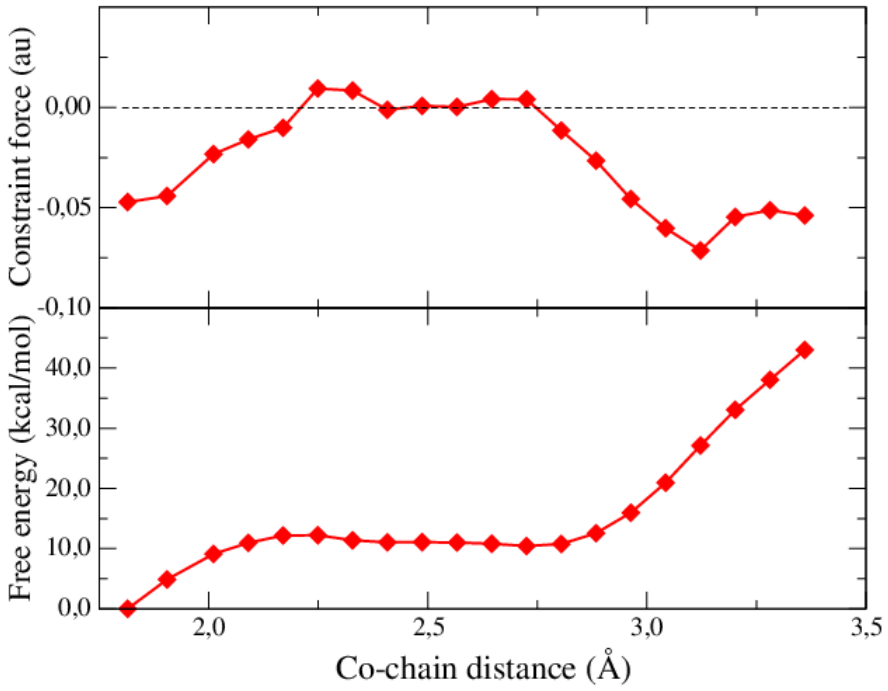

FIGURE 3.21: Constraint force (upper panel) and free energy (lower panel) for the desorption of the chain for Co-stearate at 300 K in dry conditions with the alternative reaction coordinate. The energy barrier to surpass the transition state is 12.22 kcal/mol when $d_{Co-COO} = 2.17$ Å.

The energy barrier of this particular Co-based system is calculated to be 12.22 kcal/mol when Co-COO distance reads 2.25 Å. Here, one must be attentive about the given free energy barrier values. Comparing the energy profiles and energy barriers acquired from two different reaction coordinates would lead to misdirection while interpreting the results. For this reason, one must take into account the elongation of the corresponding reaction coordinate from the equilibrium distance rather than the final constraint distance for comparison purposes. The free energy barriers leading the desorption process and the bond elongations from the equilibrium distance as a result of the constraint application were given in Table 3.3.

Despite the evident experimental outcome [246], one may presume that desorption process of the cobalt-based system in dry conditions follows a comparable reaction path with that of its iron counterpart judging by the final configuration of the system given in the (g) panel of the Figure 3.22. For earlier stages of the reaction, the oxygen share between the metal center and the carbon, and then the formation of Co seed with an attached H occurs at similar bond elongations compared with

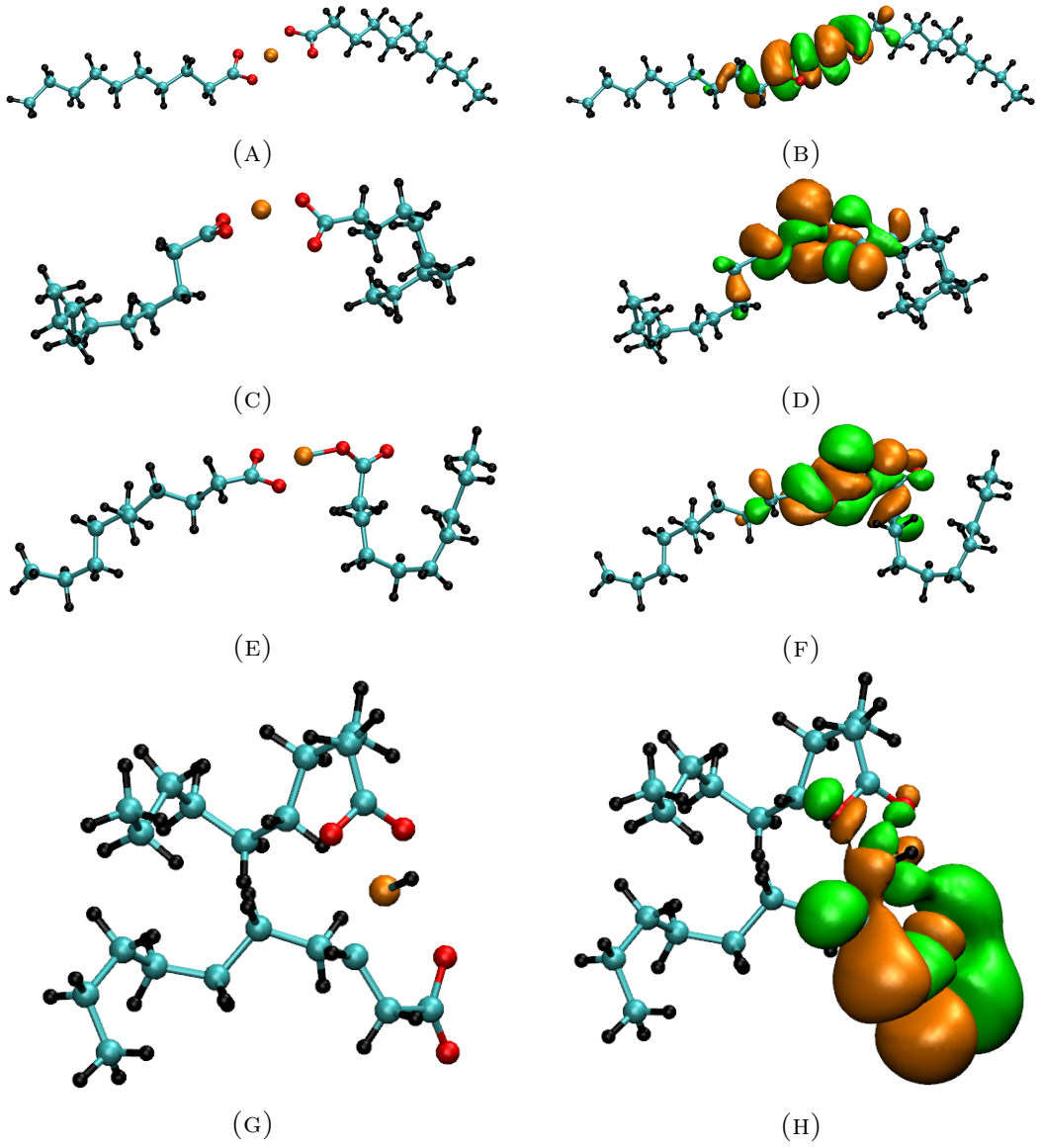

FIGURE 3.22: Configurations and HOMO states of the Co-stearate at Co-COO distances of 1.82, 2.25, 2.73, and 3.36 Å, respective to the rows. Isosurfaces are shown at values of ± 0.01 $(e/Å^3)^{1/2}$ in orange (positive values) and green (negative values). The color code is identical to that of Figure 3.16 with carbon atoms in cyan.

the iron-based system. However, as shown in Figure 3.22 (h), the mixing of the $d_{x^2-y^2}$ orbital of the cobalt with that of the carboxylate group indicates that the interaction of the metal center and the precursor complex is still intact which hinders the clean separation of the two moieties. Monotonically increasing trend in the free energy profile (Figure 3.21) starting with the ∼2.80 Å mark is also an indicator of an ongoing interaction. A similar argument can also be expanded for

the Co system with discussed earlier (see ∼3.00 Å mark in Figure 3.20).

TABLE 3.3: Summary of the free energy barriers and the amount of constrain application. The subscript "*alt*" signifies the alternative reaction coordinate described in Figure 3.19. The free energy barrier ΔF is in kcal/mol and total elongation of the reaction coordinate from the equilibrium position d_{eq} is in Å. The values in parenthesis are the total constraint application coinciding with the transition state.

	Fe		Co		Co_{alt}	
	ΔF	d_{eq}	ΔF	d_{eq}	ΔF	d_{eq}
Dry	15.02	0.44 (2.75)	20.85	0.44 (2.75)	12.22	0.43 (2.25)
1 H_2O	18.86	0.39 (2.70)	20.73	0.39 (2.70)	11.62	0.35 (2.17)
2 H_2O	5.65	0.34 (2.65)	13.90	0.60 (2.91)	×	×

3.2.3 M-stearates with one H_2O molecule

The simulation of the stearate systems in the presence of one water molecule has been performed with the identical parameters. Figure 3.23 summarizes the structural evolution of the iron stearate in these conditions. The water molecule oscillates inside the first coordination shell of the metal center, between the radii 3.1 and 3.7 Å until simulation time reaches t=6.75 ps. This behavior accounts for the increasing trend of the energy profile which peaks when the Fe-COO distance reads 2.70 Å, slightly shorter as opposed to the iron stearate in dry conditions. The energy barrier to surpass this transition state is 18.86 kcal/mol (0.82 eV).

As given in the panel (B) of Figure 3.23, withdrawal of the water molecule from the vicinity of the iron occurs. As a consequence, this system evolves to dry conditions and as expected from the results of its analogue in dry conditions, FeO seed is formed. Figure 3.24 shows the corresponding free energy profile. The general trend in the energy profile and the constraint force of the iron-based system with 1-H_2O system shares similarities with that of the one in originally dry conditions (Figure 3.18) as far as the amount of constraint application, the global minimum in the energy profile and the finalized interaction of the metal center and the hydrocarbon chain is concerned. Referring to Table 3.3, the transition state corresponds to a Fe-COO distance of 2.75 Å for Fe-stearate in dry conditions

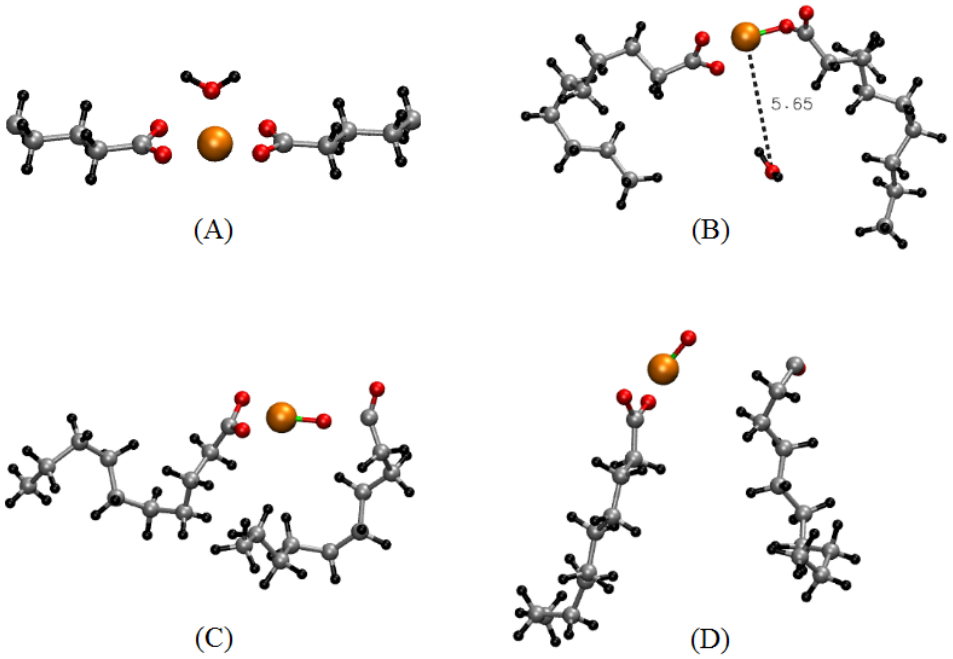

FIGURE 3.23: Structural evolution of the iron stearate with one water molecule. The system converges to dry conditions as the water molecule escapes the solvation shell of the metal center. Panel (B) shows the distance of the water molecule to Fe center. The color code is identical to that of Figure 3.16.

while it reads 2.70 Å for 1-H_2O system. Escape of the water molecule causes this distance to shorten by 0.05 Å.

The simulation of the cobalt-based system with one water molecule has been discontinued after five consecutive step of constraint application, since the escape of the water molecule from the solvation shell of the cobalt atom transforms the configuration to that of dry conditions as was encountered in the Fe-based system. In order to ensure, simulation of this system has been repeated from the initial conditions with a second constraint on the water-cobalt distance during equilibration step in order to stabilize the water molecule. However, similar behavior has been observed with this attempt too, water molecule receded from the vicinity of the metal as soon as the constraint on the water molecule is removed. Comparing the free energy profiles of both systems in their own set also supports this idea. Figure 3.25 shows the free energy profile of the cobalt system in the presence of one water molecule and it is in total agreement with the first five steps of the same system in dry conditions (Figure 3.21).

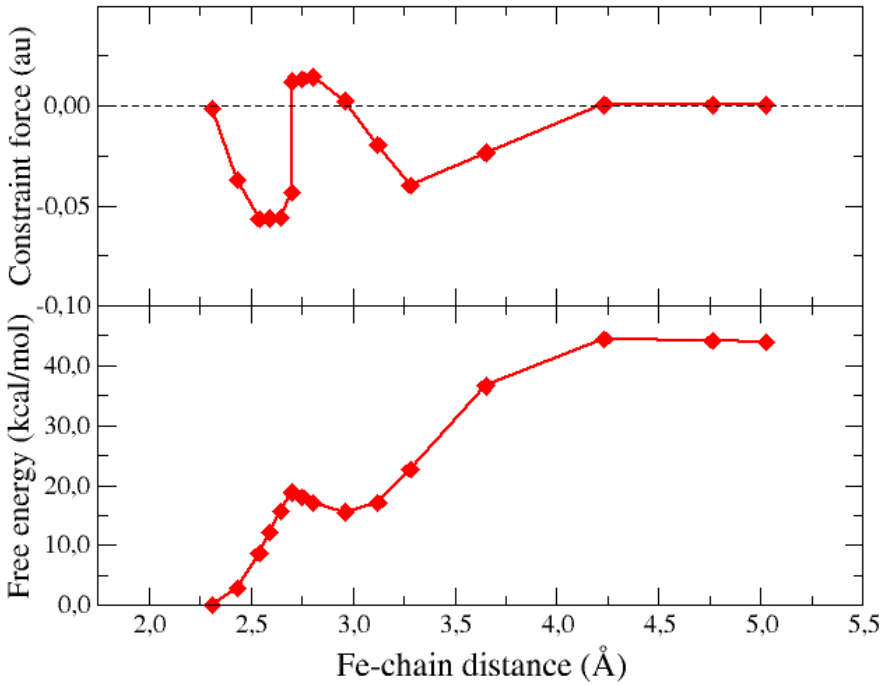

FIGURE 3.24: Constraint force (upper panel) and free and total energies (lower panel) for the desorption of the chain in Fe-based stearate at 300 K in the presence of one water molecule. The energy barrier to surpass the transition state is 18.86 kcal/mol (0.82 eV) when $d_{Fe-COO} = 2.70$ Å.

Figure 3.26 shows the structural evolution of the cobalt stearate system with the water molecule withdrawn from the solvation cell of the metal center. Contrary to the iron-based system, the definitive retraction of the water molecule occurs in a much shorter time frame, t $\approx$ 0.7 ps to be quantitative. In transition metals, the kinetics of the water exchange mechanism strongly depends on the number of occupied d-electrons, and therefore the ionic radius [257]. Presence of one additional diffuse d-orbital in the electronic configuration of Co ([Ar] $3d^7 4s^2$) apparently triggered such a variation when compared with Fe ([Ar] $3d^6 4s^2$) and as a result caused the immediate escape of the water molecule instead of circulating around the hydration shell. Furthermore, since the interaction of the water and the metal center is transient, the free energy barrier of the transition state doesn't deviate from the one for the dry conditions. In other words, the presence and relatively long-term interaction of the water molecule causes an increase in the energy barrier for the Fe-based system as much as 25% while the decrease for the cobalt case is almost negligible.

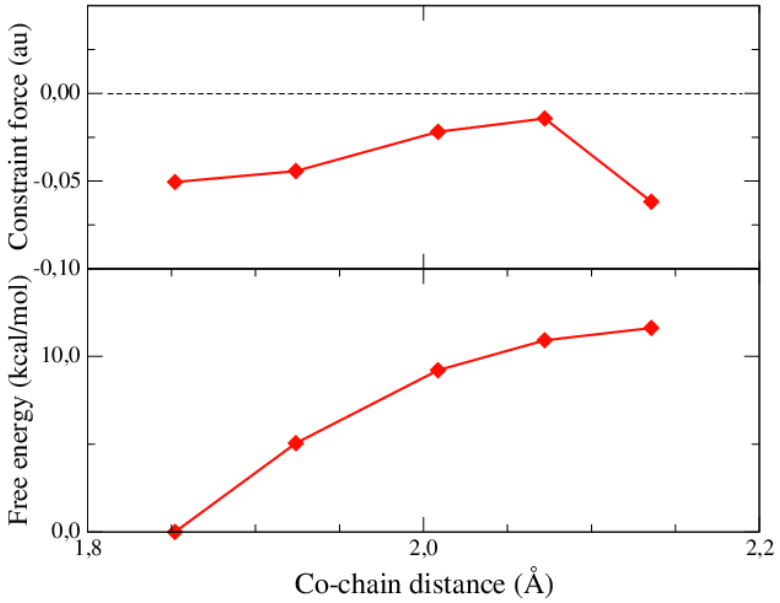

FIGURE 3.25: Constraint force (upper panel) and free energy (lower panel) for the desorption of the chain for Co-stearate at 300 K in the presence of one water molecule. Destabilization and escape of the water molecule converts this system to dry conditions also confirmed by the first five steps of Figure 3.21.

As summarized in Table 3.3, the free energy was calculated to be 12.22 kcal/mol for dry conditions, while it is 11.62 kcal/mol for the system with a runaway water molecule for the same Co-COO distance of 2.17 Å. At this point, it is important to remember that the energy barriers for Co-based systems are being compared in their own set of calculations performed with the alternative reaction coordinate. On the other hand, total distance of constraint application from the equilibrium position is also consistent for the cobalt-based system in both reaction coordinates (0.39 and 0.35 Å, see the corresponding d_{eq} values in Table 3.3). To sum up, choosing an alternative reaction coordinate that serves an identical purpose for the ligand desorption from the metal center does not alter the pathway followed by the reaction; however corresponding differences in the free energy barrier values are expected. Focusing on the results acquired up to now, it can be concluded that the iron and cobalt cannot accommodate a single water molecule when the coordination shell is not complete since the preferred coordination geometry (and number) for iron and cobalt cation in +2 oxidation state is either tetrahedral (4-fold) or octahedral (6-fold) [258].

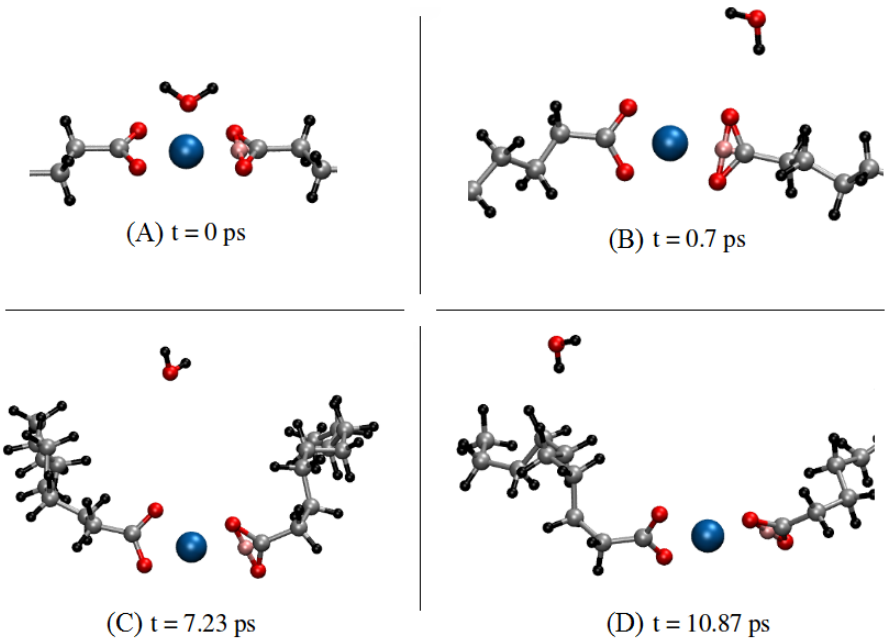

FIGURE 3.26: Structural behavior of the cobalt stearate with one water molecule for given timestamps. The water molecule prematurely escapes the solvation shell of the metal center, rendering the system to interact in dry conditions. The color code is identical to that of Figure 3.16 with the Co atom in blue.

3.2.4 M-stearates with two H_2O molecule

The initial configuration of this specific system, as seen in Figure 3.16c, shows the water molecules that are located orthogonal to the plane constituted by the four oxygen atoms of the stearate chain. Presence of two water molecules around the first solvation shell of the transition metal center completes the coordination of the metal with octahedral (6-fold) symmetry. It was predicted that the ligand desorption process would follow a different reaction pathway as a result of the hydrogen bonds formed between the water and the carboxylate group of the hydrocarbon chain, when compared with the previous case where the coordination shell of the metal has one water molecule and is, therefore, not complete.

Figure 3.27 summarizes the HOMO and LUMO states of the iron based system in the first step of constraint application, where the Fe-COO distance reads 2.43 Å. The HOMO states of the system is d_{xy} orbital from the metal center with expected contributions from the water molecules and the oxygens of the ligand.

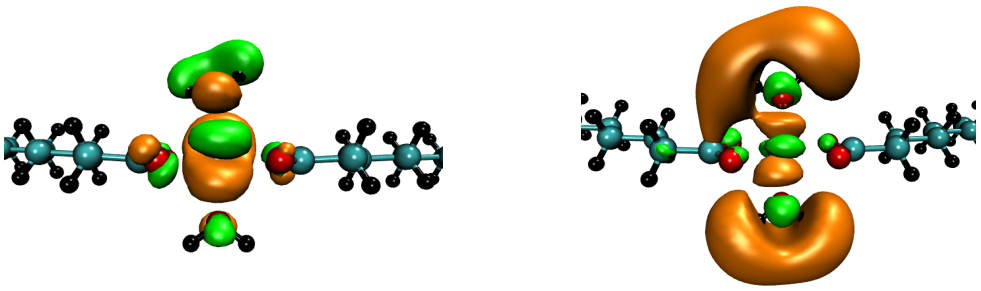

(A) (B)

FIGURE 3.27: A) HOMO and B) LUMO of the Fe-based stearate system in the presence of two water molecules for $d_{Fe-COO} = 2.43$ Å. Isosurfaces are shown at values of ± 0.025 $(e/Å^3)^{1/2}$ in orange (positive values) and green (negative values). The color code is identical to that of Figure 3.16 with carbon atoms in cyan.

Solvent exchange process is divided into three stoichiometric mechanisms in which the change in coordination number of the metal center is taken as the base quantity: The increase, decrease and no kinetically detectable behavior in the coordination number is termed to be associative, dissociative and interchange modes, respectively [259]. On the other hand, it was reported that dissociative mechanism proceeds with a low probability due to long time scale of the mean life-time of the associated moieties, e.g. water molecules, around the metal center. Briefly, kinetics of octahedral water coordination around a metal center must be considered according to the interchange mechanism. Furthermore, interchange mode is also divided into two groups; associative (I_a) and dissociative (I_d) mode, according to whether the ligands entering or leaving the coordination shell trigger an exchange process between the first and the second coordination shell of the metal center [260].

Figure 3.28 summarizes the free energy profile of the Fe-based system in the presence of two water molecules. It is remarkable that this system has a quiet distinct profile and lower free energy barrier ($\Delta F = 5.65$ kcal/mol (0.25 eV)) compared to the previously studied configurations, mostly originating from the existence of two water molecules and, as a result, the completeness of the inner solvation shell of the central metal. As the simulation proceeds, the realignment of the water molecules causes the monotonic decrease in the constraint force which includes the formation of the hydrogen bonds whose representation is given in Figure 3.29.

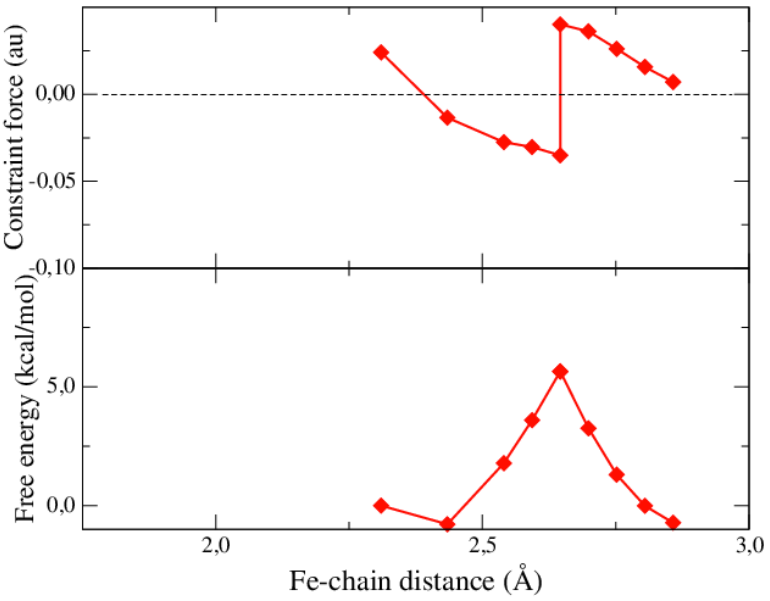

FIGURE 3.28: Constraint force (upper panel) and free energy (lower panel) for the desorption of the chain in Fe-based stearates at 300 K in the presence of two water molecules.

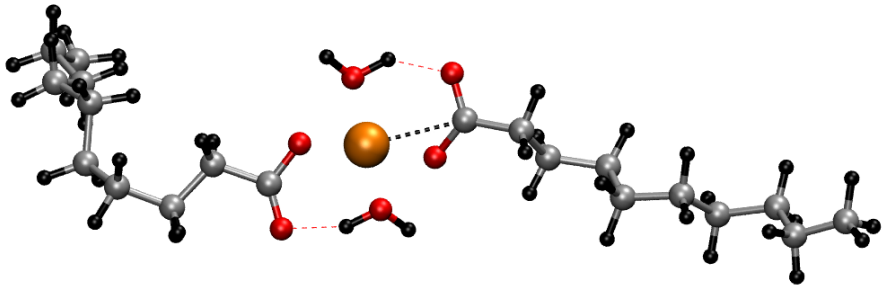

FIGURE 3.29: The configuration of the Fe-based system with two water molecules when the Fe-COO distance reads 2.65 - δ Å. Formation of the hydrogen bonds are shown in red dashed lines. The color code is identical to that of Figure 3.16.

At this instance, when the Fe-COO distance reads 2.65 - δ Å, the square planar symmetry constituted by the oxygens of the carboxylate moieties converts to rhombus by shifting to either sides; and at the same time, octahedral symmetry established by the water molecules also breaks down and becomes planar. Consequently, the first coordination shell of the iron now spans a total of 4 oxygens; two from the ligand and two from the water molecules, whose mechanism also refers to the interchange mode mentioned earlier [259]. The attempt to retract the hydrocarbon chain from the Fe center provokes the dissociative interchange

mechanism (I_d) as was also specified for octahedral iron coordination in the Table 1. of Ref.[257]. As the system evolves over time at the identical constraint (which can similarly be considered as 2.65 + δ Å), water molecules approach the ligand by circling around the first coordination shell and then bond to the oxygens.

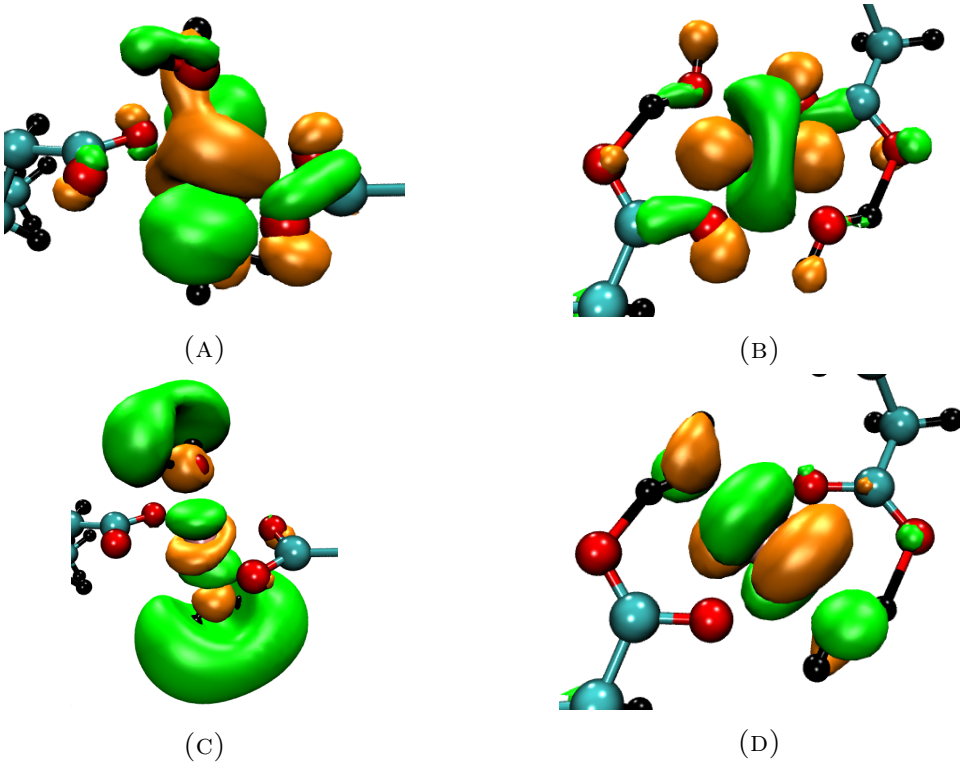

FIGURE 3.30: HOMO (top row) and LUMO (bottom row) states of the Fe-based stearate system in the presence of two water molecules for d_{Fe-COO} distances A-C) 2.65 - δ Å and B-D) 2.65 + δ Å. Water molecules lose their octahedral symmetry and constitutes a plane with the ligand around the Fe center. Isosurfaces are shown at values of ± 0.025 $(e/Å^3)^{1/2}$ in orange (positive values) and green (negative values). The color code is identical to that of Figure 3.16 with carbon atoms in cyan.

The sudden jump in the constraint force and the related peak of the energy profile coincide with the formation of these chemical bonds. These, in turn, induce variations of the electronic structure of the system. Comparison of the HOMO and LUMO states of the two configurations, before and after the breakdown of the octahedral symmetry and the migration of the water molecules, are given in Figure 3.30. Before the configurational change, the HOMO displays a mixing character due to d_{z^2} orbital from the Fe center and $1b_1$ from H_2O molecules, plus minor contributions from the ligand. While the HOMO retains its d_{z^2} symmetry

after the realignment of the water molecules, LUMO of the system transforms into a d_{xy} orbital plus additional contributions on the O atoms belonging to the coordinated water molecules. These Kohn–Sham states are characterized by eigenvalues located, on the energy scale of our DFT total energy, at -3.75 eV (HOMO) and -2.51 eV (LUMO). Hence, the system has a gap of 1.23 eV, identical to the one of the octahedral configuration. Nonetheless, the new configuration is assumed to be more stable than the initial octahedral arrangement and, as a result of the lowering in the total energy, the initial HOMO and LUMO eigenvalues (-2.44 and -1.21 eV, respectively) shift to the lower values reported above and the nature of the LUMO states switches from the typical LUMO of H_2O molecules (panel (C) of Figure 3.30) to the d_{xy} orbital of Fe.

Further manipulation of the constraint on the reaction coordinate does not disturb the resulting configuration. The final configuration presented in Figure 3.31 still points to the bonding of the oxygens of the ligand and the water molecules. Apart from the slight curving of the stearate chain, the stability of the resulting configuration is relatively conserved, minimizing the entropic contribution. As far as the transition metals are concerned, filling of d-orbitals has rather strong impact on the ligand behavior and the exchange rate constant. Comparing the octahedral coordinated compounds of iron and cobalt will disclose insights for the proposed processes.

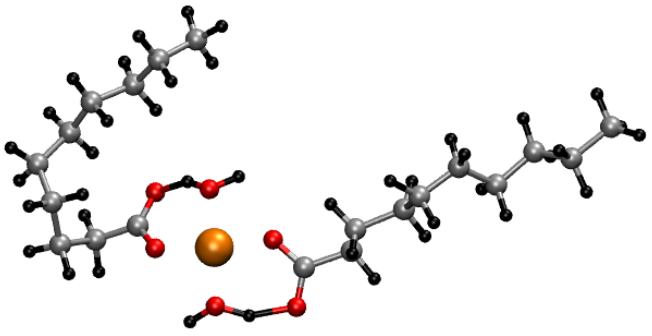

FIGURE 3.31: Final configuration of the iron stearate with two water molecules. The color code is identical to that of Figure 3.16.

Coming to the Co-based system with two water molecules, the point that needs attention is the treatment of the constraint application. For the present work, the manipulation of the distance constraint on the reaction coordinate was only realized following the full structural optimization and then the annealing procedure to

bring the system to room temperature. That being said, in order to investigate if the specific thermodynamical environment has an effect on the reaction pathway followed by the ligand desorption process, this particular system has been simulated with two different protocols as far as the order of the constraint application and the temperature treatment is concerned.

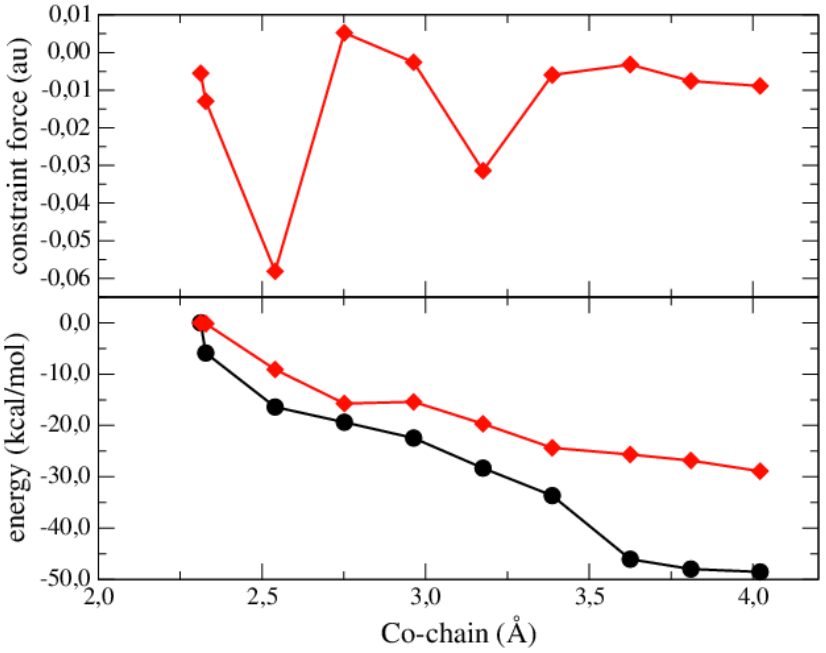

FIGURE 3.32: Constraint force (upper panel) and free and total energies (lower panel) for the desorption of the chain in Co-based stearates at 300 K in the presence of two water molecules. The red curve describes the free energy profile while the total energy is shown by the black curve.

Figure 3.32 summarizes the free energy profile of the Co-based system in the presence of two water molecules simulated in terms of the usual procedure. Monotonically decreasing free energy indicates that the desorption reaction of the ligand from the Co center is exergonic; that is, this reaction is spontaneous and does not require an energy input. The difference in the total energy and the free energy (black and red curve in the lower panel) gives an insight about the statistical fluctuations and conformational changes of the hydrocarbon chain. As given in Figure 3.33, the formation of CoO seed was realized as expected, however, the hydrocarbon chain irreversibly disintegrates following the protonation of the seed

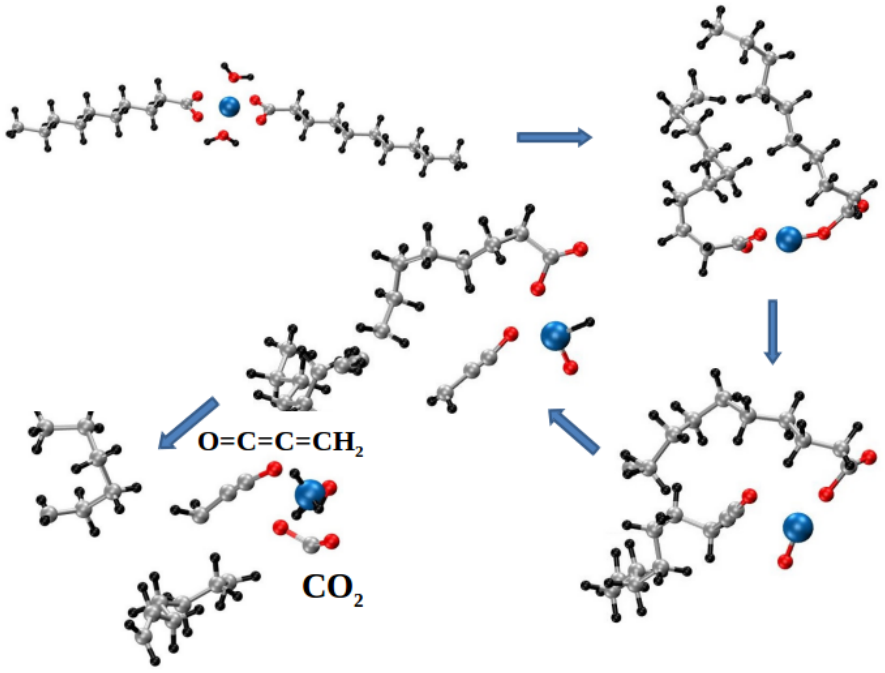

FIGURE 3.33: Final configuration of the cobalt stearate with two water molecules. Cobalt desorption process terminates with the formation of a fragmented polycarbon chain, CO_2 and protonated cobalt oxide moiety.

as the ligand is pulled away from the metal center. Furthermore, the cobalt oxide seed acquires two more hydrogens from the fragmented pieces of hydrocarbon chain and as a result, leaves the final products as CO_2 and broken stearate chains.

In the alternative procedure, the constraint application is carried out over the course of annealing procedure as opposed to the usual strategy. This way, it was possible to exploit the stability of the equilibrated structure during the ligand desorption process. Figure 3.34 summarizes the free energy profile of the identical Co-based system treated with this strategy. The contrast in the energy graphs of the two protocols is significant (see Figure 3.32). Free energy barrier is determined to be $\Delta F = 13.90$ kcal/mol (0.60 eV) when the Co-COO distance reads $d_{Co-COO} = 2.91$ Å with an elongation of 0.60 Å from the equilibrium distance. This is considerably longer than the other Co-based systems whose transition states coincide when the elongations are 0.44 and 0.39 Å for dry and 1-H_2O systems, respectively. Furthermore, the energy profile points out the exothermic nature of this particular reaction with 7.93 kcal/mol (0.34 eV) of difference in energies of the reactants and

products; whereas its Fe-based analogue (see Figure 3.28) also shows a similar feature as low as 0.72 kcal/mol (0.03 eV).

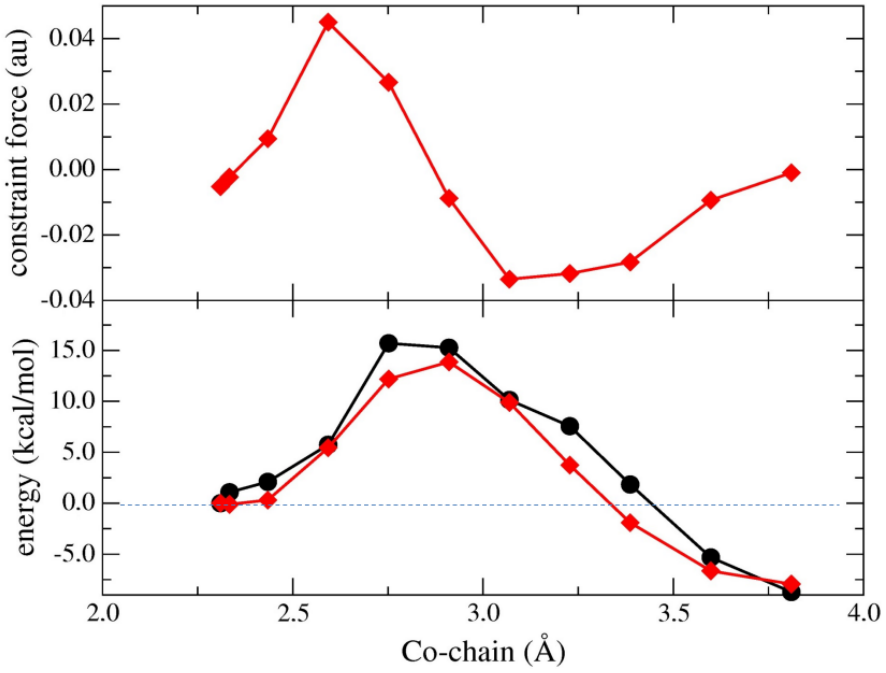

FIGURE 3.34: Constraint force (upper panel) and free and total energies (lower panel) for the desorption of the chain followed by the first reaction pathway in Co-based stearates at 300 K in the presence of two water molecules. The red curve describes the free energy profile while the total energy is shown by the black curve.

As given in Figure 3.35, ligand desorption application proceeds with the stability of the fatty acid chain and protonation of its carboxylate group. The remaining OH^- group then causes the hydroxylation of the Co center. Referring to Table 3.3, the completeness of the hydration shell causes the free energy barrier to become lower for both metals, Fe and Co. This is mainly originating from the terminated interaction of the ligand and the metal center after forming hydrogen bonds with the water molecules. However, it is crucial to note that the presence of two water molecules also inhibits the formation of seeds by altering the electronic structure, and therefore the bonding environment.

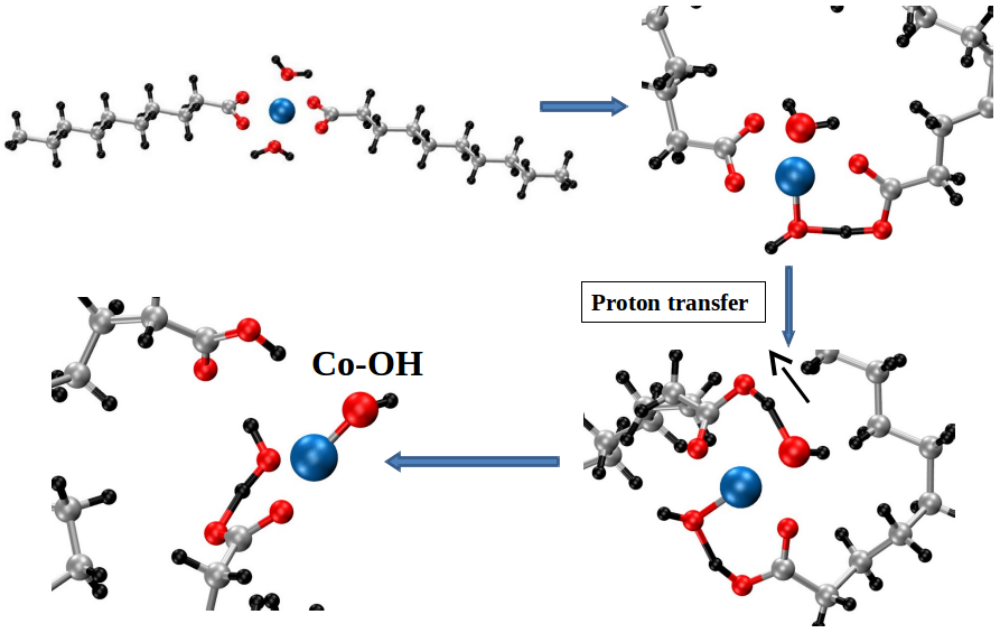

FIGURE 3.35: Second reaction pathway followed by the cobalt-based system in the presence of two water molecules. Thermodynamical environment has an effect on the final configuration compared to the previous case. Stability of the fatty acid chain is conserved while the protonation of its carboxylate group occurs with the formation of a Co-OH moiety.

Massively parallel computational studies have been performed to evaluate the effect of water traces on these scenarios. Fe- and Co-stearates have shown that the formation of iron-oxide precursors for the NPs proceeds with a significantly lower activation barrier than the analogous process for Co in the absence of water traces, i.e. about 15 kcal/mol for a Fe-stearate vs. almost 21 kcal/mol for a Co-stearate. Since the coordination geometry of Fe and Co is either tetrahedral or octahedral, it was found that single water molecule cannot be accommodated around the metal solvation shell, and therefore 1-H_2O systems transforms to dry conditions. Besides, since the timespan for the escape of the single water molecule in Fe-based system with 1-H_2O is longer than that of the Co case, energy barrier of the transition state increases considerably for Fe-stearate while it decreases very slightly for the Co case compared to their dry analogues. In both dry and 1-H_2O conditions, Fe-O seeds, precursors of the NP, can be generated for iron-based stearates. However, in the case of cobalt, fragmentation of the fatty acid chains can lead to the formation of Co-OH moieties or even triple protonated cobalt oxide precursors. These make the aggregation of the resulting NPs more difficult since these Co-based precursors

are much less controllable in terms of shape, morphology and resulting properties especially in 1-H_2O systems. It was found that the assembly of Co(II)-hydroxides is more difficult than the aggregation of the (non-protonated) Fe(II,III)-oxides.

3.3 Exohedral M–C_{60} and M_2–C_{60} (M = Pt, Pd) systems

The design of innovative, green, renewable, and sustainable energy sources has become a worldwide priority in fundamental and applied research. In this global scenario, hydrogen storage and delivery play a prominent role because of two major issues: (i) its production appears to be a clean process promoted by a relatively simple electrocatalysis and (ii) its application in fuel cells results in the production of environmentally friendly water, along with heat and electricity. From the standpoint of energetics, this process has a yield close to 75%, hence higher than a common diesel engine. Coming to the hydrogen storage and production, promising candidates are the Proton Exchange Membrane Fuel Cells (PEMFCs), because of their high capacity and wide range of applications [261]. A general PEMFC is composed of two compartments separated by an ion conducting membrane and designed to convert chemical energy into electric energy. The oxidation of the propellant at the anode and the reduction of the comburant at the cathode produce electricity, heat, and chemical byproducts. At variance with traditional batteries, the PEMFC is an open system, hence propellant and comburant must be continuously supplied. In such a scenario, the design of the catalytic support appears to be a key issue in the development of PEMFC. Using nanoparticles deposited on carbon black aggregates is an efficient way to realize nanostructures with an optimal surface/volume ratio. So far, a lot of efforts have been dedicated to graphene-based systems.[262, 263]. Yet, fullerenes are likely to disclose a wider variety of possibilities and assembly patterns because of their intrinsic curvature and controlled size. [264, 265]

We recently focused on the improvement of the stability of the catalytic support in PEMFC by exploring the possibility of using Buckminsterfullerene C_{60} molecule as support to the metallic catalyst. Metallo-fullerene complexes where the metal atoms are coordinated on the external surface of the fullerene cage, termed exohedral metallo-fullerenes, have received much less attention than endohedral M@C_{60} (M= metal) systems [266–269] and doped fullerenes obtained by C replacement with foreign atoms [270–272]. Fullerenes have been the target of studies aimed at encapsulating atoms for a long time. The purpose is to use fullerene cages as a

mean to transport and deliver dopants because of their high resistance to external chemical attacks and their thermodynamic stability. Carbon structures like nanocages and nanotubes being way less sensitive to corrosion than carbon black, it can be inferred that C_{60} could be a good candidate to replace it as well. Moreover, one can link transition metals, such as platinum and palladium, to C_{60} using coordination bonds to create metallo-fullerenes [273, 274]. It is worth pointing out that the first transmission electron microscopy (TEM) observation of Pt–C_{60} [275] has shown that clustering of fullerene molecules and formation of platinum nano-particles can be achieved under controlled conditions. Nonetheless, the interpretation of these experimental observations is elusive, mainly because the strong coupling of different physical and chemical phenomena involved. In view of the inadequacy of classical force fields to describe systems composed of C_{60} interacting with metallic atoms,[276–278] we rely on first principles simulations within the density functional theory (DFT) framework [99]. This allows to account for both structural and electronic properties, the latter being the major issue in PEMFCs. Specifically, we present a systematic study of fullerenes in interaction with Pt and Pd atoms aimed at identifying the stable structures, resulting from specific locations of the metal atoms and their number (one or two) on the external surface of the C_{60}. The geometrical information is supported by a thorough analysis of the local bonding and electronic structure modifications in terms of maximally localized Wannier functions and centers.

3.3.1 Computational Details

Concerning the M-C_{60} (M= Pt, Pd) complexes, a first set of simulations was performed on systems containing $N = 61$ atoms: 60 C, and 1 metal atom, either Pt or Pd. After finding the most stable M–C_{60} conformation, a second set of simulations was performed on systems of $N = 62$ atoms: 60 C, and 2 metal atoms, either two Pt, two Pd or a Pd–Pt pair. The electronic structure was described in the DFT framework with the generalized gradient approximation (GGA) due to Becke (B) for the exchange energy and Lee, Yang and Parr (LYP) for the correlation energy [108, 109]. This specific choice for the description of the exchange-correlation part is supported by the rich literature on the subject

[279, 280]. Valence electrons were treated explicitly, in conjunction with norm conserving pseudopotentials of the Troullier-Martins type to account for core-valence interactions [118]. The wave functions were expanded at the Γ point of the supercell on a plane wave (PW) basis set with an energy cutoff $E_c = 100$ Ry. All calculations were performed in simulations cells of side $L = 15$ Å beyond which PWs were damped according to the Barnett-Landman scheme [281] for isolated systems. This allows to get rid of spurious effects induced by periodic boundary conditions generally adopted in PWs approaches. Semi-empirical van der Waals interactions according to the Grimme formulation [142] were included to cope with the possible occurrence of weak metal–fullerene dispersion interactions [282].

The geometry of each system was fully optimized in two different ways, first by relaxing the structure via direct inversion in the iterative subspace [283], and then by performing damped molecular molecular dynamics [212]. In all dynamical simulations, the Car-Parrinello method (CPMD) was adopted for a self-consistent evolution of both the electronic and ionic degrees of freedom [76, 204]. A fictitious electron mass of 500 a.u. (i.e. in units of $m_e a_0^2$ where m_e is the electron mass and a_0 is the Bohr radius) and a time step of $\Delta t = 0.12$ fs are selected to integrate the equations of motion.

The electronic structure of the metal-fullerenes complexes is first inspected by exploiting the Kohn-Sham (KS) states. Then, the information on the bonding is refined in terms of the maximally localized Wannier functions [284, 285]. According to a standard procedure, the Wannier functions $w_n(\mathbf{r})$, along with their centers and spreads, are obtained via a unitary transformation *on the fly* of the Kohn-Sham orbitals $\psi_i(\mathbf{r})$. More precisely, among all the possible unitary transformation, the one that minimizes the spread

$$\Omega = \sum_n \left(\langle w_n | \mathbf{r}^2 | w_n \rangle - \langle w_n | \mathbf{r} | w_n \rangle^2 \right) \tag{3.1}$$

is selected. The Wannier states represent an unbiased method for partitioning the charge density. Hence, the bonding information is summarized by four numbers, the center of the orbital,

$$x_n = -\frac{L}{2\pi}\Im m \log\langle w_n|exp(-i2\pi \cdot x/L)|w_n\rangle \tag{3.2}$$

with similar expressions along the other two cartesian directions, and its related spread. Here L is the length of the simulation cell along the x direction. The analysis of the Wannier functions centers with respect to the nuclear positions allows gaining insight into the chemical bonding involved in a wealth of systems such as water [286], amorphous silicon [287], fullerenes [288], and complex electronic structure evolutions involving formation and breaking of chemical bonds [207, 289].

3.3.2 M-C_{60}, M = Pt, Pd systems

Previous models of fullerene-metal complexes [290, 291] were used to construct the initial structures for the present study. The reliability of these models was extensively benchmarked towards experiments and former calculations [292, 293]. Thus, five different initial configurations were prepared, differing in the position of the metal atom on the surface of the C_{60}, as summarized in Figure 3.36. More precisely, the metal atom is initially placed **a)** on top of a π bond between two adjacent six-carbon rings (π-66 hereafter), **b)** on top of a σ bond between a six-carbon ring and a five-carbon pentagon (σ-65 hereafter), **c)** on top of the center of an hexagonal ring, **d)** on top of the center of a pentagonal ring, and **e)** on top of a C atom of the fullerene cage.

These configurations are comprehensive of all the possible symmetries on the C_{60}. For each one of them, full structural optimizations [283] were carried until residual forces were smaller than $\times 10^{-4}$ Hartree/bohr for both metal atoms (M= Pt or Pd). At the end of each optimization cycle, a damped molecular dynamics [212] was performed to further assess the stability of the various structures on the potential energy surface.

The stability of the various configurations are summarized in Table 3.4 in terms of relative total energies. In that table the effects of the damped molecular dynamics

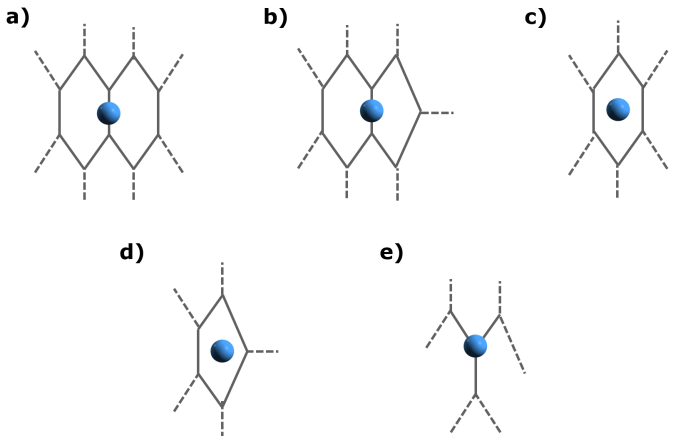

FIGURE 3.36: Schematic representation of the initial configurations used in our simulations. The labels from a to e refer to the position of the metal atom (Pt or Pd, blue spheres) on the fullerene.

becomes evident by comparing the first and second column, referring to initial and the final configurations, respectively.

TABLE 3.4: Initial and final M–C_{60} (M=Pt, Pd) configurations and relative energy differences (ΔE) between the final stable structures for each system. ΔE is in eV.

	Pt		Pd	
Initial	Final	ΔE (eV)	Final	ΔE (eV)
a	a	0.0	a	0.0
b	b	0.47	b	0.21
c	a	0.0	a	0.0
d	b	0.47	b	0.21
e	a	0.0	a	0.0

For both metal atoms, only configurations (a) and (b) represent stable states of the fullerene–metal complex. In both cases, the metal atom stands on top of a C–C bond between either two hexagons (π-66) or an hexagon and a pentagon (σ-65). These configurations remain stable also after CPMD simulations lasting about $1.5 - 2.0$ ps and, as such, can be retained as the only two realizable stable complexes. Yet, an energy difference between the two positions of the metal atoms

exists. More precisely, the (a) π-66 complex is the most stable minimum for both cases, whereas the (b) σ-65 complex is located above this minimum at 0.47 eV (Pt) and 0.21 eV (Pd). At the equilibrium, the distances of the metal atoms from the two carbon atoms of the C–C bond at the interface of two hexagons (a) or one hexagon and one pentagon (b) are listed in Table 3.5, with the labels of the C atoms corresponding to the ones shown in Figure 3.37.

TABLE 3.5: Equilibrium M-C distances, for the configurations (a) and (b). Distances are in Å.

Conf.	C atom	$d_{Pt\text{-}C}$	$d_{Pd\text{-}C}$
a	C_1	2.03	2.15
a	C_2	2.03	2.15
b	C_3	2.04	2.19
b	C_4	2.04	2.19

The fact that the σ-65 configuration is less stable than the π-66 is confirmed by a short dynamical run of about $1.5 - 2.0$ ps. One observes a mean square displacement of the metal atoms larger than 3.0 Å^2/s, promoting a departure of the metal atom from the center of the σ-65 C–C bond toward a more favorable stabilization on a nearby π-66 site. Despite the existence of a most stable π-66 configuration, the σ-65 complex has to be retained as a possible alternative equilibrium site for the metal–fullerene complex (see Figure 3.37).

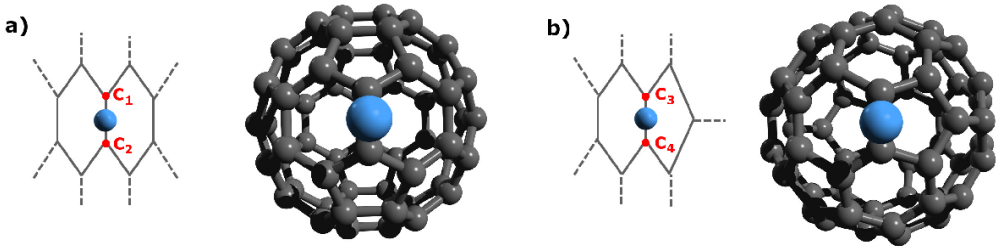

FIGURE 3.37: Schematic (left) and 3D representations (right) of the M–C_{60} complexes for the most stable structures a) π-66 and b) σ-65.

Coming to the electronic structure of the stable metal-fullerene complexes, the first feature that can be noticed is a reduction of the energy gap with respect to the pristine C_{60}. Indeed, an isolated fullerene, according to BLYP-based DFT calculations [294], has a highest occupied molecular orbital (HOMO) possessing

a h_u character and a lowest occupied one (LUMO) with a triply degenerate t_{1u} character. They are separated by an energy gap of 1.66 eV. Our calculations show that the presence of a metal atom on a π-66 site is responsible for a decrease in the gap, which reduces to 1.24 eV for Pt and 1.12 eV for Pd. We can also anticipate that the inclusion of additional metal atoms induces a further decrease in the gap to 0.46, 0.56 and 0.84 eV for the complexes Pt_2–C_{60}, PtPd–C_{60} and Pd_2–C_{60}, respectively. For each complex we seek for the electronic state best reproducing the HOMO of the isolated fullerene. These states are then aligned to our reference level, i.e. the HOMO of the bare fullerene (Figure 3.38). We can remark that the gap shrinking is due to the contribution of orbitals belonging to the metallic atoms, namely $5d^9 6s^1$ for Pt and $4d^{10}$ for Pd. These levels are located above the h_u HOMO of the C_{60}, and become the new HOMO states of the complex M–C_{60}.

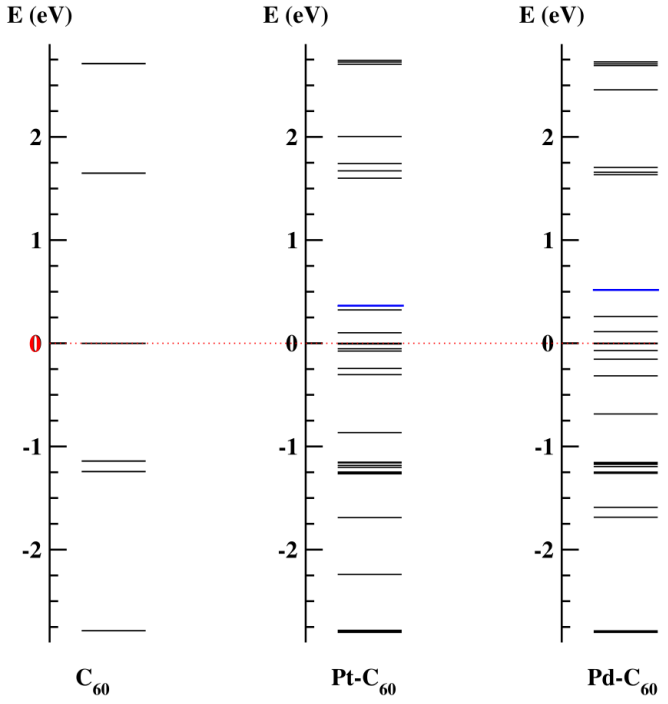

FIGURE 3.38: Kohn-Sham energy levels for the M-C_{60} (M= Pt, Pd) systems compared to the isolated fullerene. The left panel refers to the pristine C_{60}, whereas the central and right panels refer to the Pd–C_{60} and the Pt–C_{60} systems, respectively.

The empty or half-filled *s*-orbitals of metal atoms are prone to accept electrons from a general donor in the vicinity. As a result of this donation, existing chemical bonds involved in the process weaken and elongate. Such a mechanism facilitates

the back-donation of *d*-electrons of the metal atom to the π^* bond of the carbon, but also results in a decrease of the band gap [295]. This can explain the inverse relationship between the bond length and the HOMO-LUMO energy difference of the final metallo-fullerene complexes. Thus, it can be inferred that the bond length of M–C increases with the decreasing of the band gap.

For the most stable configuration (a) an insight into the nature of the electronic states is provided by the projection of the Kohn-Sham wavefunctions onto atomic orbitals centered on the atoms of interest. Specifically, for our case, the most interesting states are the ones in proximity of the energy gap, being also the ones mostly affected by the formation of M-C (M=Pt, Pd) bonds. For the sake of clarity, we limit the discussion to the case of Pt–C_{60} only, as sketched in Figure 3.39.

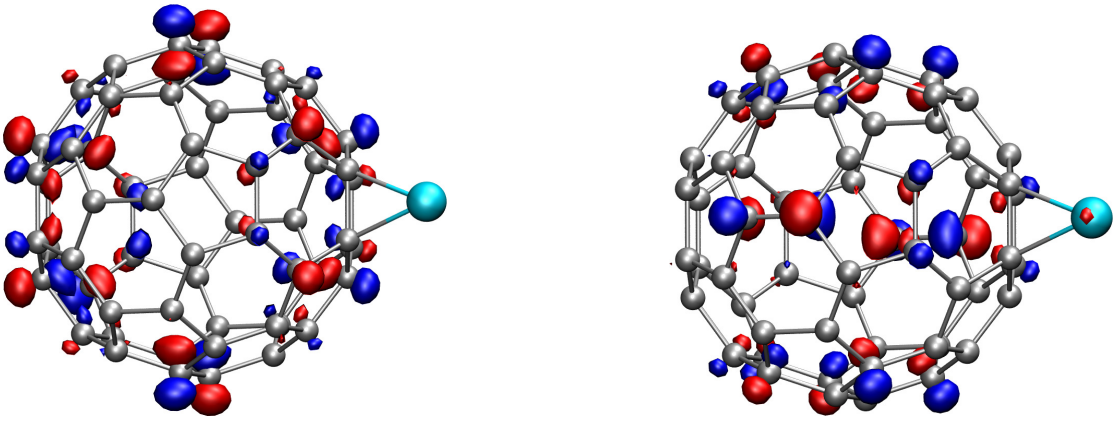

(A) LUMO+1

(B) LUMO

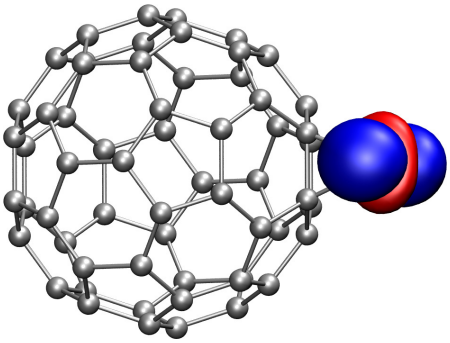

(C) HOMO

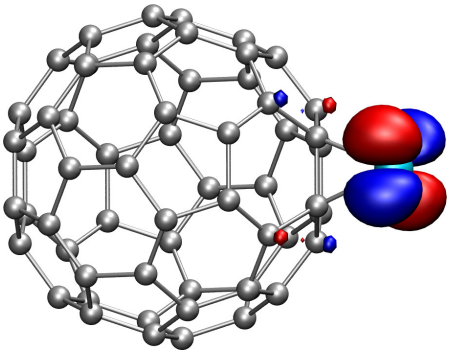

(D) HOMO-1

FIGURE 3.39: Wavefunctions of the HOMO-1, HOMO, LUMO and LUMO+1 states of the Pt–C_{60} system. Isosurfaces are shown at values of $\pm$ 0.05 $(e/\text{Å}^3)^{1/2}$ and the color code is blue for positive amplitudes and red for negative amplitudes.

A first feature to be noticed [296] is the arising of typical transition metal-like e_g states in the spectrum of the system. More precisely, the HOMO and HOMO-1 states of the Pt–C_{60} complex are basically pure d_{z^2} and $d_{x^2-y^2}$, respectively, with minor contributions on top of second-neighbor C atoms of the fullerene. Worthy of note is the presence of small amplitudes on top of the two C atoms forming the π-66 bond. Nonetheless, these two e_g states are almost entirely due to $5d$ Pt (or $4d$ for Pd) atomic orbitals of the transition metal bound to the C_{60}. Conversely, the LUMO and LUMO+1 states feature amplitudes dispersed on most of the C atoms of the fullerene (t_{1u} and t_{1g}-like [294]), with negligible contribution of the transition metal atom.

The maximally localized Wannier function centers (WFCs) provide an insightful complementary information about the nature of the chemical bonds. Their associated spreads allow to identify how many electronic states -and to which extent- contribute to the metal–fullerene bonding.

In the left panel of Figure 3.40 all the WFCs are shown as red spheres. More interesting for our purposes is the distribution of these centers in the region between the metallic Pt atom and the π-66 bond, shown in the lower panel of the same figure. A first feature worthy of note is the isotropic distribution of eight WFCs around the Pt site, all of them mainly coming from a combination of the $5d$ states of Pt.

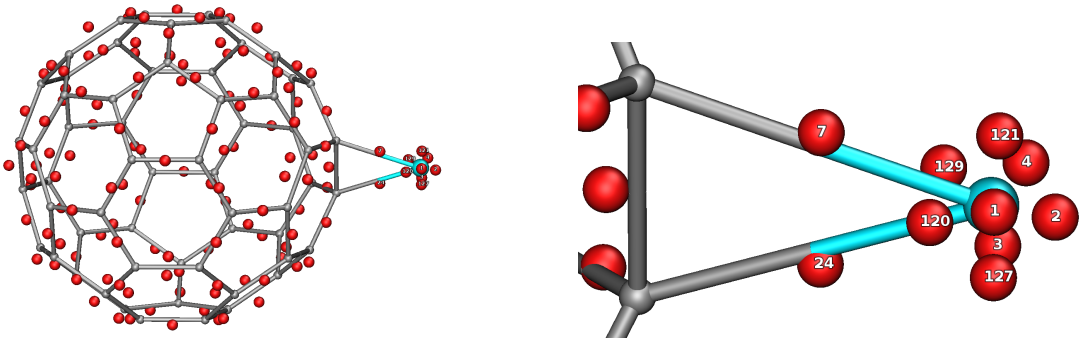

(A) (B)

FIGURE 3.40: Wannier centers for the fullerene-Pt complex (left panel) and detail around the Pt–C_{60} interface (right panel) where two specific centers, labeled 7 and 24, participate to the metal–C_{60} bonds.

These WFCs close to the Pt atoms are labeled in Figure 3.40 according to the order in which they appear after the mentioned unitary transformation. By looking at their associated spread, two groups of centers can be identified. The WFCs labeled as 2, 3, 121 and 129 are characterized by a dispersion $\sigma_{\mathrm{WFC}} = 0.78$ Å, whereas WFCs 1, 4, 120 and 127 have a slightly larger spread $\sigma_{\mathrm{WFC}} = 0.82$ Å.

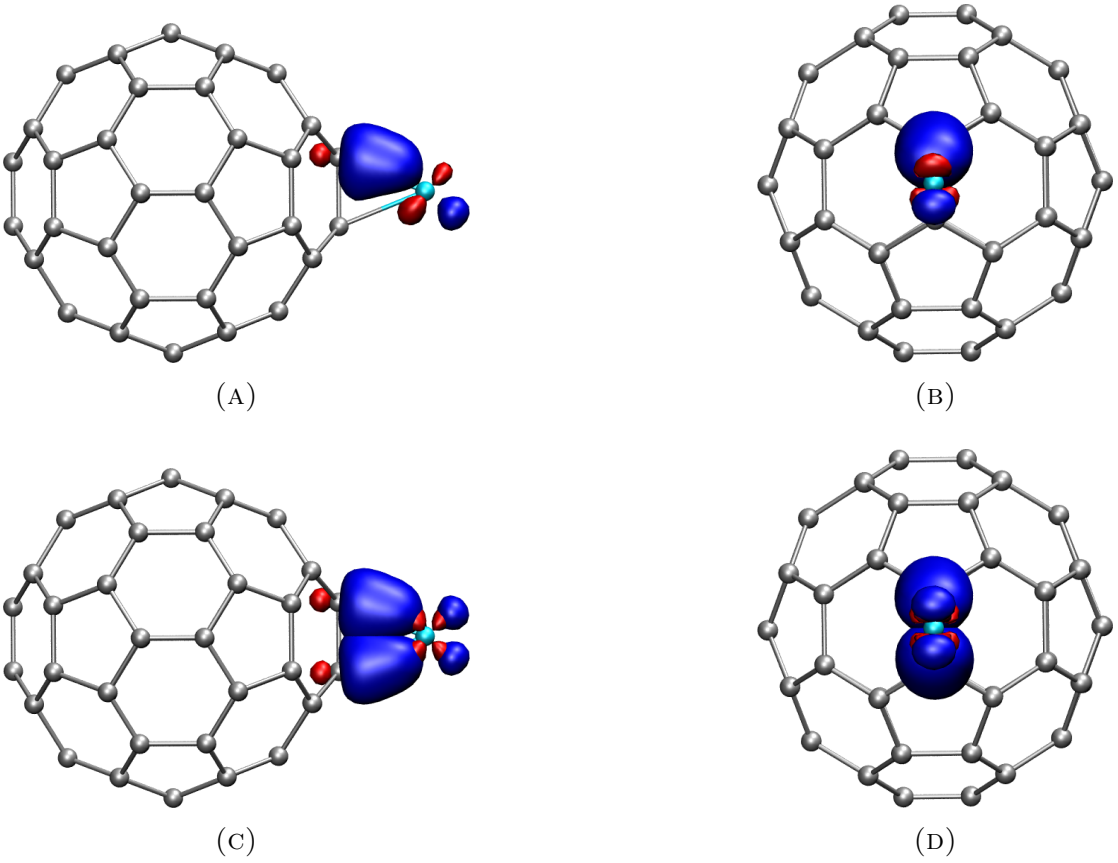

(A) (B) (C) (D)

FIGURE 3.41: Maximally localized Wannier functions for the centers involved in the Pt–C_{60} π-66 bond. Isosurfaces are shown at values of $\pm$ 0.1 $(e/\text{Å}^3)^{1/2}$ with the blue and red colors corresponding to positive and negative values, respectively.

Additionally, two WFCs with labels 7 and 24 appear to be located at nearly equal distances along the Pt–C bonds. Indeed, the distances between Pt and each one of these two WFCs amount to 1.02 Å while the distances between the C atoms forming the π-66 bond is 1.03 Å. This is a clear indication that these two WFCs account for the bonding between the metal atom and the fullerene. For this same reason, the spread associated to these WFCs is as large as 1.20 Å, and such a large dispersion accounts for the formation of stable metal-carbon bonds of the

system. A more explicit view of the Wannier functions corresponding to the WFCs 7 and 24 is shown in Figure 3.41, where the isosurface (0.1 eV/Å^3) of the localized orbitals along the Pt–C_{60} π-66 bonds extend over the whole bond length.

3.3.3 M_2-C_{60}, M= Pt, Pd systems

The introduction of a second metal into the system discloses a number of different possibilities concerning the location of the additional atom, on the simple basis of the symmetry of the system. As in the case of the initial configuration of a single metal atom, assuming the stable (a) and metastable (b) configurations of the M–C_{60} complex as a starting point, there are eight possible *a priori* scenarios. These are labeled from (a) to (h) and summarized in Figure 3.42. Moreover, an additional configuration, identified by the label (i), can be included by considering the structure (h) after reversing the position of the two metallic atoms, Pt and Pd. Static structural optimizations followed by dynamics for each one of the configurations labeled from (a) to (h) resulted in the situation summarized in Table 3.6.

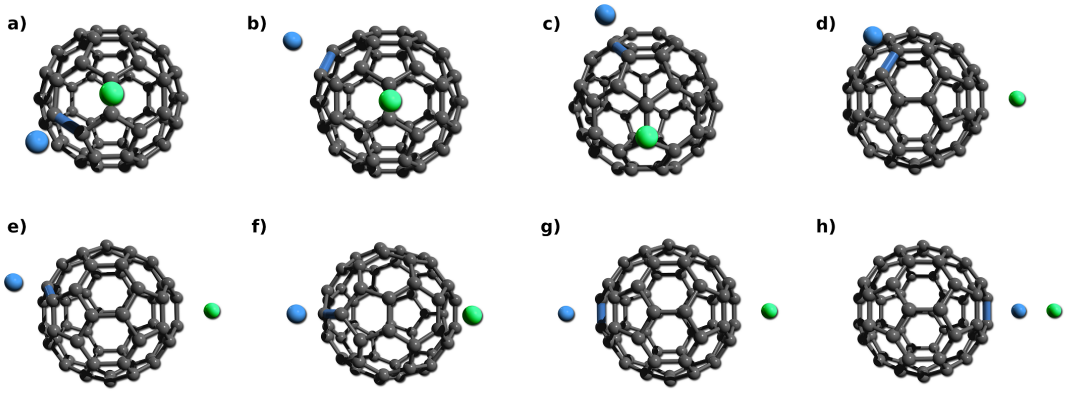

FIGURE 3.42: Schematic representation of the initial configurations for the M_2–C_{60} systems. The first metallic atom (in green) is located on the equilibrium position (on top of a π-66 bond) determined in the M–C_{60} study. Then a second metallic atom (in blue) is added on top of another π-66 bond (between two C_6 rings) highlighted in blue. Using the symmetry properties of C_{60} this leads to a maximum of 8 different initial configurations. From (a) to (g) the distance between the two M atoms increases, (h) the two M atoms are located on top of the same π bond. For $M_1 \neq M_2$ it is possible to define an additional configuration (i) where the order of the positions is inverted.

TABLE 3.6: M_2–C_{60} (M=Pt, Pd) initial and final configurations along with the total energy differences ΔE between the final configuration and the most stable configuration for each system.

	$M_1 = M_2 = Pt$		$M_1 = M_2 = Pd$		$M_1 = Pt \neq M_2 = Pd$	
Initial	Final	ΔE (eV)	Final	ΔE (eV)	Final	ΔE (eV)
a	a	0.0	a	0.0	a	0.0
b	b	0.23	b	0.20	b	0.30
c	c	0.23	c	0.19	c	0.30
d	d	0.17	d	0.18	d	0.27
e	e	0.20	e	0.18	e	0.28
f	f	0.18	f	0.17	f	0.27
g	g	0.20	g	0.18	g	0.29
h	h	0.17	h	0.81	h	0.31
					i	1.12

Namely, the most stable isomer in all cases is the one shown in Figure 3.43, in which the metal atoms, regardless of their species, are located on top of two π-66 bond (see left panel of the figure). It is noteworthy to mention that the C atoms bonded to either one of the metal atoms form a four-membered chain of adjacent neighbors along the perimeter of a pentagonal motif of the C_{60}.

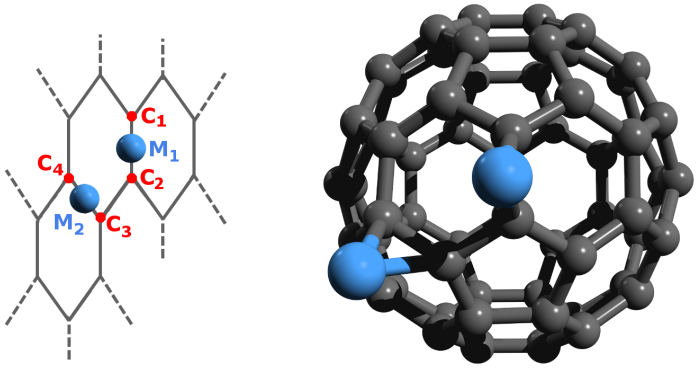

FIGURE 3.43: Schematic (left) and 3D representations (right) of the M_2–C_{60} complex for the most stable isomer (a) (see Figure 3.42).

When the two metal atoms are both Pt, all the configurations from (b) to (h) are less stable than the (a) configuration by as much as $\sim$ 0.2 eV. Interestingly, we

did not observe any attempts of the system, neither during the optimization, nor during the dynamics, to recover spontaneously the (a) structure. This is clearly due to the more selective choice we carried out when positioning the second Pt always on π-66 sites, an insight issued from the single-metal search for stable locations. Analogously, if both metal atoms are Pd, the configurations labeled from (b) to (g) are energetically above the (a) structure by ~ 0.2 eV. A noticeable difference, instead, arises when the two metallic atoms are adjacent as in the (h) configuration. In fact, because of the different nature and equilibrium relative distances of Pt with respect to Pd [297], the alignment of two Pd atoms on the same side of the fullerene becomes energetically more costly with the resulting metastable system located above the (a) configuration by 0.81 eV. This is a configuration unlikely to be accessible experimentally. Focusing on the case of two different metal atoms, the above energetical pattern is recovered. Indeed, all configurations from (b) to (h) lie above the most stable configuration (a) by about 0.3 eV. However, this time the (h) configuration is more accessible, at least if the atom closer to the fullerene is Pt. Conversely, if the order of the metal atoms is reversed, corresponding to the configuration labeled as (i) in Table 3.6, the system is located at much higher energies (1.12 eV).

Focusing on the (a) configurations, which is the ground state, the main geometrical parameters are reported in Table 3.7. Metal–carbon distances range between 2.1 and 3.8 Å.

TABLE 3.7: Final geometry for the most stable M_2–C_{60} (a) configuration. (see Figure 3.43). Distances are in Å.

	$M_1 = M_2 = Pt$		$M_1 = M_2 = Pd$		$M_1 = Pt \neq M_2 = Pd$	
	$d_{M_1\text{-}C}$	$d_{M_2\text{-}C}$	$d_{M_1\text{-}C}$	$d_{M_2\text{-}C}$	$d_{M_1\text{-}C}$	$d_{M_2\text{-}C}$
C_1	2.10	3.66	2.21	3.79	2.09	3.61
C_2	2.02	2.95	2.14	3.07	2.03	2.90
C_3	2.94	2.02	3.08	2.13	2.99	2.11
C_4	3.65	2.10	3.80	2.22	3.70	2.31
	$d_{Pt\text{-}Pt}$		$d_{Pd\text{-}Pd}$		$d_{Pt\text{-}Pd}$	
	3.01		3.25		2.91	

These relatively large variations are the result of the vicinity of the metal atoms, their mutual repulsion or attraction and the bond form with the C atoms belonging to the π-66 bonds. The last row of the table shows how the relative distance of the two metallic atoms changes according to the nature of the metals involved. Specifically, Pt atoms have a tendency to stay closer to each other (3.01 Å) than Pd atoms (3.25 Å), while two closeby different chemical species, Pt and Pd, are the best compromise to minimize the mutual repulsion and bring the two metal sites as close as 2.91 Å.

The addition of a second metal atom to the system results in a further shrinking of the energy gap with respect to both the bare fullerene [294] and the complex metal–C_{60}. The reason is the appearance of metallic states $5d^9 6s^1$ (Pt) and $d4^{10}$ (Pd) in the energy gap of the C_{60}, or more precisely, by the combination of these metallic states into d_{z^2} and $d_{x^2-y^2}$ orbitals, as sketched in Figure 3.44.

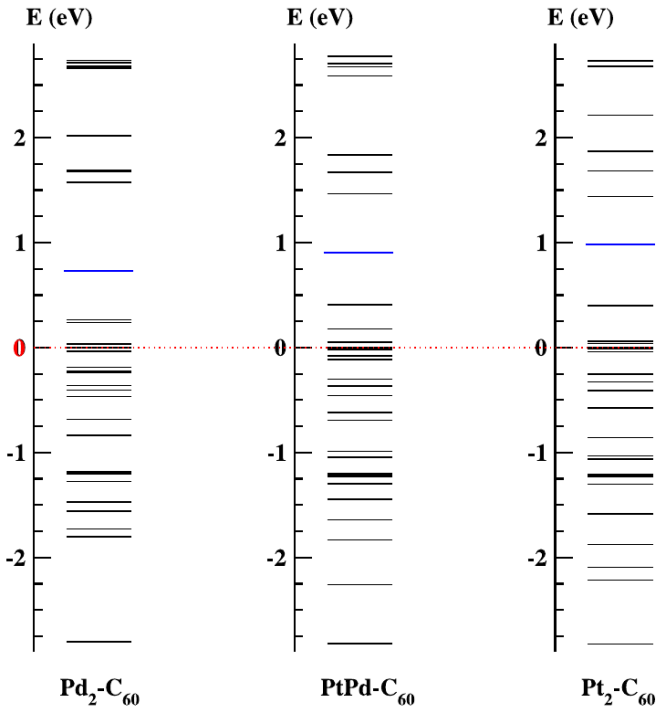

FIGURE 3.44: Band structure for the M_2–C_{60} (M= Pt, Pd) systems. Panels from left to right refer to Pd_2–C_{60}, PtPd–C_{60} and Pt_2–C_{60}, respectively.

The values of the gap of the M_2–C_{60} systems are 0.95 eV (Pd-Pd), 0.63 eV (Pt-Pd) and 0.48 eV (Pt-Pt). As in the case of single-metal systems, the HOMO states are basically d_{z^2} states centered on the metallic atoms, whereas HOMO-1 levels have

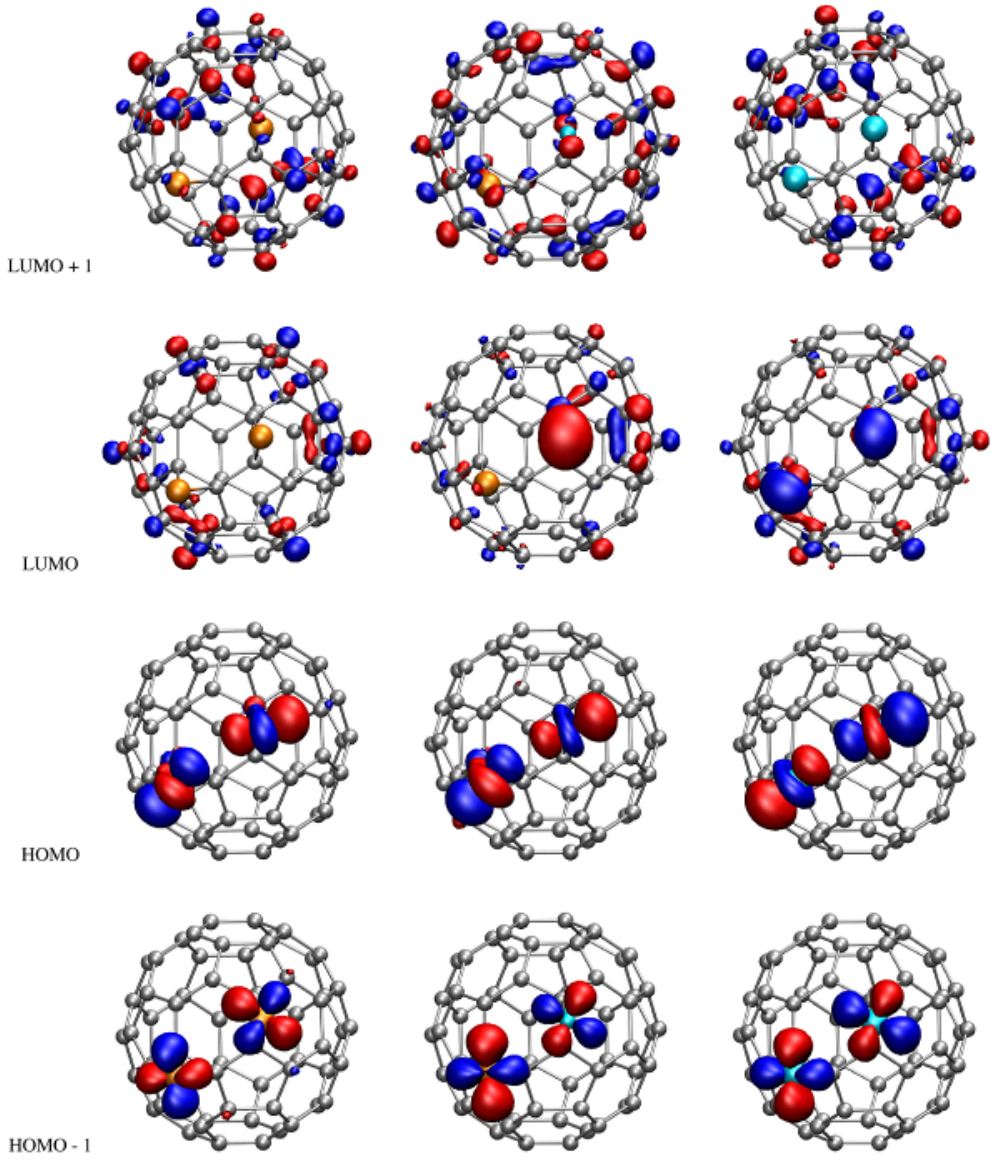

FIGURE 3.45: Wavefunctions for the eigenstates in proximity of the HOMO and LUMO levels for the most stable M_2–C_{60} (M= Pt, Pd) systems. Isosurfaces are shown at values ± 0.05 $(e/Å^3)^{1/2}$. From left to right, Pd_2-C_{60}, PtPd-C_{60}, Pt_2-C_{60}. Pd atoms are in orange and Pt atoms in cyan.

a $d_{x^2-y^2}$ character with minor amplitudes extending on the C atoms belonging to the π-66 site on which Pd and/or Pt are located; corresponding wavefunctions are shown in Figure 3.45. It can be remarked that the addition of metal atoms is a practical way to construct building blocks metal–C_{60} in which the amplitude of the gap can be tuned as a function of the metal atoms participating to the complex.

Coming to the Wannier centers representation and their associated spread, we can observe that the distribution of WFCs for both atoms resembles closely the one discussed in the case of a single metal atom. By focusing on the two doubly occupied WFCs are located roughly in the middle of the Metal–C bonds (see Figure 3.46) and characterized by a large spread typical of chemical bonds. Nonetheless, a slight difference can be remarked in the position of the two WFCs. More precisely, by focusing on the two WFCs labeled as 104 and 130 of Figure 3.46, the distances of these two centers from the closest Pt atom are 1.10 and 0.95 Å, respectively. This slight asymmetry is found also for the second Pt atom with respect to the WFCs 59 and 118. As a consequence, the associated spreads for all these four centers amounts to 1.23 Å (to be compared with the 1.20 Å found in the case of a single metal atom bound to the C_{60}). The slightly larger spread compensates the small asymmetry and ensure a stable metal–carbon bond as in the single metal case.

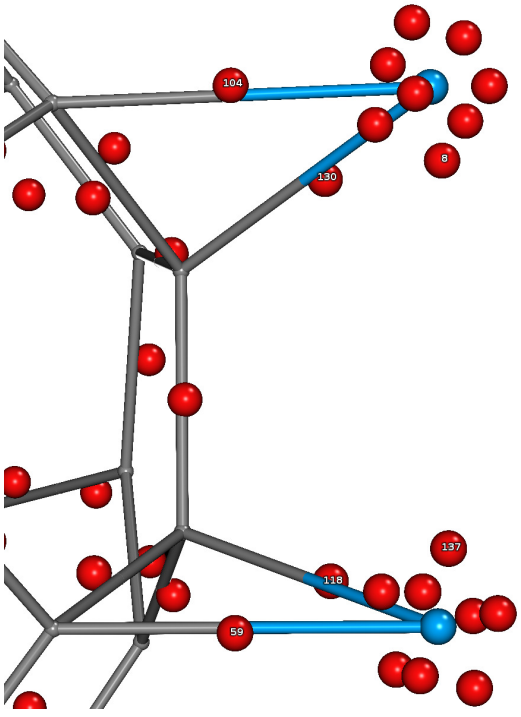

FIGURE 3.46: Positions of the main Wannier functions centers around the Pt_2–C_{60} system.

Equally interesting is the clustering effect of the metals on the fullerene [290]. In fact, by looking at the two WFCs labeled as 8 and 137, corresponding to electronic states facing each other on the two metal sites, we remark that the spread of these two states amounts to 0.97 Å, a value that is peculiar to these two specific sites.

In fact, large spreads in M–C_{60} can be found only for WFCs belonging to carbon metal bonds (see Figure 3.40 for comparison). This increased value of the spread is an indicator of the tendency of the metal atoms to clusterize on the external surface of the fullerene. Moreover, this allows to infer that the gap tuning process is a delicate issue that cannot be reduced simply to the crude algebraic addition of the results obtained on a single-metal–C_{60} complex. In fact, the approach of WFCs of nearby metal atoms is limited on the one hand by the electrostatic Coulomb repulsion and, on the other hand, by the Pauli repulsion. The subtle combination of these two interactions is responsible, from the structural point of view, for the more or less pronounced approaching of the two metals and, from the electronic point of view, for the redistribution of the electronic energy levels, hence the gap of the resulting complex.

Focusing on the use of metallo-fullerene complexes as building blocks for nanostructures prone to have applications in fuel cells, catalysis and nanoelectronics, we studied how Pt and Pd atoms can be accommodated in a stable way on the external surface of fullerenes. The atomic-scale details of the interaction between a C_{60} with one or two metallic atoms has shown that the high symmetry of the fullerene and the underlying electronic structure favor the formation of Pt and Pd adsorption sites on π-66 bonds. The additonal interaction between two metal atoms simultaneously present on the fullerene is the driving force that discriminates between stable and unstable configurations. The nature of the metal-fullerene bonds has been analyzed in detail, showing that the stability of the metal atoms on the π-66 sites is ensured by large spreads of wavefunctions that are formed as a contribution of fullerene delocalized π states and metallic d–states (and s–states for Pt). From an electronic point of view, the large gap of the fullerene is gradually filled by new electronic states due to the presence of the metals. On a wider perspective, extrapolating the present results to large composite structures, we can infer that the formation of fullerene-metal nanostructures will allow for a gap tuning of the resulting system according to the number of M_2–C_{60} building blocks and their arrangements. Equally important issues for synthesis and applications are the intimate relationships between the gap and the metal–fullerene bond lengths and the clustering effect that metallic atoms display when placed on the C_{60} external surface. This provides an important guideline for the realization of nanostructures

possessing an insulating, semiconducting or even metallic character for future nanoelectronics and nanocatalysis applications.

Chapter 4

General Conclusions

The purpose of this work is to investigate the interaction of organic and metallic complexes in the purpose of molecular electronics applications, nanocatalysis and nanoparticle synthesis by using first-principles molecular dynamics simulations within density functional theory (DFT) approach. The systems treated in this thesis poses the importance for understanding the underlying mechanism of the interacting moieties to be exploited in future applications such as single molecule electronics, full cells etc.

Three different systems have been studied in this work:

i) Interaction of single Fe and Co atoms with ferrocene molecule which is also deposited on a Cu(111) slab in the perspective of possible molecular junctions.

ii) Effects of water molecule traces on the ligand desorption process of precursor molecules, Fe and Co stearate, for functionalized Fe and Co oxide nanoparticle synthesis.

iii) Investigation of the interaction of transition metals, Pt and Pd, with buckminsterfullerene (C_{60}) molecule in the purpose of hydrogen storage and nanocatalysis applications.

Main results obtained are as follows:

Single transition metal atom deposition on ferrocene molecule deposited on Cu(111) substrate

Two distinct deposition processes are investigated in this study, differing by the chemical nature of the deposited transition metal atom. Accordingly, on top of one of the ferrocene molecules which is also deposited on a Cu(111) slab, one single Fe atom or Co atom is targeted to be deposited. Whenever standard first-principle dynamical simulations cannot follow the atom deposition processes within an affordable time scale due to relatively high free-energy barriers, Blue Moon ensemble (BME) constrained dynamics technique has been applied [147, 172].

Iron deposition follows a barrierless reaction pathway; contrary to the case of Cu deposition [69, 70], the destabilization of the ferrocene molecule occurs. The deposited Fe atom interacts with the upper Cp ring of the ferrocene and forms a stable complex. This upper Cp–ring with an iron atom attached to it then leaves the ferrocene to which it belongs at the beginning of the simulation and this newly formed Fe–C_5H_5 system becomes an independent moiety that departs from the substrate, leaving exposed the Fe atom belonging to the originally physisorbed ferrocene. In these conditions, a physisorbed Fe–C_5H_5 complex remains on the Cu(111) surface as a new and different building block for possible applications of nanocatalysis.

A second series of simulations was conducted focusing on the deposition of Co on the physisorbed ferrocene. Due to the difference in the electronic structures of Fe and Co, any attempt at depositing a Co atom on the ferrocene within the simulation protocol adopted for the Fe atom did not result in the formation of any Co–ferrocene complex, neither destabilization processes could be observed. The activation barrier was estimated and the possible reaction pathway was investigated using free energy sampling technique known as Blue Moon ensemble [147]. It has been found out that the approach of Co towards the ferrocene requires to overcome an energy barrier of 21.17 kcal/mol (0.92 eV). Beyond this distance, the Co atom starts to interact with the Cp ring and at variance with the former case, here the interaction after the overcoming of the barrier is rather strong and the Co atom inserts into the Cp ring as the sixth member. This new structure is stable in simulations with the temperature controls are removed. This newly

formed ferrocene-like double–decker structure desorbs from the Cu(111) substrate as a whole and eventually leaves the surface on longer simulation times. This can be exploited to extract ferrocene units selectively from a deposited monolayer to create motifs and patterns.

Precursor molecules for the synthesis of Fe and Co oxide nanoparticles and related dissociation processes

Physical and chemical properties of NPs strongly depend on tuning their size and morphology, and in turn the nature and intimate chemistry of the precursor molecules used as elementary building blocks for the synthesis. In order to understand the effects of coordinated water molecules around the metal center of precursor molecules, three different systems have been studied for both Fe- and Co-stearates in the presence of one or two water molecules or in their absence. Blue Moon sampling technique has been utilised to reconstruct the free energy profile.

In the absence of water molecules, it has been discovered that the desorption of Co-based precursor is following a reaction that has a higher activation barrier compared to its Fe counterpart. Besides, the desorption of the Fe-stearate produces a FeO building block that constitutes the seed for nucleation and growth processes; for Co-based system, on the other hand, the coordination of the hydrocarbon chain and the metal center remains intact, rendering the unscreening of the metal center impossible. These fundamental findings explain the variations in the morphology and size of the resulting iron and cobalt oxide nanoparticles obtained by means of experimental efforts.

In the presence of one water molecules, both systems converges to dry conditions since the single water molecule leaves the vicinity of the metal, provided that the preferred coordination of Fe and Co is either 4- or 6-fold. The interaction of the water trace with the Fe center causes a significant increase in the activation barrier. The water-Co coordination, on the other hand, is much more susceptible to the modifications in the Co-COO coordination, therefore its effect on the Co-based system is negligible.

Lastly, the existence of two water molecules coordinated around the metal induces considerable differences. According to our simulations, water traces reduce the activation barrier for the corresponding reactions, however, more importantly they prevent the unscreening of the metal center by forming two Zundel-like complexes at either sides. Besides, it has been also found that alterations in the thermodynamic environment has important consequences. The exergonic nature of the Co-based system can be manipulated by controlling the temperature during the desorption process.

Exohedral M–C_{60} and M_2–C_{60} (M = Pt, Pd) systems

In the context of M-C_{60} (M= Pt, Pd) complexes, a first set of simulations was performed on systems containing $N = 61$ atoms: 60 C, and 1 metal atom, either Pt or Pd. For both metal atoms, the most stable configurations are found to be the ones where the metal atom stands on top of a C–C bond between either two hexagons (π-66) or an hexagon and a pentagon (σ-65). Even though the σ-65 configuration is less stable than the π-66 is confirmed by subsequent runs and by observing the mean square displacement of the metal atoms exceeding 3.0 Å^2/s, this configuration is kept as an alternative equilibrium site for the metal–fullerene complex. The band gap of pristine C_{60} (1.66 eV) reduces to 1.24 eV for Pt and 1.12 eV for Pd with a metal atom on a π-66 site. Besides, it was found out that the bond length of M–C increases with the decreasing of the band gap. The maximally localized Wannier function centers (WFCs) have been used to gain insight into the nature of the chemical bonds. Existence of WFCs in the M–C bonds with associated spreads as large as 1.20 Å accounts for the formation of stable metal-carbon bonds of the system.

In the case of two metal atom in the system, eight different configurations have been prepared assuming the stable (π-66) and metastable (σ-65) configurations of the M–C_{60} complex as a starting point. The most stable isomer in all cases is found to be the ones where both metal atoms are located on top of π-66 bonds. In the case of both two Pt or Pd atoms, the remaining configurations are located above this ground state by as much as ~ 0.2 eV. The addition of a second metal atom to the system results in a further shrinking of the energy gap with respect to both

the bare fullerene and the metal–C_{60} complex previously studied. The band gap of the M_2–C_{60} systems are 0.95 eV (Pd-Pd), 0.63 eV (Pt-Pd) and 0.48 eV (Pt-Pt). Moreover, the investigation of WFCs for M_2–C_{60} systems allows one to infer that the gap tuning process is a delicate issue that cannot be reduced simply to the crude algebraic addition of the results obtained on a single-metal–C_{60} complex.

Appendix A

A.1 Average constraint force and free energy profile

Ipython is an interactive, browser-based Python shell that introduces various capabilities to the Python programming language. Mathematical operations such as data analysis, visualisation, scientific computing in general is easily performed by importing number of existing libraries such as NumPy, SciPy or Pandas. Below is an example of calculating the free energy profile along a reaction coordinate performed in Jupyter Notebook (which was called IPython Notebook until 2014) in NumPy environment which is a convenient tool for scientific computing so far as the manipulation of an N-dimensional array is in question.

CONSTRAINT

September 10, 2016

This program calculates the free energy along a reaction coordinate from the average constraint force.

```
In [1]: import numpy as np
        from numpy import *
        import math
        import matplotlib.pyplot as plt
        %matplotlib inline
```

Load the file.

```
In [2]: data = np.loadtxt("test/CONSTRAINT")
```

Extract the columns.

```
In [3]: md_step = data[:, [0]]
        id = data[:, [1]]
        Lambda = data[:, [2]]
        constr = data[:, [3]]
```

Constants and parameters.

```
In [4]: au2ps = 2.41888425 * 10**-5 #atomic units to picoseconds.
        dt = 4 #timestep in a.u.
```

Calculate the moving average of the Lagrange multiplier (`Lambda`). (See Eq. 2.116.)

```
In [5]: sum_l = np.cumsum(Lambda)
        sum_c = np.cumsum(constr)
```

```
In [6]: Lambda_av = np.divide (sum_l, np.arange(1, len(data)+1))
        constr_av = np.divide (sum_c, np.arange(1, len(data)+1))
```

Modify the necessary data, save the file and plot. (see also Figure 3.21)

```
In [7]: data[:,0] = au2ps * dt * (data[:,0]-1)
        data[:,2] = Lambda_av
        data[:,3] = constr_av
```

```
In [8]: np.savetxt('constrav_py.txt', (data), delimiter='   ')
```

```
In [9]: np.savetxt('xlagin_py.txt', Lambda_av[-1].reshape(1,))
```

```
In [10]: xxlag = np.loadtxt('test/xlag-edit.in')
```

```
In [11]: plt.plot(xxlag[:,0]*0.529177 ,xxlag[:,1],'o-')
```

Out[11]: [<matplotlib.lines.Line2D at 0x5c4136b588>]

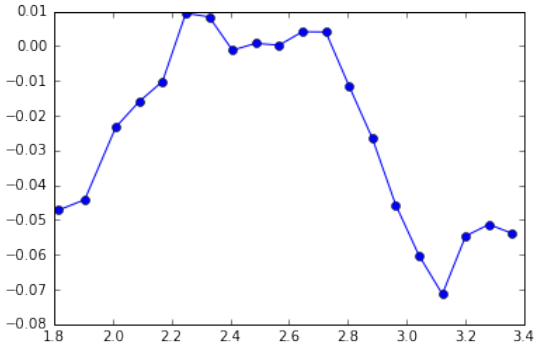

In [12]:
```
eV=27.211607
cal=23.0605
au2Angs = 0.529177
```

Integrate along the reaction coordinate and plot.

In [13]:
```
free_tot = np.empty((20, 0))

for i in range(len(xxlag)):
    free_i = -np.trapz(xxlag[:i+1,1],xxlag[:i+1,0])*eV*cal
    free_tot = np.append(free_tot, free_i)
```

In [14]:
```
z = np.c_[xxlag[:,0]*au2Angs,free_tot]
```

In [15]:
```
np.savetxt('free-py.txt', z, delimiter='   ')
```

In [16]:
```
plt.plot(xxlag[:,0]*au2Angs, free_tot, 'ro-')
```

Out[16]: [<matplotlib.lines.Line2D at 0x5c41bd0a90>]

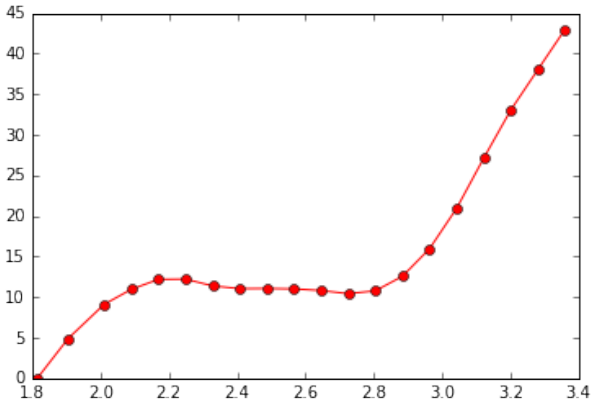

Bibliography

[1] G. E. Moore. Progress in digital integrated electronics. In *Electron Devices Meeting, 1975 International*, volume 21, pages 11–13. IEEE, 1975.

[2] M. C. Petty. Scope of Molecular Electronics. In *Molecular Electronics: From Principles to Practice*, page 7. John Wiley & Sons, Ltd, 2007.

[3] H. B. Akkerman, P. W. M. Blom, D. M. de Leeuw, and B. de Boer. Towards molecular electronics with large-area molecular junctions. *Nature*, 441:69, 2006.

[4] V. Axelrad and M. C. Smayling. 16nm with 193nm Immersion Lithography and Double Exposure. *Proceedings of SPIE*, 7641:764109, 2010.

[5] B. A. Mantooth and P. Weiss. Fabrication, assembly, and characterization of molecular electronic components. *Proceedings of the IEEE*, 91:1785, 2003.

[6] P. S. Peercy. The drive to miniaturization. *Nature*, 406:1023, 2000.

[7] J. Li, H. Morkoç, and A. Neogi. Self-Assembled Guanosine-Based Nanoscale Molecular Photonic Devices. In Zhiming M. Wang and Arup Neogi, editors, *Nanoscale Photonics and Optoelectronics*, chapter 5, pages 77–99. Springer New York, 2010.

[8] A. I. Kingon, J. P. Maria, and S. K. Streiffer. Alternative dielectrics to silicon dioxide for memory and logic devices. *Nature*, 406:1032, 2000.

[9] H. Kuhn. On possible ways of assembling simple organized systems of molecules. In A. Rich, N. Davidson, and L. Pauling, editors, *Structural Chemistry and Molecular Biology*, pages 566–571. Freeman, San Francisco, 1968.

[10] B. Mann and H. Kuhn. Tunneling through Fatty Acid Salt Monolayers. *J. Appl. Phys.*, 42:4398, 1971.

[11] A. Aviram and M. A. Ratner. Molecular rectifiers. *Chemical Physics Letters*, 29:277, 1974.

[12] J. Chen, T. Lee, J. Su, W. Wang, and M. A. Reed et al. Molecular Electronic Devices. In M. A. Reed and T. Lee, editors, *Molecular Nanoelectronics*, chapter M, pages 1–76. American Scientific Publishers, 2003.

[13] G. J. Ashwell, J. R. Sambles, A. S. Martin, W. G. Parker, and M. Szablewski. Rectifying characteristics of Mg—(C16H33-Q3CNQ LB film)—Pt structures. *J. Chem. Soc., Chem. Commun.*, page 1374, 1990.

[14] R. Gómez, C. Seoane, and J. L. Segura. The first two decades of a versatile electron acceptor building block: 11,11,12,12-tetracyano-9,10-anthraquinodimethane (TCAQ). *Chem. Soc. Rev.*, 36:1305, 2007.

[15] R. L. Carroll and C. B. Gorman. The Genesis of Molecular Electronics. *Angew. Chem. Int. Ed.*, 41:4378, 2002.

[16] L. Sun, Y. A. Diaz-Fernandez, T. A. Gschneidtner, Fr. Westerlund, S. Lara-Avila, and K. Moth-Poulsen. Single-molecule electronics: from chemical design to functional devices. *Chem. Soc. Rev.*, 43:7378, 2014.

[17] R. M. Metzger and C. A. Panetta. Toward Organic Rectifiers. In F. Carter, editor, *Molecular Electronic Devices Vol II*, page 8. Marcel Dekker, New York and Basel, 1987.

[18] R. Metzger. D-sigma-A unimolecular rectifiers. *Mater. Sci. Eng.*, C3:277, 1995.

[19] E. Torres, C. A. Panetta, and R. M. Metzger. Preparation of 2-(Hydroxymethyl)- 11,11,12,12-tetracyanoanthra- quinodimethane and Its Carbamates with Electron-Donor Moieties. *J. Org. Chem.*, 52:2944, 1987.

[20] A. Aviram, C. Joachim, and M. Pomerantz. Evidence of switching and rectification by a single molecule effected with a scanning tunneling microscope. *Chem. Phys. Lett*, 146:490, 1988.

[21] A. Aviram, C. Joachim, and M. Pomerantz. Evidence of switching and rectification by a single molecule effected with a scanning tunneling microscope. *Chem. Phys. Lett*, 162:416, 1989.

[22] Y. Zhang, X. Cai, D. Qi, Y. Bian, and J. Jiang. Charge Transfer Properties of Bis(phthalocyaninato) Rare Earth (III) Complexes: Intrinsic Ambipolar Semiconductor for Field Effect Transistors. *J. Phys. Chem. C*, 112:14579, 2008.

[23] G. Guillaud, M. Al Sadoun, M. Maitrot, J. Simon, and M. Bouvet. Field-effect transistors based on intrinsic molecular semiconductors. *Chem. Phys. Lett.*, 167:503, 1990.

[24] M. Pomerantz, A. Aviram, R. A. McCorkle, L. Li, and A. G. Schrott. Rectification of STM Current to Graphite Covered with Phthalocyanine Molecules. *Science*, 255:1115, 1992.

[25] L. A. Bumm, J. J. Arnold, M. T. Cygan, T. D. Dunbar, and T. P. Burgin et al. Are Single Molecular Wires Conducting? *Science*, 271:1705, 1996.

[26] M. A. Rampi and G. M. Whitesides. A versatile experimental approach for understanding electron transport through organic materials. *Chem. Phys.*, 281:373, 2002.

[27] D. J. Schiffrin, W. Haiss, and R. J. Nichols. Electronic Switches. In J. A. Schwarz, C. I. Contescu, and K. Putyera, editors, *Dekker Encyclopedia of Nanoscience and Nanotechnology Vol II*, page 1101. Taylor & Francis, 2004.

[28] F. Eberle, M. Saitner, H. Boyen, J. Kucera, and A. Gross et al. A molecular double decker: Extending the limits of current metal-molecule hybrid structures. *Angew. Chem. Int. Ed.*, 49:341, 2010.

[29] N. Ishikawa, M. Sugita, T. Ishikawa, S. Koshihara, and Y. Kaizu. Lanthanide Double-Decker Complexes Functioning as Magnets at the Single-Molecular Level. *J. Am. Chem. Soc.*, 125:8694, 2003.

[30] X.-Y. Zhu. Electronic structure and electron dynamics at molecule-metal interfaces: Implications for molecule-based electronics. *Surface Science Reports*, 56:1–83, 2004.

[31] Y. Zhang, X. Cai, Y. Bian, and J. Jiang. Organic semiconductors of phthalocyanine compounds for field effect transistors (FETs). In J. Jiang, editor, *Functional Phthalocyanine Molecular Materials*, volume 135, page 275. Springer-Verlag, 2010.

[32] Y. Kitagawa, T. Kawakami, S. Yamanaka, and M. Okumura. DFT and DFT-D studies on molecular structure of double-decker phthalocyaninato-terbium(III) complex. *Mol. Phys.*, 112:995, 2014.

[33] R. Temirov, S. Soubatch, A. Luican, and F. S. Tautz. Free-electron-like dispersion in an organic monolayer film on a metal substrate. *Nature*, 444:350, 2006.

[34] M. Gruenewald, C. Sauer, J. Peuker, M. Meissner, and F. Sojka et al. Commensurism at electronically weakly interacting phthalocyanine/PTCDA heterointerfaces. *Phys. Rev. B*, 91:155432, 2015.

[35] B. Stadtmüller, M. Willenbockel, S. Schröder, C. Kleimann, and E. M. Reinisch et al. Modification of the PTCDA-Ag bond by forming a heteromolecular bilayer film. *Phys. Rev. B*, 91:155433, 2015.

[36] B. Stadtmüller, T. Sueyoshi, G. Kichin, I. Kröger, and S. Soubatch et al. Commensurate registry and chemisorption at a hetero-organic interface. *Phys. Rev. Lett.*, 108:106103, 2012.

[37] B. W. Caplins, D. E. Suich, A. J. Shearer, and C. B. Harris. Metal/phthalocyanine hybrid interface states on Ag(111). *J. Phys. Chem. Lett.*, 5:1679, 2014.

[38] C. H. Schwalb, S. Sachs, M. Marks, A. Schöll, and F. Reinert et al. Electron Lifetime in a Shockley-Type Metal-Organic Interface State. *Phys. Rev. Lett.*, 101:146801, 2008.

[39] S. Heutz, A. F. Nogueira, J. R. Durrant, and T. S. Jones. Charge recombination in CuPc/PTCDA thin films. *J. Phys. Chem. B*, 109:11693, 2005.

[40] T. Zhang, L. Zhu, Z. Tian, and J. Wang. Structural , Electronic , and Magnetic Properties of Neutral and Charged Transition Metal-Bis(dicarbollide) Sandwich Clusters. *J. Phys. Chem. C*, 115:14542, 2011.

[41] G. Wilkinson, M. Rosenblum, M. C. Whiting, and R. B. Woodward. The Structure of Iron Bis-Cyclopentadienyl. *J. Am. Chem. Soc.*, 74:2125, 1952.

[42] E. O. Fischer and R. Jira. How metallocene chemistry and research began in Munich. *J. Org. Chem.*, 637:7, 2001.

[43] C. Engtrakul and L. R. Sita. Ferrocene-Based Nanoelectronics: 2,5-Diethynylpyridine as a Reversible Switching Element. *Nano Lett.*, 1:541, 2001.

[44] Q. Li, G. Mathur, M. Homsi, S. Surthi, and V. Misra et al. Capacitance and conductance characterization of ferrocene-containing self-assembled monolayers on silicon surfaces for memory applications. *Appl. Phys. Lett.*, 81:1494, 2002.

[45] Z. Liu, A. A. Yasseri, J. S. Lindsey, and D. F. Bocian. Molecular Memories That Survive Silicon Device Processing and Real-World Operation. *Science*, 302:1543, 2003.

[46] P. Zhu, X. Zhang, H. Wang, Y. Zhang, Y. Bian, and J. Jiang. Ferrocene-decorated (phthalocyaninato)(porphyrinato) double- and triple-decker rare earth complexes: Synthesis, structure, and electrochemical properties. *Inorg. Chem.*, 51:5651, 2012.

[47] Y. Matsuo, K. Tahara, and E. Nakamura. Synthesis and electrochemistry of double-decker buckyferrocenes. *J. Am. Chem. Soc.*, 128:7154, 2006.

[48] R. Marczak, M. Wielopolski, S. S. Gayathri, D. M. Guldi, and Y. Matsuo et al. Uniquely Shaped Double-Decker Buckyferrocenes-Distinct Electron Donor-Acceptor Interactions. *J. Am. Chem. Soc.*, 130:16207, 2008.

[49] A. Calborean, L. Buimaga-Iarinca, and F. Graur. DFT charge transfer of hybrid molecular ferrocene/Si structures. *Phys. Scr.*, 90:055803, 2015.

[50] R. Zanoni, M. N. Piancastelli, M. Marsi, and G. Margaritondo. Organometallic adsorption on semiconductors: a synchrotron radiation photoemission study of ferrocene and nickelocene on silicon(111)2×1. *J. Electron Spectrosc. Relat. Phenom.*, 57:199, 1991.

[51] G. A. Nemnes and A. Nicolaev. Transport in ferrocene single molecules for terahertz applications. *Phys. Chem. Chem. Phys.*, 16:18478, 2014.

[52] A. Iordache, M. Oltean, A. Milet, F. Thomas, and B. Baptiste et al. Redox control of rotary motions in ferrocene-based elemental ball bearings. *J. Am. Chem. Soc.*, 134:2653, 2012.

[53] M. Sato, K. Fukui, M. Sakamoto, S. Kashiwagi, and M. Hiroi. Charge transfer between two ferrocene groups linked by oligothiophene. *Thin Solid Films*, 393:210, 2001.

[54] Y. Lu, Y. Jiang, H. Wu, and W. Chen. Ferrocene-Functionalized Graphene Oxide Nanosheets: Efficient Electronic Communication between Ferrocene Centers across Graphene Nanosheets. *Electrochimica Acta*, 156:267, 2015.

[55] P. A. Dowben. Determining the Bonding Orientation of Molecular Adsorbates on Metal Surfaces by Angle-Resolved Photoemission Molecular adsorbates I Symmetry and selection rules I Molecularorbitals. *Zeitschrift für Physikalische Chemie*, 202:227, 1997.

[56] D. Welipitiya, P. A. Dowben, J. Zhang, W. W. Pai, and J. F. Wendelken. The adsorption and desorption of ferrocene on Ag(100). *Surface Science*, 367:20, 1996.

[57] D. Welipitiya, A. Green, J. P. Woods, P. A. Dowben, and B. W. Robertson et al. Ultraviolet and electron radiation induced fragmentation of adsorbed ferrocene. *J. Appl. Phys.*, 79:8730, 1996.

[58] C. Waldfried, D. Welipitiya, C. W. Hutchings, H. S. V. de Silva, and G. A. Gallup et al. Preferential Bonding Orientations of Ferrocene on Surfaces. *J. Phys. Chem. B*, 101:9782, 1997.

[59] F. Thibaudau, T. P. Roge, J. R. Roche, Ph. Mathiez, Ph. Dumas, and F. Salvan. A STM study on compared chemical reactivities of different Si(111) surfaces: copper growth and ferrocene adsorption. *Microsc. Microanal. Microstruct.*, 4:419, 1993.

[60] P. A. Dowben, C. Waldfried, T. Komesu, D. Welipitiya, T. McAvoy, and E. Vescovo. The occupied and unoccupied electronic structure of adsorbed ferrocene. *Chem. Phys. Lett*, 283:44, 1998.

[61] P.J. Durston and R.E. Palmer. Adsorption and decomposition of ferrocene on graphite studied by HREELS and STM. *Surface Science*, 400:277, 1998.

[62] K. Svensson, T. R. Bedson, and R. E. Palmer. Dissociation and desorption of ferrocene on graphite by low energy electron impact. *Surface Science*, 451:250, 2000.

[63] K. J. Cluff, M. Schnellbach, C. R. Hilliard, and J. Blümel. The adsorption of chromocene and ferrocene on silica: A solid-state NMR study. *J. Organomet. Chem.*, 744:119, 2013.

[64] R. A. W. Dryfe, E. C. Walter, and R. M. Penner. Electrodeposition of metal nanostructures by galvanic displacement powered with insoluble crystals of a ferrocene derivative. *ChemPhysChem*, 5:1879, 2004.

[65] T. Pradeep, D. E. Riederer, T. Ast, and R. G. Cooks. Reactions of low-energy ions with ferrocene self-assembled monolayer surfaces. *Rapid Commun. Mass Spectrom*, 7:711, 1993.

[66] K. F. Braun, V. Iancu, N. Pertaya, K. H. Rieder, and S. W. Hla. Decompositional incommensurate growth of ferrocene molecules on a Au(111) surface. *Phys. Rev. Lett*, 96:246102, 2006.

[67] Ra. Paul, R. G. Reifenberger, T. S. Fisher, and D. Y. Zemlyanov. Atomic Layer Deposition of FeO on Pt(111) by Ferrocene Adsorption and Oxidation. *Chem. Mater.*, 27:5915, 2015.

[68] I. M. Rivera and C. R. Cabrera. Mass Measurements of Ferrocene Adsorption at Gold Films with the Electrochemical Quartz Crystal Microbalance. *J. Electrochem. Soc.*, 140:L36, 1993.

[69] D. Mbongo Djimbi, S. Le Roux, C. Massobrio, and M. Boero. Metal-organic molecule-metal nano-junctions: a close contact between first-principles simulations and experiments. *J. Phys.: Condens. Matter*, 26:104206, 2014.

[70] B. W. Heinrich, L. Limot, M. V. Rastei, C. Iacovita, and J. P. Bucher et al. Dispersion and localization of electronic states at a ferrocene/Cu(111) interface. *Phys. Rev. Lett.*, 107:216801, 2011.

[71] E. Paquet and H. L. Viktor. Molecular dynamics, monte carlo simulations, and langevin dynamics: A computational review. *BioMed Research International*, 2015(ID:183918), 2015.

[72] W. W. Wood and J. J. Erpenbeck. Molecular dynamics and Monte Carlo calculations in statistical mechanics. *Ann. Rev. Phys. Chem.*, 27:319, 1976.

[73] B. J. Alder and T. E. Wainright. Phase Transition for a Hard Sphere System. *J. Chem. Phys.*, 27:1208, 1957.

[74] A. Rahman. Correlations in the motion of atoms in liquid argon. *Phys. Rev*, 136:A405, 1964.

[75] Godehard Sutmann. Classical Molecular Dynamics. In J. Grotendorst, D. Marx, and A. Muramatsu, editors, *Quantum Simulations of Complex Many-Body Systems: From Theory to Algorithms*, volume 10, pages 211–254. John von Neumann Institute for Computing, Jülich, 2002.

[76] R. Car and M. Parrinello. Unified Approach for Molecular Dynamics and Density-Functional Theory. *Phys. Rev. Lett*, 55:2471, 1985.

[77] L. Verlet. Computer "experiments" on Classical Fluids. I. Thermodynamical properties of Lennard-Jones molecules. *Phys. Rev*, 159:98, 1967.

[78] L. Verlet. Computer "experiments" on Classical Fluids. II. Equilibrium correlation functions. *Phys. Rev*, 165:201, 1968.

[79] G. L. Hornyak, H. F. Tibbals, J. Dutta, and J. J. Moore. Introduction to Nanoscience and Nanotechnology. page 1059. CRC Press, 2008.

[80] C. W. Gear. *Numerical Initial Value Problems in Ordinary Differential Equations*. Prentice Hall, NJ, USA, first edition, 1971.

[81] V. Swamy and J. D. Gale. Transferable variable-charge interatomic potential for atomistic simulation of titanium oxides. *Phys. Rev. B*, 62:5406, 2000.

[82] J. Meller. Molecular Dynamics. *Encyclopedia of Life Sciences*, pages 1–8, 2001.

[83] S. Nosé. A unified formulation of the constant temperature molecular dynamics methods. *J. Chem. Phys.*, 81:511, 1984.

[84] S. Nosé. A molecular dynamics method for simulations in the canonical ensemble. *Mol. Phys.*, 52:255, 1984.

[85] W. G. Hoover. Canonical dynamics: Equilibrium phase-space distributions. *Phys. Rev. A*, 31:1695, mar 1985.

[86] K. Zare and V. Szebehely. Time transformations in the extended phase-space. *Celestial Mechanics*, 11:469, 1975.

[87] D. J. Evans and B. L. Holian. The Nose–Hoover thermostat. *J. Chem. Phys.*, 83:4069, 1985.

[88] Chr. Møller and M. S. Plesset. Note on an approximation treatment for many-electron systems. *Phys. Rev.*, 46:618, 1934.

[89] D. R. Hartree. The wave mechanics of an atom with a non-Coulomb central field. Part I. Theory and methods. In *Mathematical Proceedings of the Cambridge Philosophical Society*, volume 24, pages 89–110. Cambridge Univ Press, 1928.

[90] V. Fock. Näherungsmethode zur Lösung des quantenmechanischen Mehrkörperproblems. *Z. Phys.*, 61:126, 1930.

[91] J. C. Slater. A simplification of the Hartree-Fock method. *Phys. Rev*, 81:385, 1951.

[92] L. H. Thomas. The calculation of atomic fields. In *Mathematical Proceedings of the Cambridge Philosophical Society*, volume 23, pages 542–548. Cambridge Univ Press, 1927.

[93] E. Fermi. Un metodo statistico per la determinazione di alcune priorieta dell'atome. *Rend. Accad. Naz. Lincei*, 6:602, 1927.

[94] P. Hohenberg and W. Kohn. Inhomogeneous Electron Gas. *Phys. Rev*, 136:B864, 1964.

[95] M. Levy. Universal variational functionals of electron densities, first-order density matrices, and natural spin-orbitals and solution of the v-representability problem. *Proc. Natl. Acad. Sci. USA*, 76:6062, 1979.

[96] M. Levy. Electron densities in search of Hamiltonians. *Phys. Rev. A*, 26:1200, 1982.

[97] E. H. Lieb, A. Shimony, and H. Feshbach. *Physics as natural philosophy: essays in honor of Laszlo Tisza on his 75th birthday.* MIT, Cambridge, 1982.

[98] E. H. Lieb. Density functionals for coulomb systems. *Int. J. Quantum Chem.*, 24:243, 1983.

[99] W. Kohn and L. J. Sham. Self-consistent equations including exchange and correlation effects. *Phys. Rev*, 140:A1133, 1965.

[100] J. P. Perdew and K. Schmidt. Jacob's ladder of density functional approximations for the exchange-correlation energy. *AIP Conf. Proc.*, 577:1–20, 2001.

[101] F. Bloch. Bemerkung zur Elektronentheorie des Ferromagnetismus und der elektrischen Leitfähigkeit. *Z. Phys.*, 57:545, 1929.

[102] P. A. M. Dirac. Note on exchange phenomena in the Thomas atom. In *Mathematical Proceedings of the Cambridge Philosophical Society*, volume 26, page 376. Cambridge University Press, 1930.

[103] D. M. Ceperley and B. J. Alder. Ground state of the electron gas by a stochastic method. *Phys. Rev. Lett.*, 45:566, 1980.

[104] D. Ceperley. Ground state of the fermion one-component plasma: A Monte Carlo study in two and three dimensions. *Phys. Rev. B*, 18:3126, 1978.

[105] J. P. Perdew and A. Zunger. Self-interaction correction to density-functional approximations for many-electron systems. *Phys. Rev. B*, 23:5048, 1981.

[106] V. P. Gupta. *Principles and Applications of Quantum Chemistry.* Academic Press, 2015.

[107] J. P. Perdew, K. Burke, and M. Ernzerhof. Generalized Gradient Approximation Made Simple. *Phys. Rev. Lett*, 77:3865, oct 1996.

[108] A. D. Becke. Density-functional exchange-energy approximation with correct asymptotic behavior. *Phys. Rev. A*, 38:3098, 1988.

[109] C. Lee, W. Yang, and R. G. Parr. Development of the Colle-Salvetti correlation-energy formula into a functional of the electron density. *Phys. Rev. B*, 37:785, 1988.

[110] N. W. Ashcroft and N. D. Mermin. Solid State Physics. chapter 8, page 132. Saunders College, Philadelphia, 1976.

[111] P. Pulay. Ab initio calculation of force constants and equilibrium geometries in polyatomic molecules: I. Theory. *Mol. Phys*, 17:197, 1969.

[112] J. C. Phillips. Energy-Band Interpolaton Scheme Based on a Pseudopotential. *Phys. Rev*, 112:685, 1958.

[113] E. Fermi. Sopra lo Spostamento per Pressione delle Righe Elevate delle Serie Spettrali. *Il Nuovo Cimento*, 11:157, 1934.

[114] J. C. Phillips and L. Kleinman. New method for calculating wave functions in crystals and molecules. *Phys. Rev*, 116:287, 1959.

[115] C. L. Reis, J. M. Pacheco, and J. L. Martins. First-principles norm-conserving pseudopotential with explicit incorporation of semicore states. *Phys. Rev. B*, 68:155111, 2003.

[116] D. Hamann, M. Schlüter, and C. Chiang. Norm-Conserving Pseudopotentials. *Phys. Rev. Lett.*, 43:1494, 1979.

[117] G. B. Bachelet, D. R. Hamann, and M. Schluter. Pseudopotentials that work: From H to Pu. *Phys. Rev. A*, 26:4199, 1982.

[118] N. Troullier and J. L. Martins. Efficient Pseudopotentials for Plane-Wave Calculations. 43:1993, 1991.

[119] D. Vanderbilt. Soft self-consistent pseudopotentials in a generalized eigenvalue formalism. *Phys. Rev. B*, 41:7892, 1990.

[120] A. Redondo, W. A. Goddard, and T. C. Mcgill. Ab initio effective potentials for silicon. *Phys. Rev. B*, 15:5038, 1977.

[121] J. S. Lin, A. Qteish, M. C. Payne, and V. Heine. Optimized and transferable nonlocal separable ab initio pseudopotentials. *Phys. Rev. B*, 47:4174, 1993.

[122] A. M. Rappe, K. M. Rabe, E. Kaxiras, and J. D. Joannopoulos. Optimized pseudopotentials. *Phys. Rev. B*, 41:1227, 1990.

[123] L. Kleinman and D. M. Bylander. Efficacious Form for Model Pseudopotentials. *Phys. Rev. Lett*, 48:1425, 1982.

[124] S. Zhang, S.-H. Wei, and A. Zunger. Intrinsic n-type versus p-type doping asymmetry and the defect physics of ZnO. *Phys. Rev. B*, 63:075205, 2001.

[125] H. R. Philipp and H. Ehrenreich. Optical Properties of Semiconductors. *Phys. Rev*, 129:1550, 1963.

[126] S. G. Louie, S. Froyen, and M. L. Cohen. Nonlinear ionic pseudopotentials in spin-density-functional calculations. *Phys. Rev. B*, 26:1738, 1982.

[127] G. P. Srivastava. Theoretical modelling of semiconductor surfaces: microscopic studies of electrons and phonons. chapter 3.4, page 57. World Scientific, 1999.

[128] P. Güttinger. Das Verhalten von Atomen im magnetischen Drehfeld. *Z. Phys.*, 73:169, 1932.

[129] W. Pauli. Die allgemeinen Prinzipien der Wellenmechanik. *Handbuch der Physik*, 24:83–272, 1933.

[130] H. Hellmann. *Einführung in die Quantenchemie*. Franz Deuticke, Leipzig, 1937.

[131] R. P. Feynman. Forces in molecules. *Phys. Rev*, 56:340, 1939.

[132] S. Clark. *Complex Structure in Tetrahedral Semiconductors*. PhD thesis, University of Edinburgh, 1994.

[133] M. Sprik. Computer Simulation of the Dynamics of Induced Polarization Fluctuations in Water. *J. Phys. Chem.*, 95:2283, 1991.

[134] J. F. Dobson, K. McLennan, A. Rubio, J. Wang, T. Gould, H. M. Le, and B. P. Dinte. Prediction of Dispersion Forces: Is There a Problem? *Aust. J. Chem.*, 54:513, 2001.

[135] W. Kohn, Y. Meir, and D. Makarov. van der Waals Energies in Density Functional Theory. *Phys. Rev. Lett.*, 80:4153, 1998.

[136] J. Klimes and A. Michaelides. Perspective: Advances and challenges in treating van der Waals dispersion forces in density functional theory. *J. Chem. Phys.*, 137:120901, 2012.

[137] P. L. Silvestrelli and A. Ambrosetti. van der Waals corrected DFT simulation of adsorption processes on transition-metal surfaces: Xe and graphene on Ni(111). *Phys. Rev. B*, 91:195405, 2015.

[138] M. P. Andersson. Density Functional Theory with Modified Dispersion Correction for Metals Applied to Self-Assembled Monolayers of Thiols on Au(111). *Journal of Theoretical Chemistry*, 2013(ID:327839), 2013.

[139] K. E. Riley, M. Pitonak, P. Jurecka, and P. Hobza. Stabilization and Structure Calculations for Noncovalent Interactions in Extended Molecular Systems Based on Wave Function and Density Functional Theories. *Chem. Rev.*, 110:5023, 2010.

[140] X. Wu, M. C. Vargas, S. Nayak, V. Lotrich, and G. Scoles. Towards extending the applicability of density functional theory to weakly bound systems. *J. Chem. Phys.*, 115:8748, 2001.

[141] T. Bucko, J. Hafner, S. Lebegue, and J. G. Angyan. Improved Description of the Structure of Molecular and Layered Crystals: Ab Initio DFT Calculations with van der Waals Corrections. *J. Phys. Chem. A*, 114:11814, 2010.

[142] S. Grimme. Semiempirical GGA-type density functional constructed with a long-range dispersion correction. *J. Comput. Chem*, 27:1787, 2006.

[143] P. W. Atkins. *The Second Law*. Scientific American Books, first edition, 1984.

[144] P. A. Apte and I. Kusaka. Evaluation of the translational free energy in a melting temperature calculation by simulation. *Phys. Rev. E*, 73:016704, 2006.

[145] J. L. Klepeis, K. Lindorff-Larsen, R. O Dror, and D. E. Shaw. Long-timescale molecular dynamics simulations of protein structure and function. *Curr. Opin. Struct. Biol.*, 19:120, 2009.

[146] E. A. Carter, G. Ciccotti, J. T. Hynes, and R. Kapral. Constrained reaction coordinate dynamics for the simulation of rare events. *Chem. Phys. Lett.*, 156:472, 1989.

[147] M. Sprik and G. Ciccotti. Free energy from constrained molecular dynamics. *J. Chem. Phys*, 109:7737, 1998.

[148] T. Mulders, P. Kruger, W. Swegat, and J. Schlitter. Free energy as the potential of mean constraint force. *J. Chem. Phys*, 104:4869, 1996.

[149] E. Darve and A. Pohorille. Calculating free energies using average force. *J. Chem. Phys*, 115:9169, 2001.

[150] Y. Deng and B. Roux. Computations of standard binding free energies with molecular dynamics simulations. *J. Phys. Chem. B*, 113:2234, 2009.

[151] S. Awasthi, V. Kapil, and N. N. Nair. Sampling Free Energy Surfaces as Slices by Combining Umbrella Sampling and Metadynamics. *J. Comput. Chem*, 37:1413, 2016.

[152] E. Weinan and E. Vanden-Eijnden. Metastability, conformation dynamics, and transition pathways in complex systems. In *Multiscale Modelling and Simulation*, pages 35–68. Springer Berlin Heidelberg, 2004.

[153] G. Ciccotti and M. Ferrario. Rare events by constrained molecular dynamics. *Journal of Molecular Liquids*, 89:1, 2000.

[154] J. Wang, Y. Deng, and B. Roux. Absolute binding free energy calculations using molecular dynamics simulations with restraining potentials. *Biophys. J*, 91:2798, 2006.

[155] A. Barducci, M. Bonomi, and M. Parrinello. Metadynamics. *WIREs Computational Molecular Science*, 1:826, 2011.

[156] P. G. Bolhuis, D. Chandler, C. Dellago, and P. L. Geissler. Transition path sampling: throwing ropes over rough mountain passes, in the dark. *Annu. Rev. Phys. Chem.*, 53:291, 2002.

[157] L. Rosso, P. Mináry, Z. Zhu, and M. E. Tuckerman. On the use of the adiabatic molecular dynamics technique in the calculation of free energy profiles. *J. Chem. Phys.*, 116:4389, 2002.

[158] T. Bucko. Ab initio calculations of free-energy reaction barriers. *J. Phys.: Condens. Matter*, 20:064211, 2008.

[159] W. K. den Otter. Thermodynamic integration of the free energy along a reaction coordinate in Cartesian coordinates. *J. Chem. Phys.*, 112:7283, 2000.

[160] W. K. den Otter and W. J. Briels. The calculation of free-energy differences by constrained molecular-dynamics simulations. *J. Chem. Phys.*, 109:4139, 1998.

[161] W. F. Van Gunsteren, X. Daura, and A. E. Mark. Computation of free energy. *Helvetica Chimica Acta*, 85:3113, 2002.

[162] C. Abrams and G. Bussi. Enhanced sampling in molecular dynamics using metadynamics, replica-exchange, and temperature-acceleration. *Entropy*, 16:163, 2014.

[163] E. Darve. Numerical Methods for Calculating the Potential of Mean Force. In B. Leimkuhler, editor, *New Algorithms for Macromolecular Simulation*, chapter 4, pages 213–249. Springer Berlin Heidelberg, 2006.

[164] M. Retegan, M. Martins-Costa, and M. F. Ruiz-López. Free energy calculations using dual-level Born-Oppenheimer molecular dynamics. *J. Chem. Phys.*, 133:064103, 2010.

[165] M. J. Ruiz-Montero, D. Frenkel, and J. J. Brey. Efficient schemes to compute diffusive barrier crossing rates. *Mol. Phys.*, 90:925, 1997.

[166] C. Hartmann and C. Schutte. A geometric approach to constrained molecular dynamics and free energy. *Comm. Math. Sci.*, 3:1, 2005.

[167] R. J. Radmer and P. A. Kollman. Free energy calculation methods: A theoretical and empirical comparison of numerical errors and a new method qualitative estimates of free energy changes. *J. Comput. Chem*, 18:902, 1997.

[168] Y. Komeiji. Implementation of the blue moon ensemble method. *Chem-Bio Informatics Journal*, 7:12, 2007.

[169] G. Ciccotti, R. Kapral, and A. Sergi. Simulating reactions that occur once in a blue moon. In S. Yip, editor, *Handbook of Materials Modeling*, volume I, chapter 5.4, pages 1597–1611. Springer Netherlands, 2005.

[170] G. Ciccotti and M. Ferrario. Blue Moon Approach to Rare Events. *Molecular Simulation*, 30:787, 2004.

[171] J. Schlitter, W. Swegat, and T. Mülders. Distance-type reaction coordinates for modelling activated processes. *J. Mol. Model*, 7:171, 2001.

[172] G. Ciccotti, R. Kapral, and E. Vanden-Eijnden. Blue moon sampling, vectorial reaction coordinates, and unbiased constrained dynamics. *ChemPhysChem*, 6:1809, 2005.

[173] D. Marx and J. Hutter. Ab initio molecular dynamics: Theory and implementation. In J. Grotendorst, editor, *Modern Methods and Algorithms of Quantum Chemistry*, volume 1, pages 301–449. John von Neumann Institute for Computing, Jülich, 2000.

[174] D. Marx and J. Hutter. *Ab Initio Molecular Dynamics: Basic Theory and Advanced Methods*. Cambridge University Press, 2009.

[175] G. Cuniberti, G. Fagas, and K. Richter. Introducing molecular electronics: A brief overview. In G. Cuniberti, G. Fagas, and K. Richter, editors, *Introducing molecular electronics*, chapter 1. Springer-Verlag Berlin Heidelberg, 2006.

[176] M. Ormaza, P. Abufager, N. Bachellier, R. Robles, and M. Verot et al. Assembly of Ferrocene Molecules on Metal Surfaces Revisited. *J. Phys. Chem. Lett.*, 6:395, 2015.

[177] T. Komeda, H. Isshiki, J. Liu, Y.-F. Zhang, N. Lorente, K. Katoh, B. K. Breedlove, and M. Yamashita. Observation and electric current control of a local spin in a single-molecule magnet. *Nat. Commun.*, 2:217, 2011.

[178] T. Uehara, R. V. Belosludov, A. A. Farajian, H. Mizuseki, and Y. Kawazoe. Electronic and Transport Properties of Ferrocene: Theoretical Study. *Jpn. J. Appl. Phys.*, 45:3768, apr 2006.

[179] Y. Zhang and M. Deng. Electrical Control of Spin States of Ferrocene on Cu(111). *J. Phys. Chem. C*, 119:21681, 2015.

[180] W. Shockley. On the surface states associated with a periodic potential. *Phys. Rev.*, 56:317, 1939.

[181] J. Kliewer, R. Berndt, E. V. Chulkov, V. M. Silkin, P. M. Echenique, and S. Crampin. Dimensionality Effects in the Lifetime of Surface States. *Science*, 288:1399, 2000.

[182] P. N. Abufager, R. Robles, and N. Lorente. FeCoCp3 Molecular Magnets as Spin Filters. *J. Phys. Chem. C*, 119:12119, 2015.

[183] S. Coriani, A. Haaland, T. Helgaker, and P. Jørgensen. The equilibrium structure of ferrocene. *ChemPhysChem*, 7:245, jan 2006.

[184] J. W. Edwards, G. L. Kington, and R. Mason. The thermodynamic properties of ferrocene. Part 1. The low-temperature transition in ferrocene crystals. *Transactions of the Faraday Society*, 56:660, 1960.

[185] T. J. Kealy and P. L. Pauson. A New Type of Organo-Iron Compound. *Nature*, 168:1039, 1951.

[186] J. D. Roberts and M. C. Caserio. Transition-metal organic compounds. In *Basic Principles of Organic Chemistry*, chapter 31, page 1504. Addison-Wesley, second edition, 1977.

[187] S. A. Miller, J. A. Tebboth, and J. F. Tremaine. Dicyclopentadienyliron. *J. Chem. Soc. (Res.)*, page 632, 1952.

[188] H. Werner. At Least 60 Years of Ferrocene - The Discovery and Rediscovery of the Sandwich Complexes. *Angew. Chem. Int. Ed.*, 51:6052, 2012.

[189] W. Pfab and E. O. Fischer. Zur Kristallstruktur der Di-cyclopentadienyl-verbindungen des zweiwertigen Eisens, Kobalts und Nickels. *Z. Anorg. Allg. Chem.*, 274:316, 1953.

[190] G. Wilkinson. The iron sandwich. A recollection of the first four months. *J. Organomet. Chem*, 100:273, 1975.

[191] D. L. Pugmire, C. M. Woodbridge, and M. A. Langell. Orientation of nickelocene on Ag (100). *Surf. Sci.*, 411:L844, 1998.

[192] J. Choi and P. A. Dowben. Cobaltocene adsorption and dissociation on Cu(111). *Surf. Sci.*, 600:2997, 2006.

[193] G. Wilkinson, P. L. Pauson, and F. A. Cotton. Bis-cyclopentadienyl Compounds of Nickel and Cobalt. *J. Am. Chem. Soc.*, 76:1970, 1954.

[194] T. Saito. *Inorganic Chemistry*. Introductory Chemistry Series Vol. III, Iwanami Shoten Publ., Japan, 2014.

[195] C. H. Wang, L. F. Xu, X.-L. Fan, and J.-T. Wang. Structural stability and electronic property of sandwich clusters (CmHm)Mn(CnHn) (m, n = 5, 6) following an 18-electron principle. *Physics Letters A*, 375:562, 2011.

[196] M. Weller, T. Overton, J. Rourke, and F. Armstrong. Inorganic chemistry. chapter 22, page 608. OUP Oxford, 6th edition, 2014.

[197] A. Haaland and J. E. Nilsson. The determination of barriers to internal rotation by means of electron diffraction. Ferrocene and ruthenocene. *Acta Chem. Scand.*, 22:2653, 1968.

[198] N. Mohammadi, A. Ganesan, C. T. Chantler, and F. Wang. Differentiation of ferrocene D5d and D5h conformers using IR spectroscopy. *J. Organomet. Chem*, 713:51, 2012.

[199] A. D. McNaught and A. Wilkinson. IUPAC. Compendium of Chemical Terminology. page 1447. Blackwell Scientific Publications, Oxford, 1997.

[200] K. L. Williamson and K. M. Masters. Macroscale and Microscale Organic Experiments. page 638. Cengage Learning, 2010.

[201] F. A. Almeida Paz, J. Klinowski, S. M. F. Vilela, J. P. C. Tomé, J. A. S. Cavaleiro, and J. Rocha. Ligand design for functional metal–organic frameworks. *Chem. Soc. Rev. Reviews*, 41:1088, 2012.

[202] N. A. Spaldin. Computational Design of a New Magnetic Ferroelectric. In M. Fiebig, V. V. Eremenko, and I. E. Chupis, editors, *Magnetoelectric Interaction Phenomena in Crystals*, pages 87–104. Springer Netherlands, 2004.

[203] T. S. Chwee and M. B. Sullivan. Adsorption studies of C6H6 on Cu (111), Ag (111), and Au (111) within dispersion corrected density functional theory. *J. Chem. Phys.*, 137:134703, 2012.

[204] CPMD; Copyright IBM Corp. 1990-2016, Copyright MPI für Festkörperforschung Stuttgart 1997-2001, http://www.cpmd.org/.

[205] M. Brookhart and M. L. H. Green. Carbon-hydrogen transition metal bonds. *J. Organomet. Chem*, 250:395, 1983.

[206] M. Brookhart, M. L. H. Green, and G. Parkin. Agostic interactions in transition metal compounds. *Proc. Natl. Acad. Sci. USA.*, 104:6908, 2007.

[207] M. Boero, M. Parrinello, S. Huffer, and H. Weiss. First Principles Study of Propene Polymerization in Ziegler-Natta Heterogeneous Catalysis. *J. Am. Chem. Soc.*, 122:501, 2000.

[208] M. Brookhart and W. B. Studabaker. Cyclopropanes from reactions of transition metal carbene complexes with olefins. *Chem. Rev.*, 87:411, 1987.

[209] A. Archambeau, F. Miege, C. Meyer, and J. Cossy. Intramolecular cyclopropanation and C-H insertion reactions with metal carbenoids generated from cyclopropenes. *Acc. Chem. Res.*, 48:1021, 2015.

[210] N. Agenet, V. Gandon, K. P. C. Vollhardt, M. Malacria, and C. Aubert. Cobalt-catalyzed cyclotrimerization of alkynes: The answer to the puzzle of parallel reaction pathways. *J. Am. Chem. Soc.*, 129:8860, 2007.

[211] J. P. Lomont, S. C. Nguyen, M. C. Zoerb, A. D. Hill, J. P. Schlegel, and C. B. Harris. Observation of a short-lived triplet precursor in CpCo(CO)-catalyzed alkyne cyclotrimerization. *Organometallics*, 31:3582, 2012.

[212] M. I. J. Probert. Improved algorithm for geometry optimisation using damped molecular dynamics. *J. Comput. Phys.*, 191:130, 2003.

[213] A. K. Gupta and M. Gupta. Synthesis and surface engineering of iron oxide nanoparticles for biomedical applications. *Biomaterials*, 26:3995, 2005.

[214] N. Pamme and C. Wilhelm. Continuous sorting of magnetic cells via on-chip free-flow magnetophoresis. *Lab on a Chip*, 6:974, 2006.

[215] R. Qiao, C. Yang, and M. Gao. Superparamagnetic iron oxide nanoparticles: from preparations to in vivo MRI applications. *J. Mater. Chem.*, 19:6274, 2009.

[216] S. Sun and H. Zeng. Size-controlled synthesis of magnetite nanoparticles. *J. Am. Chem. Soc.*, 124:8204, 2002.

[217] G. I. Frolov. Film carriers for super-high-density magnetic storage. *Technical Physics*, 46:1537, 2001.

[218] S. Kinge, M. Crego-Calama, and D. N. Reinhoudt. Self-Assembling Nanoparticles at Surfaces and Interfaces. *ChemPhysChem*, 9:20, 2008.

[219] P. N. R. Kishore and P. Jeevanandam. A novel thermal decomposition approach for the synthesis of silica-iron oxide core-shell nanoparticles. *Journal of Alloys and Compounds*, 522:51, 2012.

[220] C. T. Dinh, T. D. Nguyen, F. Kleitz, and T. O. Do. Shape-Controlled Synthesis of Metal Oxide Nanocrystals. In R.-S. Lui, editor, *Controlled Nanofabrication: Advances and Applications*, volume 3, chapter 10, page 327. CRC Press, 2012.

[221] Y. Xia, Y. Xiong, B. Lim, and S. Skrabalak. Shape-Controlled Synthesis of Metal Nanocrystals: Simple Chemistry Meets Complex Physics? *Angew. Chem. Int. Ed.*, 48:60, 2009.

[222] L. Gonzalez-Moragas, S.-M. Yu, N. Murillo-Cremaes, A. Laromaine, and A. Roig. Scale-up synthesis of iron oxide nanoparticles by microwave-assisted thermal decomposition. *Chemical Engineering Journal*, 281:87, 2015.

[223] P. Guardia, R. Di Corato, L. Lartigue, C. Wilhelm, and A. Espinosa et al. Water-soluble iron oxide nanocubes with high values of specific absorption rate for cancer cell hyperthermia treatment. *ACS Nano*, 6:3080, 2012.

[224] F. Gazeau, M. Lévy, and C. Wilhelm. Optimizing magnetic nanoparticle design for nanothermotherapy. *Nanomedicine*, 3:831, 2008.

[225] J.-H. Lee, J.-T. Jang, J.-S. Choi, S. H. Moon, S.-H. Noh, J.-W. Kim, J.-G. Kim, I.-S. Kim, K. I. Park, and J. Cheon. Exchange-coupled magnetic nanoparticles for efficient heat induction. *Nature nanotechnology*, 6:418, 2011.

[226] H. Ustunel and Ş. Erkoç. Structural Properties and Stability of Nanoclusters. *J. Comput. Theor. Nanosci.*, 4:1, 2007.

[227] J. R. Morones, J. L. Elechiguerra, A. Camacho, K. Holt, and J. B. Kouri et al. The bactericidal effect of silver nanoparticles. *Nanotechnology*, 16:2346, 2005.

[228] A. Demortière, P. Panissod, B. P. Pichon, G. Pourroy, and D. Guillon et al. Size-dependent properties of magnetic iron oxidenanocrystals. *Nanoscale*, 3:225, 2011.

[229] G. Rahmi, L. Pidial, A. K. A. Silva, E. Blondiaux, and B. Meresse et al. Designing 3D Mesenchymal Stem Cell Sheets Merging Magnetic and Fluorescent Features: When Cell Sheet Technology Meets Image-Guided Cell Therapy. *Theranostics*, 6:739, 2016.

[230] J. He, S. Duan, X. Yu, Z. Qian, and S. Zhou et al. Folate-modified Chitosan Nanoparticles Containing the IP-10 Gene Enhance Melanoma-specific

Cytotoxic CD8(+)CD28(+) T Lymphocyte Responses. *Theranostics*, 6:752, 2016.

[231] L. Zou, H. Wang, B. He, L. Zeng, and T. Tan et al. Current Approaches of Photothermal Therapy in Treating Cancer Metastasis with Nanotherapeutics. *Theranostics*, 6:762, 2016.

[232] C. R. Martin. Nanomaterials: A Membrane-Based Synthetic Approach. *Science*, 266:1961, 1994.

[233] S. J. Smith, B. Huang, S. Liu, Q. Liu, and R. E. Olsen et al. Synthesis of metal oxide nanoparticles via a robust "solvent-deficient" method. *Nanoscale*, 7:144, 2015.

[234] L. Zhang and D. Xue. Preparation and magnetic properties of pure CoO nanoparticles. *J. Mater. Sci. Lett.*, 21:1931, 2002.

[235] S. K. Pahari, N. Sutradhar, A. Sinhamahapatra, P. Pal, and A. B. Panda. Synthesis of nearly monodispersed metal oxide nanoparticles in water. *New J. Chem.*, 35:1460, 2011.

[236] H.-T. Zhang and X.-H. Chen. Controlled synthesis and anomalous magnetic properties of relatively monodisperse CoO nanocrystals. *Nanotechnology*, 16:2288, 2005.

[237] T. Hyeon, S. S. Lee, J. Park, Y. Chung, and H. B. Na. Synthesis of highly crystalline and monodisperse maghemite nanocrystallites without a size-selection process. *J. Am. Chem. Soc.*, 123:12798, 2001.

[238] J. Park, K. An, Y. Hwang, J.-G. Park, and J. I. N. Noh et al. Ultra-large-scale syntheses of monodisperse nanocrystals. *Nature*, 3:891, 2004.

[239] S. Sun, H. Zeng, D. B. Robinson, S. Raoux, and P. M. Rice et al. Monodisperse MFe2O4 (M= Fe, Co, Mn) nanoparticles. *J. Am. Chem. Soc.*, 126:273, 2004.

[240] A.-H. Lu, E. L. Salabas, and F. Schuth. Magnetic Nanoparticles: Synthesis, Protection, Functionalization, and Application. *Angew. Chem. Int. Ed.*, 46:1222, 2007.

[241] T. O. Ely, C. Amiens, B. Chaudret, E. Snoeck, and M. Verelst et al. Synthesis of Nickel Nanoparticles . Influence of Aggregation Induced by Modification of Poly (vinylpyrrolidone) Chain Length on Their Magnetic Properties. *Chem. Mater.*, 11:526, 1999.

[242] T. Pellegrino, L. Manna, S. Kudera, T. Liedl, and D. Koktysh et al. Hydrophobic nanocrystals coated with an amphiphilic polymer shell: A general route to water soluble nanocrystals. *Nano Lett.*, 4:703, 2004.

[243] N. R. Jana, Y. Chen, and X. Peng. Size-and shape-controlled magnetic (Cr, Mn, Fe, Co, Ni) oxide nanocrystals via a simple and general approach. *Chem. Mater.*, 16:3931, 2004.

[244] D. Maity, J. Ding, and J.-M. Xue. Synthesis of Magnetite Nanoparticles by Thermal Decomposition: Time, Temperature, Surfactant and Solvent Effects. *Functional Materials Letters*, 1:189, 2008.

[245] N. Pinna and M. Niederberger. Surfactant-free nonaqueous synthesis of metal oxide nanostructures. *Angew. Chem. Int. Ed.*, 47:5292, 2008.

[246] W. Baaziz. *Synthèse et caractérisation des nanoparticules spinelles et coeur-coquille à base d'oxyde de fer et de cobalt.* Phd thesis, Universite of Strasbourg, 2011.

[247] L. M. Bronstein, X. Huang, J. Retrum, A. Schmucker, and M. Pink et al. Influence of Iron Oleate Complex Structure on Iron Oxide Nanoparticle Formation. *Chem. Mater.*, 19:3624, 2007.

[248] S. Navaladian, B. Viswanathan, R. P. Viswanath, and T. K. Varadarajan. Thermal decomposition as route for silver nanoparticles. *Nanoscale Res. Lett.*, 2:44, 2007.

[249] J. E. Macdonald, C. J. Brooks, and J. G. C. Veinot. The influence of trace water concentration on iron oxide nanoparticle size. *Chem. Commun.*, page 3777, 2008.

[250] W. Baaziz, B. P. Pichon, C. Lefevre, C. Ulhaq-Bouillet, and J.-M. Greneche et al. High Exchange Bias in Fe(3-delta)O4@CoO Core Shell

Nanoparticles Synthesized by a One-Pot Seed-Mediated Growth Method. *J. Phys. Chem. C*, 117:11436, 2013.

[251] W. Baaziz, S. Begin-Colin, B. P. Pichon, I. Florea, and O. Ersen et al. High-Density Monodispersed Cobalt Nanoparticles Filled into Multiwalled Carbon Nanotubes. *Chem. Mater.*, 24:1549, 2012.

[252] W. Baaziz, B. P. Pichon, Y. Liu, J.-M. Grene, and C. Ulhaq-bouillet et al. Tuning of Synthesis Conditions by Thermal Decomposition toward Core - Shell Co(x)Fe(1-x)O@Co(y)Fe(3-y)O4 and CoFe2O4 Nanoparticles with Spherical and Cubic Shapes. *Chem. Mater.*, 26:5063, 2014.

[253] H. K. J. Powell and H. Nancollas. Coordination of Oxygen by Cobalt (II) Complexes in Aqueous Solution. A Calorimetric Study. *J. Am. Chem. Soc.*, 94:2664, 1972.

[254] B. Wagner, D. Reinen, Th. C. Brunold, and H. U. Gudel. Iron(VI) in Tetrahedral Oxo Coordination: A Single Crystal EPR Study. *Inorg. Chem.*, 34:1934, 1995.

[255] D. Marx, M. E. Tuckerman, J. Hutter, and M. Parrinello. The nature of the hydrated excess proton in water. *Nature*, 397:601, 1998.

[256] G. S. Pokrovski, J. Schott, F. Farges, and J.-L. Hazemann. Iron (III)-silica interactions in aqueous solution: Insights from X-ray absorption fine structure spectroscopy. *Geochimica et Cosmochimica Acta*, 67:3559, 2003.

[257] L. Helm and A. E. Merbach. Water exchange on metal ions: experiments and simulations. *Coord. Chem. Rev.*, 187:151, 1999.

[258] R. P. Houghton. *Metal Complexes-Organic Chemistry*. Cambridge Texts in Chemistry and Biochemistry. Cambridge University Press, 1979.

[259] C. H. Langford and H. B. Gray. *Ligand substitution processes*. Benjamin, New York, 1967.

[260] T. W. Swaddle. On the Mechanism of Octahedral Substitution. *Comment Inorg. Chem.*, 12:237, 1991.

[261] S. J. Peighambardoust, S. Rowshanzamir, and M. Amjadi. Review of the proton exchange membranes for fuel cell applications. *Int. J. Hydrogen Energy*, 35:9349, 2010.

[262] A. V. Krasheninnikov, P. O. Lehtinen, A. S. Foster, P. Pyykkö, and R. M. Nieminen. Embedding transition-metal atoms in graphene: Structure, bonding, and magnetism. *Phys. Rev. Lett.*, 102:126807, 2009.

[263] M. Sun, H. Liu, Y. Liu, J. Qu, and J. Li. Graphene-based transition metal oxide nanocomposites for the oxygen reduction reaction. *Nanoscale*, 7:1250, 2015.

[264] S. Okada and A. Oshiyama. Electronic structure of metallic rhombohedral C60 polymers. *Phys. Rev. B*, 68:235402, 2003.

[265] N. Park, M. Yoon, S. Berber, J. Ihm, and E. Osawa et al. Magnetism in all-carbon nanostructures with negative gaussian curvature. *Phys. Rev. Lett.*, 91:237204, 2003.

[266] A. Rodríguez-Fortea, A. L. Balch, and J. M. Poblet. Endohedral metallofullerenes: a unique host–guest association. *Chemical Society Reviews*, 40(7):3551, 2011.

[267] A. Rodríguez-Fortea, N. Alegret, A. L. Balch, and J. M. Poblet. The maximum pentagon separation rule provides a guideline for the structures of endohedral metallofullerenes. *Nature chemistry*, 2:955, 2010.

[268] K. Toth, J. K. Molloy, M. Matta, B. Heinrich, and D. Guillon et al. A strongly emitting liquid-crystalline derivative of Y3N@C80: Bright and long-lived near-IR luminescence from a charge transfer state. *Angew. Chem. Int. Ed.*, 52:12303, 2013.

[269] D. Felder-Flesch. Self- or Induced Organization of [60] Fullerene Hexakisadducts. In J.-F. Nierengarten, editor, *Fullerenes and Other Carbon-Rich Nanostructures*, pages 101–143. Springer Berlin Heidelberg, 2013.

[270] I. M. L. Billas, C. Massobrio, M. Boero, M. Parrinello, and W. Branz et al. First principles calculations of iron-doped heterofullerenes. *Computational Materials Science*, 17(2-4):191, 2000.

[271] M. Matsubara, J. Kortus, J. C. Parlebas, and C. Massobrio. Dynamical identification of a threshold instability in Si-doped heterofullerenes. *Phys. Rev. Lett.*, 96:155502, 2006.

[272] R. Scipioni, M. Matsubara, E. Ruiz, C. Massobrio, and M. Boero. Thermal behavior of Si-doped fullerenes vs their structural stability at T = 0 K: A density functional study. *Chem. Phys. Lett.*, 510:14, 2011.

[273] T. W. Chamberlain, J. C. Meyer, J. Biskupek, J. Leschner, and A. Santana et al. Reactions of the inner surface of carbon nanotubes and nanoprotrusion processes imaged at the atomic scale. *Nature chemistry*, 3:732, 2011.

[274] B. Y. Sun, Y. Sato, K. Suenaga, T. Okazaki, and N. Kishi et al. Entrapping of exohedral metallofullerenes in carbon nanotubes: (CsC60)n@SWNT nanopeapods. *J. Am. Chem. Soc.*, 127:17972, 2005.

[275] G. Krosnicki. *Utilisation de fullerène comme support de catalyseur pour les piles à combustible de type PEMFC.* PhD thesis, University of Strasbourg, 2011.

[276] Y. Rikiishi, Y. Kashino, H. Kusai, Y. Takabayashi, and E. Kuwahara et al. Metallic phase in the metal-intercalated higher fullerene Rb8.8(7)C84. *Phys. Rev. B*, 71:224118, 2005.

[277] K. Prassides, J. C. Hummelen, W. Andreoni, P. Giannozzi, and E. Beer et al. Isolation, Structure, and Electronic Calculations of the Heterofullerene Salt K6C59N. *Science*, 271:1833, 1996.

[278] W. Andreoni and A. Curioni. Freedom and Constraints of a Metal Atom Encapsulated in Fullerene Cages. *Phys. Rev. Lett.*, 77:834, 1996.

[279] W. Andreoni. Computational Approach to the Physical Chemistry of Fullerenes and Their Derivatives. *Annu. Rev. Phys. Chem.*, 49:405, 1998.

[280] M. Steinmetz and S. Grimme. Benchmark study of the performance of density functional theory for bond activations with (Ni,Pd)-based transition-metal catalysts. *ChemistryOpen*, 2:115, 2013.

[281] R. N. Barnett and U. Landman. Born-Oppenheimer molecular-dynamics simulations of finite systems: Structure and dynamics of (H2O)2. *Phys. Rev. B*, 48:2081, 1993.

[282] A. Scheidemann. van der Waals forces between metal microclusters and fullerenes. *Phys. Rev. A*, 49:R4293, 1994.

[283] J. Hutter, H. P. Luthi, and M. Parrinello. Electronic structure optimization in plane-wave-based density functional calculations by direct inversion in the iterative subspace. *Comput. Mater. Sci.*, 2:244, 1994.

[284] N. Marzari and D. Vanderbilt. Maximally-localized generalized Wannier functions for composite energy bands. *Phys. Rev. B*, 56:12847, 1997.

[285] R. Resta and S. Sorella. Electron Localization in the Insulating State. *Phys. Rev. Lett.*, 82:370, 1998.

[286] M. Boero. Excess electron in water at different thermodynamic conditions. *J. Phys. Chem. A*, 111:12248, 2007.

[287] P. L. Silvestrelli, N. Marzari, D. Vanderbilt, and M. Parrinello. Maximally-localized Wannier functions for disordered systems: Application to amorphous silicon. *Solid State Communications*, 107:7, 1998.

[288] I. M. L. Billas, C. Massobrio, M. Boero, M. Parrinello, and W. Branz et al. First principles calculations of Si doped fullerenes: Structural and electronic localization properties in C59Si and C58Si2. *J. Chem. Phys.*, 111:6787, 1999.

[289] F. L. Gervasio, A. Laio, M. Parrinello, and M. Boero. Charge localization in DNA fibers. *Phys. Rev. Lett.*, 94:158103, 2005.

[290] L. M. Ramaniah, M. Boero, and M. Laghate. Tantalum-fullerene clusters: A first-principles study of static properties and dynamical behavior. *Phys. Rev. B*, 70:035411, 2004.

[291] M. Matsubara, C. Massobrio, L. M. Ramaniah, E. Ruiz, and M. Boero et al. Electronic structure and localization properties of C60Ta(n) clusters (n=1,3): A first-principles study. *Phys. Rev. B*, 81:195433, 2010.

[292] B. P. Feuston, W. Andreoni, M. Parrinello, and E. Clementi. Electronic and Vibrational Properties of C60 at Finite Temperature from Abinitio Molecular-Dynamics. *Phys. Rev. B*, 44:4056, 1991.

[293] S. Saito and A. Oshiyama. Cohesive mechanism and energy bands of solid C60. *Phys. Rev. Lett.*, 66:2637, 1991.

[294] S. M. Lee, R. J. Nicholls, D. Nguyen-Manh, D. G. Pettifor, and G. A. D. Briggs et al. Electron energy loss spectra of C60 and C70 fullerenes. *Chem. Phys. Lett.*, 404:206, 2005.

[295] K. Morokuma and W. T. Borden. Ab initio calculations on (H3P)2Pt(C2H4). The effect of alkene pyramidalization on internal rotation and alkene binding energies. *J. Am. Chem. Soc.*, 113:1912, 1991.

[296] Q. Zhou, S. Coh, M. L. Cohen, S. G. Louie, and A. Zettl. Imprint of transition metal d orbitals on a graphene Dirac cone. *Phys. Rev. B*, 88:253431, 2013.

[297] G. W. Graham, P. J. Schmitz, and P. A. Thiel. Growth of Rh, Pd, and Pt films on Cu(100). *Phys. Rev. B*, 41:3353, 1990.

Résumé

Ce travail de thèse est focalisé sur l'interaction de molécules organométalliques avec des métaux de transition. Cette thématique a un large éventail d'applications dans plusieurs domaines tels que la réalisation de nanojonctions pour la nano-électronique, la bioimagerie et le stockage d'énergie magnétique, la nano-catalyse et les applications biomédicales. Dans ce cadre général, ce projet de thèse vise la modélisation à l'échelle atomique des interactions fondamentales entre les briques moléculaires afin de comprendre leur rôle dans l'assemblage et la fonctionnalisation des nanostructures. L'outil principal utilisé est la dynamique moléculaire à partir des premiers principes selon les approches Born-Oppenheimer et Car-Parrinello. La première partie de cette thèse présente une rétrospective du domaine afin de donner une vision d'ensemble des méthodes utilisées et de l'état de l'art dans ce domaine. Le deuxième chapitre donne les éléments de base de la théorie et les méthodes qui ont été utilisées dans la thèse, au développement desquels on a aussi contribué pendant ce projet de recherche. Les résultats obtenus et leur discussion critique constituent le corps principal de cette ouvrage de thèse. Ceci est organisé dans un chapitre unique (troisième chapitre), divisé en trois sous-chapitre pour des raisons de clarté.

Dynamique moléculaire, dynamique contrainte, électronique moléculaire, jonctions moléculaires, ferrocène, fullerène, précurseur métal-organique.

Résumé en anglais

The purpose of this study is to investigate the interaction of organometallic complexes with transition metals. This topic in question has a broad array of applications in a number of domain; realization of nanojunctions for molecular nanoelectronics, biological imaging and nanocatalysis. Within this general framework, this PhD project aims to model the fundamental interactions of molecular building blocks at the atomic level in order to understand their role in the assembly and functionalization of nanostructures. The principal tool used in this study is first-principles simulation methods such as the Born-Oppenheimer and Car-Parrinello molecular dynamics. The first chapter presents an emphasis of the current developments in the related field alongside of a retrospective on the historical developments that leads today's knowledge. The second chapter presents the basic elements of the theory behind the methods that were used in the thesis, whose development has also been contributed during this research project. Lastly, the third chapter which is organized in three sub-chapters enumerates and describes the results of the various systems studied.

Molecular dynamics, constrained dynamics, molecular electronics, molecular junctions, ferrocene, fullerene, metal-organic precursors.